# BULGARIAN CHEMICAL COMMUNICATIONS

2026 Volume 58 / Number 1

*Journal of the Chemical Institutes*
*of the Bulgarian Academy of Sciences*
*and of the Union of Chemists in Bulgaria*

*Bulgarian Chemical Communications, Volume 58, Issue 1 (pp. i-ii) 2026* *DOI: 10.34049/bcc.58.1.IMDM*

# IN MEMORIAM

## Dedicated to the memory of Prof. DSc Dimitar R. Mehandzhiev (1933-2026)

Dimitar R. Mehandzhiev was born on July 20, 1933, in Sofia. His life and scientific path are a vivid example of dedicated service to science and a lasting contribution to the development of Bulgarian chemistry. He completed his secondary education in 1950 in Sofia, and in 1956 he graduated with honors in Chemistry at the Sofia University "St. Kliment Ohridski", laying the solid foundations of an extremely fruitful scientific career. His first professional steps were in industry - at the Soda Plant in Devnya and the Lead Mining Plant in Kurilo (both in Bulgaria), where he gained valuable practical experience. Since 1960, his life and scientific path were permanently connected with the Institute of General and Inorganic Chemistry at the Bulgarian Academy of Sciences - the institution to which he dedicated more than four decades of purposeful and inspired work. Here, he went through all stages of scientific growth: in 1968 he defended the degree of PhD and in 1983 - the degree of Doctor of Chemical Sciences (DSc). In 1985 he was elected Senior research associate (Professor). Until 2005 he headed the laboratory "Chemical Problems of Environmental Protection" at the Institute, turning it into one of the leading scientific units in the field of catalysis and environmentally oriented research.

At the very beginning of his scientific activity, Prof. DSc Dimitar Mehandzhiev laid the foundations of the research on magnetic properties of catalysts in Bulgaria. The creation of the first apparatus in our country for measuring the magnetic susceptibility of materials and the discovery of the magneto-catalytic effect in antiferromagnets are among his fundamental contributions with significant international resonance. These studies led to the formation of new conceptual approaches for the targeted selection and design of metal oxide catalysts.

His scientific research is marked by depth, systematicity and originality. A significant part of his works is dedicated to the clarification of the relationship "composition – structure – catalytic activity" in metal oxide catalysts based on 3d-transition metals. He developed thermodynamic models for the stability of oxides, introduced new criteria for the formation of non-stoichiometric phases and for the first time gave a theoretical explanation of a number of experimental dependencies related to the structure and activity of catalysts. He established that during catalytic processes, an active layer with a specific composition and structure is formed on the surface of oxides - a discovery of great importance for understanding catalytic mechanisms.

A significant contribution has also been made by his research on mixed oxides with a spinel structure which provided stabilization of the active phase and increased resistance to catalytic poisons. It has been shown that a number of spinels based on copper, nickel, cobalt and manganese exhibit high activity and selectivity in nitrogen oxide reduction reactions, which contributed to the establishment of effective catalysts based on non-noble metals.

The achievements in the development of ecocatalysis in Bulgaria occupy a special place in his scientific legacy. Prof. DSc Dimitar Mehandzhiev is among the pioneers in this field, and under his leadership non-platinum catalysts for treatment of waste and exhaust gases, as well as innovative metal oxide systems for the oxidation of carbon monoxide at room temperature were developed. New approaches for catalytic oxidation with ozone for the purification of liquid and gaseous media have also been created. The concepts he developed for adsorption and increased reactivity of nitrogen oxides on microporous media are widely recognized and applied.

The scientific activity of Prof. DSc Dimitar Mehandzhiev is also distinguished by the creation of a sustainable scientific school. His scientific assets include over 300 scientific publications, 23 copyright certificates and patents, some of which have been implemented with tangible economic effects, and his works have been cited more than 2000 times. He is co-author of the monographs

"Magnetochemistry of the solid state" and "Catalysis and environmental protection", recognized as significant scientific and educational publications. Under his leadership, 18 dissertations for the Doctor (PhD) degree have been defended, and his students and followers continue to successfully develop the scientific directions he started. Along with his scientific activity, Prof. DSc Dimitar Mehandzhiev also had a significant contribution as a scientific organizer and public figure. In the period 1992–1995 he was Deputy Chairman of the General Assembly of the Bulgarian Academy of Sciences, from 1993 to 2005 he was Deputy Director of the Institute of General and Inorganic Chemistry, and since 1996 - member of the Executive Board of the Bulgarian Academy of Sciences. His authority as a scientist and a personality made him a long-standing member of national expert and attestation bodies. For his exceptional scientific and applied achievements, Prof. DSc Dimitar Mehandzhiev has been awarded numerous awards, including the badge of Honor of the Bulgarian Academy of Sciences, the gold badge "For Contribution to Technical Progress", the title "Honored Inventor", as well as the "Marin Drinov" Order with ribbon. His name occupies a worthy place in international biographical directories of prominent scientists and intellectuals.

***Prof. Dr. Anton Naydenov***

***Institute of General and Inorganic Chemistry***

***Bulgarian Academy of Sciences***

*Bulgarian Chemical Communications, Volume 58, Issue 1 (pp. 5-15) 2026* *DOI: 10.34049/bcc.58.1.5721*

# Chemical characterization and performance analysis of post-modified microwave pyrolyzed karanja seed bio-oil

A. Mathiarasu[1*], S. Suresh Kumar[2], R. Senthil[3], R. Pandian[4]

[*1]*Department of Mechanical Engineering, Manakula Vinayagar Institute of Technology, Kalitheerthalkuppam 605107, Puducherry, India*

[2]*Department of Mechanical Engineering, PERI Institute of Technology, Mannivakkam, Chennai 600048, Tamil Nadu, India*

[3]*Department of Mechanical Engineering, C. Abdul Hakeem College of Engineering and Technology, Ranipet, Melvisharam 632509, Tamil Nadu, India*

[4]*Department of Mechanical Engineering, Dhanalakshmi Srinivasan University, Perambalur 621212, Tamil Nadu, India*

Received: September 11, 2025; Revised: October 21, 2025

Biomass has developed as a significant energy source capable of replacing regular fossil fuels such as coal and petroleum *via* different energy conversion methods. One such technique is pyrolysis, a process that thermally decomposes biomass in the absence of oxygen to produce valuable products. Microwave pyrolysis, which uses microwave energy to generate heat, is a method employed to convert non-edible biomass, like karanja seeds, into bio-fuel. To assess the efficacy of these bio-oil fuels, a Kirloskar four-stroke, single-cylinder, direct-injection diesel engine with a rated power output of 5.2 kW was used. The engine was tested with KB20, a blend of 20% karanja seed bio-oil and 80% diesel fuel, and EKB20 (post-modified bio-oil), a similar blend containing 20% karanja seed bio-oil and 80% diesel. The engine's performance was assessed based on cylinder pressure (PC), heat release rate (HRR) and brake thermal efficiency (BTE). The bio-oils produced from karanja seed microwave pyrolysis are dark brown and have a smoky odor. These bio-oils are significantly more viscous than diesel, with a calorific value of 27 MJ/kg—40 to 50% lower than that of diesel fuel. The assessments indicated that both KB20 and EKB20 blends resulted in increased PC and a faster HRR compared to diesel fuel. However, BTE decreased by 6.8% for KB20 and by 16.3% for EKB20 at maximum power output. Moreover, the use of these bio-oil blends led to higher concentrations of nitrogen oxides ($NO_x$) and increased smoke density relative to conventional diesel fuel.

**Keywords:** Diesel engine, Emulsification, Karanja bio-oil, Microwave pyrolysis, Thermal efficiency

## INTRODUCTION

Biomass fuels are firmly produced from the biomass residues of wood products, agro-based crops, dried leaves, etc., which are considered to be some of the worldwide biggest renewable sources of energy that have a vast potential in order to replace some of the conventionally available energy sources like coal and petroleum. The application of bio-fuels in industrial [1, 2] and transportation sectors can reduce the release of gases like $CO_2$. Agronomic residues, engineering, aquatic and municipal solid wastes can be renewed into gaseous, and solid fuels by thermo-chemical or biotic processes [3, 4]. Non-edible seeds have an opportunity to be used in the manufacture of biofuels. Such waste can be turned into valuable chemicals and fuels by pyrolysis. Research works on the conversion of non-edible seeds into bio-fuels through conventional pyrolysis are reported. However, research works on microwave pyrolysis of non-edible seeds are not reported, yet though they are available for biomass like corn cob, palm waste [5-8] among transesterification, gasification, etc. The term "pyrolysis" refers to a process of heating and cooling in order to produce alternate fuels. Pyrolysis process here produces microwave irradiation which is employed as a heat source to convert the microwave energy to thermal energy. In microwave heating, uniform and rapid heating can be achieved as there is a volumetric heating of the material involved. However, it is effective only for selective materials [9-11].

Around 7.27 % of moisture content has been identified in the conventionally produced karanja seed bio-oil. This may be due to the lack of breaking of water molecules in the thermal decomposition which, when conventionally done, results in higher water content, i.e., moisture content of bio-oil. On the other hand, microwave pyrolysis results in creating bio-oil of lower humidity permitting its broad use. Even though there is appreciable moisture content in the feedstock for microwave pyrolysis which in turn reduces the necessity for removal of

* To whom all correspondence should be sent: Email: *mathiarasuanbu@gmail.com*

the moisture content in any biomass feedstock by means of microwave irradiation, the polarization of the molecules enables the collision of the water molecules improving the heating rate of the microwave pyrolysis heating process. This benefits the production of moisture-free karanja bio-oil by microwave pyrolysis in reducing knocking and delayed combustion during running of the engine, thus increasing its application [12, 13]. Emulsification is a highly effective method of enhancing fuel quality, providing the necessary stability to prevent phase separation and allowing the blending of sources [14]. Several non-ionic emulsifying agents exhibit remarkable efficiency in facilitating the emulsion process between bio-oil and diesel [15]. Hence, in this research, we capitalized on the presence of karanja seeds in the forested areas in and around Puducherry to generate karanja seed bio-oil using microwave pyrolysis. Subsequently, we employed an emulsion process to combine the bio-oil with diesel, ensuring the blend's stability for prolonged storage and enhancing the fuel's quality by eliminating moisture content *via* titration method.

## EXPERIMENTAL

Karanja tree is drought-resistant, tolerates saline soils, and grows widely in tropical Asia.The non-consumable seeds of the Karanja trees are known for their rich oxygen content which is gathered from the woodland areas of Puducherry, India. The seeds shown in Figure 1 are brown, contain inside pods, and have a bitter taste.

**Figure 1.** Karanja seeds with pods

After carefully selecting the seeds, they are extracted from their shells and finely ground. The resulting powder is then sifted using a 1 mm mesh. To facilitate the emulsification process, various chemicals including diethyl ether, dichloromethane, Span 60, and Tween 60 were procured. These substances were selected based on their proven ability to enhance emulsion stability and efficiency. Diethyl ether and dichloromethane act as effective organic solvents, promoting the dispersion of hydrophobic components while Span 60 and Tween 60—nonionic surfactants—aid in reducing interfacial tension between oil and water phases. Their amphiphilic nature and compatibility with a wide range of formulation systems make them ideal for stable emulsion formation. This work conducted a comprehensive analysis of the karanja seeds, encompassing their proximate and elemental composition. This characterization aimed to provide insights regarding the behavior of the seeds during microwave irradiation and their subsequent thermal decomposition. The manufacture of karanja bio-oil by heat pyrolysis, was performed in an experimental setup using an LG Make internal microwave oven that activates at 2.45 GHz frequency and 800 W (28 × 12 × 10 cm). The oven was customized in such a way that it has appropriate holes for the connection of a $N_2$ gas cylinder, two aligned condensers and a thermocouple (k-type) for thermal investigation. The produced moist bio-oil mixture (pyrolytic liquid) is acquired by two conical flasks [16, 17]. Quartz was preferred as the primary material for the reactor due to its transparency to microwave radiation. This characteristic allows microwave energy to effortlessly penetrate within the reactor walls (made of quartz) and directly reach the sample without any energy loss. Additionally, quartz exhibits an exceptional heat resistance, capable of withstanding high temperatures up to 1600°C [18, 19]. Figure 2 displays karanja seed bio-oil.

**Figure 2.** Bio-oil formed by microwave pyrolysis

The pyrolytic oil formed by microwave pyrolysis of karanja seed is likely to contain clusters of various organic compounds and water molecules. Usage of the produced water-containing karanja bio-oil as a fuel in an engine affects the injection conditions of the engine, ignition and appearances [20, 21]. Moisture content plays a critical role in determining

the quality and stability of pyrolytic bio-oil, often contributing to undesirable phase separation during storage and handling. This phase split is primarily due to the polar nature of water, which interferes with the homogeneity of the bio-oil mixture. To address this challenge and better characterize the components of the bio-oil, a solvent-based separation technique was employed. In this study, the biologically derived compounds present in the produced bio-oil were isolated using a liquid-liquid extraction method involving dichloromethane ($CH_2Cl_2$). The latter, a non-polar organic solvent, is particularly effective in this application due to its ability to dissolve a broad range of organic compounds while remaining highly immiscible with water [22]. This selective miscibility facilitates efficient separation of water-soluble and organic-soluble fractions, enabling more accurate downstream analysis and processing of the bio-oil. The detailed methodology for this separation process, including phase behavior and solvent interactions, has been previously described in an earlier study [23].

The analysis of the pyrolytic bio-oil produced by karanja seeds revealed a heterogeneous mixture that contained both organic and inorganic components. To achieve a homogeneous blend of pyrolytic bio-oil and diesel, an emulsification technique using Span 80 and Tween 60 was employed to stabilize the immiscible liquids. The study exhibited that the bio-oil-diesel mixture remained stable for around 40 days [24], which later evaluated the long-term stability of pyrolysis oil (bio-oil) formulations in diesel fuel containing polyethylene glycol dipolyhydroxystearate. The produced bio-oil – diesel emulsion was further examined in detail in a previous publication [23]. Three kinds of fuels were verified in a single-cylinder diesel engine in the current study. The components and fuel list are shown in Figure 3.

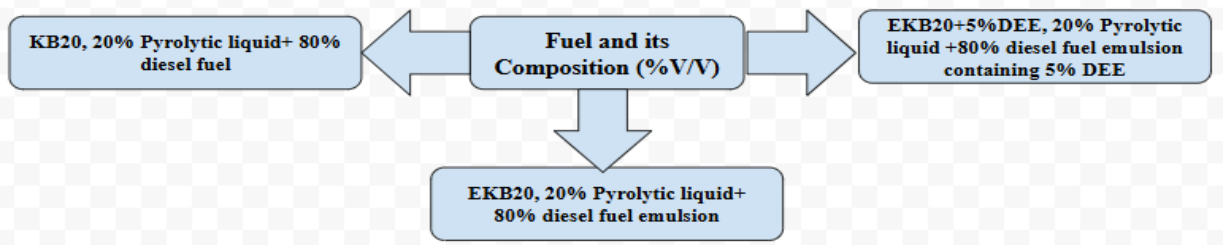


**Figure 3.** Fuel compositions used for research

The fuel characteristics of KB20 and EKB20 were assessed, encompassing measurements of viscosity using a rheometer, flash point utilizing a Cleaveland open cup device, high in calories value through a bomb calorimeter, and pH determined with a pH meter. FT-IR spectroscopy was used to study the functionally related makeup of KB20 and EKB20. The materials' infrared spectra were acquired in the 400-4000 $cm^{-1}$ region with a 4 cm aspect ratio and 32 scans.

*Experimental setup - engine*

To investigate the efficiency, combustion process, and emission properties of diesel fuels, a single-cylinder, direct-injection diesel engine with a rated power output of 5.2 kW was used. During the analysis process, the engine was operated using the produced fuels, and various other parameters related to emissions were restrained for KB20, EKB20 and diesel as fuel. The engine specifications are shown in Figure 4. The experimental procedure began by utilizing diesel fuel as the initial test fuel for conducting experiments under different engine load conditions. Baseline data were gathered, enabling the calculation of engine characteristics. The measurement results presented on the control board were documented in conjunction with the load tests performed on different outputs. A number of alternative fuels were then used to power the engine, including KB20 and EKB20. Prior to switching to the unusual fuel, the engine was initially fed with diesel fuel and ran for 15 min.

*Uncertainty analysis for the experiment*

To determine the accuracy in an experiment involving any type of instrument, uncertainty analysis is done. Either fixed or random errors are measured in uncertainty analysis. Among both, random errors are hard to resolve in between the experiments and were statistically analyzed. In such cases researchers suggest an intention method to statistically analyze the indecision of each measurement. This error exploration permits to establish the accuracy of the new data.

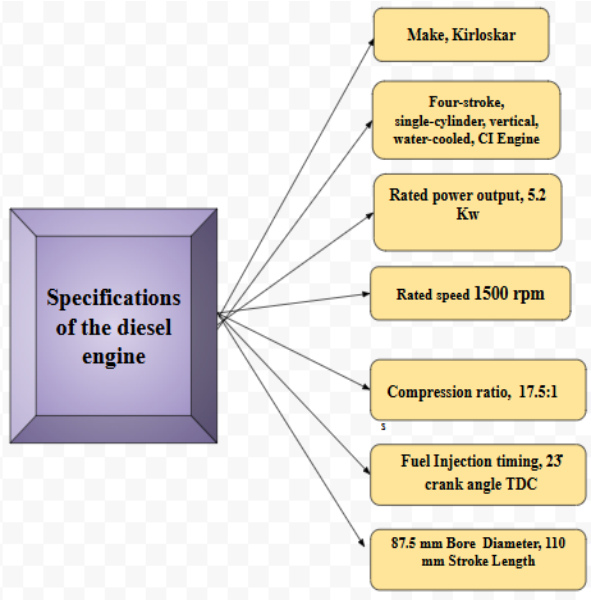


**Figure 4.** Specification of the engine

Uncertainty analysis was conducted to determine accuracy by measuring both fixed and random errors. Random errors were statistically analyzed using standard methods. For smoke opacity measurements at maximum brake power (5.2 kW), five trials were conducted with a mean value of 71.216 and standard deviation of 0.215128. This analysis establishes the reliability and accuracy of experimental data. Based on this, the accuracy of the values is hereby displayed in Figure 5 and Table 1.

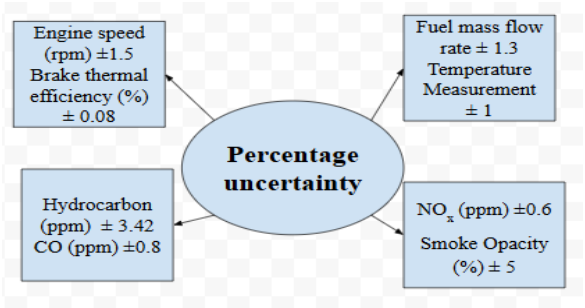


**Figure 5.** Evaluated uncertainty values at operating circumstances

**Table 1.** Uncertainty analysis for maximum brake power

| Trials | Smoke opacity for max. brake power (5.2 kw) |
|---|---|
| $X_1$ | 71.12 |
| $X_2$ | 71.1 |
| $X_3$ | 71.6 |
| $X_4$ | 71.12 |
| $X_5$ | 71.14 |
| Mean ($X_i$) | 71.216 |
| Standard deviation | 0.215128 |

## RESULTS AND DISCUSSION

*Physicochemical properties*

The obtained karanja seed bio-oil is dark brown, with smokey aroma, in nature comparing to the bio-oil produced by other types of pyrolysis processes resulting in prominent characteristics enabling to employ it in diesel engines by blending with diesel [25]. No data regarding the physical properties of the produced karanja seed bio-oil by other means of pyrolysis have been tabulated. The color differences result from the organic compounds present in the bio-oil, the blending process, and the post-modification treatment. The darker colors in bio-oil blends indicate the presence of complex organic molecules formed during pyrolysis. Based on the investigation of viscosity of karanja bio-oil and diesel, it is perceived that diesel has eight times lower energetic viscosity than karanja seed bio-oil. There is a connection between this phenomenon, fuel injection criteria and fuel properties. Viscosity affects fuel injection and atomization; flash point determines safety and ignition characteristics.

**Table 2.** Properties of bio-oil obtained by microwave pyrolysis of karanja seed

| Attributes | Diesel | Karanja seed bio-oil | KB20 | EKB20 |
|---|---|---|---|---|
| Color | Tint green | Dark brown | Black | Caramel brown |
| Cetane number | 49 | 30.11 | 41.36 | 45.14 |
| Flash point (°C) | 58 | 90 | 88 | 88 |
| Calorific value (MJ/kg) | 43.52 | 28.75 | 36.4 | 36.4 |
| Dynamic viscosity (cP) | 2.6 | 19 | 4.2 | 4.2 |

Compared with diesel, karanja seed bio-oil has lower fattening value and aniline point. The reduced aniline point of the produced fuel will reflect in ignition quality during running of the engine thereby with low cetane number. The lower cetane number of pure karanja bio-oil indicates poor ignition quality, which improves when blended with diesel. EKB20 shows better ignition quality than KB20 due

to the post-modification process that removes moisture and impurities. The comparative details are listed in Table 2 [11, 26, 27].

*Fuel chemical composition*

FTIR investigation was utilized to determine the functionalities of organic compounds found in KB20 and EKB20. Figure 6 displays the functional groups present in KB20, as determined through FTIR analysis, while Table 3 provides a comprehensive outline of the analysis. The FTIR spectral analysis of the KB20 sample reveals prominent absorption bands that indicate the presence of several key functional groups, suggesting a complex mixture of oxygenated and nitrogenated compounds in the bio-oil. Broad absorption peaks observed at 3340.1 $cm^{-1}$, 3191.6 $cm^{-1}$, and 3016.8 $cm^{-1}$ correspond to the stretching vibrations of hydroxyl (–OH) and amine (–NH) groups. These are typically attributed to aliphatic primary and secondary amines, as well as alcohols, indicating the presence of polar compounds formed during pyrolysis. The occurrence of –NH stretching at 2923.8 $cm^{-1}$ and 2864.4 $cm^{-1}$ further supports the presence of amine salts or possibly hydrogen-bonded amines, which may arise from protein decomposition during thermal treatment of the karanja biomass [28, 29].

In addition, strong absorption bands at 1719.0 $cm^{-1}$ and 1672.3 $cm^{-1}$ are characteristic of carbonyl (C=O) stretching vibrations, typically associated with aldehydes, ketones, carboxylic acids, or esters—common pyrolysis products of lignocellulosic and lipidic materials [30]. The band near 1566 $cm^{-1}$ corresponds to C=C stretching vibrations of alkenes or aromatic structures, suggesting the presence of unsaturated or aromatic hydrocarbons formed during thermal cracking. The coexistence of these functional groups highlights the chemically diverse nature of the pyrolytic bio-oil and suggests a combination of lignin-derived phenolics, fatty acid derivatives, and nitrogen-containing compounds originating from proteins or other nitrogenous components of karanja seed cake [31].

The C-H functional group and S=O functional group (at 1461.9 $cm^{-1}$ and 1407.7 $cm^{-1}$, respectively) correspond to the bending and stretching vibrations of alkane and sulfonyl chloride, respectively. Additionally, the existence of CO–O–CO functional group (at 1047.7 $cm^{-1}$) suggests the formation of anhydride, which is indicated by its stretching vibration. The maximum IR absorbance is observed for the OH (phenol s) - stretching and C=C stretching, which correspond to the lignin elements. The spectra of the various samples also show the lignin unit's distinctive vibrations [32].

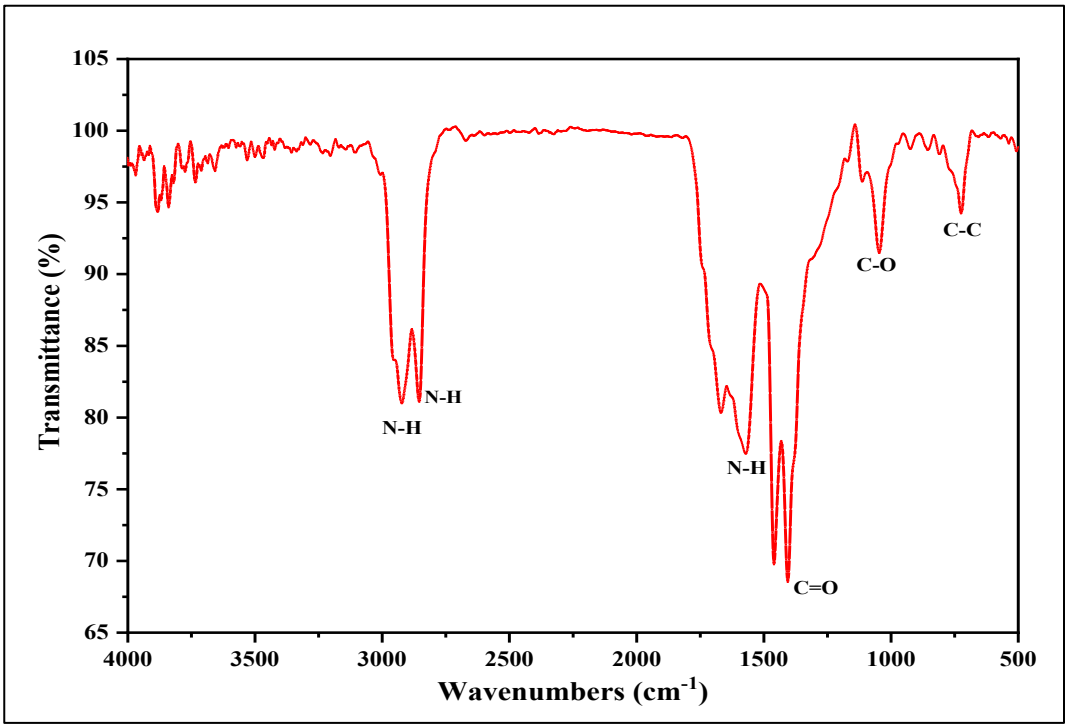


**Figure 6.** Functional groups of KB20 through FTIR.

**Table 3**. Functional groups in KB20

| Wavenumber ($cm^{-1}$) | Intensity / Appearance | Vibrational mode identified Stretching*/ Bending# | Functional group / Compound detected in karanja seed bio-oil |
|---|---|---|---|
| 3340.1 | Moderate | N–H* | Indicates presence of aliphatic primary amine |
| 3181.6 | Weak, Broad band | O–H* | Suggests alcohol functional group |
| 2923.8 | Strong, Broad absorption | N–H stretching | Corresponds to amine salt |
| 2853.4 | Strong, Broad absorption | N–H* | Associated with amine salt |
| 1719.0 | Intense Peak | C=O* | Represents carboxylic acid functionality |
| 1672.3 | Intense Peak | C=O* | Denotes conjugated acid group |
| 1566.0 | Moderate Peak | C=C* | Attributed to cyclic alkene structure |
| 1461.9 | Moderate Peak | C–H# | Typical of alkane compounds |
| 1047.7 | Broad, Strong band | CO–O–CO* | Corresponds to anhydride group |

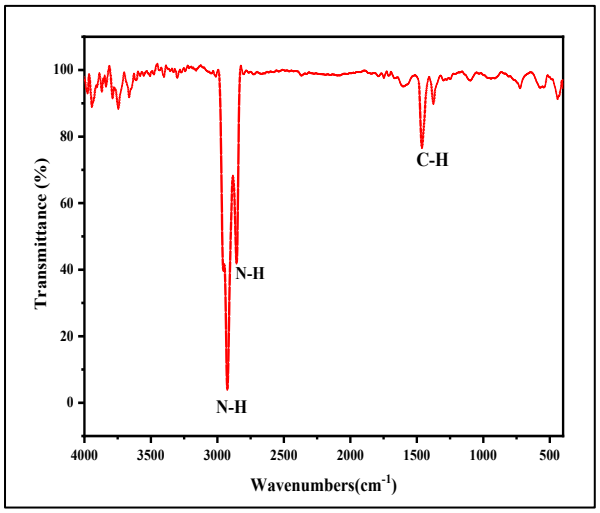


**Figure 7.** Functional groups of EKB20 through FTIR

Figure 7 displays the FTIR analysis results of EKB20, which is a bio-oil diesel emulsion, and Table 4 provides a detailed summary. The curves indicate the presence of N-H functional groups (at 2924.8 $cm^{-1}$ and 2855.5 $cm^{-1}$) in EKB20, which can be accredited to the stretching atmospheres of amine salts compounds. Additionally, a functional group corresponding to C-H (at 1461.2 $cm^{-1}$) is perceived, related with alkane folding vibration [33, 34].

**Table 4.** Functional groups in EKB20

| Wavenumber ($cm^{-1}$) | Intensity / Appearance | Group Stretching*/ Bending# with compounds |
|---|---|---|
| 2924.8 | Strong & Broad | N-H* Amine salt |
| 2855.5 | Strong & Broad | N-H* Amine salt |
| 1461.2 | Medium | C-H# Alkane |

*Performance characteristics*

- *Ignition delay (ID).* ID can be signified as the time delay, expressed in degrees of crank angle (°CA), that occurs among the initiation of injection and the onset of incineration within the engine. It represents the time with in the initial injection of fuel and the moment when combustion actually commences. This phenomenon is primarily influenced by the physicochemical properties of the fuel, its ignition quality (cetane number), as well as certain engine operating conditions. The IDs of KB20, EKB20 and diesel fuel are shown in Figure 8 for various brake control outputs. It is observed that in all fuels used for the testing, there is a drop-in ignition latency with a corresponding surge in braking power out. This kind of response is due to a decrease in the time causing the gasoline to disintegrate during mixing with air which happens when the degree of the gases rises at higher engine loads.

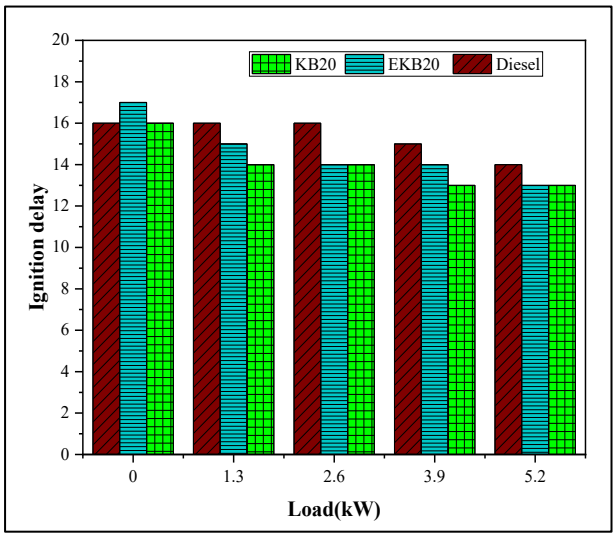


**Figure 8.** Variation of ID concerning brake power

This is due to the physicochemical properties, cetane number (ignition quality), and engine operating conditions. The incidence of moisture in fuel causes ignition delay, and the post-modification process in EKB20 helps reducing this effect. Ignition delay is observed for both EKB20 and KB20 on varying load. The prepared fuels EKB20 and KB20 exhibit a marginal moisture lower the moisture causing ignition delay in the fuel and the oil [35].

- *Cylinder gas pressure.* In Figure 9, a graphical representation of the pressure with respect to crank angle for different power outputs of the engine such as KB20, EKB20 and diesel fuel is plotted. For the prepared fuels (EKB20 and KB20), the peak pressure is higher in comparison to diesel fuel. The highest possible pressure for EKB20 is 75.86 bar, for KB20 is 72.40 bar and for diesel fuel it is 70.12 bar.

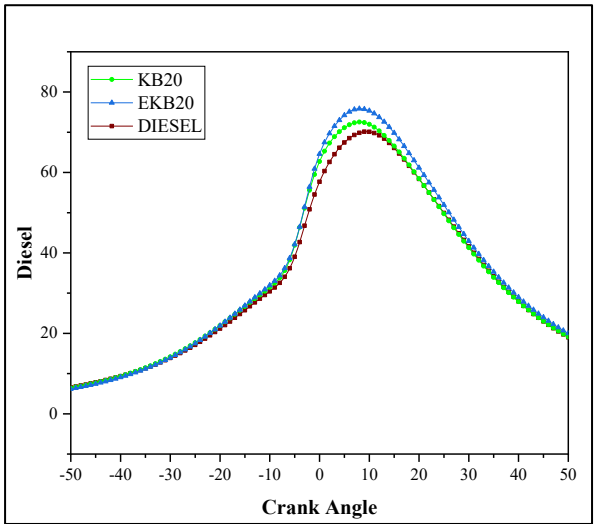


**Figure 9.** Variation of PC concerning crank angle

For EKB20 and KB20, in contrast with diesel, the peak gas pressure observed in the engine when using KB20 and EKB20 is found to be by 8% and 3% higher, correspondingly. It is essential to take into account that the peak pressure generated within the engine cylinder is chiefly determined by the quantity of fuel charred at the phase of the combustion process known as premixing. The prepared fuels EKB20 and KB20 have high peak pressure which is attained based on their lower energy content which needs larger quantities of fuel to be injected and burned during premixed combustion to produce the required power output. Therefore, for producing the required power output during the period of premixed combustion, a greater quantity of fuel gets injected and burned, which directly results in an increase in peak pressure when using respective fuels in the engine [36].

- *Net HRR.* Figure 10 illustrates the graphical representation of the net HRR at different power outputs for the prepared fuels EKB20, KB20 and also for diesel fuel in engine. The produced fuels EKB20 and KB20 exhibit the same heat release rate conditions as diesel fuel. Initially, owing to the vaporization of the fuel combination and the emission of heat, the heat release rate of the fuels causes a negative representation.

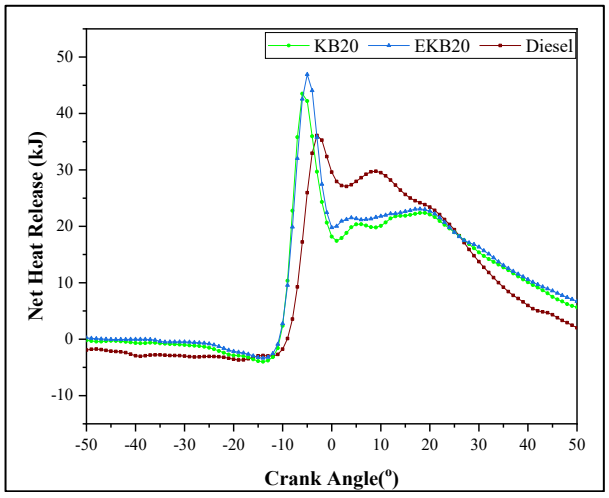


**Figure 10.** Variation of net HRR concerning crank angle

However, in the premixed incineration phase, heat release turns into positive, and also in the uncontrolled combustion point, heat release tends to result in uncontrollable situation during combustion. For all three fuels in the late combustion phase, it is experiential that there is a second peak in the HRR. On comparing diesel with KB20 and EKB20 fuels, the determined HRR occurred during the running of the engine in the rapid combustion phase. The maximum HRR for KB20 is 43.51 J/°CA, for EKB20 is 46.92 J/°CA and for diesel fuel it is 36.10 J/°CA. Due to the existence of oxygen-containing organic compounds a higher HRR was detected for the prepared fuels EKB20 and KB20. Further, when EKB20 fuel is used, micro-explosions may have developed, which automatically results in concentrated heat release rate. All three fuels show a second peak in the late combustion phase. Higher HRR in bio-oil blends is attributed to oxygen-containing organic compounds and potential micro-explosions in EKB20 [37].

- *Brake thermal efficiency.* Differences in brake thermal efficiency as a function of brake power for prepared KB20, EKB20 and diesel fuel for engine are represented in Figure 11. It is perceived that the engine produces lower BTE when EKB20 and KB20 are fueled in on comparing with fueling of diesel because of low energy density and high viscosity. For KB20 fuel, the brake thermal efficiency was 6.8% and for EKB20 fuel it was by 16.3% lower at the power output that is specified for the engine comparing to fuel. This reduction is due to the lower energy density and higher viscosity of bio-oil blends, which affect combustion efficiency and require more fuel to produce the same power output [38-40].

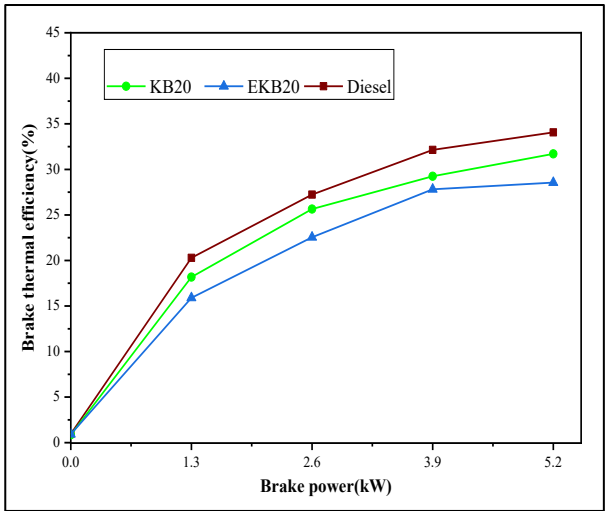


**Figure 11.** Variation in BTE concerning brake power output

- *Specific fuel consumption (SFC).* The mass or volume of fuel that is spent for a certain amount of time by an engine to produce a particular amount of engine braking power is referred to as the engine's particular use of fuel. It is a technical measurement that quantifies the fuel efficiency of an engine. The differences in the SFC for rated brake power outputs for prepared fuels KB20, EKB20 and for diesel fuel are represented in Figure 12. The SFC is noted to be by 20% greater in value for KB20 and by 36% greater when EKB20 fuel is used in the engine. The high viscosity nature of the prepared fuel KB20 and EKB20 increased the amount of gasoline that the engine required in order to develop the necessary power output. The high-viscosity nature of bio-oil blends increases the amount of fuel required to develop the necessary power output, leading to higher fuel consumption rates [20].

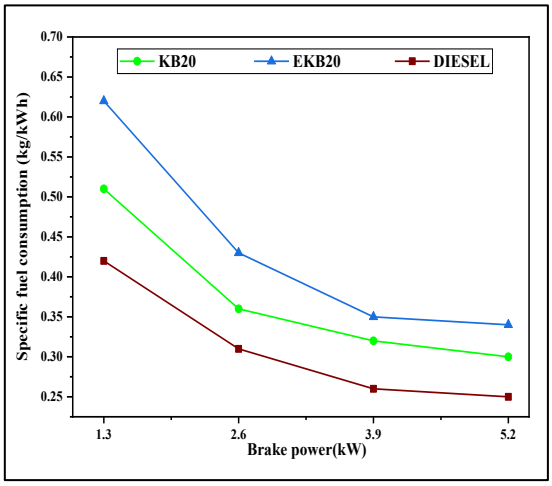


**Figure 12.** Variation in SFC concerning brake power output

*Smoke opacity*

Smoke zones constituted in the engine are based on higher fuel viscosity, poor fuel atomization, inadequate ignition that arises in fuel-rich zones, lower fuel volatility, and inappropriate fuel-air mixture. Figure 13 represents the differences in smoke opacity of EKB20, KB20 and diesel fuel. Due to the formation of fuel-rich zones because of enormous addition of fuel with increase in brake power the smoke opacity gets increased. It is perceived that the smoke density with EKB20 and KB20 is by 15% and 13% higher in value when comparing with diesel fuel at all rated power outputs. These differences are due to the development of organic compounds with higher molecular mass and the smoke formation is caused by higher fuel viscosity, poor fuel atomization, inadequate ignition in fuel-rich zones, lower fuel volatility, and inappropriate fuel-air mixture. The development of organic compounds with higher molecular weight also contributes [41, 42].

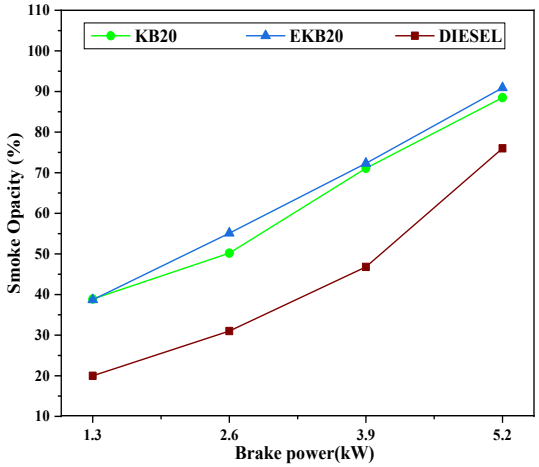


**Figure 13.** Variation of smoke opacity concerning brake power output

### *$NO_X$ emission*

$NO_x$ emissions are technically described as a blend of nitric oxide (NO) and nitrogen dioxide ($NO_2$), with NO being the primary nitrogen oxide formed during the ignition of fuel in a diesel engine. Nitrogen, when exposed to temperatures higher than 1500 °C, will react with oxygen ($O_2$) to produce nitrogen oxides ($NO_x$). There is a correlation between decreased radiating heat transfer, raised flame temperature, quick HRR, and sufficient supply of oxygen in the combustion zones. All of these factors lead to enhanced $NO_x$ generation [43, 44]. The variation in $NO_x$ formation in engines operating with different brake power outputs is compared for KB20, EKB20, and diesel fuel in Figure 14. In this emission analysis it is noted that by increasing the brake power the output reacts in an increase of temperature during the combustion process built on the admission of excess fuel into the incineration chamber resulting in an increase of $NO_x$ during the combustion process. It is found that there are higher $NO_x$ concentrations for both KB20 and EKB20 associated to diesel at all loads. At the peak brake power output, the $NO_x$ emission was observed to be by 26% higher for both KB20 and EKB20 compared to diesel. This is related to the higher HRR of KB20 and EKB20 when equated to diesel fuel [2]. This increase correlates with the higher heat release rates of bio-oil blends, elevated combustion temperatures, reduced heat transfer, and adequate oxygen supply in combustion zones, all contributing to enhanced $NO_x$ formation above 1500°C [37-39].

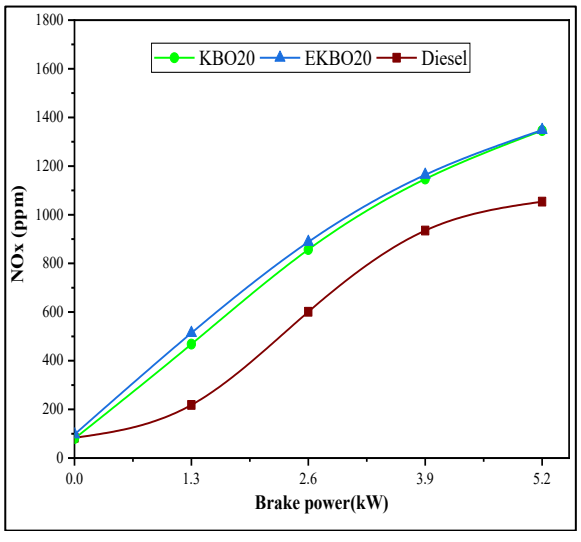


**Figure 14.** Variation of $NO_x$ concerning brake power output

### *CO emission*

Because of the inadequate burning of carbon in the fuel, CO emissions are produced. In general, diesel engines function with an air-fuel ratio that is considered low under various load conditions, leading to significantly lower CO emissions compared to spark-ignition (SI) engines. Figure 15 illustrates CO emissions at different engine brake power outputs. It is evident that the CO emission is highest at all rated power outputs for the verified fuels. This can be attributed to the injection of a higher amount of fuel during the rated power output, resultant in a higher fuel-to-air ratio. This, in turn, leads to incomplete or improper combustion, causing an increase in CO releases. EKB20 is by 20% higher and KB20 is by 8% lower when compared to diesel fuel.

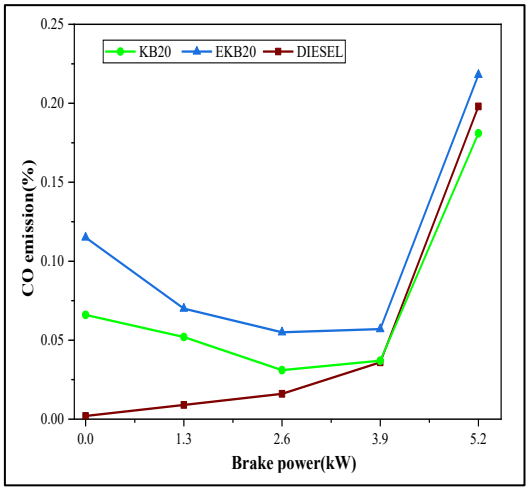


**Figure 15.** Variation of CO concerning brake power output

This might be due to the more viscous nature of the bio-oil blends which deliberately results in the development of larger droplets of the fuel used and is also due to incomplete combustion [45]. Also, CO emissions result from inadequate carbon combustion and increase with power output due to higher fuel injection rates creating higher fuel-to-air ratios. The more viscous nature of bio-oil blends leads to larger fuel droplets and incomplete combustion [43].

### *Hydrocarbon emission*

Unburned hydrocarbons are mostly formed when fuel is trapped in different engine mechanisms in an internal combustion engine running diesel. Vital aspects such as indecorous evaporation of fuel and fuel-rich zone correspondingly end in higher development of unburned hydrocarbons. Figure 16 shows the alterations in the emission of hydrocarbons for various power outputs. With gradual increasing the power outputs it is observed that here is a subsequent increase in hydrocarbon emission for all the fuels prepared. Because of the charge consistency and advanced oxygen availability at the lower loads there is lower

emission, whereas on increasing load conditions the emissions are high because of the high quantity of fuel injected during the combustion process. It is also observed that there is high hydrocarbon emission on comparing to the diesel fuel for both EKB20 and KB20 (Figure 16.

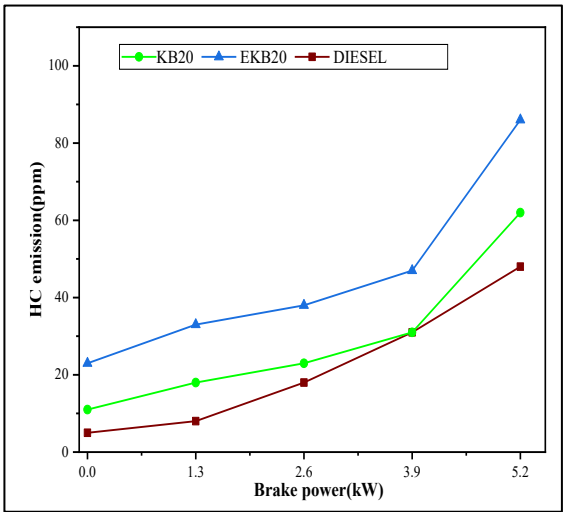


**Figure 16.** Variation of HC concerning brake power output.

This phenomenon can be due to the increased latent heat of humidity present in the fuel, which vaporizes during combustion. This leads to flame quenching, particularly at the combustion chamber walls of the engine, resulting in incomplete combustion. As a result, at the rated power outputs, the hydrocarbon emissions for EKB20 are observed to be 79% compared to diesel fuel, while for KB20, the increase is by 29% higher related to diesel fuel. This increase is attributed to the presence of moisture in the fuel, which increases the latent heat during vaporization, leading to flame quenching at the combustion chamber walls and resulting in incomplete combustion [36].

## CONCLUSIONS

This investigation successfully demonstrated the viability of converting non-edible karanja seeds into bio-oil through microwave pyrolysis, yielding a dark brown product with characteristic smoky odor. Comprehensive physicochemical characterization established that while bio-oil exhibited viscosity approximately eight times higher than that of conventional diesel, its calorific value of 28 MJ/kg—though by 40-50% lower than diesel—remains within acceptable ranges for biofuel applications. The enhanced viscosity can be attributed to the presence of long-chain fatty acids and oxygenated compounds inherent to pyrolytic bio-oils, which also contribute to improved lubricity properties beneficial for engine components. Engine performance trials with EKB20 and KB20 fuel blends revealed favorable combustion characteristics, including elevated cylinder pressure and accelerated heat release rates, indicating more efficient fuel-air mixing and combustion propagation. These findings suggest improved atomization and combustion kinetics despite the physicochemical differences from petroleum diesel. Although brake thermal efficiency decreased by 6.8% for KB20 and by 16.3% for EKB20 relative to baseline diesel at rated power output, these reductions are considerably modest given the renewable nature of the fuel source and can be offset through minor engine optimization strategies such as injection timing adjustment or compression ratio modification. The observed increases in $NO_x$ emissions and smoke density during combustion of both blends align with typical biofuel combustion patterns, where higher oxygen content promotes elevated combustion temperatures conducive to thermal $NO_x$ formation, while incomplete combustion of heavier molecular fractions contributes to particulate matter generation. These emissions remain manageable through exhaust gas recirculation systems or selective catalytic reduction technologies already employed in modern diesel engines. Significantly, this study validates the technical feasibility of utilizing karanja-based biofuels as sustainable alternatives to fossil diesel, particularly advantageous considering karanja's non-edibility. Therefore, karanja seed-derived bio-oil blends represent promising, environmentally responsible fuel alternatives warranting further development and commercialization for sustainable energy transition in compression ignition engines.

***Acknowledgement:*** *Not applicable.*
***Author contributions:*** *The authors have accepted responsibility for the entire content of this manuscript and approved its submission.*
***Conflict of interest:*** *On behalf of all authors, the corresponding author states that there is no conflict of interest.*
***Research funding:*** *Not applicable.*
***Data availability:*** *Not applicable.*

REFERENCES


1. J. H. Chang, S. Selvaraj, S. Manikandan, S. Nagarani, A. Senthilkumar, M. S. Samuel, E. Selvarajan, A. J. John, M. Kumar, *Biomass Conv. Bioref*., **202**, 108167 (2025).
2. A. A. Azni, W. A. W. A. K. Ghani, A. J. Idris, M. F. Z. a'afar, M. A. M. Salleh, N. S. Ishak, *Renew. Energy*, **142,** 123 (2019).
3. C. B. John, S. Baskar, *Fuel,* **405,** 136627 (2026).
4. J. P. Pandian, M. Pugazhvadivu, B. Prabu, K. Velmurugan, V. S. K. Venkatachalapathy, *Jordan J. Mech. Ind. Eng.,***15,** 273 (2021).
5. A. V. Bridgwater, G. V. C. Peacocke, *Renew. Sustainable Energy Rev.*, **4,** 1 (2000).
6. A. M. Al-Qahtani, *Energies, 1***6,** 6876 (2023).
7. A. Alcala, A. V. Bridgwater, *Fuel*, **109**, 417 (2013).
8. A. V. Bridgwater, *Catal. Today*, **29**, 285 (1996).
9. F. Yu, S. Deng, P. Chen, Y. Liu, Y. Wan, A. Olson, D. Kittelson, R. Ruan, *Appl Biochem Biotechnol.,* **137,** 957 (2007).
10. C. Wu, V. L. Budarin, M. J. Gronnow, M. De Bruyn, J. A. Onwudili, J. H. Clark, P. T. Williams, *J. Anal. Appl. Pyrolysis,* **107**, 276 (2014).
11. A. Mathiarasu, M. Pugazhvadivu, *Biomass Conv. Bioref*., **13**, 2895 (2023).
12. F. Mushtaq, R. Mat, F. N. Ani, *Renew. Sustain. Energy Rev*., **39**, 555 (2014).
13. F. Motasemi, A. A. Salema, M. T. Afzal, *Trans. ASABE.*, **58,** 869 (2015).
14. A. Farooq, H. Shafaghat, J. Jae, S. C. Jung, Y. K. Park, *J. Environ. Manage.,* **231**, 694 (2019).
15. Z. Guo, S. Wang, X. Wang, *Energy.,* **66,** 250 (2014).
16. A. Mathiarasu, M. Pugazhvadivu, *AIP Conf. Proc*., 2225, 040002 (2020).
17. A. Mathiarasu, M. Pugazhvadivu, *IOP Conf. Ser.: Earth Environ. Sci.,* **312**, 012022 (2019).
18. E. Antunes, M. V. Jacob, G. Brodie, P. A. Schneider, *J. Anal. Appl. Pyrolysis,* **129**, 93 (2018).
19. F. Motasemi, M. T. Afzal, A. A. Salema, J. Mouris, R. M. Hutcheon, *Fuel,* **124**, 151 (2014).
20. S. I. Yang, M. S. Wu, C. Y. Wu, K. H. Chen, T. M. Wu, Y. L. Hsu, Y. Y. Ku, *Adv. Mater. Res.*, **591**, 325 (2012).
21. A. K. Hossain, P. A. Davies, *Renew. Sustain. Energy Rev.,* **21**, 165, (2013).
22. T. Aysu, *Bioresour. Technol.,* **191,** 253 (2015).
23. M. Anbu, R. Balakichenin, P. Muthaiyan, S. Sundaramoorthy, K. T. T. Amesho, V. Subramani, *Environ. Sci. Pollut. Res.,* **30**, 125006 (2023).
24. J. A. Martin, C. A. Mullen, A. A Boateng, *Energy Fuels*, **28**, 5918 (2014).
25. A. S. Ahmed, *Int. J. Renew. Energy Res*., **13**, 14 (2023).
26. N. K. Nayan, S. Kumar, R. K. Singh, *Bioresour. Technol.,* **124**, 186 (2012).
27. K. P. Shadangi, K. Mohanty, *Renew. Energy,* **63**, 337 (2014).
28. A. A. Salema, F. N. Ani, *APCBEE Procedia*, **3,** 188 (2012).
29. F. Stankovikj, A. G. McDonald, G. L. Helms, G. P. Manuel, *Energy Fuels*, **30**, 6505 (2016).
30. S. Black, J. R. Ferrell, *Energy Fuels*, **30**, 1071 (2016).
31. S. Hosseinnezhad, H. F. Ellie, K. S. Brajendra, B. Mufeed, K. Bidhya, *RSC Adv.*, **5**, 75519 (2015).
32. L. Rosi, M. Bartoli, M. Frediani, *Waste Manag.,* **73,** 511 (2018).
33. B. Biswas, N. Pandey, Y. Bisht, R. Singh, J. Kumar, T. Bhaskar, *Bioresour. Technol.,* **237**, 57 (2017).
34. M. Bartoli, L. Rosi, A. Giovannelli, P. Frediani, M. Frediani, *J. Anal. Appl. Pyrolysis*, **119**, 224 (2016).
35. M. Mohamed, C. K. Tan, A. Fouda, M. S. Gad, O. Abu-Elyazeed, A. F. Hashem, *Energies*, **13**, 5708 (2020).
36. S. Sivalakshmi, T. Balusamy, *Fuel,* **106,** 106 (2013).
37. M. Mani, G. Nagarajan, S. Sampath, *Fuel*, **89**, 1826 (2010).
38. R. Prakash, R. K. Singh, S. Murugan, *J. Energy Inst.,* **88,** 64 (2015).
39. A. Zahir Hussain, A. Santhoshkumar, A. Ramanathan, *J. Therm. Anal. Calorim.,* **141**, 2277 (2020).
40. V. Volli, R. K. Singh, S. Murugan, *Waste Biomass Valor.,* **5,** 661 (2014).
41. R. Sinha, S. Kumar, R. K. Singh, *Biomass Conv. Bioref.,* **3**, 327 (2013).
42. R. Prakash, R. K. Singh, S. Murugan, *Energy*, **55,** 610 (2013).
43. I. Kalargaris, G. Tian, S. Gu, *Fuel.,* **211**, 797 (2018).
44. I. Kalargaris, G. Tian, S. Gu, *Fuel Process. Technol.*, **161,** 125 (2017).
45. N. Vedaraman, S. Puhan, G. Nagarajan, K. C. Velappan, *Int. J. Green Energy,* **8,** 383 (2011).

*Bulgarian Chemical Communications, Volume 58, Issue 1 (pp. 16-22) 2026* *DOI: 10.34049/bcc.58.1.5717*

# Discrimination of radish seed cultivars using fluorescence spectroscopy and advanced machine learning algorithms

T. Yari Dramane[1] , V. Slavova[2*], A. Yasar[3], T. L. Dimitrova[4]

[1]*Graduate School of Natural and Applied Sciences, Department of Computer Engineering, Selcuk University, Konya, Türkiye*

[2]*Department of Breeding, Maritsa Vegetable Crops Research Institute, Brezovsko shosse 32, 4000 Plovdiv, Agricultural Academy, Bulgaria*

[3]*Department of Mechatronics Engineering, Selcuk University, Konya, Türkiye*

[4]*University of Plovdiv "Paisii Hilendarski", 24 Tsar Assen Str., 4000, Plovdiv, Bulgaria*

Received: July 30, 2025; Revised: October 19, 2025

The differentiation of seed varieties plays a vital role in modern agriculture, since seed type and quality directly influence germination rate, plant vigor, crop yield, and ultimately, farmers' profitability. In recent years, the integration of decision support systems with advanced analytical tools has become increasingly important to ensure accurate and practical solutions for farmers. Within this scope, the present study addresses the classification of radish seed varieties, namely French breakfast, Nacional 2, Espresso F1, and Red large, by combining fluorescence spectroscopic techniques with state-of-the-art machine learning algorithms. The rationale behind the proposed approach lies in the complementary strengths of both methods: fluorescence spectroscopy provides a non-destructive, rapid, and sensitive characterization of seeds, while machine learning algorithms enhance the ability to recognize subtle spectral differences and achieve reliable classification outcomes.

In this study, four classifiers: Fine Tree, Quadratic Support Vector Machine (SVM), Fine k-Nearest Neighbor (KNN), and Neural Networks were employed to evaluate their performance on fluorescence spectral data. The findings revealed that all applied algorithms produced satisfactory classification accuracies exceeding 90%, thereby confirming the robustness of the proposed framework. Notably, the Quadratic SVM model achieved the highest performance with an accuracy of 100%, demonstrating its superior capability in distinguishing radish seed varieties with complete precision.

These results highlight that the synergy between spectroscopic data and machine learning models can be effectively utilized in practice for agricultural decision support. The developed methodology offers farmers a practical, non-invasive, and highly accurate tool for radish seed variety identification, which may significantly contribute to improved seed management, resource optimization, and sustainable agricultural practices.

**Keywords:** Radish seeds, fluorescence spectroscopic techniques, machine learning techniques

## INTRODUCTION

Radish (*Raphanus sativus*) is an annual root vegetable of the *Brassicaceae* family. Its origin traces back to Central Asia [1], and it has been cultivated as a food crop since approximately 1000 BC in regions including China, Japan, Egypt, Rome, and Greece. Varieties of radish are typically divided into two main categories: European-type and Chinese-type [2]. Radishes are primarily eaten raw, often in salads, as they are not well-suited for cooking. They are easy to grow, adaptable to a variety of soils, and have a rapid growth cycle [3]. Cultivation usually involves direct seeding in the soil, where the plants reach full maturity [4].

The development of rapid and precise non-destructive techniques, such as optical analysis, can facilitate the study and monitoring of seed germination, ensuring high-quality planting material for both farmers and the agricultural industry [5]. Optoelectronic approaches offer advantages including non-contact operation, speed, selectivity, and preservation of sample integrity. These benefits make it feasible to implement non-invasive methods for assessing radish seeds. To date, however, no studies have applied these techniques to radish.

Belyakov (2019) [6] presented findings from research on cereal seeds. Characteristic excitation wavelengths reported were 362 nm [7], 424 nm [8], and 485 nm [9]. These studies demonstrated that during the maturation of cereal seeds such as wheat, oats, and corn, immature seeds tend to show excitation at shorter wavelengths, while mature seeds predominantly emit longer-wavelength radiation. The ratio of long- to short-wavelength emissions changes over time and can be statistically described using linear models, which are essential for constructing reference databases.

Furthermore, Belyakov *et al.* (2021) [10]

* To whom all correspondence should be sent:
E-mail: *vanya_plachkova@abv.bg*

developed a sensor capable of determining seed physiological maturity by irradiating seeds with two specific wavelengths and measuring the resulting photoluminescence. Maximum luminescence was observed to be less pronounced compared to the excitation spectrum [11]. Spectral luminescence of forage seeds was also measured after scarification, revealing that repeated scarification induced qualitative changes, including the appearance of a new peak at 423 nm. These observations can similarly be applied to radish seeds, both standard varieties and first-generation hybrids, enabling the design of fiber-optic systems to evaluate planting material.

Optical properties of seeds from other crops, such as legumes [12] and tomatoes [13], have been studied using comparable methods. Typically, the excitation spectrum falls between 355–500 nm, showing a primary peak at 424 nm and a secondary peak at 485 nm. The emission spectrum ranges within 420–650 nm, with maxima around 500–520 nm. The water content of seeds including any impurities, is expressed as a percentage of the total seed mass [14].

A recent study demonstrated that fluorescence spectroscopic data on garlic cultivars can reliably represent different species, achieving a classification accuracy of 99.93% using Neural Network algorithms after hyperparameter optimization [15].

Therefore, this study aims to develop a non-invasive methodology for differentiating between radish seed varieties through integration of fluorescence spectroscopy with advanced machine learning algorithms. This research contributes to the literature by being the first to propose an optoelectronic framework specifically for radish seeds, thereby supporting modern decision support systems in agriculture.

The main contributions of this study can be summarized as follows:

- Novel methodology: We propose, for the first time, an optoelectronic framework that integrates fluorescence spectroscopy with advanced machine learning algorithms for the classification of radish seed varieties.
- Comprehensive dataset: Experimental data were obtained from four distinct radish cultivars (French breakfast, Nacional 2, Espresso F1, and Red large) with sufficient replicates, ensuring robust evaluation.
- Detailed performance evaluation: Multiple machine learning models (Fine Tree, Quadratic SVM, Fine KNN, and Neural Network) were comparatively assessed using 10-fold cross-validation, with reported classification accuracies consistently above 90%.
- Insightful analysis: The study highlights the discriminative spectral region (475–555 nm) and provides a discussion of why Quadratic SVM achieved superior performance.
- Practical implications: The proposed non-destructive approach offers a fast, accurate, and reproducible method for seed quality assessment, which can support farmers, seed producers, and breeding programs in agricultural decision-making.
- Future perspectives: The methodology sets the foundation for future integration of deep learning algorithms and portable sensor-based systems, enabling real-time applications in precision agriculture.

## MATERIALS AND METHODS

### *Materials*

For this investigation, four radish genotypes were selected, including three conventional cultivars and one first-generation hybrid. The characteristics of each genotype are summarized as follows:

*French breakfast*: This cultivar demonstrates adaptability to both spring and autumn field production. The roots are generally solitary and elongated, with a distinctive white tip. The internal tissue is crisp and pale, providing a favorable texture. The crop reaches physiological maturity within approximately 30 days, and the recommended seeding density is between 1.5 and 2.5 kg per hectare.

*Nacional 2:* An early-maturing cultivar, Nacional 2 produces large, globular roots exhibiting a vibrant red exterior with contrasting white tips. The flesh is tender and crisp, with a mild and pleasing flavor profile.

*Espresso F1*: This early-harvest hybrid is characterized by round, red roots and a robust root structure with firm attachment to the foliage. The variety shows excellent post-harvest durability and transportability, making it suitable for winter cultivation and very early-season field production.

*Red large*: A medium-early cultivar designed for both spring and autumn planting, Red large develops deep-red, single roots with white, flavorful flesh. This variety is distinguished by its resistance to cracking and high sensory quality, which enhances marketability.

These genotypes were chosen to encompass a range of morphological traits, maturation rates, and post-harvest qualities, providing a representative sample for the study of seed and root characteristics.

*Fluorescence spectroscopy*

The mobile fiber-optical spectral installation for the study of fluorescence signals is specifically designed for the rapid analysis of plant biological samples. 120 seeds from each of the 10 variants for the varieties Espresso F1, Red large, French breakfast and Nacional 2 were tested. The graphs presented for AI processing are averaged. It was chosen to work with a laser diode with emission radiation of 245 nm because the system is designed for wide application in plant breeding for the analysis of various types of plant samples, and some of them have an emission wavelength with low intensity levels. Figure 1 presents the averaged spectral distributions of seeds of the varieties Espresso F1, French breakfast, Nacional 2 and Red large. This source was chosen after preliminary studies and experimental tests showed that this is the optimal wavelength for the analysis of optically active biological media. The mobile experimental setup used for fluorescence spectroscopy is presented in Figure 2 and includes the following components:

- Laser diode (LED): Emission at 245 nm, supplied at 3 V, enclosed in a hermetically sealed TO39 metal housing. It operates with a voltage drop of 1.9–2.4 V and a current consumption of 0.02 A.
- Rod lens (achromatic doublet type): Consists of two bonded lenses with different dispersion coefficients (Schott and Corning) and an anti-reflective coating. The optical design minimizes chromatic aberration by compensating for lens differences.
- Quartz glass (4 cm²): Transparent to visible, ultraviolet, and infrared light, with weak light absorption. Its high purity ensures superior optical and thermal properties compared to conventional glass.
- CMOS detector: Photosensitive area of 1.9968 × 1.9968 mm, sensitivity range of 200–1100 nm, and spectral resolution of $\delta\lambda = 5$. It is optimized for precise signal detection with minimal data loss.
- Multimode optical fiber (FG200LEA): Core diameter of 200 µm, with a step-index refractive structure.

During operation, the seed sample is irradiated by the LED, inducing fluorescence emission. The emitted signal is collected at a 45° angle using the rod lens, transmitted through the optical fiber, and detected by the CMOS sensor.

This system offers several advantages:

1. Improved transmission efficiency through the inclusion of a rod lens, reducing air gaps between optical elements.
2. Optimized fiber coupling design, achieved with a durable housing that minimizes signal loss.
3. Efficient signal collection at 45°, enhancing sensitivity and accuracy of fluorescence detection.

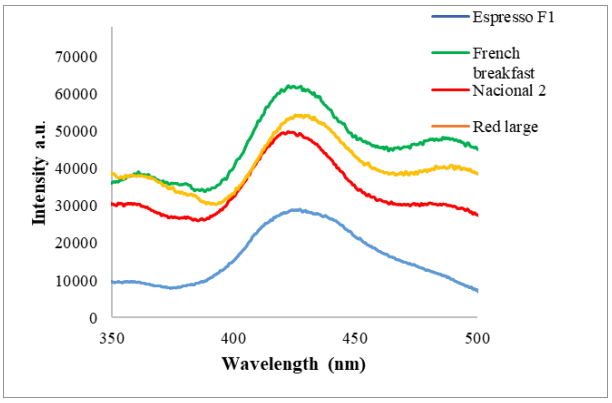


**Figure 1.** Averaged spectral distributions of seeds of the varieties Espresso F1, French breakfast, Nacional 2 and Red large

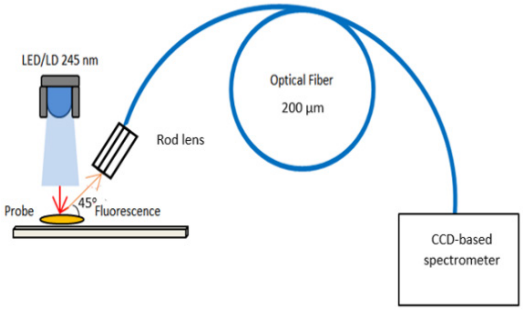


**Figure 2.** Mobile experimental installation used for fluorescence spectroscopy

No signal normalization is required for spectral analysis processing. The software used to generate the spectra from the spectrometer used in the scheme of Figure 2 allows for editable data acquisition parameters per channel, such as detector integration time, automatic dark current correction, signal averaging, spline interpolation, and spectral smoothing. The software was chosen because of its ability to generate time series in which the output of user-defined functions, integrals, peaks (intensity, wavelength) can be tracked simultaneously over time.

## RADISH SEEDS CLASSIFICATIONS

In the classification of the radish seeds (French breakfast, Nacional 2, Espresso F1 and Red large) obtained by using fluorescence spectroscopy techniques, machine learning (ML) algorithms such as Fine Tree, Quadratic Support Vector Machine (SVM), Fine K Nearest Neighbor (KNN) and Neural Network (NN) were applied. During the application process of these algorithms cross-validation

approach was used. Then, 10-fold cross-validation approach and ML algorithms were applied to make classification and analysis process more objective and free from randomness. All algorithms were implemented in MATLAB R2022b using the built-in Classification Learner Toolbox. The default hyperparameter settings were applied as follows: for classification, several machine learning models were employed using preset default configurations to maintain reproducibility and avoid manual tuning of hyperparameters. The Fine Decision Tree was limited to a maximum of 100 splits, using Gini's diversity index to determine node splits. The Quadratic SVM utilized a quadratic kernel, with a box constraint (C) value of 1, while the kernel scale was automatically calculated. The Fine k-Nearest Neighbor (KNN) model was configured with a single neighbor (k=1), Euclidean distance measurement, and uniform weighting for all neighbors. The Neural Network (NN) consisted of a single hidden layer containing 10 neurons, applying the tan-sigmoid activation function and trained using the scaled conjugate gradient method.

Model evaluation was carried out using a 10-fold cross-validation approach. The dataset was divided into ten equal segments; in each iteration, nine segments were used for model training and one for testing. This cycle was repeated ten times so that each segment served as a test set once. The final performance metric was obtained by averaging accuracy results across all folds, ensuring comprehensive utilization of the dataset for both training and testing. The cross-validation procedure applied in this study is illustrated in Figure 3.

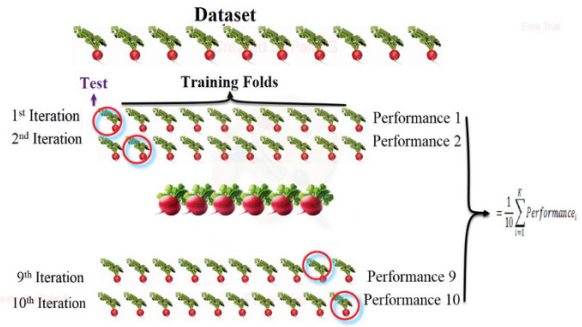


**Figure 3.** k folds Cross-Validation

In the training and testing processes, the selected algorithms provided the most satisfactory results. Generally, the performance of the classification algorithms is measured using classification metrics contained in the confusion matrix (Figure 4) such as accuracy, sensitivity, specificity and F1-score given in equations (1) to (4), respectively. From these metrics, only the accuracy is used in this work to evaluate the performance of the used algorithms. The accuracy value is the measure of prediction made by the algorithm and its value is obtained using equation (1) given below. In this equation, TP means True Positive, FN means False Negative, FP means False Positive, and TN means True Negative.

| Multi Class Confussion Matrix | | Predicted Class | | | |
|---|---|---|---|---|---|
| | | $Class_1$ | $Class_2$ | ..... | $Class_N$ |
| Actual Class | $Class_1$ | $C_{1,1}$ | $FP_{2,1}$ | ..... | $C_{1,N}$ |
| | $Class_2$ | $FN_{2,1}$ | $TP_{2,2}$ | ..... | $FN_{2,N}$ |
| | ..... | ..... | ..... | ..... | ..... |
| | $Class_N$ | $C_{N,1}$ | $FP_{2,N}$ | ..... | $C_{N,N}$ |

**Figure 4.** Example of multiclass confusion matrix [16].

$$Accuracy = \frac{TP+TN}{TP+TN+FP+FN} * 100 \quad (1)$$

$$Sensitivity = \frac{(TP)}{(TP+FN)} * 100 \quad (2)$$

$$Precision = \frac{(TP)}{(TP+FP)} * 100 \quad (3)$$

$$F1-Score = \frac{(2TP)}{(2TP+FP+FN)} * 100 \quad (4)$$

From the given metrics, only the classification accuracy was used to evaluate the performances of the each algorithm. The applied procedure was used to classify radish seed variety based on fluorescence spectroscopic data using machine learning algorithms (Figure 5).

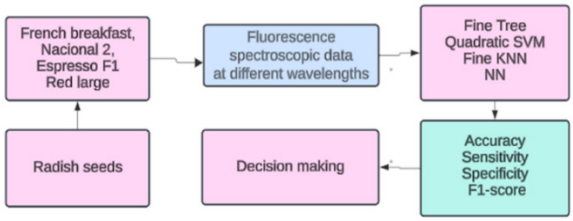


**Figure 5.** Procedure applied to classify radish seeds.

## RESULTS AND DISCUSSION

This study presents the analysis of radish seed varieties using fluorescence spectroscopic data combined with machine learning algorithms. Four classification models: Fine Tree, Quadratic SVM, Fine KNN, and Neural Network were applied to distinguish between different radish varieties, with classification accuracy serving as the primary performance metric.

Prior to classification, the raw spectral data were pre-processed to enhance signal quality and comparability across samples. Baseline correction and spectral normalization were implemented to remove intensity variations caused by measurement

conditions, while a smoothing filter was applied to reduce random noise. From the pre-processed spectra, it was observed that the wavelength region between approximately 475 and 555 nm contained the most discriminative information for distinguishing seed varieties.

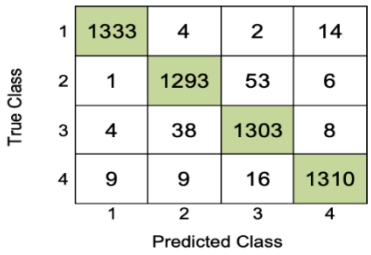


**Figure 6a**. Confusion matrix results - Fine Tree**.**

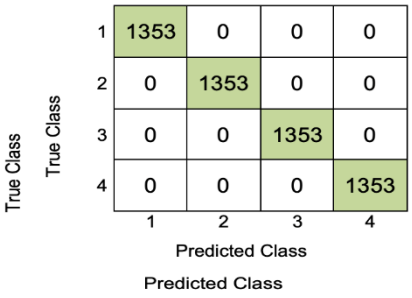


**Figure 6b.** Confusion matrix results - SVM.

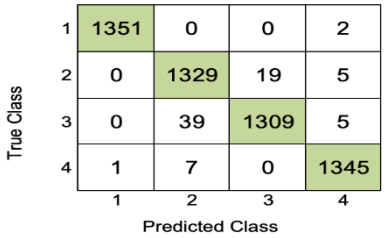


**Figure 6c.** Confusion matrix results - KNN.

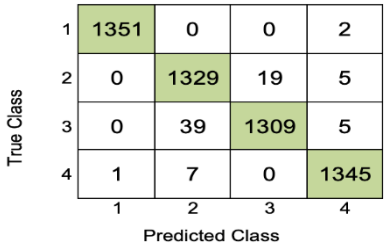


**Figure 6d.** Confusion matrix results - Neural Network.

This interval corresponded to the region where emission spectra exhibited the greatest variance among cultivars, whereas wavelengths outside this range contained largely redundant or noisy information. For this reason, the 475–555 nm interval was selected to maximize classification accuracy while minimizing computational complexity.

In the classification process, machine learning techniques such as Fine Tree, Quadratic SVM, Fine KNN, and Neural Network models were used to classify radish varieties. The implementation of these models was carried out using Matlab R2022b software. Classification of fluorescence spectroscopy data measured from radish seeds was performed with 10-fold cross-validation using standard machine learning parameters. The confusion matrices summarizing the classification results for each model are presented in Figures 6a–d.

The classification performance of four machine learning models Fine Tree, Quadratic SVM, K-Nearest Neighbors (KNN), and Neural Network was systematically evaluated using the metrics accuracy, precision, sensitivity (recall), and F1-score, derived from the confusion matrices (Tables 1–4). The averaged performance metrics for each classifier are summarized in Table 5.

Among the evaluated models, the Quadratic SVM classifier achieved flawless classification, attaining 100% accuracy, precision, sensitivity, and F1-score across all classes. This result indicates that SVM effectively captures the discriminative features present in the fluorescence spectra of radish seed varieties, providing highly reliable and consistent predictions. Similarly, the Neural Network model exhibited near-optimal performance, with an overall accuracy of 99.28%, precision of 98.57%, sensitivity of 98.56%, and F1-score of 98.56%. The slightly lower but still excellent performance of the Neural Network suggests its strong capacity to model complex nonlinear relationships inherent in the spectral data.

**Table 1.** Classification performance results of the Fine Tree model

| | Accuracy | Precision | Sensitivity | F1-Score |
|---|---|---|---|---|
| *Class 1* | 89.91 | 76.92 | 80 | 78.43 |
| *Class 2* | 86.24 | 69.23 | 72 | 70.59 |
| *Class 3* | 85.32 | 73.33 | 73.33 | 73.33 |
| *Class 4* | 94.5 | 92.59 | 86.21 | 89.29 |

**Table 2.** Classification performance results of the SVM model

| | Accuracy | Precision | Sensitivity | F1-Score |
|---|---|---|---|---|
| *Class 1* | 100 | 100 | 100 | 100 |
| *Class 2* | 100 | 100 | 100 | 100 |
| *Class 3* | 100 | 100 | 100 | 100 |
| *Class 4* | 100 | 100 | 100 | 100 |

**Table 3.** Classification performance results of the KNN model

| | Accuracy | Precision | Sensitivity | F1-Score |
|---|---|---|---|---|
| *Class 1* | \ | 98.90 | 99.70 | 99.30 |
| *Class 2* | 93.46 | 87.25 | 86.47 | 86.86 |
| *Class 3* | 93.59 | 86.77 | 87.73 | 87.25 |
| *Class 4* | 99.37 | 99.25 | 98.23 | 98.74 |

**Table 4.** Classification performance results of the Neural Network model

| | Accuracy | Precision | Sensitivity | F1-Score |
|---|---|---|---|---|
| *Class 1* | 99.94 | 99.93 | 99.85 | 99.89 |
| *Class 2* | 98.71 | 96.65 | 98.23 | 97.43 |
| *Class 3* | 98.84 | 98.57 | 96.75 | 97.65 |
| *Class 4* | 99.63 | 99.12 | 99.41 | 99.26 |

**Table 5.** Classification performance metrics using standard parameter values

| Classifier Model | Accuracy | Precision | Sensitivity | F1-Score |
|---|---|---|---|---|
| Fine Tree | 88.99 | 78.02 | 77.89 | 77.91 |
| Quadratic SVM | 100.00 | 100.00 | 100.00 | 100.00 |
| Fine KNN | 96.52 | 93.04 | 93.03 | 93.04 |
| Neural Network | 99.28 | 98.57 | 98.56 | 98.56 |

The KNN classifier also demonstrated robust performance, with 96.52% accuracy, 93.04% precision, 93.03% sensitivity, and 93.04% F1-score. While marginally lower than SVM and NN, these results confirm that KNN is capable of accurate classification, albeit with slightly reduced discrimination in cases of overlapping spectral features.

In contrast, the Fine Tree classifier presented comparatively lower performance, achieving 88.99% accuracy, 78.02% precision, 77.88% sensitivity, and 77.91% F1-score. Although the Fine Tree successfully distinguished between the four radish seed classes, its lower precision and sensitivity values highlight potential limitations in handling subtle spectral variations, indicating that tree-based methods may be less suited for highly complex spectral datasets.

Overall, these findings underscore the superiority of advanced classifiers, particularly Quadratic SVM and Neural Networks, in providing both high accuracy and robustness in the classification of radish seed varieties. The results also suggest that model selection is critical for achieving reliable performance, with nonlinear and kernel-based approaches outperforming simpler, tree-based algorithms when dealing with high-dimensional spectral data.

## CONCLUSION

This study demonstrates the successful application of fluorescence spectroscopy, combined with machine learning algorithms, for the non-invasive classification of radish seeds. Among the evaluated models, the SVM and Neural Network classifiers exhibited superior performance, achieving nearly perfect accuracy, precision, sensitivity, and F1-score, while KNN also provided robust results. The Fine Tree classifier, although less accurate, still achieved a reasonable classification, highlighting the importance of model selection for handling complex spectral data.

The novelty of this work lies in applying optoelectronic analysis specifically to radish seeds, a crop for which such an approach has not been previously reported. The proposed methodology enables rapid, accurate, and non-destructive evaluation of seed quality, reducing reliance on traditional germination tests and supporting informed decisions in seed selection and crop management.

Future research should focus on expanding the dataset to include more diverse radish varieties and growth conditions to enhance model generalizability. Additionally, integrating advanced deep learning techniques and developing portable, sensor-based systems could facilitate real-time, field-level applications. These improvements would further strengthen the reliability of seed quality assessment and support the adoption of smart agricultural technologies in precision farming.

## REFERENCES

1. A. Kjær, J. Øgaard Madsen, Y. Maeda, Y. Ozawa, Y. Uda, *Agricultural and Biological Chemistry*, **42**, 1721 (1978).
2. Y. Kaneko, C. Kimizuka-Takagi, S. Bang, Y. Matsuzawa, *Vegetables*, 160 (2007).
3. R. M. P. Gutiérrez, R. L. Perez, *The Scientific World Journal*, **4**, 837 (2004).
4. K. M. Bae, S.C. Sim, J.H. Hong, K.J. Choi, D.H. Kim, Y.S. Kwon, *Horticulture, Environment, and Biotechnology*, **56**, 224 (2015).
5. Z. Huyan, S. Ding, X. Liu, Y. Yu, *Analytical Methods*, **10**, 3207 (2018).
6. V.M. Belyakov, *Inzhenernye Tekhnologii i Sistemy*, **2**, 319 (2019).
7. V.K. Rewatkar, *Romanian Journal of Biophysics*, **30**(3) (2020).
8. W. Zhang, R. Lv, Y. Sun, H. Gu, *Agricultural Sciences*, **12**, 574 (2021).

9. S.P. Singh, K. Vogel-Mikuš, P. Vavpetič, L. Jeromel, P. Pelicon, J. Kumar, R. Tuli, *Planta*, **240**, 289 (2024).
10. M. Belyakov, E. Sokolova, V. Listratenkova, N. Ruzanova, L. Kashko, in: *E3S Web of Conferences*, **273**, 1003 (2021).
11. B.V. Olegovna, D.V. Vitalyevna, D.A. Grigoryevna, *International Scientific Review*, **4**, 31 (2017).
12. W.H. Su, S.A. Fennimore, D.C. Slaughter, *Biosystems Engineering*, **186**, 167 (2019).
13. C. Li, X. Wang, Z. Meng, *Optical Design and Testing VII,* **10021**, 516 (2016).
14. J. Boothe, C. Nykiforuk, Y. Shen, S. Zaplachinski, S. Szarka, P. Kuhlman, M. Moloney, *Plant Biotechnology Journal*, **8,** 606 (2010).
15. A. Yasar, V. Slavova, S. Genova, *Tehnički Glasnik*, **18**, 531(2024).
16. A. Golcuk, A. Yasar, *Journal of Food Composition and Analysis*, **119**, 105253 (2023).

*Bulgarian Chemical Communications, Volume 58, Issue 1 (pp. 23-29) 2026* *DOI: 10.34049/bcc.58.1.5724*

# Impact of polyols on microbiological viability and sweetness perception in frozen yogurt

P. Boyanova[1]*, A. Chavdarova[1], V. Dobreva[1], D. Gradinarska[1], B. Goranov[1], A. Balabanov[1], V. Slavova[2]

[1] *University of Food Technologies, 26 Maritza Blvd., 4000 Plovdiv, Bulgaria*
[2] *Department of Breeding, Maritsa Vegetable Crops Research Institute, Agricultural Academy, 32 Brezovsko chaussee, 4000 Plovdiv, Bulgaria*

Received: October 10, 2025; Revised: October 25, 2025

This study evaluated the effect of replacing sucrose in frozen yogurt with polyols: 18% maltitol (YIC-2) and a combination of 9% maltitol and 9% blend of erythritol with steviol glycosides (YIC-3), on the survival of *Lactobacillus* spp., *Streptococcus thermophilus*, and *Bifidobacterium* spp. over 60 days at –18 °C. The control sample with 18% sucrose (YIC-1) showed the highest survival of *Bifidobacterium* spp. (6.33±0.13 log CFU/g), followed by the maltitol variant (YIC-2) at 6.25±0.25 log CFU/g. Both maintained counts above the 6 log CFU/g threshold, indicating probiotic potential. The combination of 9% maltitol, 9% erythritol, and steviol glycosides (YIC-3) showed a significant decline to 5.40± 0.20 log CFU/g, below the therapeutic minimum. These results suggest that erythritol may limit the survival of sensitive probiotic *Bifidobacterium* strains during long-term storage (beyond 14 days). The sensory triangle test revealed statistically significant differences between YIC-1 and YIC-2 ($p = 0.0004$) and between YIC-1 and YIC-3 ($p = 0.024$), but no significant difference between YIC-2 and YIC-3 ($p = 0.939$).

**Keywords**: polyols, frozen yogurt, *Bifidobacterium* spp., lactic acid bacteria, sensory profile

## INTRODUCTION

Ice cream is a frozen dairy product high in fat and sugar, providing significant energy but lacking therapeutic benefits. The nutritional composition of conventionally made ice cream includes 36.0–43.0% dry matter and 8.0–15.0% non-fat milk solids. It contains 8.0–20.0% fat, 4.0–4.8% protein, 12.0–20.0% sugar, 0.1–0.7% stabilizers and emulsifiers [1]. Increased consumption of foods high in added sugars leads to excess calorie intake. It often causes the overproduction of insulin, which inhibits lipolysis and glycogenolysis while promoting the synthesis of triglycerides and glycogen, thereby contributing to chronic diseases such as obesity and hypertension [2, 3].

The availability of numerous sugar substitutes and sweeteners has enabled the development of reduced-energy, sugar-free dietary foods [4]. Ice cream is a suitable food matrix for incorporating lactic acid starter cultures and polyols, meeting the demand for healthier products [5-8]. Frozen yogurts resemble ice cream in texture but are distinguished by a pronounced lactic acid taste [8]. By the end of storage, these products must contain a sufficient number of viable lactic acid bacteria from the starter culture [9]. Various authors have investigated technological approaches to producing lactic acid ice creams with different ratios of fermented milk to ice cream mix [10, 11]. According to research, the viability of probiotic cultures in frozen yogurts remains higher throughout storage than in fermented milks, since low storage temperatures (–18 to –20 °C) slow metabolism and cellular aging [12, 13]. A concentration of $10^6$ CFU/g of probiotic bacteria in the final product has been proposed as a "therapeutic minimum" [14]. According to the International Dairy Federation [15], to achieve probiotic potential, the number of viable *Bifidobacteria* spp. should not be less than $10^6$ CFU/g, and at least $10^7$ CFU/g for other starter culture microorganisms.

Sugar alcohols (polyols) are generally recognized as safe (GRAS) and approved by the European Food Safety Authority [16, 17]. Their inclusion in food products allows classification as "sugar-free" in accordance with European regulations [18]. Genovese *et al.* [19, 20] reported that polyols can successfully replace sugar in functional ice cream without negatively affecting taste or physical stability. Polyols have a mild sweetness and sugar-like texturizing properties [21, 22]. Maltitol provides about 90% of the sweetness of sucrose, has a glycemic index of 35, and an energy value of 2.4 kcal/g, while also contributing to the desired texture of frozen desserts. According to Regulation (EU) No

* To whom all correspondence should be sent: Email: *pboyanova@uft-plovdiv.bg*

1169/2011 [23], erythritol is considered practically non-caloric (0 kcal/g) compared to 2.4 kcal/g for other polyols. A key distinguishing feature of erythritol is its glycemic index of 0 [24], but its lower sweetness (60–80% of sucrose) often requires combination with intense sweeteners [17, 24].

The objective of this study was to determine the viability of *Lactobacillus* spp., *Streptococcus thermophilus*, and *Bifidobacterium* spp. in sugar-free frozen yogurt over 60 days of storage at –18 °C, and to investigate the influence of maltitol, alone and in combination with erythritol and steviol glycosides, on perceived sweetness when used as sucrose replacers.

## MATERIALS AND METHODS

### *Frozen yogurt formulations*

Three variants of frozen yogurts were developed: one control sample containing 18% sucrose (YIC-1), and two sugar-free variants – one with 18% maltitol (YIC-2), and another with a combination of 9% maltitol and 9% blend of erythritol with steviol glycosides (YIC-3). The steviol glycosides are used only to adjust sweetness in the erythritol-steviol glycoside mixture (Bioenergie, Gerhard Wagner GmbH, Austria). Because of their high sweetening potency and the minimal amounts used, these intense sweetening agents do not affect the total solids content and the physicochemical properties of the frozen yogurt mix.

For the preparation of the ice cream mix, the following raw materials were used: farm cow's milk (3.90 ± 0.12% fat, 3.00 ± 0.03% protein, 4.70 ± 0.02% lactose, 8.30 ± 0.03% solids-not-fat), fresh cream containing 58.0±0.10% fat, 1.8±0.1% protein, 2.40±0.1% lactose, 4.55±0.12 solids-not-fat (Manole Milk Ltd., Bulgaria), 0.70% of an emulsifier–stabilizer blend (Cremodan SE 38, Danisco Ingredients, Denmark), and milk protein concentrate powder MPC85 (Lactoprima Pro, Balt Milk, Kaunas, Lithuania). The milk base was standardized to 34.0±0.5% total solids, 4.0 ± 0.5% protein, and 10.0 ± 0.5% fat. Depending on the type of fermented ice cream, the following sweeteners were added: 18% sucrose (Zahira, AGRANA Zucker GmbH, Austria), 18% maltitol P200 (Roquette, France), and a combination of 9% maltitol and 9% blend of erythritol with steviol glycosides (Bioenergie, Gerhard Wagner GmbH, Austria).

A two-stage homogenization of the standardized ice cream mix with sugar and a sugar substitute was performed using a homogenizer (150 L/h, Gaulin, Italy) at 63–65°C and 20 MPa pressure. The homogenized ice cream mixes were pasteurized at 85°C for 10 min, then cooled to 8 ± 1°C. Physical aging of the ice cream mixes was conducted at 8°C for 16 h.

For the preparation of probiotic yoghurt, the same milk base (10.0±0.5% fat, 4.0±0.5% protein, 0.7% stabilizer) was used, but without the addition of any sweetening agents. The homogenized milk mix (63–65°C, 20 MPa) was pasteurized at 92 °C for 10 min and cooled to 38±1°C. DVS starter culture ABY-3 with probiotic potential (Chr. Hansen, Denmark) was used for fermentation. The microbial composition of the starter culture included *Lactobacillus delbrueckii* subsp. *bulgaricus*, *Streptococcus thermophilus*, and probiotic strains *Bifidobacterium animalis* subsp. *lactis* (BB-12®) and *Lactobacillus acidophilus* (LA-5®). The lactic acid fermentation was carried out at 38±1°C until a pH of 4.6–4.7 was reached.

Before freezing, the ice cream mixes were blended with the probiotic yoghurt in a 1:1 ratio. The resulting fermented ice cream mixtures were frozen in an ice cream machine (Gelato Chef 2200, 150 W, 1.8 L) for 40 min at t = −6 ÷ −5°C. After freezing, the frozen yogurt samples were packaged in 250 g-containers and stored at −18°C for 60 days.

### *Chemical analyses*

Total solids were determined gravimetrically by drying at 104±1°C to constant weight (Kern XM5 moisture analyzer, Germany). Fat content was determined according to the BDS EN ISO 7328:2009 standard [25]. Protein content was determined by the Kjeldahl method using a conversion factor of 6.38 [26]. The contents of sugars (sucrose, lactose, glucose, galactose, and fructose) were determined by high-performance liquid chromatography (HPLC) according to the method described by Petkova *et al.* [27]. Analyses were performed using an HPLC system (Hewlett Packard 1100) equipped with a refractive index detector (RID) and operated with Chromeleon 7.3 software. Separation was achieved on a C18 column (5 µm) using acetonitrile/water (80:20, v/v) as the mobile phase at a flow rate of 1.4 mL/min and a column temperature of 40 °C. pH was measured potentiometrically (InoLab pH 720, WTW GmbH, Germany). Overrun (%) was determined gravimetrically according to Marshall *et al.* [30].

### *Microbiological analyses*

Viable counts were determined in yogurt, mixes (before and after freezing), and stored frozen yogurt (0, 14, 25, 45, and 60 days).

*Lactobacillus* spp. and *S. thermophilus* were enumerated according to BDS ISO 7889:2005 [28] by colony count at 37°C. MRS agar (Merck,

Darmstadt, Germany) was used for *Lactobacillus* spp., and M17 agar (Merck, Darmstadt, Germany) for *S. thermophilus*. Plates were incubated at 37°C for 72 h (*Lactobacillus* spp.) and 48 h (*S. thermophilus*). Plates with 15–300 colonies were used for calculation, and results were expressed as log CFU/g.

*Bifidobacteria* spp. were enumerated according to ISO/FDIS 29981 [29] using BSC propionate agar base (HiMedia Laboratories Pvt. Ltd., India) supplemented with mupirocin (HiMedia) to inhibit non-target bacteria. Bifido Selective Supplement A (HiMedia), containing 25 mg mupirocin in 5 mL, was added to the agar cooled to 45–50°C before pouring plates. Inoculated plates were incubated anaerobically at 37°C for 72 h using Anaerocult® A and Anaerotest® (HiMedia). The results were expressed as log CFU/g.

The survival rate (SR, %) of microorganisms was calculated according to Equation (1):

$$SR\ (\%) = \frac{\log CFU\ Nt}{\log CFU\ No} \times 100 \quad (1)$$

where $CFU_0$ is the initial viable count before freezing and $CFU_t$ is the viable count at the end of storage.

*Sensory evaluation*

A triangle test was applied as a discriminatory sensory method for detecting differences between similar products. The test involved 20 trained panelists. Each panelist received a triad of samples containing two identical and one different sample, presented in plastic cups coded with three-digit numbers to ensure impartiality. Panelists were informed that two of the samples were identical and one was different, and they were instructed to identify the odd sample, even if they were unsure. Each sample (50 g) was served at t = –10 ± 2 °C. Results from the triangle test were processed and analyzed statistically using XLSTAT Sensory 2022.

*Statistical analysis*

All analyses were conducted in quadruplicate, and the results are presented as mean values ± standard deviation (SD). One-way analysis of variance (ANOVA) was applied to compare the means of frozen yogurt samples during the storage period. Differences were considered statistically significant at $p<0.05$. Data processing was performed with Statgraphics 19.0.

## RESULTS AND DISCUSSION

Table 1 shows the physicochemical parameters of the control frozen yogurt sample (YIC-1) with 18% sucrose, as well as the frozen yogurt samples with complete sucrose replacement – YIC-2 (18% maltitol) and YIC-3 (a combination of 9% maltitol, 9% blend of erythritol, and steviol glycosides). All samples showed similar total solids contents, ranging from 34.10% to 35.77%, with no meaningful differences. The protein content (3.57%÷3.67%) and fat content (10.59%÷10.84%) were also very similar across the three formulations, indicating that replacing sucrose with polyols does not significantly change the main chemical properties of frozen yogurt with no added sugar.

**Table 1.** Physicochemical characteristics of frozen yogurt with 18% sucrose (YIC-1, control sample) and samples with 18% maltitol (YIC-2) and a combination of 9% maltitol, 9% blend of erythritol, and steviol glycosides (YIC-3).

| Indices | YIC-1 | YIC-2 | YIC-3 |
|---|---|---|---|
| Dry matter, % | 35.8±0.9$^{b}$ | 34.1±0.5$^{a}$ | 34.8±0.5$^{ab}$ |
| Fat, % | 10.6±0.1$^{a}$ | 10.7±0.1$^{ab}$ | 10.8±0.1$^{b}$ |
| Protein, % | 3.6±0.02$^{b}$ | 3.6±0.01$^{a}$ | 3.7±0.01$^{b}$ |
| Sugars, % | 20.0±0.1$^{a}$ | 3.2±0.1$^{b}$ | 3.4±0.1$^{c}$ |
| pH | 5.4±0.1$^{a}$ | 5.5±0.1$^{a}$ | 5.5±0.1$^{a}$ |
| Overrun, % | 40.8±0.7$^{b}$ | 22.6±1.9$^{a}$ | 79.5±2.3$^{c}$ |

Note: Data are expressed as mean values (n = 4) ± standard deviation (SD). Mean values within the same row followed by different lowercase letters (a, b, c) are significantly different ($p < 0.05$).

The most significant differences ($p<0.05$) were in sugar content (sucrose, lactose, glucose, galactose, and fructose). The control sample with sucrose had a sugar level of 20.01±0,1%, whereas YIC-2 with 18% maltitol and YIC-3 with a combination of 9% maltitol and 9% erythritol showed sugar levels of 3.20±0.1% and 3.40±0.1%, respectively. Similar results have been reported by other studies involving maltitol and erythritol in dairy frozen desserts, which maintained the nutritional profile while lowering simple sugars [9].

In terms of overrun, significant differences were established ($p<0.05$). The lowest value was recorded for YIC-2 (22.61%), while YIC-3 exhibited a nearly fourfold higher overrun (79.55%). This can be attributed to the different cryoscopic activity of the polyols and their effects on mix viscosity, which determine the ability to retain air bubbles during freezing [30, 31].

In the studied frozen yogurt samples (pH 4.90±0.01), the concentration of viable microbial cells from the starter culture was measured using the standard plate count method. The results, shown as

log CFU/g, were as follows: *Lactobacillus* spp. – 8.27±0.24 log CFU/g, *Streptococcus thermophilus* – 9.49±0.01 log CFU/g, and *Bifidobacterium* spp. – 8.60±0.11 log CFU/g. These values demonstrate a high level of viable cells for microbial species typical of fermented dairy products with probiotic potential. They are well above the commonly accepted minimum of 6 log CFU/g needed for probiotic effectiveness [32, 33].

The microbial viability was assessed after preparing fermented frozen yogurt mixes with sucrose and sugar substitutes, after freezing (1 day), and throughout storage up to day 60 (Table 2). Before freezing, a decrease in *Lactobacillus* spp., *Streptococcus thermophilus*, and *Bifidobacterium* spp. was noted in the mixes due to diluting the probiotic yogurt 50:50 with an ice cream base lacking live bacterial microorganisms (Table 2). This caused a mechanical reduction in logarithmic counts – about 12% for lactobacilli, 0.6% for streptococci, and 15% for bifidobacteria. Despite this, all frozen yogurt samples (YIC-1, YIC-2, YIC-3) maintained microbial counts above the minimum probiotic threshold of $10^6$–$10^7$ CFU/g viable cells [32].

After freezing, *Lactobacillus* spp. and *S. thermophilus* showed high survival rates (96.82–98.91% and 95.77 – 96.85%, respectively) across all samples. *Bifidobacterium* spp. survival rates varied significantly ($p<0.05$), from 79.59% to 85.42%, with YIC-1 (sucrose) having the highest (99.68%) and YIC-3 (maltitol–erythritol) the lowest (79.59%) survival rate. This trend aligns with findings by Muzammil *et al.* [34] that freezing causes partial viability loss mainly due to mechanical stress from mixing and air incorporation [35]. *Lactobacillus* spp. and *S. thermophilus* are facultative anaerobes, unlike bifidobacteria, which are strict anaerobes. The overrun during freezing was highest in YIC-3 (79.55±2.3%), possibly explaining the lower bifidobacteria survival, while YIC-2 (maltitol) had the lowest overrun (22.61±1.9%), aiding better probiotic maintenance.

**Table 2.** Viable cell counts of the starter culture (log CFU/g) in frozen yogurt with 18% sucrose (YIC-1, control), 18% maltitol (YIC-2), and a combination of 9% maltitol, 9% erythritol, and stevia (YIC-3) during 60 days of storage at –18 °C.

| Frozen yogurt sample | Starter culture microbial species (log CFU/g) | | Storage period (days) | | | | |
|---|---|---|---|---|---|---|---|
| | | Before freezing | 1 | 14 | 25 | 45 | 60 |
| YIC-1 | *Lactobacillus* spp. | $7,25±0,10^{X}$ | $7,15 ±0,07^{b,X}$ | $7,07 ±0,15^{b,Y}$ | $6,77 ±0,14^{a,X}$ | $6,76 ±0,03^{a,X}$ | $6,57 ±0,3^{a,X}$ |
| | *S. thermpophilus* | $9,43±0,30^{Y}$ | $9,11 ±0,27^{a,X}$ | $9,07 ±0,34^{a,X}$ | $8,94 ±0,48^{a,X}$ | $8,99 ±0,05^{a,X}$ | $8,80 ±0,33^{a,Y}$ |
| | *Bifidobacterium* spp. | $7,31±0,13^{X}$ | $7,0 ±0,40^{b,XY}$ | $6,90 ±0,33^{b,X}$ | $6,98 ±0,48^{b,X}$ | $6,60 ±0,22^{ab,X}$ | $6,33 ±0,13^{a,X}$ |
| YIC-2 | *Lactobacillus* spp. | $7,31±0,12^{X}$ | $7,23 ±0,20^{b,X}$ | $6,80 ±0,08^{a,X}$ | $6,70 ±0,01^{a,X}$ | $6,62 ±0,32^{a,X}$ | $6,49 ±0,33^{a,X}$ |
| | *S. thermpophilus* | $9,52±0,30^{Y}$ | $9,29 ±0,49^{b,X}$ | $8,92 ±0,42^{ab,X}$ | $8,69 ±0,22^{ab,X}$ | $8,66 ±0,22^{a,X}$ | $8,31 ±0,58^{a,XY}$ |
| | *Bifidobacterium* spp. | $7,34±0,30^{X}$ | $6,40 ±0,17^{b,Y}$ | $6,24 ±0,17^{b,X}$ | $6,29 ±0,27^{b,X}$ | $6,29 ±0,11^{b,X}$ | $6,25 ±0,21^{a,Y}$ |
| YIC-3 | *Lactobacillus* spp. | $7,23±0,1^{X}$ | $7,00 ±0,07^{c,X}$ | $6,82 ±0,13^{b,X}$ | $6,69 ±0,10^{a,X}$ | $6,62 ±0,07^{ab,X}$ | $6,62 ±0,10^{a,X}$ |
| | *S. thermpophilus* | $9,45±0,59^{Y}$ | $9,05 ±0,27^{b,X}$ | $8,90 ±0,37^{bx}$ | $8,64 ±0,18^{b,X}$ | $8,66 ±0,27^{b,X}$ | $7,72 ±0,62^{a,X}$ |
| | *Bifidobacterium* spp. | $7,30±0,23^{X}$ | $5,81 ±0,25^{b,X}$ | $5,76 ±0,26^{b,X}$ | $5,66 ±0,20^{ab,X}$ | $5,44 ±0,06^{a,X}$ | $5,40 ±0,20^{a,X}$ |

*Values of log (CFU/ g) are expressed as mean ± standard deviation (SD). Mean values within the same row and column followed by different lowercase letters are significantly different ($p < 0.05$). **Letter designations are used as follows: X, Y, Z indicate differences in the concentration of starter culture microorganisms between the frozen yogurt samples during storage, while a, b, c indicate differences in the concentration of starter culture microorganisms within the same sample during storage.

**Table 3.** Sensory differentiation of fermented frozen yogurts sweetened with sucrose (YIC-1), maltitol (YIC-2), and maltitol–erythritol–stevia (YIC-3)

| Parameter | Frozen yogurt samples | | |
|---|---|---|---|
| | YIC-1 vs YIC-3 | YIC-1 vs YIC-2 | YIC-2 vs YIC-3 |
| Number of panelists (N) | 19 | 19 | 20 |
| Number of correct answers | 11 | 14 | 4 |
| % correct responses | 57.89 | 73.68 | 20.0 |
| Significance threshold | 11 | 11 | 11 |
| d-prime (d′) | 1.869 | 2.717 | 0.0 |
| p-value | 0.024 | 0.000381 | 0.939 |
| Statistical power (%) | 59.6 | 96.1 | 3.8 |
| Statistical significance | Yes | Yes | No |

On day 1, *Lactobacillus* spp. levels were similar (7.2–7.3 log CFU/g) across the variants ($p>0.05$). They slightly decreased during storage, with YIC-2 and YIC-3 reaching 6.49 and 6.62 log CFU/g, respectively, while YIC-1 remained relatively stable at 6.57 log CFU/g by day 60. Although the differences were not statistically significant ($p>0.05$), sucrose seemed to offer a more stable environment for *Lactobacillus*.

*S. thermophilus* started at 9.1–9.2 log CFU/g and remained viable after freezing. The most notable decline (SR=85.30%) was in YIC-3, dropping from 9.05 to 7.72 log CFU/g. YIC-1 and YIC-2 also decreased gradually, ending at 8.80 and 8.31 log CFU/g, with survival rates of 96.60% and 89.45%, respectively. This indicates better stability in *S. thermophilus* with sucrose and maltitol compared to the maltitol–erythritol mix.

All samples initially had *Bifidobacterium* spp. levels around 7.30–7.34 log CFU/g, indicating good initial inoculation. After 60 days, *Bifidobacterium* spp. of YIC-1 decreased to 6.33 log CFU/g but remained above the probiotic threshold. YIC-2 remained similar at 6.25 log CFU/g, while YIC-3 declined to 5.40 log CFU/g, falling below the effective probiotic level. This reduction in YIC-3 may be linked to erythritol, which, at 9%, despite being moderate, can affect probiotic viability due to its physicochemical properties [36]. Previous research shows that erythritol may inhibit *Lactobacillus* and *Bifidobacterium* at higher concentrations by creating osmotic stress and antimicrobial effects. Nevertheless, in this study, the combination with maltitol did not cause a sharp initial decline, suggesting that moderate erythritol levels are acceptable in fermented frozen dairy products without losing probiotic benefits. However, viability remains lower than with sucrose (YIC-1) or maltitol alone (YIC-2). All samples showed a steady, moderate decline in *Bifidobacterium* spp. during 60-day storage, with no sudden drops. This could be due to the osmotic properties of sucrose and maltitol, which help reduce freezing stress and minimize mechanical damage [37]. Disaccharides and polyols can act as cryoprotectants, forming a stable glassy matrix that shields cell membranes and proteins from freezing damage [38, 39]. These mechanisms help improve probiotic resilience during freezing or lyophilization [40].

A triangle test was used to evaluate perceptible differences between fermented frozen yogurt samples containing sucrose (YIC-1) and those with sugar substitutes—maltitol (YIC-2) and a mixture of maltitol, erythritol, and steviol glycosides (YIC-3). For the statistical analysis, the Thurstonian model was applied, and the d-prime (d′) value was calculated to measure the panelists' sensitivity to differences among the samples (Table 3).

When comparing frozen yogurt samples YIC-1 (sucrose) and YIC-3 (maltitol, erythritol, and steviol glycosides), 57.89% of assessors correctly identified the odd sample, which exceeds the chance level of 33.33%. The d-prime value was 1.869, indicating a perceptible ability to distinguish between the sample pairs. Statistical analysis showed a p-value of 0.024, below the significance level ($\alpha=0.05$). Therefore, the null hypothesis ($H_0$) that there is no difference between YIC-1 and YIC-3 was rejected in favor of the alternative hypothesis ($H_a$). This confirms that sucrose (YIC-1) is perceived differently from the low-intensity sweeteners maltitol, erythritol, and steviol glycosides (YIC-3). The power of the test was 59.60%, which is acceptable for sensory testing. These results demonstrate that participants could significantly ($p<0.05$) distinguish the sucrose-sweetened frozen yogurt from those sweetened with maltitol, erythritol, and steviol glycosides.

The comparison between sucrose (YIC-1) and maltitol (YIC-2) showed that 73.68% of participants correctly identified the odd sample, well above the chance level of 33.33%. The calculated d-prime of 2.717 indicates high sensitivity to differences between YIC-1 and YIC-2. The p-value was 0.000381, which is far below 0.05, confirming the significance of the findings. The test's power was 96.06%, demonstrating strong reliability. This

indicates that panelists could clearly distinguish between the sucrose-sweetened sample (YIC-1) and the maltitol-sweetened sample (YIC-2).

When comparing the maltitol sample (YIC-2) and the maltitol-erythritol-stevia combination (YIC-3), only 20% of participants correctly identified the two samples, which is below the expected random-guess rate of 33.33%. The d-prime was 0, suggesting no perceptible difference according to the Thurstonian model. The p-value was 0.939, well above 0.05, indicating no significant difference, and the null hypothesis was not rejected. The test's power was only 3.76%, implying a very low likelihood of detecting a difference if it exists. These results suggest that participants perceived YIC-2 and YIC-3 as practically indistinguishable.

The differences in sweetness between sucrose and the sweeteners maltitol, erythritol, and stevia are influenced by their chemical structures and interactions with sweetness receptors in the mouth. Sucrose has a balanced, intense, and long-lasting sensation. Conversely, polyols like maltitol and erythritol have lower sweetness levels, approximately 70–90% and 60–70% of the sweetness of sucrose, respectively, and shorter perception duration. Moreover, erythritol imparts a cooling sensation, further altering the overall flavor profile.

## CONCLUSIONS

The replacement of sucrose with maltitol in frozen yogurt preserved the viability of probiotic cultures (*Lactobacillus* spp., *S. thermophilus*, and *Bifidobacterium* spp.) above the recommended therapeutic minimum throughout 60 days of storage at –18 °C. The combination of maltitol and erythritol with steviol glycosides led to a decline in the survival of *Bifidobacterium* spp. below the probiotic threshold after 60 days of storage, which may be associated with the presence of erythritol at a concentration of 9%, known to affect sensitive strains under prolonged storage conditions. Sensory analysis confirmed that sucrose- and maltitol-sweetened yogurts were clearly distinguishable, while the difference between maltitol and maltitol-erythritol-steviol glycosides formulations was not perceptible. These findings indicate that maltitol is a suitable sucrose substitute for developing frozen yogurt with probiotic potential, whereas formulations containing erythritol require further optimization to ensure microbial stability.

***Acknowledgement:*** *This research was supported by the Science Fund of the University of Food Technologies – Plovdiv, under Contract No. 01/24-N.*

## REFERENCES

1. S. S. Deosarkar, S. D. Kalyankar, R. D. Pawshe, C. D. Khedkar, in: Encyclopedia of Food and Health, B. Caballero, P. Finglas, F. Toldrá (eds.), Academic Press, Oxford, 2016, p. 385.
2. J. M. Rippe, T. J. Angelopoulos, *Eur. J. Nutr.*, **55**, 45 (2016).
3. P. Prinz, *Eur. J. Clin. Nutr.*, **73**, 1216 (2019).
4. A. Kolodziejczyk, J. Nowak, *Nutrients*, **17**, 1899 (2025).
5. M. E. Moriano, C. Alamprese, *LWT – Food Sci. Technol.*, **75**, 329 (2017).
6. D. Kalicka, A. Znamirowska, M. Pawlos, M. Buniowska, K. Szajnar, *Int. J. Dairy Technol.*, **72**, 456 (2019).
7. J. Kiepś, *Foods*, **11**, 2295 (2022).
8. S. Adil, A. H. Jana, B. M. Mehta, P. B. Chandgude, *Agric. Rev.*, **42**, 233 (2021).
9. C. Soukoulis, in: *Proc. 3rd Int. Conf. Ice Cream Technol.*, Athens, Greece, 2008, p. 112.
10. C. Ozdemir, M. Demirci, T. Demirci, *Milchwissenschaft – Milk Sci. Int.*, **60**, 293 (2005).
11. D. W. Olson, K. J. Aryana, W. Prinyawiwatkul, *J. Dairy Sci.*, **104**, 5006 (2021).
12. A. Abdelazez, H. Abdelmotaal, A. Darwish, Z. T. Zhu, H. Yang, J. Zhao, *Food Sci. Biotechnol.*, **26**, 1651 (2017).
13. R. H. Davidson, S. E. Duncan, C. R. Hackney, W. N. Eigel, J. W. Boling, *J. Dairy Sci.*, **83**, 1390 (2000).
14. C. P. Champagne, N. J. Gardner, D. Roy, *Crit. Rev. Food Sci. Nutr.*, **45**, 61 (2005).
15. International Dairy Federation (IDF), Milk and Milk Products – Definition and Evaluation of Probiotic in Dairy Products, Bulletin No. 277, IDF, Brussels (1992).
16. EFSA Panel on Food Additives and Nutrient Sources added to Food (ANS), *EFSA J.*, **8**, 1338 (2010).
17. EFSA Panel on Food Additives and Nutrient Sources added to Food (ANS), *EFSA J.,* **8**, 1650 (2010).
18. European Commission Regulation (EC) No. 1333/2008 of the European Parliament and of the Council of 16 December 2008 on food additives, *Off. J. Eur. Union,* **L354**, 16 (2008).
19. A. Genovese, P. Fava, C. Leonardi, G. Santagata, G. Gentile, *Foods*, **11**, 2974 (2022).
20. A. Genovese, A. Balivo, A. Salvati, R. Sacchi, *Food Res. Int.*, **161**, 111892 (2022).
21. P. De Cock, in: Sweeteners and Sugar Alternatives in Food Technology, K. O'Donnell, M. W. Kearsley (eds.), Wiley-Blackwell, Hoboken, 2012, p. 213.
22. V. Dobreva, R. Hadjikinova, I. Petrova, G. Dobrev, M. Hadjikinova, J. *Hyg. Eng. Des.*, **33**, 162 (2020).
23. European Commission Regulation (EU) No. 1169/2011 of the European Parliament and of the Council of 25 October 2011 on the provision of food information to consumers, *Off. J. Eur. Union*, **L304**, 18 (2011).
24. G. Livesey, *Nutr. Res. Rev.*, **16**, 163 (2003).
25. BNS ISO 7328:2008, Milk-based edible ices and ice mixes – Determination of fat content – Gravimetric

method (Reference method), Bulgarian Institute for Standardization, Sofia, 2008.
26. ISO 8968-1 / IDF 20-1:2014, Milk and Milk Products — Determination of Nitrogen Content — Part 1: Kjeldahl Method and Calculation of Crude Protein, International Organization for Standardization, Geneva, 2014.
27. N. Petkova, M. Ognyanov, M. Todorova, N. Dencheva, L. Kuleva, *Bulg. Chem. Commun.*, **45**, 305 (2013).
28. BDS ISO 7889:2005, Yogurt — Enumeration of characteristic microorganisms — Colony-count technique at 37 °C, Bulgarian Institute for Standardization, Sofia (2005).
29. ISO/FDIS 29981, Milk products — Enumeration of presumptive bifidobacteria — Colony-count technique at 37 °C, International Organization for Standardization, Geneva, 2010.
30. M. R. Muse, R. W. Hartel, *J. Dairy Sci.*, **87**, 1 (2004).
31. G. El-Nagar, G. Clowes, C. M. Tudorică, V. Kuri, C. S. Brennan, *Int. J. Dairy Technol*., **55**, 10 (2002).
32. Codex Alimentarius Commission, Standard for fermented milks – CODEX STAN 243-2003, FAO/WHO, Rome, 2003.
33. E. M. Buys, P. J. Jooste, R. Nyanzi, *J. Dairy Sci*., **105**, 4507 (2022).
34. H. Muzammil, *Int. J. Nutr. Food Sci.*, **7**, 116 (2018).
35. W. McGlynn, S. E. Duncan, C. R. Hackney, W. N. Eigel, J. W. Boling, *J. Dairy Sci.*, **83**, 666 (2000).
36. H. J. Moon, M. Jeya, I. W. Kim, J. K. Lee, *Appl. Microbiol. Biotechnol.*, **86**, 1017 (2010).
37. C. Santivarangkna, U. Kulozik, P. Foerst, *J. Appl. Microbiol.*, **105**, 1 (2008).
38. C. A. Morgan, N. Herman, P. A. White, G. Vesey, *J. Microbiol. Methods*, **66**, 183 (2006).
39. F. Fonseca, C. Béal, G. Corrieu, *Biotechnol. Adv*., **34,** 725 (2016).
40. A. S. Carvalho, J. Silva, P. Ho, P. Teixeira, F. X. Malcata, P. Gibbs, *Int. Dairy J*., **14**, 835 (2004).

*Bulgarian Chemical Communications, Volume 58, Issue 1 (pp. 30-36) 2026* *DOI: 10.34049/bcc.58.1.5703*

# Impact of drying techniques on protein denaturation in *Tenebrio molitor*: A thermal analysis *via* differential scanning calorimetry

H. Idakiev[1*], D. Aleksandrova[1], G. Boye[2], P. Först[2], N. Vorhauer-Huget[3]

[1]*University of Chemical Technology and Metallurgy, Sofia, Bulgaria*
[2]*Technical University of Munich, Germany*
[3]*Otto-von-Guericke-University Magdeburg, Germany*

Received: May 22, 2025; Revised: October 31, 2025

The increasing global demand for protein, driven by rapid population growth, calls for sustainable production methods with minimal environmental impact. *Tenebrio molitor* (mealworms) offer a promising, sustainable protein source for both, feed and food, applications. In industrial mealworm production, optimized drying techniques, essential for maintaining product quality, are critical. The key to selecting the drying technology and process conditions is the protein content of the final product. This study, therefore, compares drying time and product quality of *T. molitor* from freeze-drying and oven drying at 40°C and 60°C and investigates the potentials and limits of differential scanning calorimetry (DSC) to quantitatively assess protein denaturation of the dried product.

**Keywords:** Protein denaturation, sustainable protein source, mealworm, *Tenebrio molitor*, freeze-drying, oven drying, differential scanning calorimetry (DSC)

## INTRODUCTION

According to a report by the United Nations, the global population is expected to reach at least 11.5 billion by 2050, leading to an increase in global food demand by up to 70% compared to the current situation [1]. Traditional sources of animal protein, such as beef, pork, and chicken may not be sufficient to meet this demand. Therefore, the development of sustainable protein production methods with minimal negative environmental impact is regarded as a potential route to overcome the expected gap [2, 3]. Novel protein sources include single-cell proteins, fish protein concentrates, and edible insects. Since 2010, the Food and Agriculture Organization (FAO) has recognized the potential of insects as human food and animal feed to ensure food security [4, 5].

Entomophagy, or consumption of insects, has been practiced for many years across various regions worldwide. Insect-based foods are consumed by over two billion people globally and are readily available in the U.S. and European markets. Over 2,000 insect species have been identified as edible. Various cultures use insects, particularly their larvae, as everyday food. Examples include termites in Kenya, mopane worms in Zimbabwe, and grasshoppers in Mexico. These insects are often regarded as delicacies due to their flavor and high nutritional value [3, 10]. Edible insects offer relatively high nutritional values, have a high biodiversity and allow efficient production with lower environmental pollution at the same time [6]. Insects demonstrate high feed conversion capacity and produce fewer greenhouse gas emissions compared to traditional livestock, while requiring less water and land. Consequently, the consumption of insects contributes positively to environmental sustainability, food and nutrition security, and a healthy lifestyle [3].

Insects are nutrient-dense, with a generally high protein and fat content, a high biological value, and good digestibility. Additionally, they provide micronutrients, including minerals and vitamins. Thus, insects represent a potential supplement for various commercial foods. Despite the widespread consumption of whole insects in different regions, many consumers remain hesitant to accept them due to their unappealing appearance. This issue can be addressed by processing insects into less recognizable forms. The use of insect flour, which renders the insects nearly invisible when incorporated into dishes, is expected to enhance acceptance by an increasing number of consumers [6].

The mealworm, which is the larval stage of the flour beetle, is gaining attention as a suitable candidate for alternative protein sources for large-scale production and integration into the European food and feed industry. The primary bioactive compounds in mealworms that offer health benefits include bioactive peptides, omega-3 fatty acids, oleic acid, and chitosan [11]. They contain 52.35%

* To whom all correspondence should be sent:
E-mail: *hidakiev@uctm.edu*

protein, 24.7% fat, and approximately 2% carbohydrates and fiber, providing a balanced nutritional profile that meets WHO recommendations for adults. Nutrition by mealworms fulfills human amino acid requirements. They are rich in both monounsaturated and polyunsaturated fatty acids, as well as trace elements such as magnesium, copper, iron, and zinc [5, 10, 12, 13].

Processing conditions, particularly heat treatment, can lead to conformational changes associated with the physicochemical properties of proteins and other ingredients. Hot air drying and freeze-drying are the commonly used processing methods that extend shelf life and facilitate the incorporation of mealworms into food products that are more easily perceived by consumers. Hot air drying can be realized with relatively simple equipment. The drying rate, and thus, process time and throughput, are essentially controlled by the applied temperature. However, already relatively low temperatures of 40°C significantly deteriorate mealworm quality and protein content [7]. Freeze-drying, instead, preserves both, color and protein content, but yields long drying times and low energy efficiency [8].

Differential scanning calorimetry (DSC) is a thermal analysis technique used to measure the heat flow associated with material transitions as a function of temperature. In DSC, a sample is heated (or cooled) at a constant rate, and the heat absorbed or released by the sample is recorded. This allows for the determination of thermal properties such as melting points, glass transition temperatures, and protein denaturation. DSC is particularly valuable for evaluating protein stability and quality in food processing, as it can provide insights into protein unfolding, aggregation, and overall thermal behavior. It is widely used to study the impact of different processing techniques, such as drying or cooking, on the structural integrity of proteins and other biomolecules.

This study aims to compare drying rates and quality parameters of mealworm subjected to freeze-drying and oven drying at 40 °C and 60 °C. Differential scanning calorimetry was employed to evaluate the thermal properties and protein stability of mealworms post-drying, providing a quantitative assessment of product quality.

## EXPERIMENTAL

### *Sample collection*

*Tenebrio molitor* larvae used in this study were supplied by SAHAWA UG, Germany, as well as from ENTAVA Insektenshop, Germany. During rearing, the larvae were primarily fed a diet consisting of wheat bran, grains, and NaCl. The larvae were delivered frozen and packaged in breathable mesh and stored at −20 °C in a freezer until use.

### *Drying procedures*

Moisture content before and after drying was determined by thermogravimetric analysis (TGA) using a moisture analyzer (Model MA100, Sartorius, Germany).

Drying experiments were conducted on chopped mealworms using two techniques: oven drying and freeze-drying. During the drying process, weight loss was monitored by interrupting the process at regular intervals and weighing the samples with a precision balance (Secura225D-1S, Sartorius, Germany). Drying curves were generated based on these measurements. Drying was terminated once the drying rate approached zero, i.e., when no further mass loss was observed.

- *Oven drying* was performed using an oven dryer (Memmert, Germany) at two temperature settings: 40 °C and 60 °C.
- *Freeze-drying* was carried out using a freeze dryer (Model BETA 1-16, Martin Christ Gefriertrocknungsanlagen GmbH, Germany). The drying parameters were as follows: pressure 0.1 mbar, ice condenser temperature 50 °C, and shelf temperature 20 °C.

After drying, all mealworms were stored in a desiccator. Experiments with SAHAWA UG samples were repeated once for validation, while those with ENTAVA larvae were not repeated.

### *DSC characterization*

Differential scanning calorimetry (DSC) was used to characterize the thermal behavior of the samples, both before and after drying, using a DSC 92 calorimeter (SETARAM, France). For analysis, the dried worms were ground in a coffee grinder until a fine flour was obtained. Undried worms were crushed using a pestle, analogous to the preparation before drying. The samples were inserted into open aluminum crucibles and compressed using a die tool (punch) for measurements. The weight of the sample varied between 10 and 20 mg. Calibration of the device was carried out with aluminum oxide powder. After each run, the samples were weighed to determine the mass loss during the measurement.

Due to the relatively unknown thermal behavior of mealworms, it is advisable to scan at different measurement rates and across various temperature intervals, starting at a lower temperature, to assess the unfolding kinetics and to determine the optimal settings for conducting the measurements [14].

To identify the appropriate DSC settings for subsequent measurements, initial experiments were conducted with untreated mealworms, as well as mealworms dried in an oven at 60 °C and primarily those dried in a freeze dryer, across different temperature intervals and scan rates. The measurements were performed using liquid nitrogen as a coolant, facilitating a temperature range of 0-100 °C or 0-120 °C. Different scan rates of 1, 2, and 10 K/min were employed to evaluate the kinetics of protein unfolding and to establish optimal measurement settings. The measurement sequence and various setting parameters for the DSC trial are presented in Figure 1.

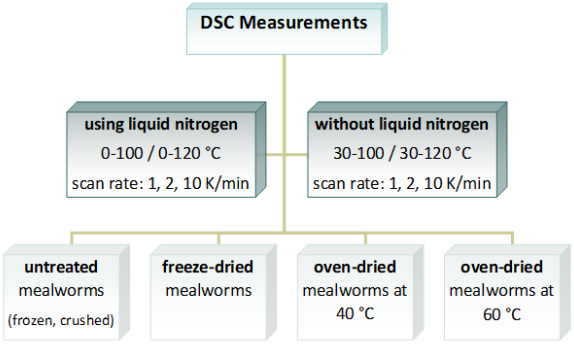


**Figure 1.** Block diagram of DSC measurements

## RESULTS AND DISCUSSION

### *Comparison of drying processes*

- *Drying curves.* The drying curves of the three studied cases (40°C, 60°C, freeze-drying) are given in Fig. 2. As expected, drying at 60°C is fastest at the start of drying. However, the scarce, measurement-dependent data do not allow any conclusion to be drawn about drying periods. Nevertheless, the curves suggest that a first drying period did not occur in any of these experiments (40°C, 60°C, freeze-drying).

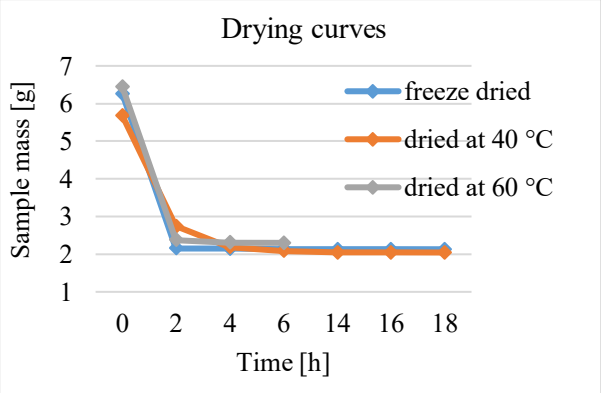


**Figure 2**. Drying curves for different drying conditions. The overall drying times are indicated in the plots.

Surprisingly, freeze-drying is almost as fast as drying at 40°C. The drying rates at the start are very similar in both cases.

### *Residual moisture content*

The residual moisture content was measured for each one experiment with a TGA. Non-dried mealworms have a moisture content of approximately 65%, which aligns with the values reported in the literature (59-68%) [15]. As can be seen from the data collected in Table 1, on average, all dried samples had a residual moisture content of less than 5 m% (TGA-based value). Table 1 indicates that higher process temperatures yield lower values.

**Table 1.** Residual moisture contents of SAHAWA UG larvae.

| | Result from TGA (m %) |
|---|---|
| Untreated | 65.04 |
| Oven drying at 40°C | 4.12 |
| Oven drying at 60°C | 3.62 |
| Freeze-drying | 4.90 |

### *Visual appearance*

After drying, a noticeable difference in color was observed, as shown in Fig. 3. Mealworms dried at 40 °C and 60 °C exhibit a visibly darker color compared to those dried in the freeze-dryer. The color of the samples from the freeze-dryer is closer to that of the non-dried samples. Non-enzymatic browning reactions (Maillard reaction) could apparently be avoided by the selected freeze-drying conditions, whereas they strongly affected drying at 40°C and 60°C [7]. As shown in Fig. 3, both oven samples exhibit a very similar color, indicating a similar degree of deterioration. According to literature, Maillard reaction and protein denaturation reactions can result in a reduction of protein, amino acid and peptide contents of up to 20 % [5, 7, 15].

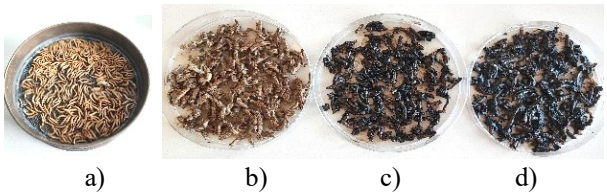


**Figure 3.** Visual appearance of mealworms: a) before drying, b) after freeze-drying, c) after oven drying at 40°C, d) after oven drying at 60°C.

- *Determining optimal DSC parameters.* Differential scanning calorimetry (DSC) measurements were conducted to analyze the thermal properties in terms of protein denaturation

of mealworms subjected to various drying conditions. Firstly, the optimal settings for conducting the measurements were determined. The measurements were conducted at different scan rates of 1, 2, and 10 K/min within the temperature range of 30-120 °C, in consultation with the literature [14]. Among the scan rates tested, 2 K/min provided the most defined thermogram. At 1 K/min, the denaturation peak shifted to lower temperatures, while 10 K/min was too fast to resolve unfolding kinetics. A scan rate of 10 K/min was too rapid to adequately monitor the unfolding kinetics of the protein; consequently, no endothermic characteristic peak is observed in the resulting curve, which is typically expected during protein denaturation [6, 16].

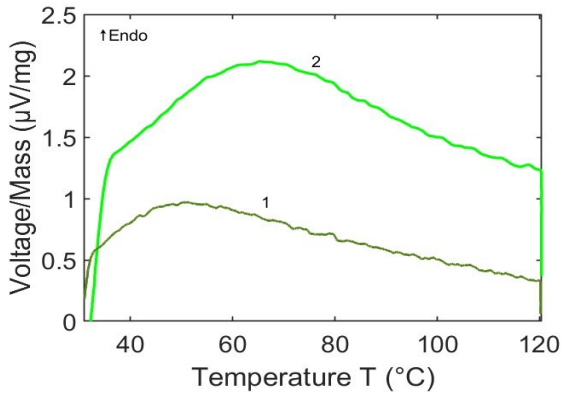


**Figure 4.** DSC thermogram of mealworms dried in a freeze dryer at a scan rate of 1 K/min (curve 1) and 2 K/min (curve 2)

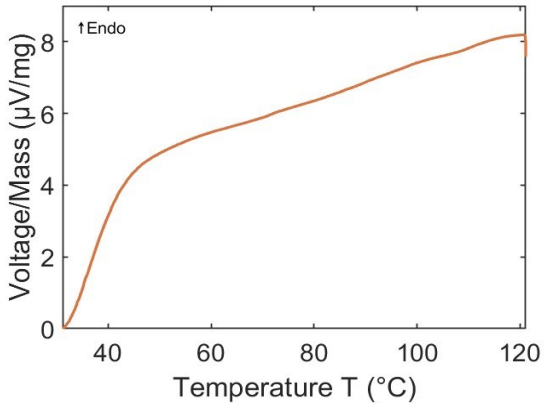


**Figure 5.** DSC thermogram of mealworms dried in a freeze dryer at a scan rate of 10 K/min

- *Thermal behavior of freeze-dried mealworms*. According to Fig. 4, the measurement is conducted using freeze-dried mealworms within a temperature range of 30 to 120 °C. The graph shows that the peak begins at temperatures below 30 °C. Since setting the appropriate temperature range is crucial for obtaining a complete thermogram when measuring unknown samples, the sample should be retested over a wider temperature range to fully capture the heat transfer dynamics [14]. Therefore, the measurement with freeze-dried mealworms was conducted in the presence of a coolant (liquid nitrogen), to achieve a broader measurement temperature range of 0 to 120 °C.

The results show that the use of a coolant positively affects the complete formation of the endothermic peak. Therefore, it was decided that all DSC measurements in this study will be conducted in the presence of liquid nitrogen as a coolant, starting at a temperature of 0 °C.

- *Comparison between drying methods.* The results obtained (Fig. 6) indicate that there is no clearly defined peak; however, an endothermic thermal process is observed in the range of 40 to 80 °C, immediately followed by an exothermic region. To investigate how the curve develops over a broader temperature range, a measurement was conducted from 0 to 200 °C.

The expansion of the measurement temperature range to 200 °C (Fig. 7) reveals that the curve in the exothermic region continues to rise with increasing temperature without reaching an exothermic peak. Therefore, it was concluded that heating to such high temperatures is unnecessary, as other studies indicate that the protein denaturation temperature in mealworms lies within the range of 55 °C to 80 °C [6]. Thus, a temperature range of 0 to 100 °C is deemed optimal for the measurements. For this reason, it was decided to conduct all measurements in this study in the presence of liquid nitrogen as a coolant, within a temperature range of 0 to 100 °C at a scan rate of 2 K/min.

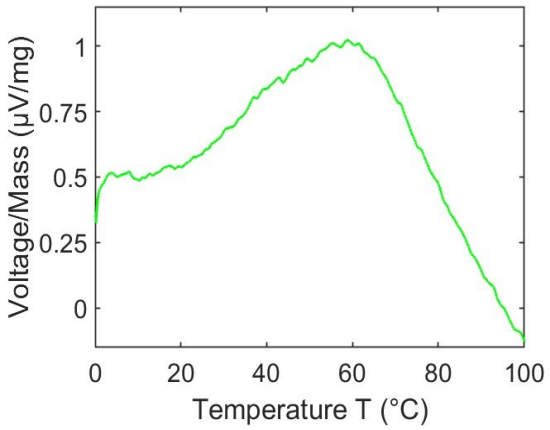


**Figure 6.** Measurement in the temperature range of 0 to 100 °C with liquid nitrogen as a coolant.

According to Fig. 6, calorimetric measurements reveal an endothermic event occurring in the range

of 30–80 °C, with a temperature peak around approx. 60 °C, though a well-defined peak is absent.

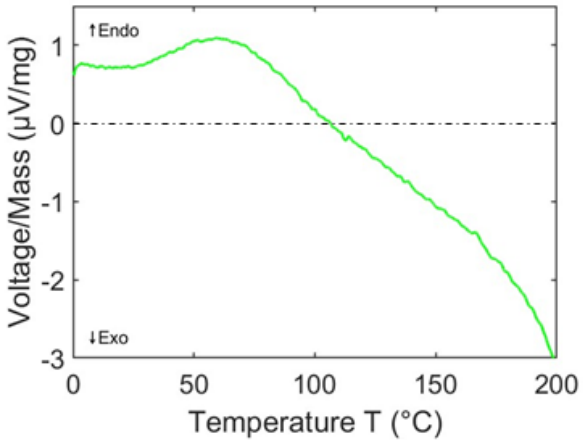


**Figure 7.** Expansion of the measurement temperature range to 200 °C.

This endothermic phenomenon may be attributed to protein denaturation, as it falls within the temperature range for protein denaturation in mealworms reported in other studies (55 °C to 80 °C) [6].

For the DSC measurements, the entire form of *T. molitor* was used, meaning that the sample also contained various complex components such as hemolymph, skeletal muscle, enzymes, chitin, oil, and other substances [17]. This sample complexity may explain the lack of a distinct peak. In other studies [6, 17], pre-treatment of the mealworm sample, such as defatting of mealworm flour using ethanol or hexane followed by protein extraction was conducted. The resulting protein extract was then processed into a dilute protein solution, potentially resulting in more pronounced peaks in DSC thermograms.

- *Discussion of protein denaturation and aggregation.* Protein unfolding during thermal denaturation involves the absorption of heat to break intramolecular bonds (non-covalent and, in some cases, disulfide bonds) and is therefore an endothermic process. When hydrogen bonds or other hydrophilic interactions that maintain the tertiary structure of the proteins are disrupted by heating, initially buried hydrophobic regions within the proteins are exposed on the protein surface and interact with hydrophobic regions in other protein molecules, leading to aggregation [18].

Thus, the exothermic region in the thermogram (Fig. 7) can be attributed to protein aggregation, which is known to be an exothermic event, as reported in other studies [14, 19]. Additionally, one study has demonstrated that the presence of such an exothermic region is due to the degradation of chitin components in the composition of insects, occurring at 300-400 °C [8]. There is also evidence of lipid oxidation contributing to exothermic regions in the DSC thermogram [20]. However, this is not the focus of the current study.

The graph (Fig. 8) illustrates the DSC thermogram of untreated mealworms (frozen, not dried). Fig. 8 shows a significant endothermic peak, which may be attributed to the denaturation process. According to Akhtar *et al.*, the protein denaturation temperature in mealworms ranges from 55 °C to 80 °C [6]. Figure 8 shows a peak at approximately 70 °C. However, future investigations should focus on measuring water-solubilized samples with moisture levels similar to those of frozen mealworms. Nevertheless, the detected peak might also be associated with the effects of water loss from the sample during the measurement (from 0 to 100 °C). According to the literature, fresh mealworms have a moisture content ranging from 59% to 68% [15], aligning with the values measured in this study. The change in the amount of absorbed heat flow due to the denaturation of proteins is much less significant than the change caused by the breaking of hydrogen bonds or water loss [21]. This is because water possesses an extensive network of hydrogen bonds, resulting in a considerably higher heat capacity compared to organic compounds like proteins. Furthermore, water is more ordered and densely packed near the protein surface. Since water cannot form hydrogen bonds with nonpolar entities, the hydrogen bonding between water molecules at the protein's surface is maximized. As the temperature rises, the ordered water shell around the protein begins to dissipate, leading to increased heat absorption during the measurement [21, 22].

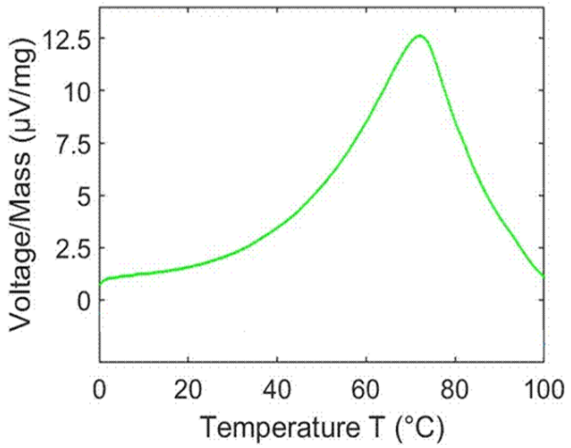


**Figure 8.** DSC thermogram of untreated mealworms (frozen, not dried).

The following graph (Fig. 9) presents a comparison of the measurement results for

mealworm samples dried in a freeze-dryer, in an oven at 40 °C, and in an oven at 60 °C. This graph clearly shows that the peak temperatures of endothermic processes decrease with increasing drying temperature. While the peak temperature for freeze-dried samples is approximately 60 °C, it drops to around 55 °C for samples dried in an oven at 40 °C, and further to about 50 °C for samples dried at 60 °C.

As illustrated in the graph, the freeze-dried samples require the largest amount of absorbed heat flow for protein unfolding in the mealworms. This may be due to the preservation of native protein in the freeze-dried mealworm samples [8], although residual moisture in the samples could also play a role.

However, the measured signal for samples dried in an oven at 40 °C is reduced by about one-third compared to the lyophilized samples, possibly due to a lower amount of remaining native protein and the presence of aggregates following the drying process, as reported in other studies [15, 16]. It should also be noted that mealworms dried at 40 °C contain less residual moisture, which may also influence the results.

Mealworms dried at 60 °C absorb the least heat flow. This may be because the drying temperature is close to the denaturation temperature of proteins in mealworms, potentially resulting in a significant portion of the native protein already being denatured. Additionally, the low residual moisture could contribute to the smaller signal observed in the thermogram.

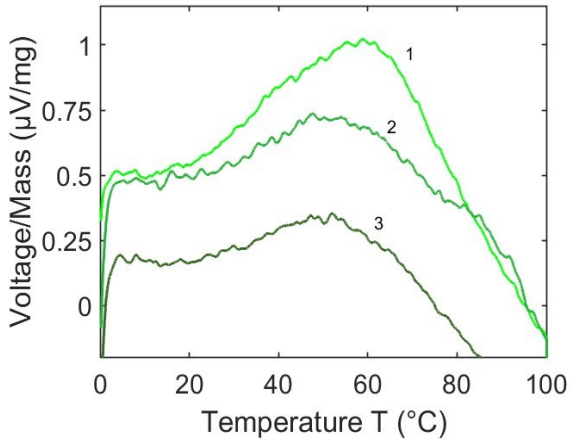


**Figure 9.** Comparison of the DSC thermograms of mealworms dried in a freeze-dryer (curve 1), in an oven at 40 °C (curve 2), and in an oven at 60 °C (curve 3)

Figure 9 shows a progressive reduction in peak temperature and enthalpy with increasing drying temperature, supporting the hypothesis that higher thermal exposure induces partial protein denaturation during processing.

## CONCLUSION

Drying is a critical step in mealworm processing, yet it can negatively affect the functionality of native proteins [5]. This study investigated how different drying methods influence the denaturation temperature and protein quality of the samples. Differential scanning calorimetry (DSC) measurements were performed on both untreated (frozen, undried) mealworms and those subjected to freeze-drying or oven drying at 40 °C and 60 °C.

The results indicate that both freeze-drying and drying in an oven at 40 °C and 60 °C have a significant impact on the protein denaturation of *T. molitor* larvae. The gentler effect of freeze-drying on the color of edible insects can be attributed to the lower drying temperatures, which help prevent thermal browning reactions, while the elevated temperatures in the oven promote non-enzymatic browning of the samples [7].

As the drying temperature increases, the heat capacity peak associated with mealworm protein denaturation decreases and shifts to lower temperatures. This shift is likely due to conformational changes in the proteins that occur during the drying process. Moreover, the thermograms obtained show a significantly higher endothermic heat quantity for freeze-dried mealworms compared to those dried in an oven at 40 °C and 60 °C. This increase in absorbed heat in the lyophilized samples may be linked to a more native protein structure, but it may also be influenced by residual moisture in the samples.

The DSC measurements suggest that the complexity of the samples leads to a lack of defined peaks in the thermograms. Therefore, a pre-treatment of the mealworm samples, such as defatting mealworm flour and protein extraction [6, 17] is recommended to achieve more distinct peaks in the thermograms [14].

In conclusion, freeze-drying is more suitable for preserving the native protein structure in mealworms, while oven drying at higher temperatures leads to partial denaturation and potential loss of functionality. For more precise thermal characterization, further work using purified protein fractions is recommended.

## REFERENCES

1. World Population Prospects Highlights, 2019 Revision Highlights, 2019 Revision (2019) United Nations 2019.
2. How to Feed the World in 2050, 2009, https://www.fao.org/fileadmin/templates/wsfs/docs/

expert_paper/
How_to_Feed_the_World_in_2050.pdf
3. Y. Akhtar, M.B. Isman, Insects as an Alternative Protein Source, Proteins in Food Processing (2nd edn.), 2018, p. 263, doi: 10.1016/B978-0-08-100722-8.00011-5
4. U. Berthelot, S. R. Piché, G. Brisson, A. Doyen, *Future Foods*, **9**, 100382 (2024) doi: 10.1016/j.fufo.2024.100382
5. B. Purschke, H. Brüggen, R. Scheibelberger, H. Jäger, *European Food Research and Technology*, **244**, 269 (2018) doi: 10.1007/s00217-017-2953-8
6. H. Lee, J. Kim, D. Ji, C. Lee, *Food Science Animal Resources*, **39**(2), 296 (2019) doi: 10.5851/kosfa.2019.e24
7. N. Kröncke, S. Grebenteuch, C. Keil, S. Demtröder, L. Kroh, A.F. Thünemann, R. Benning, H. Haase, *Insects*, **10**(4), 84 (2019) doi: 10.3390/insects10040084
8. C. Monisha, M. Loganathan, *Journal of Food Processing and Preservation*, **46**(6), (2021) doi: 10.1111/jfpp.16184
9. J.C. Ribeiro, J.P. Marques, T.R. Fernandes, M.E. Pintado, S.M.P. Carvalho, L.M. Cunha, *LWT,* **191** (1), 115646 (2024) doi: 10.1016/j.lwt.2023.115646
10. B. A. Rumpold, O. S. Schlüter, *Molecular Nutrition & Food Research*, **57**(5), 802 (2013) doi: 10.1002/mnfr.201200735
11. I. Hanif, A. Apriantini, Y. C. Endrawati, *Jurnal Ilmu Produksi dan Teknologi Hasil Peternakan*, **11**(3), 153 (2023) doi: 10.29244/jipthp.11.3.153-162
12. E. Zielińska, B. Baraniak, M. Karaś, K. Rybczyńska, A. Jakubczyk, *Food Research International*, **77**(3): 460 (2015) doi: 10.1016/j.foodres.2015.09.008
13. S. Costa, S. Pedro, H. Lourenço, I. Batista, B. Teixeira, M. Narcisa, N.M. Bandarra, D. Murta, R. Nunes, C. Pires, *NFS Journal*, **21**, 57 (2020) doi: 10.1016/j.nfs.2020.10.001
14. I.B. Durowoju, K.S. Bhandal, J. Hu, B. Carpick, M. Kirkitadze, *Journal of Visualized Experiments*, **121**, 55262 (2017) doi: 10.3791/55262
15. N. Kröncke, V. Böschen, J. Woyzichovski, S. Demtröder, R. Benning, *Innovative Food Science & Emerging Technologies*, **50**, 20 (2018) doi: 10.1016/j.ifset.2018.10.009
16. S.D. Arntfield, E.D. Murray, *Canadian Institute of Food Science and Technology Journal*, **14**(4), 289 (1981) doi: 10.1016/S0315-5463(81)72929-8
17. T.K. Kim, M. H. Lee, H.I. Yong, S. Jung, H.D. Paik, H.W. Jang, Y.S. Choi, *Foods*, **9**(10), 1443 (2020) doi: 10.3390/foods9101443
18. S.M. Fitzsimons, D.M. Mulvihill, E.R. Morris, *Food Hydrocolloids*, **21** (4), 638 (2007) doi: 10.1016/j.foodhyd.2006.07.007
19. M. Roldan, T. Antequera, M. Armenteros, J. Ruiz, *Food Chemistry*, **149**, 129 (2014) doi: 10.1016/j.foodchem.2013.10.079
20. P. Gill, T.T. Moghadam, B. Ranjbar, *J. Biomol. Tech.,* **21**(4), 167 (2010).
21. C.H. Tang, S.M. Choi, C.Y. Ma, *International Journal of Biological Macromolecules*, **40** (2), 96 (2007) doi: 10.1016/j.ijbiomac.2006.06.013
22. C. M. Johnson, *Archives of Biochemistry and Biophysics,* **531**(1–2), 100 (2013) doi: 10.1016/j.abb.2012.09.008

*Bulgarian Chemical Communications, Volume 58, Issue 1 (pp. 37-43) 2026* *DOI: 10.34049/bcc.58.1.5574*

# Investigation of antioxidant activities of *Ganoderma* mushroom

N. Hayrat[1], B. Kilinc[1,2], B. Yilmaz[2], A. Kul[3], Sh. Tarbiat[4]*, V. Enisoglu Atalay[1,4]*, T. Catal[1,4]*

[1]*Istanbul Protein Research-Application and Innovation Center (PROMER), Uskudar University 34662 Uskudar, Istanbul, Türkiye*
[2]*Graduate School of Sciences, Programme of Biotechnology, Uskudar University, 34662 Uskudar, Istanbul, Türkiye*
[3]*Faculty of Pharmacy, Department of Basic Pharmaceutical Sciences, Istanbul University, 34452, Istanbul, Türkiye*
[4]*Department of Molecular Biology and Genetics, Uskudar University 34662 Uskudar, Istanbul, Türkiye*

Received: May 07, 2023; Revised: October 29, 2025

*Ganoderma lucidum* is a highly popular medicinal mushroom that has been used for centuries to treat various diseases. *Ganoderma lucidum* contains biologically active components and these components give *Ganoderma lucidum* its antimicrobial and antioxidant properties. In this study, we aimed to investigate the antioxidant activites of *Ganoderma lucidum*. *Ganoderma lucidum* DMSO extracts for both mycelium and fruiting body were prepared. DPPH radical scavenging activity and ferric-reducing antioxidant power (FRAP) assays were applied in order to understand the antioxidant features of *G. lucidum*. The chemical composition of the DMSO extracts of *G. lucidum* was analyzed using gas chromatography. The chemical compounds and antioxidant actitivies were evaluated using computational methods. The ethanol extracts of the fruiting body of *G. lucidum* (*GL*) exhibited DPPH·radical scavenging activity with an IC50 value of 15.01± 0.06 mg/ml. However, the mycelium part of *Ganoderma* (*GE*) showed the poorest antiradical-scavenging capacity (IC50 =30.53 ± 0.03) and the least press diminishing capacity (41.17 ± 0.019) within the water-dissolvable *Ganoderma lucidum* may show antioxidant activities, and structural characteristics of its bioactive ingredients may play a crucial role in the mechanism of antioxidant action.

**Keywords:** antioxidant, computational chemistry, DPPH, *Ganoderma lucidum*

## INTRODUCTION

*Ganoderma lucidum* (*GL*) is a fungus with a woody structure and a shiny appearance that goes by several names, including "Reishi," "Ling Zhi," and "Mannentake". *Ganoderma* is a traditional medicinal mushroom that has been used for millennia to improve longevity, healing, and health in east countries such as China, Japan, and Korea [1-3]. Depending on the climate conditions such as humidity, heat, lighting, etc., the color, bitterness and shape of Reishi mushroom differ from each other even if they have the same strain [4]. *Ganoderma* species belong to the group *Basidiomycota*, class *Homobasidiomycetes*, order *Aphyllophorales*, family *Polyporaceae* [5]. Latest pharmacologic studies with *Ganoderma* extracts have revealed that they have antibacterial properties and they also inhibit lipid peroxidation/oxidative DNA damage. Treatment of *S. aureus* infections has limitations since it creates resistance to antibacterial compounds and reduces the effectiveness of the chemicals used, as well as making the microbe more tolerant and harmful. Various *Ganoderma* extracts have been proven to inhibit the growth of both Gram-positive and Gram-negative bacteria [1]. Many animal model and molecular based studies have conducted to proven the various pharmacological effects of *G. lucidum* in traditional Chinese medicine [6]. According to ancient Chinese medicine, while *GL* has functions such as increasing body resistance against microbial infections and prolonging life, recent studies with *Ganoderma* extracts have revealed various therapeutic effects [5] such as anticancer, anti-inflammatory, antitumor, antioxidant, immunomodulatory, antidiabetic, immunodeficiency, antiviral, anti-hypertensive, antibacterial, antifungal, antiatherosclerotic, antiaging, antiandrogenic, antihepatotoxic, able to scavenge free radicals, neuroprotective, increasing sleep, suppressing cholesterol synthesis, hypoglycemia, preventing lipid peroxidation and oxidative DNA damage, hepatoprotective, preserving gut health, preventing obesity, migraines, high blood pressure, loss of appetite, gastritis, hemorrhoids, menstrual pain, constipation and cardiovascular issues [7]. These mushrooms are widely utilized in Chinese medicine, where they are believed to boost energy, enhance the immune system, and extend lifespan [8]. Additionally, triterpenoids, the main components of *G. lucidum*, are reported to play an important role in the pharmacological effects mentioned. During the past three decades, more than 150 triterpenoid compounds have been isolated from the genus

* To whom all correspondence should be sent:
Email: *tunc.catal@uskudar.edu.tr*
*vildan.enisoglu@uskudar.edu.tr*
*shirin.tarbiat@uskudar.edu.tr*

*Ganoderma* sp. Among the triterpenoids, ganoderic acid A (GA), ganoderic acid B (GB), ganoderic acid G (GG), ganoderic acid E (GE), ganoderenic acid D (GED), and ganoderic acid D (GD) are the main components. The effect of *G. lucidum* on cancer is based on glucan and triterpenes that it contains. Beta glucans are thought to activate the immune system, and triterpenes are thought to have a cytotoxic effect against various cancer cells [9].

*Ganoderma lucidum* polysaccharides are known as antitumor agents, but although *GL* extracts contain biologically active compounds like glycosides, carbohydrates, phenolic compounds and triterpenoids, their antibacterial activity is partly due to the inhibitory properties of polysaccharides. When it comes to antibacterial agents, extracts can inhibit both Gram-negative and Gram-positive bacteria, so some studies have focused on the activity of isolated polysaccharides, as well as research on extracts derived from mycelium and fruiting body. In general, extracts in organic solvents such as dichloromethane, hexane, methanol and ethyl acetate, as well as aqueous extracts of *G. lucidum* act against *Enterobacter aerogenes*, *Bacillus cereus*, *Pseudomonas aeruginosa*, *Escherichia coli* and *Staphylococcus aureus* [10].

*Staphylococci* are invasive Gram-positive bacteria that cause a variety of diseases in humans and animals. These include bacteriuria, enterocolitis, osteomyelitis, pneumonia, acne, carditis, meningitis, arthritis and septicemia. Antibiotic-resistant *Staphylococci* have evolved as an unavoidable genetic response to the selective pressure of antimicrobial therapy. The ability of microbial species to adapt rapidly to changes in their environment was demonstrated by the development of resistance when an antibiotic enters clinical use [11]. When an antibacterial compound is applied, limitations arise in the treatment of *S. aureus* infections, as it creates resistance and reduces the effect of the compounds used, and it also makes the microorganism more tolerant and more dangerous [12, 13]. Therefore, it is important to investigate new potential treatments.

In this study, it was aimed to identify the chemical composition and investigate the antioxidant features of *Ganoderma* mushroom. Computational chemistry methods were applied to evaluate the antioxidant activity of *G. lucidum* for the first time.

## EXPERIMENTAL

### *Materials and methods*

*Ganoderma lucidum* powder was used for preparation of mushroom extracts (Gano Excel Co.). 300 mg of powder were mixed with 10 mL of DMSO and placed on a shaker for 24 h at room temperature. Then the solution was filtered by 0.22 μm syringe filter. DMSO extraction method was used for both fruiting body (*GL*) and mycellium (*GE*) of *G. lucidum* separately [14].

### *DPPH radical scavenging activity assay*

The antioxidant capacity of two *Ganoderma* extracts in three solvent types: aqueous (a mixture of 82 parts of distilled water with 10 parts of methanol and 8 parts of acetic acid); ethanol; and hexane, was determined by the stable DPPH radical scavenging activity described by the method of Villano *et al*. (2007) [15].

DPPH· radical, a stable free radical, reacts with an antioxidant and is reduced to DPPH-H which is detected by the decrement in absorbance in spectrophotometry. The degree of discoloration reveals the antioxidant chemicals in extracts' scavenging activity in terms of their capacity to donate hydrogen. To prepare the reaction mixture, 1 ml of DPPH· solution was added to each of 4 ml-sample solutions from three solvent types. The absorbance of the resulting solution was measured by spectrophotometry at 517 nm, following incubation at 20°C for 30 min. The $IC_{50}$ values of the extracts in the DPPH assay were calculated, and low $IC_{50}$ values referred to higher antioxidant capacity. The results were compared to ascorbic acid (AA) used as a reference.

### *Ferric-reducing antioxidant power (FRAP) assay*

With a few minor adjustments, the Oyaizu 1986 assay was used to test the ferric reduction ability of the samples and the reference [16]. The test was based on the reducing-power of the transformation of ferrous ($Fe^{2+}$) to ferric ($Fe^{3+}$) ions, which produces a blue complex and increases absorbance at 700 nm. Samples of varying concentrations (0.1-1.5 mg) were combined with phosphate buffer (2.5 ml) in 1 ml of methanol. The mixture was incubated at 50°C for 20 min. To the mixture aliquots of trichloroacetic acid (2.5 ml) were added and the mixture was centrifuged at 3000 rpm for 10 min. A freshly made ferric chloride solution (0.5 ml) and distilled water(2.5 ml) were combined with the solution's upper layer (2.5 ml). The absorbance was measured at 700 nm, ascorbic acid was used as reference standard. Increased absorbance of the reaction mixture indicates increase in reducing power [17].

*GC-MS analysis*

The *G. lucidum* and *G. excellium* were purchased from Gano Excel company. One capsule (480 mg) from each was opened and transferred to a 15 mL-tube separately. Then, 10 mL of ethanol was added to each, and sonicated for 30 min. The dried samples were treated for 90 min at 30 °C with 150 µl of hydroxylammonium chloride (25.0 mg/mL) in pyridine. The samples were derivatized with the addition of 270 µl MSTFA + 30 µl TFA and incubation at 90 °C for 90 min after cooling to room temperature. A vial of GC-MS was used to transfer 50 ml of the derivatized samples for analysis. GC–MS analysis of the constituent sugars was performed on a Shimadzu GC-2010 plus gas chromatograph (Shimadzu Scientific Instruments, Columbia, MA, USA), equipped with an Rtx®-5MS column (30 m × 0.25 mm ID, 0.10 µm film thickness) (Restek, USA). Helium was used as carrier gas. The oven temperature program was set as follows: keeping at 50 °C for 2 min, ramping at 4 °C $min^{-1}$ up to 250 °C and keeping at 250 °C for 8 min. The temperatures of the transfer line and ion source were set at 270 and 250°C, respectively. Mass spectra were scanned from 40–400 m/z at a rate of 0.5 scans $s^{-1}$ and the electron impact ionization energy was 70 eV. Data handling was supported by the software GC-MS solution, ver. 2.51 (Shimadzu). The compounds of extracts were identified using the National Institute Standard and Technology (NIST) library. The relative percentages of the compounds were calculated based on the GC peak areas.

*Theoretical calculations*

Geometry optimizations and ferric reducing mechanism (Eq. 1) modeling of candidate antioxidant molecules myristic acid, arabitol, mannitol, inositol, and stearic acid were performed by HF/6-31+Gdp method in hexane, ethanol and mixture. IEF-PCM method was used for the solvent optimizations. All computational calculations were implemented in GaussView 5 [18] molecular visualization and Gaussian 09 software [19].

The chemical mechanism of the ferric reducing reaction is given in Eq. 1 [20]. In the mechanism modeling of ferric reducing, the energy changes during the capture of $e^-$ in the $Fe^{III+} \rightarrow Fe^{II+}$ conversion of the candidate antioxidant molecules determined above, were investigated.

$$[Fe^{III}(TPTZ)_2]^{3+} + ArOH \rightarrow [Fe^{II}(TPTZ)_2]^{2+} + ArO^{\cdot} + H^+ \quad (1)$$

*Statistical analysis*

The results were expressed as mean ± SD of at least three independent determinations. Multi-group comparisons were analyzed using one-way ANOVA followed by a post hoc Tukey test. At $p<0.05$, differences were accepted statistically significant.

## RESULTS AND DISCUSSION

*DPPH radical scavenging activity assay*

The antioxidant properties of *Ganoderma* extracts (*GE* and *GL*, respectively) with three different solvents; aqueous, ethanol (EtOH), and hexane, were evaluated using two methods: DPPH· radical scavenging activity and ferric reducing antioxidant power (FRAP). Summary of the results is presented in Table 1.

**Table 1**. Antioxidant activity of *GL* and *GE* mushrooms extracted in three solvent types, with DPPH radical scavenging assay and ferric reducing antioxidant power (FRAP) assay. Values are the mean ± standard deviation (n = 3). Differences between samples in the three extracted solvents in each assay are statistically significant (P <0.01). NA= no activity.

| Samples | Solvent | DPPH activity $Ic_{50}$ values (Mg/Ml) | FRAP G /Mmol Aa equivalent |
|---|---|---|---|
| *Gl* | Aqueous | 67.4 ± 0.01 | 8.4 ± 0.02 |
| | Ethanol | 15.01± 0.06 | 4.46 ± 0.03 |
| | Hexane | 30.95 ± 0.05 | 7.50 ± 0.01 |
| *Ge* | Aqueous | 72.2 ± 0.01 | 41.17 ± 0.01 |
| | Ethanol | 30.53 ± 0.03 | 26.78 ± 0.03 |
| | Hexane | Na | 37.5 ± 0.01 |
| Ascorbic acid | - | 9.12± 0.01 µg/Ml | – |

According to the results of the DPPH radical scavenging assay, *GL* exhibited radical scavenging activity in all solvent types, which was highest in the ethanolic extract. The EtOH extracts of *GL* exhibited DPPH·radical scavenging activity with an $IC_{50}$ value of 15.01± 0.06 mg/ml. *GE* showed moderate DPPH· radical scavenging activity compared to *GL,* while no activity was observed by the *GE* hexanic extract. Ascorbic acid, known for its significant antioxidant activity, was used as the reference. ($IC_{50}$ = 9.12± 0.01 µg/ml).

*Ferric reducing antioxidant power (FRAP) assay*

Considering the results obtained using the FRAP assay, the EtOH extract of *GL* possessed the highest reducing power relative to that of ascorbic acid (4.46 ± 0.03 g /mmol AA) used as the reference. When compared to the *GL* extracts, the *GE* extracts displayed much lower antioxidant activity based on their ascorbic acid equivalences (41.17 ± 0.01, 26.78 ± 0.03, 37.5 ± 0.01 (g/mmol AA) for aqueous, ethanolic and hexanic extracts, respectively. The antioxidant ability of *GL* and *GE* could be attributed to the presence of a variety of biomolecules in *GL*

and *GE* and their specific ability to prevent oxidation. Data from GC-MS analysis indicated that sugars (disaccharides and monosaccharides) and sugar alcohols are the most abundant biomolecules (more than 50%), followed by fatty acids (dicarboxylic fatty acids, saturated fatty acids, mono and polyunsaturated fatty acids) in both samples (Table 2).

**Table 2.** GC-MS results of *Ganoderma* (*GE* and *GL*).

| RT | Compound | *GE* % | *GL* % |
|---|---|---|---|
| 8.158 | Succinic acid | 0.90 | 2.39 |
| 13.533 | Malic acid | 1.88 | 8.70 |
| 14.300 | Erythritol | - | 2.19 |
| 20.492 | Xylitol | 9.20 | 10.08 |
| 21.792 | Azelaic acid | - | 2.07 |
| 21.433 | Ribose | 2.27 | - |
| 22.942 | Myristic acid | 1.15 | - |
| 25.758 | Sorbitol | 3.28 | 6.74 |
| 26.150 | Fructose | 5.14 | 3.19 |
| 26.333 | Arabitol | 5.89 | 1.92 |
| 27.750 | Glucose | 8.97 | 10.65 |
| 28.042 | Mannitol | 10.19 | 1.94 |
| 28.100 | Galactose | 8.55 | 8.18 |
| 29.500 | Inositol | 6.01 | 3.85 |
| 30.325 | Palmitic acid | 3.36 | 4.15 |
| 32.000 | Linoleic acid | 1.23 | 7.71 |
| 32.333 | Oleic acid | 11.44 | 10.92 |
| 36.275 | Stearic acid | 7.51 | 6.05 |
| 39.392 | Eicosanoic acid | 1.69 | 2.05 |
| 41.158 | Sucrose | 4.91 | - |
| 42.992 | Turanose | 2.39 | 4.15 |
| 44.967 | Palatinose | 4.05 | 3.05 |
| | Total | 100.00 | 100.00 |

The antioxidant activity of the studied samples might be related to the important bioactive molecules such as reducing sugars, organic acids like malic acid and succinic acid, also unsaturated fatty acids, which predominated over saturated fatty acids in both samples [21, 22]. However, sugars and sugar alcohols also exhibit anti-radical capacity, which is mostly dependent on the number of aliphatic hydroxyl groups in sugar alcohols of monosaccharides [23]. Sugars and sugar alcohols are soluble in water and ethanol due to the presence of multiple hydroxyl groups in their chemical structure. Neither sugars nor sugar alcohols are soluble in hexane due to the polarity mismatch between the solute and solvent particles. The hydroxyl groups are less reactive compared to the functional groups found in potent antioxidants like vitamin C, E and phenolic compounds which can effectively donate hydrogen atoms to neutralize free radicals [23].

Compared to *GL, GE* exhibited poorer antiradical-scavenging ability ($IC_{50}$ =72.2 ± 0.01) and lower ferric reducing ability (41.17 ± 0.019) in the aqueous solvent. These results could be explained by pointing out the fact that while higher amounts of sugars were found in *GE*, higher amounts of organic acids were recorded in *GL* (about 11%) in which malic acid predominates over succinic acid. Unsaturated fatty acids predominated over saturated fatty acids in both samples, and their amount is higher in *GL* compared to *GE.* The antioxidant effect of unsaturated fatty acids can be explained by their chemical structure and biological activity. Unsaturated fatty acids contain one or more double bounds through which they intract with free radicals. The hydrogen atoms adjacent to the double bonds are particularly active and bring about the hydrogen donating abilty to unsaturated fatty acids, and therefore lead to the neutralization of free radicals and prevent oxidative damage [22]. Biomolecule content found in the studied samples was comparable to the one reported by Mau *et al.* (2001), for cultivated *G. lucidum* from Serbia [24]. However, *GL* and *GE* from different origins, measured by the same *in vitro* assays, previously showed higher antioxidant properties than that we obtained here [25]. The outcomes of two antioxidant assays indicate that both samples revealed antioxidant properties. Nevertheless, the ethanolic extracts outperformed aqueous and hexane extract in terms of antioxidant efficacy in both samples suggesting that the type of solvent for extraction and their specific interactions with free radicals affect the impact of individual molecules on the antioxidant capacity of samples. It is expected that hydrophilic ingredients soluble in polar solvents, including the sugars possessed by the samples, are mostly soluble in ethanol and water yet organic acids and fatty acids are mostly soluble in nonpolar solvents like hexane [26], which suggests the difference in antioxidant activity from the different solvents. Therefore, the structural characteristics of bioactive ingredients, as well as the possible interactions between them and their solvents play a crucial role in the mechanism of antioxidant action.

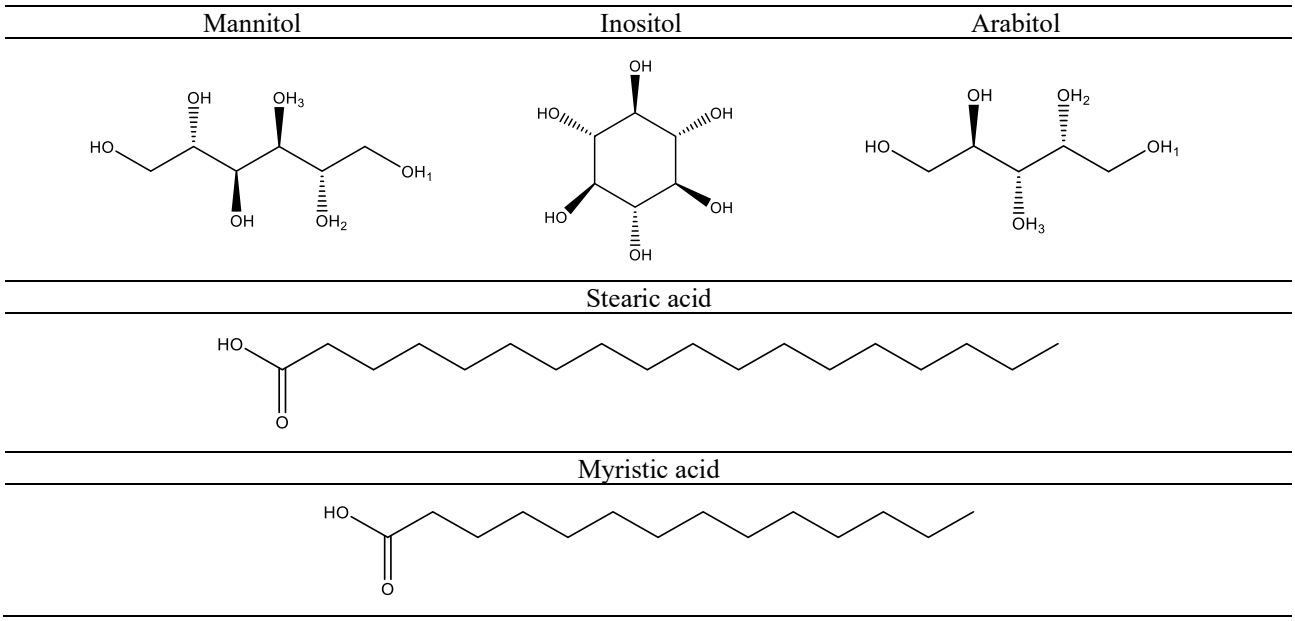


**Fig. 1.** 2D structures of candidate antioxidant molecules.

*GC/MS analysis*

The components obtained after derivatization of the capsules containing *Ganoderma lucidum* (*GE* and *GL*) are given in Table 2. Various candidate antioxidant molecules were detected using GC-MS analysis (Fig. 1), When Table 1 is examined, from both DPPH and FRAP methods, chosen as antioxidant activity determination methods in this study, is found that the antioxidant activity of *GL* extract is higher than that of *GE.* The antioxidant activity of *GE* ts demonstrated with a more significant difference, especially in the examination made with the FRAP method. When the GC-MS analyses of these extracts given in Table 1 are evaluated in terms of the percentage of active ingredients, it is thought that the antioxidant activity of *GE* and *GL* extracts may be caused by arabitol, mannitol, inositol, and stearic acid molecules (Fig. 1). Myristic acid was detected in *GE* extracts. At this point, the molecular modeling of the FRAP method was made using quantum chemical methods, and it was examined which of the molecules listed above caused this activity. The chemical mechanism of the FRAP method is given in Eq. 2 below [20]. In the mechanism modeling of FRAP, the energy changes during the capture of $e^-$ in the $Fe^{III+} \rightarrow Fe^{II+}$ conversion of the candidate antioxidant molecules determined above were investigated.

*Theoretical calculations*

$$[Fe^{III}(TPTZ)_2]^{3+}+ArOH \rightarrow [Fe^{II}(TPTZ)_2]^{2+}+ArO^{\cdot}+H^+ \quad (2)$$

For the mannitol compound, the calculated reaction energies of the ferric-reducing mechanism were evaluated using the HF/6-31G+dp method in all investigated solvents. The antioxidant activity of each of the OH bonds of the mannitol compound, which has 3 different inductive effects, in the analyzed solvent, is higher than the antioxidant activities of stearic acid, inositol, arabitol and myristic acid molecules. It was determined that $H^+$ transfer, which plays a critical role in the ferric reducing mechanism, is easier. On the other hand, calculations performed to determine which –OH bond confers the highest antioxidant activity revealed that the –OH groups located at the mannitol-OH3 position (1206.06 kJ·mol$^{-1}$) in the mannitol molecule and at the arabitol-OH2 position (1210.85 kJ·mol$^{-1}$) in the arabitol molecule exhibit the lowest bond dissociation energies, indicating their greater contribution to antioxidant activity. It contributes more because it breaks more easily than -OH bonds. On the other hand, in accordance with the literature, it was observed that the increase in the polarity of the solvent supported the antioxidant activity as it facilitated the charge separations [27]. The dipole moment order of the selected solvents in this study is hexane (1.9 D) < ethanol (16.2 D) and aqueous solvent (68.0 D). The basidiomycetous fungus *Ganoderma lucidum* (family *Ganodermataceae*) has been utilized in traditional Eastern medicine for generations. This medicinal mushroom is thought to help people live longer by preserving their vitality [28]. The polysaccharides from *Ganoderma lucidum* are used as a biological macromolecule material in medicine, food and

cosmetics [29]. According to the GC-MS results, it was determined that both capsules were rich in polysaccharides, consistent with the literature. *Ganoderma lucidum*'s considerable antioxidant effect, which reduces oxidative damage, is thought to be responsible for at least some of its health advantages [30]. The extracts of *G. lucidum* have shown *in vitro* antioxidant activities which may be due to the presence of flavonoids and phenolics. The solubility of bioactive components varies depending on the extracting solvents chosen. Generally, some active phytochemicals are insoluble in water, but soluble in alcohol, according to some studies [27]. Since the biological properties of the molecules detected in various herbal extracts can be defined by computational chemistry methods [31], it may be possible to use the molecules identified in *Ganoderma* mushroom as drug candidates for treatment purposes in various diseases in the future.

## CONCLUSIONS

In this study, in order to comprehend the antioxidant properties of *G. lucidum*, DPPH radical scavenging activity and ferric-reducing antioxidant power (FRAP) assays were used. Using gas chromatography, the chemical make-up of the DMSO extracts of *G. lucidum* was examined. Applying computational approaches, the chemical components and antioxidant activities were assessed. With an IC50 value of 15.01–0.06 mg/ml, the ethanol extracts of *G. lucidum* demonstrated DPPH radical scavenging action. The antioxidant activity of *GL* (fruiting body) extract was found to be greater than that of *GE* (mycellium) extract. Arabitol, mannitol, inositol, and stearic acid which may be the source of the antioxidant action in *GE* and *GL* extracts, were identified using GC/MS. In conclusion, the antioxidant properties of *Ganoderma lucidum* were identified.

***Declaration of competing interest:*** *The authors declare that there is no conflict of interest regarding the publication of this paper.*

***Funding:*** *This research did not receive any specific grant from funding agencies in the public, commercial, or not-for-profit sectors.*

***Acknowledgements:*** *The authors thank Prof. Dr. Safiye Sağ Erdem for software support.*

## REFERENCES

1. B. Sanodiya, G. Thakur, R. Baghel, G. Prasad, P. Bisen, *Current Pharmaceutical Biotechnology,* **10**, 717 (2009).
2. K. K. Hapuarachchi, C. R. Cheng, T. C. Wen, R. Jeewon, P. Kakumyan, *Mycosphere,* **8**, 1653 (2017).
3. G. G. Yue, K. P. Fung, G. M, Tse, P. C. Leung, C. B. Lau, *Journal of Alternative and Complementary Medicine,* **12**, 777 (2006).
4. T. Mizuno, G. Wang, J. Zhang, H. Kawagishi, T. Nishitoba, Li. J, *Food Reviews International*, **11**, 151 (1995).
5. S. G. Jonathan, F. E. Awotona, *African Journal of Biomedical Research,* **13,** 131 (2010).
6. K. S. Bishop, C. H. Kao, Y. Xu, M. P. Glucina, R. R. Paterson, L. R. Ferguson, *Phytochemistry*, **114**, 56 (2015).
7. R. R. Paterson, *Phytochemistry*, **67**, 1985 (2006).
8. A. Unlu, E. Nayir, O. Kirca, M. Ozdogan, *J BUON*, **21,** 792 (2016).
9. C. R. Cheng, Y. F. Li, P. P. Xu, R. H. Feng, M. Yang, S. H. Guan, D. A. Guo, *Food Chemistry*, **130**, 1010 (2012).
10. K. Mustarin, N. Bisko, R. Blieva, G. Al-Maali, T. Krupodorova, Z. Narmuratova, Z. Saduyeva, A. Zhakipbekova, *Turkish Journal of Biochemistry*, **47,** 483 (2022).
11. B. R. Lyon, R. Skurray, *Microbiol Reviews*, **51**, 88 (1987).
12. N. K. Archer, M. J. Mazaitis, J. W. Costerton, J. G. Leid, M. E. Powers, M. E. Shirtliff, *Virulence*, **2**, 445 (2011).
13. B. Aslam, W. Wang, M. I. Arshad, M. Khurshid, S. Muzammil, M. H. Rasool, M. A. Nisar, R. F. Alvi, M. A. Aslam, M. U. Qamar, M. K. F. Salamat, Z. Baloch*, Infect Drug Resistance*, **11**, 1645 (2018).
14. A. Barbieri, V. Quagliariello, V. Del-Vecchio, M. Falco, A. Luciano, N. J. Amruthraj, G. Nasti, A. Ottaiano, M. Berretta, R. V. Iaffaioli, C. Arra, *Nutrients*, **9,** 210 (2017).
15. D. Villaño, M. S. Fernández-Pachón, M. L. Moyá, A. M. Troncoso, M. C. García-Parrilla, *Talanta*, **71**, 230 (2007).
16. M. Oyaizu, *Japan Journal of Nutrition*, **44**, 307 (1986).
17. S. Tarbiat, S. Turutoglu, M. Ekingen, *Current Topics in Nutraceutical Research*, **18**, 354 (2020).
18. R. Dennington, T. Keith, J. Millam, GaussView, Version 5, Semichem Inc., Shawnee Mission KS, 2009.
19. M. J. Frisch, G. W. Trucks, H. B. Schlegel, G. E. Scuseria, M. A. Robb, J. R. Cheeseman, J. A. Montgomery, J. T. Vreven, K. N. Kudin, J. C. Burant, J. M. Millam, S. S. Iyengar, J. Tomasi, V. Barone, B. Mennucci, M. Cossi, G. Scalmani, N. Rega, G. A. Petersson, H. Nakatsuji, M. Hada, M. Ehara, K. Toyota, R. Fukuda, J. Hasegawa, M. Ishida, T. Nakajima, Y. Honda, O. Kitao, H. Nakai, M. Klene, X. Li, J. E. Knox, H. P. Hratchian, J. B. Cross, C. Adamo, J. Jaramillo, R. Gomperts, R. E. Stratmann, O. Yazyev, A. J. Austin, R. Cammi, C. Pomelli, J. W. Ochterski, P. Y. Ayala, K. Morokuma, G. A. Voth, P. Salvador, J. J. Dannenberg, V. G. Zakrzewski, A. D. Daniels, O. Farkas, A. D. Rabuck, K. Raghavachari, J. V. Ortiz, Gaussian 09, Gaussian Inc., Pittsburgh PA.

20. N. B. Sadeer, D. Montesano, S. Albrizio, G. Zengin, M. F. Mahomoodally, *Antioxidants*, **9,** 709 (2020).
21. L. Zhang, Z. Peijun, C. Xia, Y. Cheng, X. Guo, Y. Li, *Aquaculture Research* **51,** (2020).
22. D. Richard, K. Kefi, U. Barbe, P. Bausero, F. Visioli, *Pharmacological Research*, **57**, 451 (2008).
23. K. W. Kang, S. H. Kwak, S. Y. Yun, S. K. Kim, *Toxicological Research*, **23**, 143 (2007).
24. J. L Mau, H. C. Lin, C. C. Chen, *Research International*, **34**, 521 (2001).
25. D. Stojkovic, L. Barros, R. C. Calhelha, J. M. Glamoclija, A. Ciric, L. J. L. D. van Griensven, M. Sokovic, I. C. F. R. Ferreira, *BIOS Applied Metabolic Systems*, **65**, 42 (2013).
26. J. P. Mikkola, T. Salmi, R. Sjoholm, Journal of Chemical Technology & Biotechnology, **76**, 90 (2001).
27. J. J. Fifen, M. Nsangou, Z. Dhaouadi, O. Motapon, N. Jaidane, *Computational and Theoretical Chemistry*, **966**, 232 (2011).
28. L. X. Sun, L. H. Chen, Z. B. Lin, Y. Qin, J. Q. Zhang, J. Yang, J. Ma, T. Ye, W. D. Li, *Journal of Pharmacy Pharmacology*, **63**, 1595 (2011).
29. S. Mehta, S. Jandaik, *Journal of Pure and Applied Microbiology*, **6**, 1997 (2012).
30. C. YouGuo, S. ZongJi, C. XiaoPing, *Carbohydrate Polymers*, **78**, 258 (2009).
31. V. Atalay, S. Asar, *The European Chemistry and Biotechnology Journal*, **1**, 27 (2024). https://doi.org/10.62063/ecb-15

*Bulgarian Chemical Communications, Volume 58, Issue 1 (pp. 44-51) 2026* *DOI: 10.34049/bcc.58.1.5725*

# Unveil mechanism of action of parthenolide-9-one as an inhibitor for human erythroleukemia *via* molecular modeling, ADMET and MMGBSA analysis

H. D. Nguyen*

*Faculty of Biology, Thai Nguyen University of Education, 24000, Thai Nguyen, Vietnam*

Received: October 17, 2025; Revised: November 22, 2025

Leukemia poses a substantial global health challenge highlighting the demand for innovative therapies. Acute erythroid leukemia, an uncommon and aggressive variant of acute myeloid leukemia, presents difficulties owing to unfavorable prognosis and scarce treatment guidelines. Apoptosis emerges as a central therapeutic target in oncology, enabling targeted destruction of tumor cells and alleviating resistance. Caspase-3, a key effector enzyme, initiates apoptotic cascades by substrate cleavage, establishing it as an essential regulator in cancer. The present investigation assessed the molecular action of parthenolide-9-one as anti-erythroleukemic activity *via* inducing caspase-3 (3PD1) using *in silico* techniques. Molecular docking revealed parthenolide-9-one's superior affinity and orientation in the 3PD1 site compared to doxorubicin. Dynamic simulations over 100 ns confirmed enduring stability and uniform interactions. ADMET profiling indicated favorable pharmacokinetics for parthenolide-9-one, characterized by strong absorption and minimal metabolic engagement despite Ames toxicity. These observations position parthenolide-9-one as a viable candidate for erythroleukemic intervention *via* caspase-3-driven apoptosis, providing a basis for the development of refined derivatives that target apoptotic pathways in malignancy.

**Keywords:** Apoptosis, caspase-3, human erythroleukemia, molecular modeling, parthenolide-9-one.

## INTRODUCTION

Leukemia is a specific type of hematological malignancy involving the abnormal proliferation of white blood cells, with 486,777 new cases and 305,033 deaths in 2022 [1]. Acute erythroid leukemia is a rare and aggressive subtype of acute myeloid leukemia which is often associated with poor prognosis and challenging treatment due to its rarity and lack of established protocols [2, 3]. Current chemotherapy employs agents to eradicate cancer cells by inhibiting their proliferation, while also damaging normal cells. Apoptosis constitutes a primary target in oncology, facilitating selective cell demise and resistance mitigation [4].

Computational-aided drug discovery involves techniques like virtual screening, molecular modeling, and property prediction to identify promising compounds [5]. This approach can help identify potential new drug candidates and optimize existing treatments for acute erythroid leukemia, potentially leading to improved patient outcomes and quality of life [6].

Plant-derived compounds have played a crucial role in the development of effective cancer treatments, with many current chemotherapy drugs originating from natural sources. These drugs target various cellular processes crucial for cancer cell growth and division [7]. Among these, a sesquiterpenoid named parthenolide-9-one exhibits diverse biological activities, including *in vitro* cytotoxicity, *in vivo* antitumor activity, and antiviral activity [8, 9]. Parthenolide-9-one also demonstrates cytotoxicity against the human erythroleukemic cell line (HEL cells) *via* inducing apoptosis in a dose- and time-dependent manner [10]. However, molecular mechanisms of parthenolide-9-one remain partially clarified, especially *via* computational methods such as molecular docking, dynamic simulations, and ADMET predictions. Thus, the present study aimed to investigate its anti-erythroleukemic activity through integrated computational tools to better understand the mechanism of action. These findings establish a foundation for empirical validation and refinement of parthenolide-9-one for effective erythroleukemia therapy.

## MATERIALS AND METHODS

### *Materials*

The structure of parthenolide-9-one (molecular formula of $C_{15}H_{18}O_4$ and molecular weight of 262.1205 *m/z)*, was collected from Pubchem database (https://pubchem.ncbi.nlm.nih.gov/). Doxorubicin, a chemotherapy drug approved for the treatment of various cancers, with a molecular formula of $C_{27}H_{29}NO_{11}$ and a molecular weight of

* To whom all correspondence should be sent:
E-mail: *hungnd@tnue.edu.vn*

543.1741 m/z, was chosen as the reference (Figure 1).

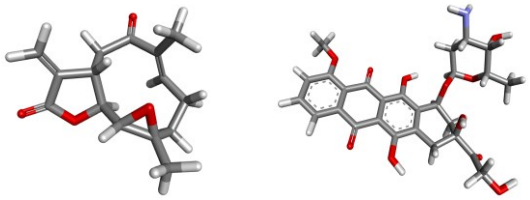

A B

**Figure 1.** 3D structures of parthenolide-9-one (A) and doxorubicin (B).

### *Evaluation of the biological activity of parthenolide-9-one*

The evaluation of the biological activity of parthenolide-9-one against human erythroleukemic cell line (HEL cells) has been carried out in a previous study [10].

### *Molecular docking*

Three-dimensional ligand structures were constructed in .pdb format using Biovia Discovery Studio Visualizer, retaining polar hydrogen atoms, calculating Gasteiger charges, and assigning full torsional flexibility. The three-dimensional structure of caspase-3 (PDB ID: 3PD1) was retrieved from the RCSB Protein Data Bank in .pdb format [11]. Molecular docking of protein and ligands employed AutoDock Tools, with grid dimensions set at x = 70, y = 52, z = 50, and spacing of 0.375 Å. Docking site coordinates were designated as x = 38.861 Å, y = 12.723 Å, z = 68.578 Å within the 3PD1 binding pocket. The Lamarckian genetic algorithm determined low-energy ligand-protein binding conformations.

### *Molecular dynamics simulation*

Molecular dynamics simulations of the optimal docked conformation with caspase-3 (3PD1) were performed over 100 ns using GROMACS version 2024.4 [12]. The protein structure was refined with Swiss-PdbViewer to address missing atoms and residues [13]. Ligand topologies were derived using SwissParam [14]. A triclinic box with the SPC water model solvated the protein-ligand complex, incorporating 0.15 M sodium chloride. Structure optimization involved 50,000 energy minimization steps followed by 200 ps of NVT and 200 ps of NPT equilibration at 300 K and 1.0 bar. Trajectory data were recorded every 10 ns, and analyses of RMSD, RMSF, Rg, hydrogen bonds, and SASA were conducted using Grace software. Conformational stability comparisons were performed using UCSF Chimera 1.19 for superimposition [15].

### *Drug likeness and ADMET prediction*

*In silico* studies, employing computational simulations, provide a standard method for assessing ADMET properties of drug candidates, aiding prediction of their *in vivo* behavior and informing drug discovery [16]. Consequently, the drug-likeness of selected iridoids was evaluated using pkCSM, a web server for predicting pharmacokinetic and toxicity profiles of small molecules [17].

### *Molecular mechanics generalized born surface area (MMGBSA) analysis*

The MM/GBSA method, executed in gmx_MMPBSA with the charmm36-jul2022.ff force field, computed binding free energies for parthenolide-9-one–3PD1 and doxorubicin–3PD1 complexes. The generalized born model estimated electrostatic solvation energy in a continuum solvent, while non-polar solvation energy was derived from solvent-accessible surface area calculations. Analysis of molecular dynamics trajectories involved 125 snapshots extracted at 80 ps intervals over 80 ns (20–100 ns), providing an average binding energy that reflects dynamic protein-ligand interactions and reveals binding affinity and stability under simulated conditions.

## RESULTS AND DISCUSSION

### *Docking analysis*

Before ligand docking with 3PD1, active sites within the binding pocket were identified. Structural analysis of 3PD1 using Biovia Discovery Studio Visualizer revealed inhibition-related active sites (Fig. 2A).

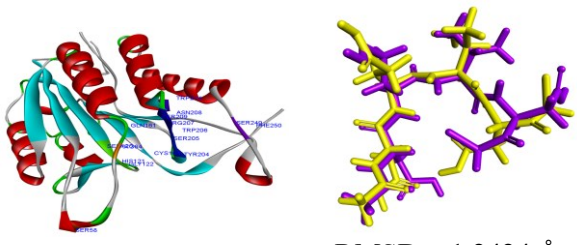


A B

**Figure 2.** Active sites within the 3PD1 protein (A) and superimposition of the docked and native ligands for validation of the molecular docking protocol (violet = native, yellow = docked) (B).

Redocking of the co-crystallized ligand confirmed the protocol's validity (Fig. 2B), with an RMSD of 1.2424 Å, and the ligand overlay verified accuracy. An RMSD below 2 Å validates the docking protocol's reliability [18]. The docked

complexes were evaluated based on their lowest binding energy values (kcal/mol). Table 1 summarizes the ligand interactions within the binding pockets of the 3PD1 protein. Figure 3 illustrates the interactions between the protein and ligands, including hydrogen bonds, van der Waals forces, and hydrophobic interactions.

**Table 1.** Interactions of docked ligands with the 3PD1 protein

| N° | Docked ligands | Binding energy (kcal/mol) | Hydrogen bond interaction | Van der Waals interaction | Hydro-phobic interaction |
|---|---|---|---|---|---|
| 1 | Parthenolide-9-one | -7.81 | Arg64, Gly122, Gln161, Arg207 | Thr62, Ala162, Ser205 | His121, Cys163, Tyr204 |
| 2 | Doxorubicin | -6.31 | Cys163, Arg207, Phe250, Asp253 | Thr62, Ser205, Trp206, Asn208, Ser249, Ser251, Phe252, Phe256 | His121, Arg207 |

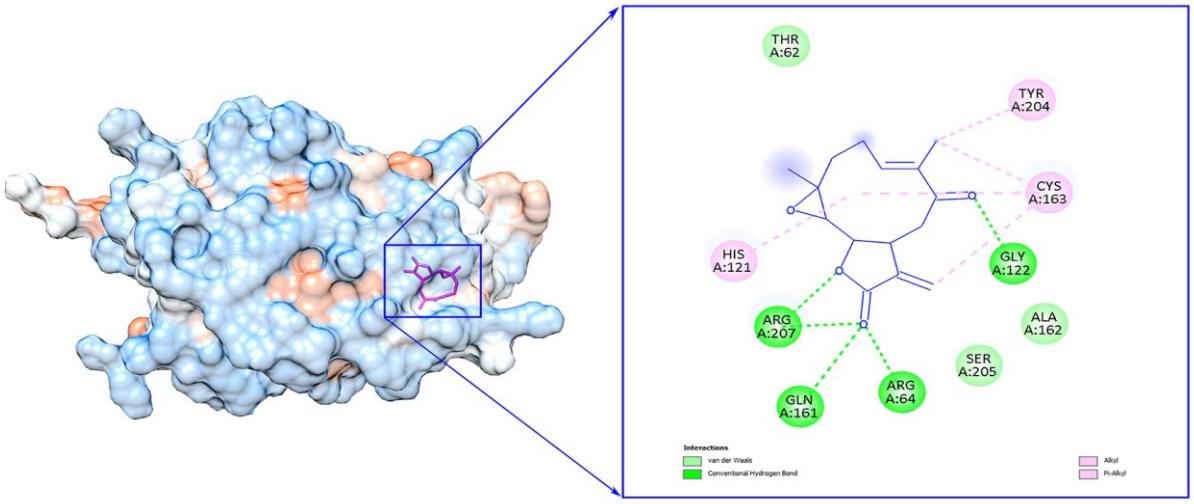


A

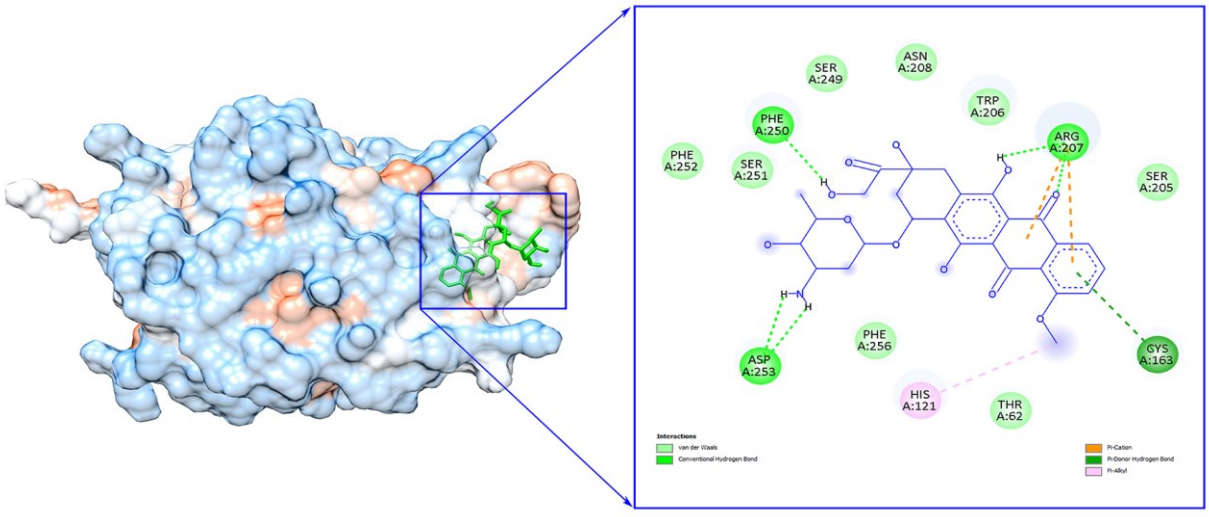


B

**Figure 3.** Molecular docking and two-dimensional interaction schematics for parthenolid-9-one (A) and doxorubicin (B) in complex with the 3PD1 protein.

Parthenolide-9-one exhibited interactions with the protein 3PD1 through four hydrogen bonds with amino acids Arg64, Gly122, Gln161, and Arg207, three van der Waals interactions with amino acids

Thr62, Ala162, and Ser205, and three hydrophobic interactions with amino acids His121, Cys163, and Tyr204. Among these, amino acids Arg64, His121, Gly122, Gln161, Cys163, Tyr204, Ser205, and Arg207 are located within the active sites of the protein 3PD1 (Fig. 3A). The binding energy for parthenolide-9-one with the protein 3PD1 was -7.81 kcal/mol.

Doxorubicin interacted with protein 3PD1 through four hydrogen bonds with amino acids Cys163, Arg207, Phe250, and Asp253, eight van der Waals interactions with Thr62, Ser205, Trp206, Asn208, Ser249, Ser251, Phe252, and Phe256, and two hydrophobic bonds with His121 and Arg207. Among these interactions, three amino acid residues, including His121, Ser205, Trp206, Arg207, Asn208, and Phe250, are placed within the active sites of the protein 3PD1. The binding energy for doxorubicin with the protein 3PD1 was -6.31 kcal/mol (Fig. 3B).

Parthenolide-9-one and doxorubicin were assessed for interactions with protein 3PD1, a target in apoptosis pathways relevant to human erythroleukemic cells. Both compounds formed hydrogen bonds, van der Waals, and hydrophobic interactions, contributing to ligand-protein complex stability [19]. Hydrogen bonds and hydrophobic contacts primarily drive binding specificity, while van der Waals interactions support structural integrity [20]. More negative binding energies correlate with stronger ligand-receptor affinity [21]. Parthenolide-9-one's superior binding energy and active-site interactions suggest enhanced potential for apoptosis induction in human erythroleukemic cells. Molecular dynamics simulations are recommended to further investigate parthenolide-9-one's dynamic behavior within 3PD1's binding pocket, using docked structures to compare with doxorubicin and validate its anti-cancer potential.

### *Molecular dynamics simulation*

Molecular dynamics simulations, executed using GROMACS, were employed to analyze the binding behavior of the ligand-protein complex [22]. In this study, a molecular dynamics simulation analysis was carried out on the complexes parthenolide-9-one+3PD1 and doxorubicin+3PD1 to examine the RMSD, RMSF, Rg, H-bonds, and SASA. As a result, the total energy was calculated as -553,884 kcal/mol for parthenolide-9-one+3PD1 and -687,553 kcal/mol for doxorubicin+3PD1. The potential values were calculated as -554,504 kcal/mol for parthenolide-9-one+3PD1 and -688,276 kcal/mol for doxorubicin+3PD1. The system was equilibrated at a temperature of 300K.

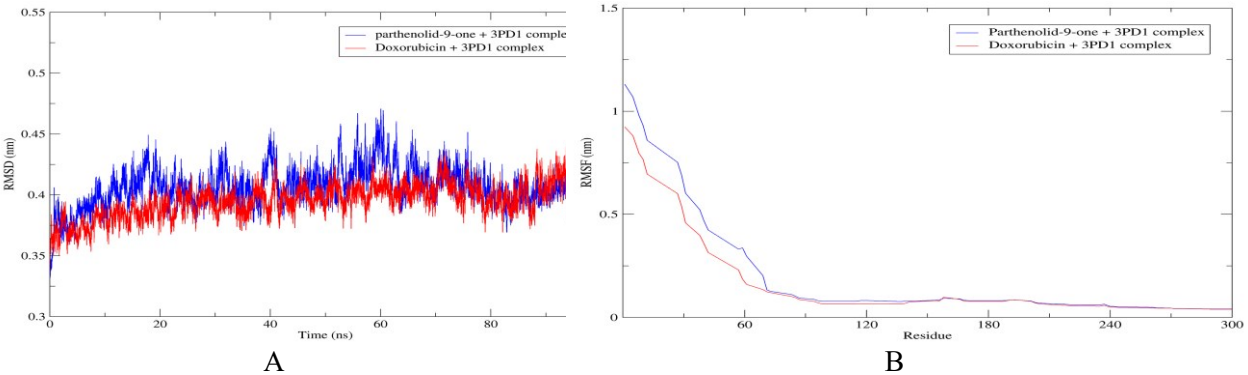


A B

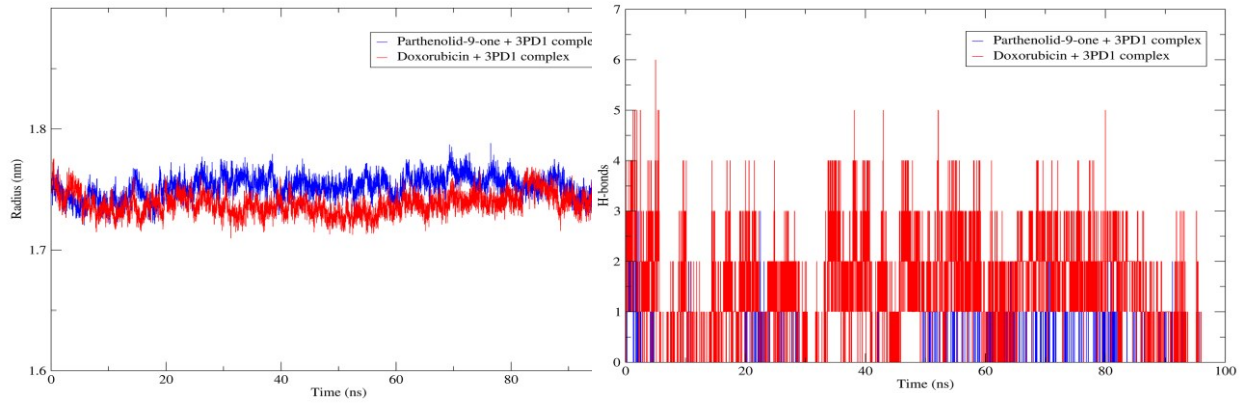


C D

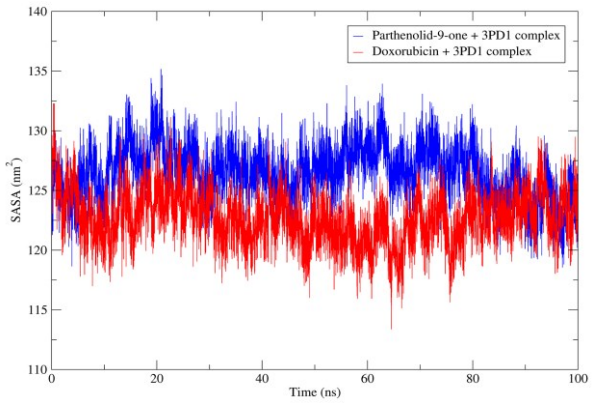


E

**Figure 4.** Results of MD simulation of parthenolide-9-one (blue) and doxorubicin (red) with 3PD1 protein. (A) RMSD, (B) RMSF, (C) Rg, (D) H-bonds, (E) SASA.

The RMSD values for the parthenolide-9-one+3PD1 and doxorubicin+3PD1 complexes ranged between 0.34 and 0.47 nm over a 100 ns simulation, with an average of approximately 0.42 nm throughout the simulation period (Fig. 4A). This result demonstrates that both parthenolide-9-one and doxorubicin sustained stable associations with protein 3PD1, exhibiting minor structural fluctuations indicative of equilibrated systems. The comparable average RMSD values for the parthenolide-9-one+3PD1 complex and the doxorubicin+3PD1 complex imply similar overall stability, consistent with the more negative docking binding energy of parthenolide-9-one (-7.81 kcal/mol) relative to doxorubicin (-6.31 kcal/mol).

Figure 4B illustrates the RMSF values for caspase-3 (3PD1), highlighting regions of structural flexibility that correspond to conformational variations. Conversely, residues in the active sites interacting with the ligands, including Arg64, His121, Gly122, Gln161, Cys163, Tyr204, Ser205, and Arg207 for parthenolide-9-one, and His121, Ser205, Trp206, Arg207, Asn208, and Phe250 for doxorubicin, display low RMSF values, denoting increased rigidity. The regions spanning residues 90–300, encompassing the binding pocket, exhibit diminished RMSF values for both complexes, underscoring pronounced structural stability and consistent ligand associations during the 100 ns simulation [23].

The Rg values for the complexes are presented in Figure 4C. The Rg values for both parthenolide-9-one9+3PD1 and doxorubicin+3PD1 complexes exhibited consistent stability, with an average fluctuation around 1.75 nm throughout the 100 ns simulation, signifying a compact conformation for caspase-3 (3PD1). This constancy suggests that ligand binding to the active sites of 3PD1, particularly involving residues 64–207, has a minimal influence on the protein's overall structure, thereby maintaining its conformational stability throughout the simulation duration [24].

Hydrogen bond counts in the parthenolide-9-one–3PD1 and doxorubicin–3PD1 complexes were measured to examine binding dynamics during simulation. Persistent bonds occurred throughout, with parthenolide-9-one ranging 1–4 and doxorubicin 1–6, denoting stable pocket interactions. Doxorubicin's broader range suggests higher variability, whereas parthenolide-9-one's narrower range indicates greater consistency over 100 ns, bolstering anticancer potential *via* superior docking energy (-7.81 *vs*. -6.31 kcal/mol) (Fig. 4D).

The SASA value was examined to assess solvent exposure levels in the 3PD1 complexes with parthenolide-9-one and doxorubicin. The SASA profiles exhibit oscillatory patterns in both complexes throughout the 100 ns simulation, with the parthenolide-9-one complex showing marginally reduced variability compared to the doxorubicin complex, suggesting ligand-induced alterations in solvent accessibility (Fig. 4E). These variations indicate structural adjustments at the 3PD1-ligand interface, which may affect binding affinity and stability, in agreement with parthenolide-9-one's superior docking binding energy of -7.81 kcal/mol relative to doxorubicin's -6.31 kcal/mol.

Supplementary evaluations using RMSD, RMSF, Rg, SASA, and hydrogen bond occupancy provided insights into the stability and dynamics of parthenolide-9-one–3PD1 and doxorubicin–3PD1 complexes. RMSD and RMSF revealed reduced fluctuations in parthenolide-9-one for overall stability and local flexibility. Rg assessments indicated equivalent protein compactness. SASA confirmed lower solvent exposure variability in parthenolide-9-one. Hydrogen bond analysis demonstrated a narrower, consistent range for

parthenolide-9-one. These parameters substantiate parthenolide-9-one's superior interactions with 3PD1, consistent with its binding energy (-7.81 *vs*. -6.31 kcal/mol). This stability enhances inhibition under physiological conditions and emphasizes anticancer potential in human erythroleukemic cells.

*Drug likeness and ADMET prediction*

ADMET evaluations were executed *via* the pkCSM platform to investigate the oral bioavailability of parthenolide-9-one and doxorubicin [25], with comprehensive findings detailed in Table 2.

Parthenolide-9-one showed human intestinal absorption of 98.971%, exceeding doxorubicin's 62.372%. Both express low absorption providing adequate gastrointestinal bioavailability, with parthenolide-9-one offering a notable advantage. Water solubility favored parthenolide-9-one at -2.674 log mol/L over doxorubicin's -2.915 log mol/L. $CaCO_2$ permeability was higher for parthenolide-9-one (1.278 log Papp in $10^{-6}$ cm/s) than for doxorubicin (0.457 log Papp in $10^{-6}$ cm/s), indicating superior membrane passage. Parthenolide-9-one evades P-glycoprotein substrate/inhibitor functions, thereby enhancing bioavailability by limiting efflux, unlike doxorubicin, which is a substrate without I/II inhibition, potentially hindering absorption and promoting resistance *in vivo*.

Distribution parameters for parthenolide-9-one revealed a restricted volume of distribution (VDss 0.037 log L/kg), contrasting with doxorubicin's wider distribution (1.647 log L/kg). Blood-brain barrier (BBB) thresholds define log BB >0.3 as favorable and <-1 as poor. Parthenolide-9-one's log BB of -0.055 indicates moderate permeability, while doxorubicin's -1.379 signifies limited crossing. Central nervous system (CNS) criteria categorize log PS > -2 as permeable and < -3 as impermeable. Parthenolide-9-one at -2.855 exhibits restricted CNS access, while doxorubicin at -4.307 shows inferior penetration. Fraction unbound (Fu) values of parthenolide-9-one at 0.492 *vs*. doxorubicin's 0.215, denote a greater free fraction for parthenolide-9-one to improve distribution, whereas doxorubicin's lower Fu suggests increased protein binding and bioavailability limitations.

**Table 2.** Predicted ADMET properties of parthenolide-9-one and doxorubicin

| ADMET properties | Unit | Parthenolide-9-one | Doxorubicin |
|---|---|---|---|
| Water solubility | (Log mol/L) | -2.674 | -2.915 |
| $CaCO_2$ permeability | (Log Papp in 10-6 cm/s) | 1.278 | 0.457 |
| Intestinal absorption (Human) | (% Absorbed) | 98.971 | 62.372 |
| Skin permeability | (Log Kp) | -3.353 | -2.735 |
| P-glycoprotein substrate | Yes/No | No | Yes |
| P-glycoprotein I inhibitor | Yes/No | No | No |
| P-glycoprotein II inhibitor | Yes/No | No | No |
| VDss | (Log L/kg) | 0.037 | 1.647 |
| Fraction unbound (human) | (Fu) | 0.492 | 0.215 |
| BBB permeability | (Log BB) | -0.055 | -1.379 |
| CNS permeability | (Log PS) | -2.855 | -4.307 |
| CYP2D6 substrate | Yes/No | No | No |
| CYP3A4 substrate | Yes/No | No | No |
| CYP1A2 inhibitor | Yes/No | No | No |
| CYP2C19 inhibitor | Yes/No | No | No |
| CYP2C9 inhibitor | Yes/No | No | No |
| CYP2D6 inhibitor | Yes/No | No | No |
| CYP3A4 inhibitor | Yes/No | No | No |
| Total clearance | (Log ml/min/kg) | 1.18 | 0.987 |
| Renal OCT2 substrate | Yes/No | No | No |
| AMES toxicity | Yes/No | Yes | No |
| Max. tolerated dose (human) | (Log mg/kg/day) | 0.27 | 0.081 |
| hERG I inhibitor | Yes/No | No | No |
| hERG II inhibitor | Yes/No | No | Yes |
| Oral rat acute toxicity (LD50) | (mol/kg) | 2.144 | 2.408 |
| Oral rat chronic toxicity (LOAEL) | (Log mg/kg_bw/day) | 2.216 | 3.339 |
| Hepatotoxicity | Yes/No | No | Yes |
| Skin sensation | Yes/No | No | No |
| T. Pyriformis toxicity | (Log ug/L) | 0.403 | 0.285 |
| Minnow toxicity | (Log mM) | 2.208 | 4.412 |

**Table 3.** Free energy of binding obtained using MMGBSA (kcal/mol).

| N° | Parthenolide-9-one + 3PD1 | Doxorubicin + 3PD1 | N° | Parthenolide-9-one + 3PD1 | Doxorubicin + 3PD1 |
|---|---|---|---|---|---|
| ΔBOND | 0.00 | 0.00 | Δ1-4 VDW | -0.00 | -0.00 |
| ΔANGLE | 0.00 | -0.00 | Δ1-4 $E_{EL}$ | 0.00 | 0.00 |
| ΔDIHED | 0.00 | -0.00 | $\Delta E_{GB}$ | 8.65 | 27.11 |
| ΔUB | 0.00 | 0.00 | $\Delta E_{SURF}$ | -1.37 | -2.26 |
| ΔIMP | -0.00 | -0.00 | $\Delta G_{GAS}$ | -13.36 | -31.82 |
| ΔCMAP | 0.00 | 0.00 | $\Delta G_{SOLV}$ | 7.27 | 24.86 |
| ΔVDWAALS | -9.71 | -16.40 | **ΔTOTAL** | **-6.08** | **-6.96** |
| $\Delta E_{EL}$ | -3.65 | -15.41 | | | |

Parthenolide-9-one and doxorubicin present metabolic profiles that limit variability and interaction risks. Neither serves as a substrate for CYP2D6 or CYP3A4, nor inhibits CYP1A2, CYP2C19, CYP2C9, CYP2D6, or CYP3A4, reflecting negligible CYP450 engagement and low drug-drug interaction potential [26]. This non-reactive profile for parthenolide-9-one suggests stable metabolism, which bolsters therapeutic consistency. In contrast, doxorubicin's analogous traits align with its established application; however, oversight of alternative metabolic routes remains prudent for optimizing anticancer effects.

Excretion parameters were evaluated to outline clearance profiles of parthenolide-9-one and doxorubicin as potential therapeutics before removal. Predicted total clearance for parthenolide-9-one attained 1.18 log ml/min/kg, exceeding doxorubicin's 0.987 log ml/min/kg, denoting quicker systemic clearance for parthenolide-9-one. This variance, combined with neither as a renal OCT2 substrate, implies longer retention for doxorubicin, possibly permitting infrequent dosing. Higher clearance of parthenolide-9-one may necessitate frequent dosing for therapeutic maintenance, yet its -7.81 kcal/mol binding energy ensures robust target binding despite swift clearance.

Toxicity parameters were assessed to evaluate the safety profiles of parthenolide-9-one and doxorubicin. Parthenolide-9-one showed AMES toxicity, suggesting mutagenicity, unlike doxorubicin. Despite mutagenic concerns, parthenolide-9-one's strong 3PD1 binding (-7.81 kcal/mol) supports anticancer potential for erythroleukemic cells, warranting *in vivo* validation.

From the *in silico* ADMET evaluations of parthenolide-9-one and doxorubicin, the former manifests a viable pharmacokinetic profile despite AMES toxicity, characterized by superior absorption, moderate distribution, inert metabolism, and balanced clearance. Its robust binding to 3PD1 (-7.81 kcal/mol) underscores potential as a lead for anticancer treatment, targeting erythroleukemic cells *via* apoptosis. Parthenolide-9-one could underpin derivatives with refined safety, elevated efficacy, and novel apoptosis-directed mechanisms.

*Free binding energy (MMGBSA) analysis*

Binding free energies of the complexes were computed *via* the MM/GBSA approach in gmx_MMPBSA using the charmm36-jul2022.ff force field. Binding energy (ΔG_binding) equals G_complex - (G_receptor + G_ligand), or ΔH - TΔS, where effective free energy approximates without entropy for relative affinity comparisons. The effective binding energy was averaged from 125 snapshots taken at 80 ps intervals (20–100 ns) to capture the dynamic protein-ligand interactions under simulated conditions. MMGBSA values appear in Table 3. Effective free energies registered: -6.08 kcal/mol for parthenolide-9-one+3PD1 and -6.96 kcal/mol for doxorubicin+3PD1, indicate comparable affinities, with doxorubicin slightly more potent, aligning partially with docking trends favoring parthenolide-9-one.

## CONCLUSIONS

The present study integrated molecular docking, dynamics simulations, and ADMET predictions to investigate parthenolide-9-one, focusing on its interaction with caspase-3 (3PD1). Docking results showed parthenolide-9-one's greater binding affinity and fit at the 3PD1 site *vs.* doxorubicin. 100 ns dynamics simulations verified stable parthenolide-9-

one–3PD1 binding, confirming reliable engagement with this apoptosis regulator. These findings endorse parthenolide-9-one as a caspase-3 modulator for apoptosis in erythroleukemic cells. Computational results necessitate experimental verification. Future work should prioritize laboratory assessments to fully examine parthenolide-9-one's interactions, including cellular impacts on efficacy and safety.

REFERENCES


1. F. Bray, M. Laversanne, H. Sung, J. Ferlay, R. L. Siegel, I. Soerjomataram, A. Jemal, *CA. Cancer J. Clin.*, **74**, 229 (2024).
2. P. Fernandes, N. Waldron, T. Chatzilygeroudi, N. S. Naji, T. Karantanos, *Int. J. Mol. Sci.*, **25**, 6256 (2024).
3. K. Gera, D. Martir, W. Xue, J. R. Wingard, *J. Clin. Oncol.*, **41**, e19031 (2023).
4. S. Elmore, *Toxicol. Pathol.*, **35**, 495 (2007).
5. S. K. Niazi, Z. Mariam, *Endocr. Diabetes Metab.*, **7**, e462 (2024).
6. S. Ghosh, S. Basu, T. Kayal, G. Ashok, S. Ramaiah, A. Anbarasu, *Discov. Appl. Sci.*, **7**, 491 (2025).
7. G. M. Cragg, D. J. Newman, *J. Ethnopharmacol.*, **100**, 72 (2005).
8. E. Abdel-Sattar, A. T. McPhail, *J. Nat. Prod.*, **63**, 1587 (2000).
9. [9] E. Abdel Sattar, A. M. Galal, G. S. Mossa, *J. Nat. Prod.*, **59**, 403 (1996).
10. S. Xu, Y. Tang, Y. Li, J. Yang, W. Gu, X. Hao, C. Yuan, *Bioorg. Chem.*, **139**, 106707 (2023).
11. J. Walters, P. Swartz, C. Mattos, A. C. Clark, *Arch. Biochem. Biophys.*, **508**, 31 (2011).
12. D. Van Der Spoel, E. Lindahl, B. Hess, G. Groenhof, A. E. Mark, H. J. C. Berendsen, *J. Comput. Chem.*, **26**, 1701 (2005).
13. N. Guex, M. C. Peitsch, *Electrophoresis*, **18**, 2714 (1997).
14. V. Zoete, M. A. Cuendet, A. Grosdidier, O. Michielin, *J. Comput. Chem.*, **32**, 2359 (2011).
15. E. F. Pettersen, T. D. Goddard, C. C. Huang, G. S. Couch, D. M. Greenblatt, E. C. Meng, T. E. Ferrin, *J. Comput. Chem.*, **25**, 1605 (2004).
16. L. Tao, P. Zhang, C. Qin, S. Y. Chen, C. Zhang, Z. Chen, F. Zhu, S. Y. Yang, Y. Q. Wei, Y. Z. Chen, *Adv. Drug Deliv. Rev.*, **86**, 83 (2015).
17. D. E. V Pires, T. L. Blundell, D. B. Ascher, *J. Med. Chem.*, **58**, 4066 (2015).
18. [M. J. Alves, H. J. C. Froufe, A. F. T. Costa, A. F. Santos, L. G. Oliveira, S. R. M. Osório, R. M. V Abreu, M. Pintado, I. C. F. R. Ferreira, *Molecules*, **19**, 1672 (2014).
19. R. Patil, S. Das, A. Stanley, L. Yadav, A. Sudhakar, A. K. Varma, *PLoS One*, **5**, e12029 (2010).
20. G. G. Ferenczy, M. Kellermayer, *Comput. Struct. Biotechnol. J.*, **20**, 1946 (2022).
21. S. Henrich, I. Feierberg, T. Wang, N. Blomberg, R. C. Wade, *Proteins Struct. Funct. Bioinforma.*, **78**, 135 (2010).
22. J. Martin, E. Frezza, *Front. Mol. Biosci.*, **9**, 970109 (2022).
23. C. Soremekun, D. Jjingo, D. Kateete, O. Nash, H. Grallert, A. Peters, T. Chikowore, C. Batini, O. Soremekun, S. Fatumo, *Next Res.*, **1**, 100041 (2024).
24. Z. K. Bagewadi, T. M. Yunus Khan, B. Gangadharappa, A. Kamalapurkar, S. Mohamed Shamsudeen, D. A. Yaraguppi, *Saudi J. Biol. Sci.*, **30**, 103753 (2023).
25. M. Zia, S. Parveen, N. Shafiq, M. Rashid, A. Farooq, M. Dauelbait, M. Shahab, A. M. Salamatullah, S. Brogi, M. Bourhia, *ACS Omega*, **9**, 2161 (2024).
26. F. P. Guengerich, Pharmacology and Toxicology of Cytochrome P450 – 60th Anniversary (Advances in Pharmacology, vol. 95), Academic Press, Boston, 2022.

*Bulgarian Chemical Communications, Volume 58, Issue 1 (pp. 52-58) 2026* *DOI: 10.34049/bcc.58.1.5719*

# Potential buffers based on borax, orthophosphoric and metaphosphoric acid

M. Georgieva[1*], S. Kozhukharov[2, 3], Ch. Girginov[4], A. Dishliev[5], P. Petkov[3]

[1]*Institute of Mineralogy and Crystallography, Bulgarian Academy of Sciences, Acad. Georgi Bonchev Str., Bl. 107, 1113 Sofia, Bulgaria*

[2]*LAMAR – Laboratory for Advanced Materials Research, University of Chemical Technology and Metallurgy, 8 Kliment Ohridski Blvd., 1797 Sofia, Bulgaria*

[3]*Department of Physics, University of Chemical Technology and Metallurgy, 8 Kliment Ohridski Blvd., 1797 Sofia, Bulgaria*

[4]*Department of Physical Chemistry, University of Chemical Technology and Metallurgy, 8 Kliment Ohridski Blvd., 1797 Sofia, Bulgaria*

[5]*Department of Mathematics, University of Chemical Technology and Metallurgy, 8 Kliment Ohridski Blvd., 1756 Sofia, Bulgaria*

Received: September 02, 2025; Revised: October 30, 2025

The solution composition and pH are factors of key importance for the efficiency of any chemical and electrochemical surface treatment procedure. In this sense, the present brief study is an attempt to obtain stable and reliable buffer solutions through mixing of two compounds, acting as alkaline and acidic buffer components, respectively. The alkaline component was a 0.050 M solution of sodium tetraborate decahydrate ($Na_2B_4O_7.10H_2O$). Two potential buffer solutions were prepared by the addition of either 0.050 M orthophosphoric acid or a similar quantity of metaphosphoric acid as the acidic compound. The study was performed in two stages: (i) evaluation of the resulting pH after different volume ratios between the respective alkaline and acidic components, and (ii) determination of their buffering capacity by precise instrumental titrations, assisted by a digital high-precision pH meter. The results show that both solutions behave as relatively reliable buffers.

**Keywords:** pH buffers, borate and phosphate compositions, pH ranges, buffering capacity

## INTRODUCTION

Although phosphating is a well-known procedure [1, 2], the optimization of this process continues to be the object of intensive research activities [3, 4]. In this respect, special attention has been paid to the formation of phosphate conversion coatings containing Ca [5], Mg [6], Zn [7–10], Ba [11], Ni [12], Mn [13–15], V [16], and Ce [17]. In addition, various nanoparticle additions have been proposed, such as $ZrO_2$ [18], $K_2O/TiO_2$ [19], $ZnO/TiO_2$, [20], $WO_3/BiVO_4$, [21], $Al_2O_3/Mo$ [22], $MoS_2$ [23], Nd modified $ZnAl_2O_4$ [24], Bi-doped $FeVO_4$ [25], etc. Furthermore, this approach has been proposed for the improvement of zinc coatings on steels [26] and for enhancing the adhesion of organic coatings [27].

For this reason, some authors have paid special attention to pH as a technological parameter for the successful deposition of reliable Zn–P conversion coatings on steel [28] and magnesium alloys [29, 30]. In some of these studies, the authors propose strongly acidic conditions. However, such conditions are not suitable for magnesium and aluminum alloy treatments due to the high solubility of these metals in strongly acidic or alkaline media. Therefore, nearly neutral borate and phosphate buffer solutions were proposed for the sealing of cerium conversion coatings deposited on preliminarily anodized aluminum alloys [31]. The compositions of these buffers and their pH ranges are described elsewhere [32].

Other authors have proposed the deposition of Mo-Mn-V conversion coatings under weakly acidic conditions [33], or the use of borate buffer solutions for the passivation of aluminum alloys [34]. Moreover, the use of boron-containing compounds has been shown to have a beneficial effect on the electrochemical film formation of aluminum alloys [35].

The necessity of developing buffers that contain both boron and phosphorus becomes even more evident, given the recent trend toward the development of Ni–B layers [36, 37], doped and reinforced Ni–B composites [38, 39], and Ni–Co–P layers [40–43], as well as the important role of B-compounds in the respective electrolytes. Indeed, according to some authors [44, 45], boron incorporation in Ni-based layers decreases the grain size and changes the morphology from faceted to dome-like. Additionally, borate buffers have recently

* To whom all correspondence should be sent:
E-mail: *mgeorgieva@imc.bas.bg*

been studied for water oxidation in hydrogen production [46, 47] and for water purification [48].

Consequently, more detailed research regarding the pH ranges and potential buffering properties of mixtures of relatively easily accessible boron- and phosphorus-containing compounds is necessary.

In this context, the present brief study is devoted to the investigation of the pH ranges and buffering effects of mixtures of borax (as the alkaline component) with orthophosphoric or metaphosphoric acid (as the acidic components). It is part of a wider systematic study aiming to provide valuable data on the pH ranges of various boron- and phosphorus-containing compounds.

## EXPERIMENTAL

### *pH Range determination*

A set of phosphate/borate mixtures was obtained by mixing the initial solutions in defined volume ratios. The compositions of the initial solutions are summarized in Table 1. The alkaline component (CAS 1303-96-4) was a product of Merck (Germany). The orthophosphoric acid (CAS 7664-38-2) was also a product of Merck (Germany), whereas the metaphosphoric acid (Art. No. 01-320) was a product of Ferak GmbH (Germany). According to the manufacturer, the latter product is a mixture of $HPO_3$ (40–44%) and $NaPO_3$ (50–60%), with remnants of $H_3PO_3$ and traces of various impurities.

The pH determinations were performed using a precise HI 255 combined meter, manufactured by Hanna Instruments, equipped with an HI 1131 commercial universal glass electrode. The device was calibrated prior to each measurement set. Data acquisition was performed through five measurements under identical conditions. Each individual measurement involved a 5-min immersion of the electrode in the stirred solution at room temperature. The solutions were pre-stirred for another 5 min immediately prior to each measurement.

The mean pH values were obtained from the raw data from each of the five measurements for every volume ratio. The calculations were performed according to the following expression:

$$pH = pH_{av} \pm \Delta pH \,, \tag{1}$$

where: $pH_{av}$ is the average pH value obtained from five measurements, and ΔpH is the standard deviation.

The average pH values were calculated by Equation (2):

$$pH_{av} = \sum_{i=1}^{i=n} \frac{pH_i}{n} \,, \tag{2}$$

where: $pH_{av}$ – average pH value; $pH_i$ – each pH value obtained from the respective measurement, from i = 1 to i = n; n – total number of the pH measurements (in the present case, n = 5).

The standard deviation was calculated by Equation (3):

$$\Delta pH_{av} = \pm \sqrt{\sum_{i=1}^{i=n} \frac{\left(pH_i - pH_{av}\right)^2}{n(n-1)}} \tag{3}$$

All designations are similar to those in Equation (2). For clarity, the data in Tables 2 and 3 are illustrated in Figure 2. The figure was constructed after determining the ratios of the used solution volumes, following Equation (4):

$$VR_1 = \frac{V_1}{V_1 + V_2} \text{ or } VR_2 = \frac{V_2}{V_1 + V_2} \,, \tag{4}$$

where: VR – volume ratio of the used primary solutions; $V_1$ – volume of the alkaline solution, forming the buffer mixture (mL); $V_2$ – volume of the acidic solution, forming the buffer mixture (mL).

**Table 1.** Exact buffer solution component compositions.

| Buffer | Component type | Calculated concentration | Actual content |
|---|---|---|---|
| BPB-1 | Alkaline component | $Na_2B_4O_7.10H_2O$ - 0.05 M (borax) | 19.2663 g of 99.5 % pure compound to 1 $dm^3$ aqueous solution |
| | Acidic component | o-$H_3PO_4$ - 0.05 M (orthophosphoric acid) | 3.40 ml of 85 % acid to 1 $dm^3$ aqueous solution |
| BPB-2 | Alkaline component | $Na_2B_4O_7.10H_2O$ - 0.05 M (borax) | 19.2663 g of 99.5 % pure compound to 1 $dm^3$ aqueous solution |
| | Acidic component | $HPO_3$ / $NaPO_3$ mixture* (metaphosphoric acid) | 5.4560 g of industrial product to 1 $dm^3$ aqueous solution |

*The weight of metaphosphoric acid was selected to be equal to the weight of 3.40 mL orthophosphoric acid considering its density equal to 1.88 g/ml according to the product label.

Figure 2 represents the correlations between VR, calculated from the volumes in Table 2 and the pH values of the resulting buffer solutions. Considering the importance of the raw data for this study, the acquired values from the direct measurements were combined with the calculated average pH values and their standard deviations.

*Buffering capacity determination*

The buffering capacity determination was performed after defining the volume ratios between the alkaline and the acidic borate or phosphate solutions, which correspond to buffer mixtures with pH ≈ 7. The experimental activities were carried out through five-fold titrations with standardized alkaline NaOH or HCl solutions. The titrant standardizations were performed using a primary 0.05 M $(COOH)_2$ standard solution. It was obtained by dissolving 6.3334 ± 0.0001 g of $(COOH)_2.2H_2O$ (99.5%), provided by Chim-spectar Ltd. (Bulgaria), in 1 $dm^3$ of distilled water in a volumetric flask. The need for standardization using a primary standard solution is predetermined by the susceptibility of the NaOH precursor to carbonation and hydration upon contact with ambient air, and by the volatility of HCl.

The buffering capacity was calculated using Equation (5), after five-fold titrations with the respective alkaline and acidic standard solutions:

$$BC = \frac{MV_{ss}}{\Delta(pH)V_{buff}}.\frac{1}{n}, \quad (5)$$

where: BC is the buffering capacity (mol $pH^{-1}$); $MV_{ss}$ is the quantity of the added standard solution of a known alkaline or acidic compound (mol). In the present case, the data for the standard solution molarity are shown in Table 1, whereas, their volumes, expended for the titrations are summarized in Table 4. Δ(pH) is the pH change (dimensionless). In this case, its value is assumed to be unity. $V_{buff}$ is the volume of the buffer solution subjected to titration (15 mL in the present case). The coefficient (1/n) is attributed to the compound, whose solution is subjected to pH measurement. If it is alkaline, then n is the number of $OH^-$ anions per molecule of the compound. If it is acidic, then n is the number of $H_3O^+$ (i.e., $H^+$ cations) moieties per molecule of the dissolved compound. In both cases, for NaOH and HCl, its value is: 1/n = 1.

The titrations were performed instrumentally using the already described pH meter, until the pH value of the potential buffer solution shifted by one unit. For this purpose, 15 mL of the respective neutral potential buffer solutions were titrated with the alkaline and acidic standard solutions described above.

## RESULTS AND DISCUSSION

*Results from pH range determination*

The pH range determination was performed consecutively for the $Na_2B_4O_7$ / o-$H_3PO_4$ system (denoted as BPB-1) and subsequently for the $Na_2B_4O_7$ / $(HPO_3)_n$ system (denoted as BPB-2). The results for the former case are shown in Table 2 and Fig. 1, respectively.

The data in Table 2 show that the pH interval of BPB-1 buffer is rather large, ranging from about pH ≈ 9.6 down to nearly pH ≈ 1.7. When the mixture is composed by equal volumes of both alkaline and acidic component solutions, the resulting mixture exhibits a slightly alkaline reaction. Neutral BPB-1 type solutions can be obtained when the amount of orthophosphoric acid predominates. At higher acid contents, the pH drops sharply. Probably, $(B_4O_7)^{2-}$ ions decompose in acidic media, but detailed analysis of such processes is beyond the scope of the present research.

The images in Fig. 1 show that the pH dependence on the borax / orthophosphoric acid content ratios can be divided into three regions. In the most alkaline range, down to pH ≈ 8.5, the line has a rather weak slope. In the middle range, including the neutral pH, this dependence reaches unity (i.e., 45°). Below pH ≈ 6, the curve slope becomes much steeper, along with a slight decrease in the curve overlap rate. At the lowest pH values, the curves become almost horizontal again.

**Table 2.** Volumes of added component solutions and resulting pH values of the BPB-1 buffer

| Component solution volumes (ml) | | Volume ratios | | Consecutive measurement number | | | | | Calculated pH mean values |
|---|---|---|---|---|---|---|---|---|---|
| $Na_2B_4O_7$ | o-$H_3PO_4$ | $VR_1$ | $VR_2$ | $pH_1$ | $pH_2$ | $pH_3$ | $pH_4$ | $pH_5$ | |
| 40 | 0 | 1.000 | 0.000 | 9.592 | 9.585 | 9.587 | 9.584 | 9.589 | 9.587 ± 0.033 |
| 20 | 10 | 0.667 | 0.333 | 9.126 | 9.110 | 9.128 | 9.114 | 9.117 | 9.119 ± 0.085 |
| 20 | 20 | 0.500 | 0.500 | 8.328 | 8.322 | 8.326 | 8.324 | 8.321 | 8.324 ± 0.034 |
| 15 | 25 | 0.375 | 0.625 | 6.876 | 6.863 | 6.861 | 6.859 | 6.865 | 6.865 ± 0.097 |
| 10 | 20 | 0.333 | 0.667 | 6.472 | 6.473 | 6.468 | 6.459 | 6.456 | 6.466 ± 0.119 |
| 10 | 30 | 0.250 | 0.750 | 5.847 | 5.836 | 5.831 | 5.832 | 5.832 | 5.836 ± 0.114 |
| 5 | 35 | 0.125 | 0.875 | 2.107 | 2.099 | 2.089 | 2.081 | 2.072 | 2.090 ± 0.666 |
| 0 | 40 | 0.000 | 1.000 | 1.747 | 1.760 | 1.754 | 1.750 | 1.749 | 1.752 ± 0.263 |

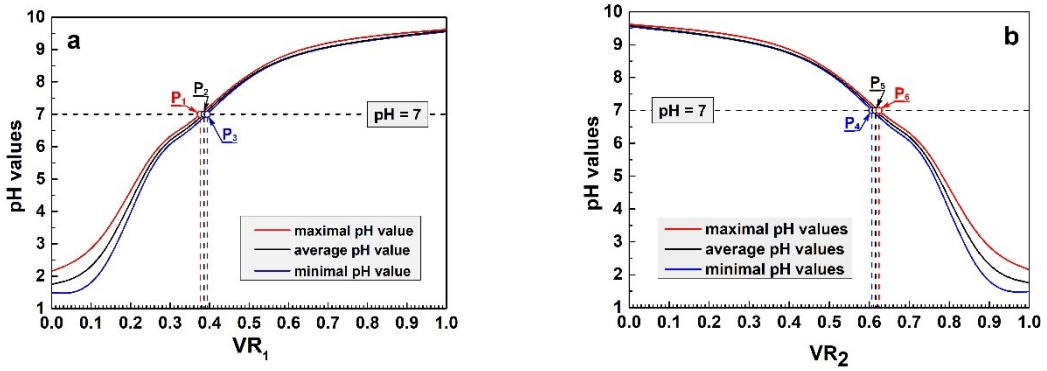


**Fig. 1.** Correlation between the pH value ranges for $Na_2B_4O_7$ / o-$H_3PO_4$ potential buffer volume ratios and the primary component solutions: (a) for $VR_1$ and (b) for $VR_2$.

**Table 3.** Added volumes of the component solutions and resulting pH values of BPB-2 buffer.

| Solution component volumes (ml) | | Volume ratios | | Consecutive measurement number | | | | | Calculated pH mean values |
|---|---|---|---|---|---|---|---|---|---|
| $Na_2B_4O_7$ | $(HPO_3)_n$ | $VR_1$ | $VR_2$ | $pH_1$ | $pH_2$ | $pH_3$ | $pH_4$ | $pH_5$ | |
| 40 | 0 | 1.000 | 0.000 | 9.592 | 9.585 | 9.587 | 9.584 | 9.589 | 9.587 ± 0.033 |
| 20 | 10 | 0.667 | 0.333 | 9.308 | 9.292 | 9.290 | 9.298 | 9.293 | 9.296 ± 0.078 |
| 20 | 20 | 0.500 | 0.500 | 8.859 | 8.858 | 8.853 | 8.857 | 8.858 | 8.857 ± 0.026 |
| 15 | 25 | 0.375 | 0.625 | 8.108 | 8.107 | 8.115 | 8.112 | 8.114 | 8.111 ± 0.044 |
| 10 | 20 | 0.333 | 0.667 | 7.421 | 7.425 | 7.422 | 7.422 | 7.424 | 7.423 ± 0.022 |
| 10 | 30 | 0.250 | 0.750 | 5.758 | 5.759 | 5.764 | 5.766 | 5.768 | 5.763 ± 0.076 |
| 5 | 35 | 0.125 | 0.875 | 2.377 | 2.364 | 2.354 | 2.349 | 2.345 | 2.358 ± 0.546 |
| 0 | 40 | 0.000 | 1.000 | 1.906 | 1.910 | 1.909 | 1.904 | 1.889 | 1.904 ± 0.447 |

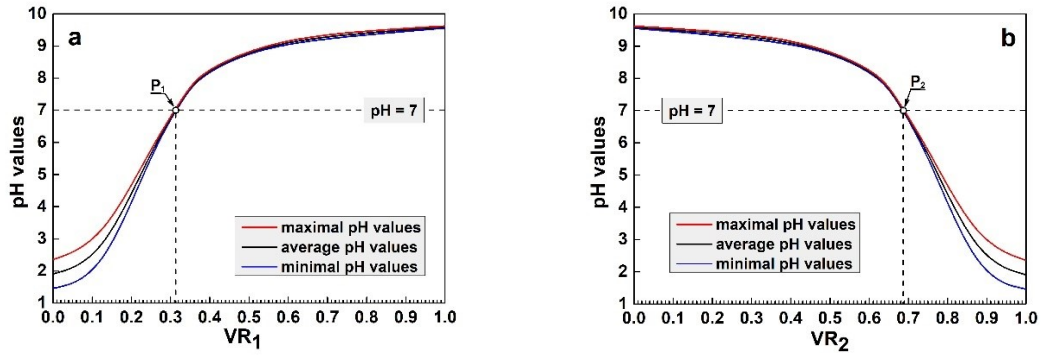


**Fig. 2.** Correlation between the pH value ranges for BPB-2 potential buffer volume ratios and the primary component solutions: (a) for $VR_1$ and (b) for $VR_2$.

**Table 4.** Results of the secondary standard solution titrations.

| Buffer code | Standard for titration | Consecutive measurement number | | | | | Calculated mean values ($cm^3$) |
|---|---|---|---|---|---|---|---|
| | | Volume 1 ($cm^3$) | Volume 2 ($cm^3$) | Volume 3 ($cm^3$) | Volume 4 ($cm^3$) | Volume 5 ($cm^3$) | |
| BPB-1 | NaOH, | 3.85 | 3.90 | 3.90 | 3.90 | 3.90 | 3.89 ± 0.57 |
| | HCl | 3.55 | 3.55 | 3.50 | 3.50 | 3.50 | 3.52 ± 0.78 |
| BPB-2 | NaOH, | 3.15 | 3.10 | 3.15 | 3.10 | 3.20 | 3.12 ± 1.83 |
| | HCl | 3.55 | 3.60 | 3.50 | 3.55 | 3.55 | 3.55 ± 1.00 |

The curves show that neutral mixtures can be obtained within rather narrow $VR_1$ and $VR_2$ intervals. In the former case, the neutral pH range is enclosed between $P_1$ and $P_3$ (Fig. 1a), corresponding to $VR_1$ between 0.37 and 0.40. The highest probability of obtaining a neutral pH is indicated by $P_2$. It corresponds to a mixture prepared by combining 38.5 mL of 0.05 M $Na_2B_4O_7$ solution and adding 0.05 M o-$H_3PO_4$ solution up to 100 mL. In turn, analysis of Fig. 1b shows that a neutral pH can be obtained by mixing 62 mL of 0.05 M o-$H_3PO_4$ solution and adding 0.05 M borax solution up to 100 mL, corresponding to $P_5$. However, preparation of such a neutral mixture requires high precision due to the narrowness of the range enclosed between $P_4$ and $P_6$.

Identical analyses were carried out for the borax / metaphosphoric acid, and the respective data are summarized in Table 3 and illustrated in Fig. 2.

The data in Table 3 are quite similar to those of the previous system described above. In brief, the pH range is rather wide, and neutral pH is achievable when the acidic component predominates. The respective curves in Fig. 2 are simpler in shape compared to those of the previous system. Here, no intermediate range is observable; instead, the low slope at pH above 8 directly transitions to a sharp decline down to the most acidic values. Final curve bends, combined with curve splitting similar to those in the previous figure, are also observable.

Here, juxtapositions of the maximal, average, and minimal pH value curves are observable at the pH = 7 line. According to $VR_1$ ($P_1$, Fig. 2a), 31 mL of 0.05 M borax solution should be mixed with 69 mL of 0.05 M metaphosphoric acid solution, and *vice versa,* according to $VR_2$ ($P_2$, Fig. 2b).

### *Results from the buffering capacity determination*

Prior to the definition of the buffering capacity (BC), the exact concentrations of the secondary standard solutions were determined by titration with the $(COOH)_2$ primary standard solution. The titrations were performed instrumentally using the pH meter described in the experimental part. The respective titrations with 15 mL of the primary standard solution required 30.66 ± 0.32 mL of the NaOH solution. The respective calculations resulted in an average NaOH concentration value of $49.156\times10^{-3}$ M. Knowing this value, it was possible to define the HCl concentration. It was determined by five titrations of the HCl solution with the NaOH secondary standard. The average volume of the HCl solution expended for these titrations was 14.69 ± 0.28 mL. Hence, the calculations showed that the HCl secondary standard solution had average concentration values of $50.193\times10^{-3}$ M.

Both secondary solutions were used to determine the buffering capacity of BPB-1 and BPB-2 mixtures, described in Table 1. Again, instrumental titrations were applied to 15 mL neutral pH solutions of BPB-1 and BPB-2. The obtained values are shown in Table 4.

Similar titrations were performed with the commercial *Reagecon* (UK) buffer for neutral media. The respective expended solution volumes were 7.40 mL for the NaOH solution and 11.10 mL for the HCl standard. Thus, comparison with the results in Table 4 shows that, when titrated with the alkaline (NaOH) standard solution, both investigated mixtures exhibit buffering properties approximately twice weaker than those of the commercial buffer. In turn, titrations with the acidic (HCl) standard revealed that both investigated mixtures have about three times weaker buffering properties.

The data in Table 4 were used for BC definition using Equation (5). The calculations revealed the buffering capacities of the investigated mixtures. Accordingly, using the NaOH standard solution, the buffering capacities of investigated mixtures were: $BC_{BPB\text{-}1}^{NaOH} = 12.75\times10^{-3}$ mol $pH^{-1}$ and $BC_{BPB\text{-}2}^{NaOH} = 10.22\times10^{-3}$ mol $pH^{-1}$, respectively. In turn, the buffering capacities of these mixtures determined with the HCl standard solution were: $BC_{BPB\text{-}1}^{HCl} = 11.78\times10^{-3}$ mol $pH^{-1}$ and $BC_{BPB\text{-}2}^{HCl} = 11.88\times10^{-3}$ mol $pH^{-1}$. These results revealed that the neutral mixtures of borax with either orthophosphoric or metaphosphoric acid possess almost identical buffering capacity values.

The relatively weak buffering effect of the proposed $Na_2B_4O_7$ - o-$H_3PO_4$ and $Na_2B_4O_7$ - $(HPO_3)_n$ systems could be explained by considering the difference between the standard reduction potentials [49-51] of the respective anions, as shown in Equations (6 – 9):

$$(B(OH)_4)^- + 3e^- \rightarrow B_{(s)} + 4OH^- \quad E^o = -1.811\ V_{SHE} \tag{6}$$

$$B(OH)_3 + 3H^+ + 3e^- \rightarrow B_{(s)} + 3H_2O \quad E^o = -0.890\ V_{SHE} \tag{7}$$

$$H_3PO_3 + 2H^+ + 2e^- \rightarrow H_3PO_2 + H_2O \quad E^o = -0.50\ V_{SHE} \tag{8}$$

$$H_3PO_4 + 2H+ + 2e- \rightarrow H_3PO_3 + H_2O \quad E^o = -0.28\ V_{SHE} \tag{9}$$

The differences among these standard reduction potential values predetermine that redox couples appear between the boron- and the phosphorus-containing anions. This fact probably results in decomposition of the tetraborate anions and formation of other water-soluble compounds.

However, their analysis is not among the main objects of the present research.

In turn, the similarity between the weak buffering capacities of both systems can be explained by the fact that, in aqueous media, the metaphosphoric acid ($HPO_3$) converts to orthophosphoric acid ($H_3PO_4$), following reaction (Eq. 10):

$$HPO_3 + H_2O \rightarrow H_3PO_4 \quad (10)$$

Finally, analysis of all facts described above leads to the inference that both systems possess rather similar properties and could substitute each other in real technological processes.

## CONCLUSIONS

The present brief study is part of a wider systematic research effort aiming to provide valuable data for the pH ranges of various boron- and phosphorus-containing compounds. It is devoted to defining the pH ranges and the buffering effects of mixtures between borax (as the alkaline component) and orthophosphoric or metaphosphoric acid (as the acidic components).

In both cases, the pH range is rather wide, and a neutral pH is achievable when the acidic component predominates.

For the former investigated mixture, neutral pH could be achieved at a rather narrow initial component solution ratio. Most probably, a mixture prepared by 38.5 mL of 0.05 M $Na_2B_4O_7$ solution and addition of 0.05 M o-$H_3PO_4$ solution up to 100 mL should possess neutral pH. In turn, neutral pH can be also obtained by 62 mL of 0.05 M o-$H_3PO_4$ solution and further addition of 0.05 M borax solution up to 100 mL.

For the latter investigated system, 31 mL of 0.05 M borax solution should be mixed with 69 mL of 0.05 M metaphosphoric acid solution, and *vice versa*, in order to reach neutral pH value.

Finally, the buffering capacities of both systems were calculated after multiple titrations with secondary standard solutions of NaOH or HCl. Comparison with the results from titrations using a commercial buffer showed that the proposed here potential buffers possess relatively weak buffering properties.

Further analysis of the result indicated that both systems possess almost identical buffering capacities.

Finally, both systems, proposed in the present study, can be used as additives to electrolytes for the electrochemical deposition of active layers for corrosion protection, alternative energy sources and environmental protection purposes. However, their unsatisfactory buffering properties necessitate pH monitoring of electrolytes containing BPB-1 and BPB-2.

In this sense, the present study provides data regarding the pH ranges and the respective contents of the components (i.e., borax, ortho- or metaphosphoric acids) composing these mixtures.

***Acknowledgement:*** *The authors would like to thank the Bulgarian National Scientific Fund for its financial support under Contract No. KП-06-H89/8. This work also utilized equipment from the distributed research infrastructure INFRAMAT, included in the Bulgarian National Roadmap for Research Infrastructure and supported by the Bulgarian Ministry of Education and Science.*

## REFERENCES

1. A. Zavarella, US Patent US2476345A, (1946).
2. J. Bogi, R. Macmillan, *J. Mater. Sci.,* **12**, 2235 (1977).
3. V. S. Konovalova, V. E. Rumyantseva, *Eng. Proc.,* **56**(1), 54 (2023) https://doi.org/10.3390/ASEC2023-15378
4. P. Lazar, N. Cimpoesu, B. Istrate, A. M. Cazac, D.-P. Burduhos-Nergis, M. Benchea, A.-C. Berbecaru, G. Badarau, G. D. Vasilescu, M. Popa, C. Bejinariu, *Coatings,* **14**(2), 182 (2024) https://doi.org/10.3390/coatings14020182
5. I. Mendolia, C. Zanca, F. Ganci, G. Conoscenti, F. Carfì Pavia, V. Brucato, V. La Carrubba, F. Lopresti, S. Piazza, C. Sunseri, R. Inguanta, *Surf. Coat. Technol.,* **408,** 126771 (2021). https://doi.org/10.1016/j.surfcoat.2020.126771
6. M. Fouladi, A. Amadeh, *Electrochim. Acta,* **106,** 1–12 (2013) https://doi.org/10.1016/j.electacta.2013.05.041
7. B. Díaz, L. Freire, M. Mojío, X. R. Nóvoa, *J. Electroanal. Chem.,* **737,** 174 (2015). https://doi.org/10.1016/j.jelechem.2014.06.035.
8. J. Duchoslav, A. Himmelbauer, P. Kürnsteiner, H. Groiss, M. Kehrer, T. Stehrer, D. Stifter, *Appl. Surf. Sci.,* **665,** 160308, (2024). https://doi.org/10.1016/j.apsusc.2024.160308
9. S. Silva-Fernández, B. Díaz, I. Feijoo, X. R. Nóvoa, C. Pérez, *J. Electroanal. Chem.,* **975,** 118759 (2024). https://doi.org/10.1016/j.jelechem.2024.118759
10. F. Lissandrello, N. Lecis, L. Magagnin, *Electrochim. Acta*, **478,** 143840 (2024) https://doi.org/10.1016/j.electacta.2024.143840
11. Ch. Li, X. Di, Sh. Ren, J. Wang, Zh. Wang, T. Li, *Mater. Lett.,* **379,** 137685 (2025) https://doi.org/10.1016/j.matlet.2024.137685
12. A. Heydarian, A. Najafi, G. Khalaj, *J. Mater. Res. Technol.,* **30,** 7308 (2024) https://doi.org/10.1016/j.jmrt.2024.05.103
13. S. Silva-Fernández, B. Díaz, R. Figueroa, X. R. Nóvoa, C. Pérez, *Surf. Coat. Technol.,* **476,** 130260 (2023) https://doi.org/10.1016/j.surfcoat.2023.130260.

14. L. Guo, Q. Huang, C. Zhang, J. Wang, G. Shen, C. Ban, L. Guo, *Corros. Sci.,* **178,** 108960 (2021). https://doi.org/10.1016/j.corsci.2020.108960.
15. Y. Zhang, X. Chen, H. Tan, *Internat. J. Electrochem. Sci.,* **18**(9), 100274 (2023). https://doi.org/10.1016/j.ijoes.2023.100274
16. M. Abbasi, M. M. Attar, *J. Coat. Technol. Res.,* **14,** 1435–1445 (2017). https://doi.org/10.1007/s11998-017-9960-3.
17. F. Bahremand, T. Shahrabi, B. Ramezanzadeh, S. A. Hosseini, *Sci. Rep.,* **13,** 12169 (2023). https://doi.org/10.1038/s41598-023-38540-9.
18. M. Tamilselvi, P. Kamaraj, M. Arthanareeswari, S. Devikala, J. Arockiaselvi, T. Pushpamalini, M*aterials Today, Proceed.*, **5**(2, 3), 8880 (2018) https://doi.org/10.1016/j.matpr.2017.12.321
19. W. Wang, Y. Tian, H. Shen, X. Zhang, *J. Alloys Compd.,* **955,** 170247 (2023) https://doi.org/10.1016/j.jallcom.2023.170247
20. V.S. Kathavate, P. P. Deshpande, *Surf. Coat. Technol.*, **394,** 125902 (2020) https://doi.org/10.1016/j.surfcoat.2020.125902
21. S. R. Arunima, M. J. Deepa, L. Elias, T. R. Aju Thara, C. V. Geethanjali, S. M. A. Shibli, *Appl. Surf. Sci.* **543,** 148822 (2021). https://doi.org/10.1016/j.apsusc.2020.148822
22. A. H. Riyas, C. V. Geethanjali, S. Arathy, A. Anil, S. M. A. Shibli, *Appl. Surf. Sci.* **593,** 153370 (2022). https://doi.org/10.1016/j.apsusc.2022.153370
23. Ch. V. Geethanjali, L. Elias, B. I. Bijimol, S. M. A. Shibli, *Langmuir,* **40**(39), 20389 (2024). https://doi.org/10.1021/acs.langmuir.4c01648
24. S. P. Aswathy, A. S. Kumar, V. S. Saji, S. M. A. Shibli, *Adv. Eng. Mater.*, **27**(2), 2401351 (2025). https://doi.org/10.1002/adem.202401351.
25. S.P. Aswathy, C.V. Geethanjali, A. S. Kumar, V. S. Saji, S.M.A. Shibli, *Surf. Int.,* **45,** 103882 (2024). https://doi.org/10.1016/j.surfin.2024.103882.
26. D. Fachikova, T. Liubenova, G. Ilieva, *Arch. Metall. Mater.,* **68**(3), 973 (2023) https://doi.org/10.24425/amm.2023.145462
27. Ts. L. Liubenova, D. I. Fachikova, *J. Chem. Technol. Metall.,* **58**(6), 1057 (2023).
28. S. Silva-Fernández, B. Díaz, I. Feijoo, X. R. Nóvoa, C. Pérez, *Electrochim. Acta*, **457,** 142510 (2023) https://doi.org/10.1016/j.electacta.2023.142510.
29. N. V. Phuong, K. H. Lee, D. Chang, S. Moon, *Corros Sci.*, **74,** 314 (2013). https://doi.org/10.1016/j.corsci.2013.05.005.
30. Ch. Zhang, S. Liao, B. Yu, X. Lu, X.-B. Chen, T. Zhang, F. Wang, *Corros. Sci.,* **150,** 279 (2019). https://doi.org/10.1016/j.corsci.2019.01.046
31. S. Kozhukharov, Ch. Girginov, S. Portolesi, A. Tsanev, V. Lilova, M. Georgieva, E. Lilov, P. Petkov, *J. Electrochem. Sci. Eng.,* **14**(5), 559 (2024) http://dx.doi.org/10.5599/jese.1949559J.
32. S. Portolesi, S. Kozhukharov, T. Haralanova, Ch. Girginov, *Proceeds Univ. Ruse (Bulgaria),* **61**(10.1), 68 (2022).
33. Y. Luo, W. Zhu, Z. Su, W. Li, A. Yi, K. Li, K. Chen, J. Song, Y. Duan, Y. Li, *Surf. Coat. Technol.,* **458,** 129313. (2023). https://doi.org/10.1016/j.surfcoat.2023.129313
34. J. Chen, Y. Ma, J. Yin, T. Hu, Q. Zhou, *Internat. J. Electrochem. Sci.* **16**(11), 211122 (2021). https://doi.org/10.20964/2021.11.02
35. Ch. Girginov, St. Kozhukharov, B. Tzaneva, *Bulg. Chem. Commun.,* **54**(B1), 21 (2022). https://doi.org/10.34049/bcc.54.B1.0430
36. M. Ahmad, A. S. Samra, S. Habib, R. Kahraman, B. Mansoor, R. A. Shakoor, *Sci. Rep.,* **15**, 26707 (2025). https://doi.org/10.1038/s41598-025-12319-6
37. V. Vitry, L. Bonin, *Surf. Coat. Technol.,* **311**, 164 (2017). https://doi.org/10.1016/j.surfcoat.2017.01.009
38. X. Hou, J. Song, S. Xu, Y. He, Y. Bai, Y. Sun, H. Liu, Q. Yuan, Q. Chen, K. Wei, *J. Solid State Electrochem.,* **29**, 289 (2025). https://doi.org/10.1007/s10008-024-06057-4
39. O. Hukumdar, U. Kumlu, A. Keskin, M. A. Akar, *Materials Testing*, **67** (1), 17 (2025). https://doi.org/10.1515/mt-2024-0262
40. A. Chakraborti, S.K. Das, P. Sahoo (eds.), Advances in Materials, Manufacturing and Design. INCOM 2024. Lecture Notes in Mechanical Engineering. Springer, Singapore, (2025). https://doi.org/10.1007/978-981-97-6667-3_13
41. P. Ji, X. Zhang, J. Wan, C. Zhang, Q. Yang, X. Zhang, L-Y. Gan, Y. Xi, *Surf. Int.* **33,** 102290, (2022). https://doi.org/10.1016/j.surfin.2022.102290
42. Y. Shen, Y. Ding, X. Sun, D. Liu, R. Xiao, Y. An, *ACS Omega* **9**(1), 942 (2024). https://doi.org/10.1021/acsomega.3c06301
43. Y. Messaoudi, H. Belhadj, M. R. Khelladi, A. Redjechta, A. Azizi, *Trans IMF*, **101**, **5,** 281 (2023). https://doi.org/10.1080/00202967.2023.2226967
44. A. Bahramian, M. Eyraud, F. Vacandio, P. Knauth, *Microelectr. Eng.* **206,** 25 (2019). https://doi.org/10.1016/j.mee.2018.12.008
45. R.A. Shakoor, R. Kahraman, U. Waware, Y. Wang, W. Gao, *Mater. Design.* **64,** 127 (2014). https://doi.org/10.1016/j.matdes.2014.07.026
46. G. Ruan, N. Fridman, G. Maayan, *Chem. Eur. J.,* **28,** e202202407, 1 (2022). https://doi.org/10.1002/chem.202202407
47. Y. Meng, G. Ni, X. Jin, J. Peng, Q.Y. Yan, *Mater. Today Nano*, **12,** 100095 (2020). https://doi.org/10.1016/j.mtnano.2020.100095
48. S. Park, S. Oh, I. Kim, *Water,* **13**(19), 2698 (2021). https://doi.org/10.3390/w13192698
49. E. H. Swift, E. A. Butler, Quantitative Measurements and Chemical Equilibria, Freeman, New York, 1972.
50. G. Milazzo, S. Caroli, V. K. Sharma, Tables of Standard Electrode Potentials, Wiley, London, 1978.
51. A. J. Bard, B. Parsons, J. Jordon (eds.) Standard Potentials in Aqueous Solutions, Dekker, New York, 1985.

*Bulgarian Chemical Communications, Volume 58, Issue 1 (pp. 59-65) 2026* *DOI: 10.34049/bcc.58.1.5720*

# Comparison between ortho- and meta-phosphoric acid containing phosphate potential buffering systems

M. Georgieva[1*], S. Kozhukharov[2,3], Ch. Girginov[4], A. Dishliev[5], P. Petkov[3]

[1]*Institute of Mineralogy and Crystallography, Bulgarian Academy of Sciences, Acad. Georgi Bonchev Str., Bl. 107, 1113 Sofia, Bulgaria*

[2]*LAMAR – Laboratory for Advanced Materials Research, University of Chemical Technology and Metallurgy, 8 Kliment Ohridski Blvd., 1797 Sofia, Bulgaria*

[3]*Department of Physics, University of Chemical Technology and Metallurgy, 8 Kliment Ohridski Blvd., 1797 Sofia, Bulgaria*

[4]*Department of Physical Chemistry, University of Chemical Technology and Metallurgy, 8 Kliment Ohridski Blvd., 1797 Sofia, Bulgaria*

[5]*Department of Mathematics, University of Chemical Technology and Metallurgy, 8 Kliment Ohridski Blvd., 1756 Sofia, Bulgaria*

Received: September 02, 2025; Revised: October 30, 2025

All chemical methods in aqueous media require pH measurement and adjustment. The most reliable method for pH regulation is the addition of suitable buffers. That is why the present brief study is devoted to the evaluation of the potentials for elaboration of buffer solutions by the addition of phosphoric acid to 0.066 M disodium monohydrogen orthophosphate dihydrate ($Na_2HPO_4.2H_2O$) solution. The selected acidic components were dilute solutions of either orthophosphoric ($H_3PO_4$) or metaphosphoric ($(HPO_3)_n$) acids. This study was performed in two consecutive stages: (i) evaluation of the resulting pH after different volume ratios between the respective acidic and alkaline components, and (ii) determination of their buffering capacity by precise instrumental titrations, assisted by a digital high-precision pH meter. The results show that both solutions can be used as reliable buffers.

**Keywords:** disodium monohydrogen phosphate**,** orthophosphoric acid, metaphosphoric acid, pH ranges, buffering capacity

## INTRODUCTION

For decades, phosphating has been a fundamental metal finishing procedure [1, 2]. Recently, it has been applied for further enhancement of the protective properties of cerium conversion coatings (CeCC) [3–5]. In this sense, Tsanev *et al.* [6] and Andreeva *et al.* [7] have proposed phosphate sealing of CeCC layers with simultaneous calcium phosphate formation. This approach appears rather attractive since it enables potential applications for bone-like implants, as recently proposed in various review and research works [8–14]. Furthermore, the biocompatibility of calcium phosphate-based materials enables their use for controlled drug delivery [15, 16] and cancer therapy [17]. Finally, the phosphating of CeCC layers appears as an alternative approach for the synthesis of cerium phosphate materials, which have recently shown great potential for various applications, as noted by several authors [18-21].

Another important field of application of phosphates is the formation of vanadium phosphate layers for Li- and Na-ion batteries [22-25]. In this sense, the trend is focused on the modification of the chemical composition [26-28], alternative phosphate materials [29], and vanadium phosphate recycling [30]. In addition, multifunctional Ni-Co-P layers also represent a major area of scientific research activity [31-35], along with doped Ni-P layers [35-40]. In particular, Ignatova *et al.* [41, 42] paid special attention to the impact of the type [41] and content [42] of the phosphorus source on the properties of the resulting Ni-Co-P coatings.

Some authors have also emphasized the impact of pH on the formation of electroplated coatings [43] and ferrite nanoparticles [44, 45]. Consequently, there is a need to develop mixtures of phosphorus compounds with defined pH ranges and buffering capacities. In response to this necessity, the present brief study forms part of a systematic description of a variety of phosphate/borate [46, 47] mixtures, including descriptions of their pH ranges and buffering properties. Moreover, the description of the experimental procedures in the present work could

* To whom all correspondence should be sent:
E-mail: *mgeorgieva@imc.bas.bg*

assist other research activities aimed at elaborating suitable electrolytes for spontaneous and electrochemical formation of advanced active layers such as those described above. Consequently, the content of this paper can serve as a valuable information source for the development of advanced innovative phosphate-containing layers for corrosion protection of Mg [48], Zn [49, 50], Al [4, 51, 52], and Ti [53] alloys, as well as mild steel [54, 55].

Therefore, the aim of the present work is to evaluate the pH buffering potentials of two mixtures prepared from an alkaline phosphate and two phosphorus-containing acids. The experiments were performed using a 0.066 M solution of disodium monohydrogen phosphate and 0.050 M ortho- or meta-phosphoric acids. The respective measurements were performed using a precision pH meter.

## EXPERIMENTAL

### *pH Range determination*

A set of potential phosphate buffer systems (PBS) was obtained by mixing the initial solutions in defined volume ratios. The compositions of the initial solutions are summarized in Table 1.

**Table 1.** Compositions of the initial alkaline and acidic component solutions.

| Buffer | Component type | Calculated concentration | Real content |
|---|---|---|---|
| PBS-1 | Alkaline component | $Na_2HPO_4.2H_2O$ - 0.066 M | 11.9520 g of 99.5% pure compound to 1 $dm^3$ solution |
| | Acidic component | o-$H_3PO_4$ - 0.050 M | 3.40 ml of 85% acid |
| PBS-2 | Alkaline component | $Na_2HPO_4.2H_2O$ - 0.066 M | 11.9520 g of 99.5% pure compound to 1 $dm^3$ solution |
| | Acidic component | 40-44% ($HPO_3$) to 50-60% $Na_3PO_4$ | 5.4560 g of industrial product to 1 $dm^3$ solution |

*The weight of metaphosphoric acid was selected to be equal to the weight of 3.40 ml of orthophosphoric acid considering its density equal to 1.88 g/ml according to the product label.

The alkaline component with CAS No. 10028-24-7 was a product of Merck (Germany). The orthophosphoric acid with CAS No. 7664-38-2 was also provided by Merck (Germany), whereas the metaphosphoric acid (Art. No. 01-320) was delivered by Ferak-Laborat GmbH (Germany). This product is described by the producer as a mixture of $HPO_3$ (40–44%) and $NaPO_3$ (50–60%) with remnants of $H_3PO_3$ and traces of various impurities.

The pH determinations were performed using a precise HI 255 combined meter, a product of Hanna Instruments. It was equipped with a HI 1131 commercial universal glass electrode. The device was calibrated prior to each measurement set. Data acquisition was performed through five measurements under identical conditions. Each individual measurement was performed after 5 min of electrode immersion in the stirred solution at room temperature. The solutions were pre-stirred for another 5 min immediately before each measurement.

The mean pH values were acquired from the raw data for each set of five measurements for each volume ratio. The calculations were performed according to the expression below:

$$pH = pH_{av} \pm \Delta pH\,, \tag{1}$$

where: $pH_{av}$ is the average pH value obtained from five measurements, and ΔpH is the standard deviation.

The average pH values were calculated using Equation (2):

$$pH_{av} = \sum_{i=1}^{i=n} \frac{pH_i}{n}\,, \tag{2}$$

where: $pH_{av}$ – average pH value; $pH_i$ – individual pH value obtained from the respective measurement ($i$ = 1 to n); n – total number of pH measurements (in this case, n = 5).

The standard deviation was calculated using Equation (3):

$$\Delta pH_{av} = \pm\sqrt{\sum_{i=1}^{i=n} \frac{\left(pH_i - pH_{av}\right)^2}{n(n-1)}}\,, \tag{3}$$

where: all quantities are as defined in Equation (2).

For clarity, the data in Tables 2 and 3 are illustrated in Figure 2. It was plotted after defining the ratios of the solution volumes according to Equation (4):

$$VR_1 = \frac{V_1}{V_1 + V_2} \text{ or } VR_2 = \frac{V_2}{V_1 + V_2}\,, \tag{4}$$

where: VR – volume ratio of the used primary solutions; $V_1$ – volume of the alkaline solution composing the buffer mixture (mL); $V_2$ – volume of the acidic solution composing the buffer mixture (mL). Figure 2 represents the correlations between VR, calculated from the volumes in Table 2, and the pH values of the resulting buffer solutions.

Considering the importance of the raw data for this study, the values obtained from direct measurements are combined with the calculated average pH values and their standard deviations in Table 2.

*Buffering capacity determination*

The buffering capacity determination was performed after defining the volume ratios between the alkaline and acidic borate or phosphate solutions corresponding to buffer mixtures with pH ≈ 7. The experimental work was carried out through five-fold titrations with standardized alkaline NaOH or HCl solutions. The titrant standardizations were performed using a primary 0.05 M $(COOH)_2$ standard solution. It was obtained by dissolving 6.3334 ± 0.0001 g of $(COOH)_2.2H_2O$ (99.5%), supplied by Chim-spectar Ltd. (Bulgaria), in 1 $dm^3$ of distilled water in a volumetric flask. The necessity for standardization using primary standard solutions is determined by the susceptibility of NaOH to carbonation and hydration upon contact with ambient air, and by the volatility of HCl.

The buffering capacity was calculated using Equation (5) after five-fold titrations with the respective standardized alkaline and acidic solutions:

$$BC = \frac{MV_{ss}}{\Delta(pH)V_{buff}}.\frac{1}{n}, \qquad (5)$$

where: BC is the buffering capacity (mol.$pH^{-1}$); $MV_{ss}$ is the quantity of the added standard solution of known alkaline or acidic compound (mol). In the present case, the data for the standard solution molarity are shown in Table 5, whereas their volumes, used for titrations, are summarized in Table 6. Δ(pH) is the pH change (dimensionless). In the present case, its value is assumed to be unity. $V_{buff}$ is the volume of the buffer solution subjected to titration (15 mL in the present case). The coefficient (1/n) corresponds to the compound whose solution is subjected to pH measurement. If the compound is alkaline, then n = number of $OH^-$ anions per molecule. If it is acidic, then n = number of $H_3O^+$ (i.e., $H^+$ cations) moieties per molecule of the dissolved compound. In both cases, for NaOH and HCl, its value is 1/n = 1.

The titrations were performed instrumentally using the already described pH meter, until the pH value of the potential buffer solution shifted by one unit. For this purpose, 15 mL of the respective neutral potential buffer solutions were titrated with the standardized alkaline and acidic solutions described above.

## RESULTS AND DISCUSSION

*Results from pH range determination*

Systematic research activities were performed, comprising the pH ranges and buffering capacities of the proposed potential buffers. Hence, the possible pH interval of the compositions prepared with o-$H_3PO_4$ is presented in Table 2 and illustrated in Figure 1.

The data show that the possible pH values of these compositions cover a large interval: from above pH ≈ 10 down to nearly pH ≈ 1.75. Moreover, neutral pH values can be reached when the alkaline compound (i.e., $Na_2HPO_4$) is present in prevailing amounts.

In turn, Figure 1 shows that a neutral pH can be reached only in points $P_1$ and $P_2$, both corresponding to about 62 mL of 0.05 M $Na_2HPO_4$ solution and the addition of orthophosphoric acid up to a total mixture volume of 100 mL.

Similar results were obtained for the second potential buffer system prepared with the addition of metaphosphoric acid. Table 3 presents results that are almost identical to those described above. Hence, the pH range extends between pH ≈ 10 and pH ≈ 2, and a neutral medium was achieved at twice the $Na_2HPO_4$ content.

Figure 2 also shows only two points, $P_1$ and $P_2$, which indicate that a neutral mixture can be obtained with about 59 mL of $Na_2HPO_4$ and 41 mL of $(HPO_3)_n$, when both solutions have approximately similar molarities.

**Table 2.** Added component solution volumes and resulting pH values of PBS-1 mixtures.

| Component solution volumes (ml) | | Volume ratios | | Consecutive measurement number | | | | | Calculated mean pH values |
|---|---|---|---|---|---|---|---|---|---|
| $Na_2HPO_4$ | o-$H_3PO_4$ | $VR_1$ | $VR_2$ | $pH_1$ | $pH_2$ | $pH_3$ | $pH_4$ | $pH_5$ | |
| 40 | 0 | 1.000 | 0.000 | 10.050 | 10.049 | 10.046 | 10.042 | 10.039 | 10.045 ± 0.046 |
| 20 | 10 | 0.667 | 0.333 | 7.085 | 7.084 | 7.085 | 7.086 | 7.087 | 7.085 ± 0.014 |
| 20 | 20 | 0.500 | 0.500 | 6.506 | 6.505 | 6.503 | 6.502 | 6.504 | 6.504 ± 0.024 |
| 15 | 25 | 0.375 | 0.625 | 5.392 | 5.379 | 5.372 | 5.371 | 5.368 | 5.376 ± 0.179 |
| 10 | 20 | 0.333 | 0.667 | 3.630 | 3.618 | 3.607 | 3.608 | 3.609 | 3.614 ± 0.270 |
| 10 | 30 | 0.250 | 0.750 | 3.187 | 3.183 | 3.177 | 3.175 | 3.172 | 3.179 ± 0.192 |
| 5 | 35 | 0.125 | 0.875 | 2.176 | 2.167 | 2.161 | 2.151 | 2.155 | 2.163 ± 0.393 |
| 0 | 40 | 0.000 | 1.000 | 1.747 | 1.760 | 1.754 | 1.750 | 1.749 | 1.752 ± 0.263 |

**Table 3.** Added component solution volumes and resulting pH values of PBS-2 systems.

| Component solution volumes (ml) | | Volume ratios | | Consecutive measurement number | | | | | Calculated mean pH values |
|---|---|---|---|---|---|---|---|---|---|
| $Na_2HPO_4$ | $(HPO_3)_n$ | $VR_1$ | $VR_2$ | $pH_1$ | $pH_2$ | $pH_3$ | $pH_4$ | $pH_5$ | |
| 40 | 0 | 1.000 | 0.000 | 10.050 | 10.049 | 10.046 | 10.042 | 10.039 | 10.045 ± 0.046 |
| 20 | 10 | 0.667 | 0.333 | 7.193 | 7.192 | 7.194 | 7.194 | 7.190 | 7.193 ± 0.023 |
| 20 | 20 | 0.500 | 0.500 | 6.717 | 6.710 | 6.708 | 6.710 | 6.710 | 6.711 ± 0.052 |
| 15 | 25 | 0.375 | 0.625 | 6.205 | 6.184 | 6.180 | 6.176 | 6.172 | 6.183 ± 0.208 |
| 10 | 20 | 0.333 | 0.667 | 5.985 | 5.996 | 5.995 | 5.990 | 5.989 | 5.991 ± 0.076 |
| 10 | 30 | 0.250 | 0.750 | 3.024 | 3.027 | 3.026 | 3.023 | 3.031 | 3.026 ± 0.103 |
| 5 | 35 | 0.125 | 0.875 | 2.338 | 2.342 | 2.332 | 2.328 | 2.323 | 2.333 ± 0.326 |
| 0 | 40 | 0.000 | 1.000 | 1.906 | 1.910 | 1.909 | 1.904 | 1.889 | 1.904 ± 0.447 |

**Table 4.** Results of the secondary standard solution titrations.

| Buffer code | Standard for titration | Consecutive measurement number | | | | | Calculated mean values ($cm^3$) |
|---|---|---|---|---|---|---|---|
| | | Volume 1 ($cm^3$) | Volume 2 ($cm^3$) | Volume 3 ($cm^3$) | Volume 4 ($cm^3$) | Volume 5 ($cm^3$) | |
| PBS-1 | NaOH | 6.60 | 6.65 | 6.65 | 6.75 | 6.65 | 6.66 ± 0.82 |
| | HCl | 8.65 | 8.55 | 8.60 | 8.60 | 8.55 | 8.59 ± 0.49 |
| PBS-2 | NaOH | 6.25 | 6.20 | 6.20 | 6.25 | 6.25 | 6.23 ± 0.44 |
| | HCl | 8.10 | 8.05 | 8.15 | 8.15 | 8.10 | 8.11 ± 0.52 |

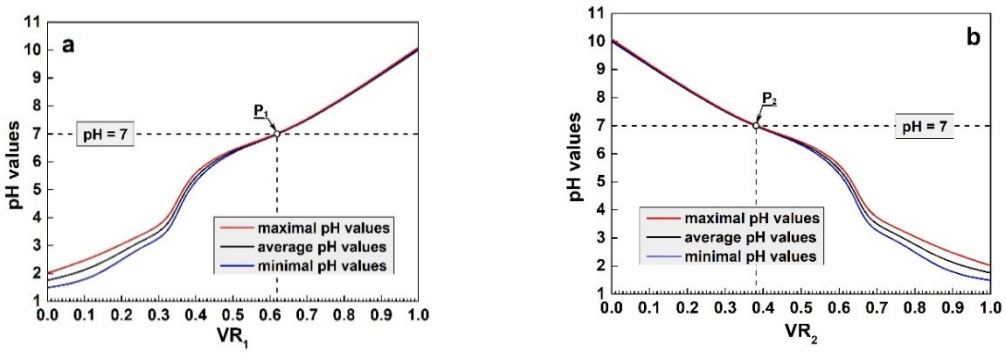


**Fig. 1.** Correlation between the pH value ranges for phosphate potential buffer based on o-$H_3PO_4$ and the primary composing solutions: (a) for $VR_1$ and (b) for $VR_2$.

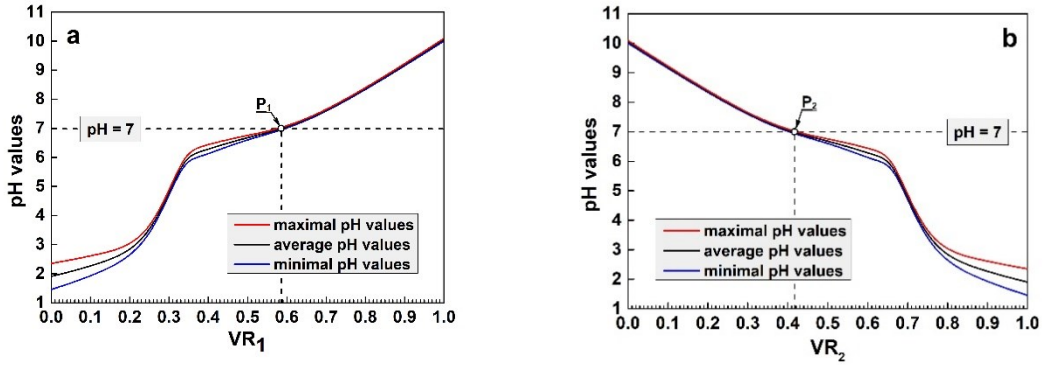


**Fig. 2.** Correlation between the pH value ranges for phosphate potential buffer based on $(HPO_3)_n$ and the primary composing solutions: (a) for $VR_1$ and (b) for $VR_2$.

The curves in both figures show the same trend. In the alkaline pH range, straight lines with slopes approaching unity (i.e., 45°) are observed, whereas clear curvatures (Fig. 1) or sharp bends (Fig. 2) occur in the mid-range. At the lowest pH values, below pH ≈ 4 (Fig. 1) or pH ≈ 3 (Fig. 2), the curves again exhibit a lower slope. A slight curve splitting appears

in the acidic pH range in both cases, although data reproducibility remained rather high.

*Results from the buffering capacity determination*

This procedure required preliminary determination of the exact concentrations of both secondary standard solutions. It was performed through their instrumental titrations with the $(COOH)_2$ primary standard solution, using the pH meter described in the experimental part. The respective titrations with 15 mL solutions of the primary standard required 30.66 ± 0.32 mL of the NaOH solution, revealing that the average NaOH concentration value is $49.156\times10^{-3}$ M. This value was further used for the determination of the HCl concentration. It was defined by five titrations of the HCl solution with the NaOH secondary standard. Thus, the average volume of the HCl solution expended for these titrations was 14.69 ± 0.28 mL. Hence, the calculations have shown that the HCl secondary solution concentration had an average value of $50.193\times10^{-3}$ M.

These secondary standard solutions were used for the definition of the buffering capacity (BC) of the phosphate mixtures with neutral pH. For that purpose, titrations were performed using the secondary standard solutions on 15 mL samples of PBS-1 and PBS-2, respectively. The acquired data are summarized in Table 4.

Additionally, similar titrations were performed using the *Reagecon* (UK) commercial buffer for neutral media. Hence, 7.40 mL of NaOH solution and 11.10 mL of HCl standard were expended. These values fall within the range of the data in Table 4. Consequently, both phosphate mixtures could be used as reliable buffers.

Further, the buffering capacities (BC) of the investigated phosphate mixtures were determined by applying the data described above in Equation (5). The respective results show that the titrations with the alkaline solution resulted in: $BC_{PBS\text{-}1}{}^{NaOH} = 21.83\times10^{-3}$ mol $pH^{-1}$ for the former mixture and $BC_{PBS\text{-}2}{}^{NaOH} = 20.41\times10^{-3}$ mol $pH^{-1}$. In turn, the titrations with the acidic secondary standard resulted in the following BC values: $BC_{PBS\text{-}1}{}^{HCl} = 28.74\times10^{-3}$ mol $pH^{-1}$ and $BC_{PBS\text{-}2}{}^{HCl} = 27.13\times10^{-3}$ mol $pH^{-1}$.

The analysis of these numerical data leads to the inference that both PBS-1 and PBS-2 systems possess comparable buffering capacity values. The reason for this is that, when dissolved in water, metaphosphoric acid converts to orthophosphoric acid due to hydration (Eq. 6):

$$HPO_3 + H_2O \rightarrow H_3PO_4 \quad (6)$$

Nevertheless, comparison of the buffering capacities of the studied systems reveals that the use of o-$H_3PO_4$ is preferable, since the BC of PBS-1 slightly exceeds that of PBS-2.

## CONCLUSIONS

The present work deals with the determination of possible pH intervals and the assessment of the pH buffering potentials of two mixtures prepared from an alkaline phosphate and two phosphorus-containing acids. The experiments were performed using a 0.066 M solution of disodium monohydrogen phosphate and 0.050 M ortho- or metaphosphoric acids. The respective measurements were carried out using a precision pH meter.

The experiments have shown that a rather wide pH range can be achieved by varying the ratios between the initial component solutions.

In the case of the $Na_2HPO_4$ / o-$H_3PO_4$ system, neutral pH can be reached by mixing 62 mL of 0.05 M $Na_2HPO_4$ solution with orthophosphoric acid to obtain a 100 mL mixture.

In the latter case, a neutral mixture can be obtained by about 59 mL of $Na_2HPO_4$ and 41 mL of $(HPO_3)_n$, when both solutions have approximately similar (i.e., ~0.05 M) molarities.

The buffering properties of both PBS-1 and PBS-2 were compared with those of a commercial buffer and also numerically evaluated. The respective results have shown that the proposed potential buffer systems exhibit reliable buffering properties comparable to those of the commercial product. Moreover, their buffering capacities were determined, and the acquired results show that both systems can be used as buffers for the purpose of chemical synthesis of various advanced coatings and other types of materials.

In addition, further data analysis has shown that the use of o-$H_3PO_4$ is preferable, since the buffering capacity of PBS-1 slightly exceeds that of PBS-2, although the difference between their values is insignificant.

***Acknowledgement:*** *The authors express their gratitude for the financial support provided by the Bulgarian National Scientific Fund under Contract No. KII-06-H89/8. Research equipment of the distributed research infrastructure INFRAMAT (part of the Bulgarian National Roadmap for Research Infrastructure), supported by the Bulgarian Ministry of Education and Science, was also used in this investigation.*

REFERENCES


1. A. Zavarella, US Patent US-2476345A, 1946.
2. J. Bogi, R. Macmillan, *J. Mater. Sci.,* **12**, 2235 (1977).
3. D. K. Heller, W. G. Fahrenholtz, M. J. O'Keefe, *Corros. Sci.,* **52**, 360 (2010).
4. S. Cherneva, R. Andreeva, D. Stoychev, *Materials,* **18(2)**, 424 1 (2025) https://doi.org/10.3390/ma18020424
5. R. Andreeva, A. Tsanev, D. Stoychev, *Bulg. Chem. Commun.,* **55**(4), 390 (2023) https://doi.org/10.34049/bcc.55.4.5491
6. A. Tsanev, R. Andreeva, D. Stoychev, *Materials,* **16**(19), 6499 (2023) https://doi.org/10.3390/ma16196499
7. R. Andreeva, A. Tsanev, D. Stoychev, *Metals,* **14**(7), 768 (2024) https://doi.org/10.3390/met14070768
8. N. W. Kucko, R.-P. Herber, S. C. G. Leeuwenburgh, J. A. Jansen, Chapter 34 - Calcium Phosphate Bioceramics and Cements, Principles of Regenerative Medicine, 3rd edn., 2019, p. 591 https://doi.org/10.1016/B978-0-12-809880-6.00034-5
9. R. A. Surmenev, M. A. Surmeneva, A. A. Ivanova, *Acta Biomaterialia,* **10**(2), 557 (2014) https://doi.org/10.1016/j.actbio.2013.10.036
10. X. Hou, L. Zhang, Z. Zhou, X. Luo, T. Wang, X. Zhao, B. Lu, F. Chen, L. Zheng, *J. Funct. Biomater.,* **13(4),** 187 (2022) https://doi.org/10.3390/jfb13040187
11. D. Moreno, F. Vargas, J. Ruiz, M. E. López, *Bol. Soc. Esp. Cerám. Vidrio,* **59**(5), 193 (2020). https://doi.org/10.1016/j.bsecv.2019.11.004
12. W. Habraken, Pamela Habibovic, M. Epple, M. Bohner, *Materials Today,* **19**(2), 69 (2016). https://doi.org/10.1016/j.mattod.2015.10.008
13. M. Tavoni, M. Dapporto, A. Tampieri, S. Sprio, *J. Compos. Sci.,* **5**(9), 227 (2021). https://doi.org/10.3390/jcs5090227
14. A-M. Yousefi, *J. Appl. Biomater. Funct. Mater.,* 1 (2019). https://doi.org/10.1177/2280800019872594
15. A. M. Rheima, A. A. Abdul-Rasool, Z. T. Al-Sharify, H. K. Zaidan, D. M. Athair, S. H. Mohammed, E. Kianfar, *Case Studies Chem. Envir. Eng.,* **10,** 100869 (2024). https://doi.org/10.1016/j.cscee.2024.100869
16. A. D. Trofimov, A. A. Ivanova, M. V. Zyuzin, A. S. Timin, *Pharmaceutics,* **10**(4), 167 (2018). https://doi.org/10.3390/pharmaceutics10040167
17. L-F. Chen, Y-T. Ye, R-Y. Meng, H-Y. Xia, B-Q. Chen, S-B. Wang, R. K. Kankala, A-Z. Chen, *ACS Mater. Lett.,* **6**(10), 4819 (2024) https://doi.org/10.1021/acsmaterialslett.4c01432
18. T. O. Shekunova, A. E. Baranchikov, O. S. Ivanova, L. S. Skogareva, N. P. Simonenko, Yu. A. Karavanova, V. A. Lebedev, L. P. Borilo, V. K. Ivanov, *J. Non-Cryst. Solids,* **447**, 183 (2016). https://doi.org/10.1016/j.jnoncrysol.2016.06.012
19. T. O. Kozlova, E. D. Sheichenko, D. N. Vasilyeva, D. A. Kozlov, I. V. Kolesnik, I. V. Tronev, M. A. Teplonogova, A. E. Baranchikov, V. K. Ivanov, *Nanosyst. Phys. Chem. Math.,* **15**(2), 215 (2024). https://doi.org/10.17586/2220-8054-2024-15-2-215-223
20. A. E. Baranchikov, T. O. Kozlova, S. Ya. Istomin, A. V. Mironov, T. M. Vasilchikova, A. A. Gippius, T. V. Plakhova, D. N. Vasilyeva, V. K. Ivanov, *Chemistry Select.,* **9**(17), e202401010 (2024).
21. T. V. Plakhova, M. A. Vyshegorodtseva, I. F. Seregina, R. D. Svetogorov, A. L. Trigub, D. A. Kozlov, A. V. Egorov, M. D. Shaulskaya, D. M. Tsymbarenko, A. Yu. Romanchuk, V. K. Ivanov, S. N. Kalmykov, *Chemosphere*, **368**, 143664 (2024). https://doi.org/10.1016/j.chemosphere.2024.143664
22. S. Banerjee, R. B. Choudhary, S. Ansari, *Future Batteries,* **4,** 100010 (2024). https://doi.org/10.1016/j.fub.2024.100010
23. R. Yin, Zh. Guo, R. Liu, X-S. Tao, *Chinese Chem. Lett.,* **36**(2), 109643 (2025). https://doi.org/10.1016/j.cclet.2024.109643
24. S. Shraer, A. Dembitskiy, I. Trussov, A. Komayko, D. Aksyonov, N. Luchinin, A. Morozov, S. Pollastri, G. Aquilanti, S. Ryazantsev, V. Nikitina, A. Abakumov, E. Antipov, S. Fedotov, *En. Stor. Mater.,* **68,** 103358 (2024). https://doi.org/10.1016/j.ensm.2024.103358
25. S.-M. Chang, C.-E. Liu, C.-C. Yang, T.-F. Hung, *Electrochim. Acta,* **514,** (2025) 145678. https://doi.org/10.1016/j.electacta.2025.145678
26. O. Yakubovich, G. Kiriukhina, V. Nesterova, A. Volkov, S. Fedotov, O. Dimitrova, *Minerals,* **15**(1), 3 (2025). https://doi.org/10.3390/min15010003
27. J. Mei, X. Wang, J. Wen, Ch. Shang, Zh. Zhang, Ch. Chen, Zh. Huang, P. Hu, *J. En. Stor.,* **103A**, 114257 (2024). https://doi.org/10.1016/j.est.2024.114257
28. H. K. Razzaq, C-C. Yang, M. N. Mustafa, A. Numan, M. Khalid, *Prog. Mater. Sci.,* **151,** 101424 (2025). https://doi.org/10.1016/j.pmatsci.2024.101424
29. S. N. Marshenya, A. G. Scherbakov, A. D. Dembitskiy, A. A. Golubnichiy, I. A. Trussov, A. A. Savina, S. M. Kazakov, D. A. Aksyonov, E. V. Antipov, S. S. Fedotov, *Dalton Trans*., **53,** 15928 (2024). https://doi.org/10.1039/D4DT02288B
30. A. Sh. Samarin, A. V. Ivanov, S. S. Fedotov, *Clean Technol.,* **5**(3), 881 (2023). https://doi.org/10.3390/cleantechnol5030044
31. K. N. Ignatova, St. V. Kozhukharov, G. V. Avdeev, I. A. Piroeva, *Bulg. Chem. Commun.,* **50A,** 61 (2018).
32. L. Dzib-Pérez, O. Bilyy, A. Leon-Gronimo, J. G. Castaño-Gonzalez, P. Quintana, R. Domínguez-Maldonado, J. González-Sánchez, *Mater. Sci.,* **58,** 1 (2022). https://doi.org/10.1007/s11003-022-00623-9
33. Y. Messaoudi, H. Belhadj, M. R. Khelladi, A. Redjechta, A. Azizi, *Trans. IMF*, **101**(5), 281 (2023). https://doi.org/10.1080/00202967.2023.2226967
34. Y. Shen, Y. Ding, X. Sun, D. Liu, R. Xiao, Y. An, *ACS Omega,* **9**(1), 942 (2024). https://doi.org/10.1021/acsomega.3c06301
35. A. Chakraborti, S.K. Das, P. Sahoo, in: Lecture Notes in Mechanical Engineering. Springer-Singapore, P. Sahoo, T.K. Barman (eds.), Advances in Materials,

Manufacturing and Design. INCOM 2024. 2025, p. 351 https://doi.org/10.1007/978-981-97-6667-3_13
36. V. B. Chintada, T. R. Gurugubelli, R. Koutavarapu, *J. Mater. Sci.: Mater Electron.,* **33,** 950 (2022). https://doi.org/10.1007/s10854-021-07366-4
37. Z. Li, Z. Farhat, *J. Bio. Tribo. Corros.,* **7,** 97 (2021). https://doi.org/10.1007/s40735-021-00535-2
38. J. M. Costa, D. G. Portela, A. F. de Almeida Neto, in: Alloy Materials and Their Allied Applications, I. R. Boddula, M. I. Ahamed, A. M. Asiri (eds.), Scrivener Publ. New Jersey, USA, 2020, https://doi.org/10.1002/9781119654919.ch3
39. G. Qiao, Sh. Wang, X. Wang, X. Chen, X. Wang, H. Cui, *Adv. Compos. Hybr. Mater.,* **5,** 438 (2022). https://doi.org/10.1007/s42114-021-00268-
40. P. Ji, X. Zhang, J. Wan, Ch. Zhang, Q. Yang, X. Zhang, L.-Y. Gan, Y. Xi, *Surf. Int.,* **33,** 102290 (2022). https://doi.org/10.1016/j.surfin.2022.102290
41. K. Ignatova, S. Kozhukharov, M. Alakushev, *Mater. Chem. Phys.,* **219,** 175 (2018). https://doi.org/10.1016/j.matchemphys.2018.08.025
42. K. Ignatova, Y. Marcheva, S. Kozhukharov, *Proceeds. Univ. Ruse (Bulgaria),* **55**(10.1), FRI-21-P-CT(R)-03, 12 (2016).
43. S. Sadeghi, H. Ebrahimifar, *J. Mater. Eng. Perform.,* **30,** 2409 (2021). https://doi.org/10.1007/s11665-021-05462-4
44. R. Jabbar, S. H. Shahatha, N. K. Taieh, B. Magid, A. F. Showard, *Ceram. Internat.,* **50**(17B), 31114 (2024). https://doi.org/10.1016/j.ceramint.2024.05.417
45. P. A. Vinosha, S. J. Das, *Mater. Today,* **5(2-3),** 8662 (2018). https://doi.org/10.1016/j.matpr.2017.12.291
46. M. Georgieva, S. Kozhukharov, Ch. Girginov, V. Lilova, NATO Science for Peace and Security Series B: Physics and Biophysics, Chapter 8, 2025, p. 115, https://doi.org/10.1007/978-94-024-2316-7_8
47. M. Georgieva, S. Kozhukharov, Ch. Girginov, V. Lilova, NATO Science for Peace and Security Series B: Physics and Biophysics, Chapter 9, 2025, 131, https://doi.org/10.1007/978-94-024-2316-7_9
48. R. Chaharmahali, A. Fattah-Alhosseini, K. Babaei, *J. Magnes. Alloys,* **9**(1), 21 (2021). https://doi.org/10.1016/j.jma.2020.07.004
49. G. D. López, P. L. Williams, J. L. Lorca, M. Echeverry-Rendón, *Surf. Int.,* **72,** 107243 (2025). https://doi.org/10.1016/j.surfin.2025.107243
50. T. L. Liubenova, D. I. Fachikova, *J. Chem. Technol. Metall.,* **58**(6), 1057 (2023).
51. G. P. Ilieva, D. I. Ivanova, L. B. Fachikov, *J. Chem. Technol. Metall.,* **56**(2), 353 (2021).
52. L. B. Fachikov, G. P. Ilieva, D. I. Ivanova, *Prot. Met. Phys. Chem. Surf.,* **57,** 796 (2021). https://doi.org/10.1134/S2070205121040092
53. M. Logesh, S.-G. Ahn, H.-C. Choe, *Ceram. Internat.,* **51A,** 22, 36182 (2025). https://doi.org/10.1016/j.ceramint.2025.05.339
54. V. Rumyantseva, V. Konovalova, B. Narmaniya, *Journal of Physics: Conference Series*, **2131**(429), 042027 (2021). https://doi.org/10.1088/1742-6596/2131/4/042027
55. C.M. Griffiths, N. Wint, G. Williams, H.N. McMurray, *Corros. Sci.,* **198,** 110111, 1 (2022). https://doi.org/10.1016/j.corsci.2022.110111

*Bulgarian Chemical Communications, Volume 58, Issue 1 (pp. 66-73) 2026* *DOI: 10.34049/bcc.58.1.5712*

# A comparative study of the chemical composition of oil–bearing *Rosa damascena* Mill. cultivated in Bulgaria and in Japan

R. H. Nenova[1*], D. A. Nedeva[1], A. M. Dobreva[1], T. I. Shimazaki[2], K. N. Kalinov[1*]

[1] *Institute of Roses and Aromatic Plants, Department of Aromatic and Medicinal Plants, Agricultural Academy, 49 Osvobozhdenie Blvd., 6100 Kazanlak, Bulgaria*
[2] *"No Limit Production"LTD, 99 Georgi S. Rakovski Str., 1000 Sofia, Bulgaria*

Received: July 04, 2025; Revised: December 09, 2025

The oil-bearing rose, *Rosa damascena* Mill., is an emblematic species of high economic importance for Bulgaria, a crop whose cultivation is largely determined by meteorological and environmental factors. We report the first successful cultivation of *R. damascena* Mill. in Japan, where no prior data on its growth exist. This study aimed to compare the yield and chromatographic profiles of rose oils produced in Bulgaria and Japan. The essential oil yield, calculated on a dry weight basis, was determined to be 0.191% (w/w) for the Bulgarian rose oil and 0.07 % (w/w) for the Japanese rose oil. Gas chromatography with flame ionization detection (GC–FID) analysis identified the main aroma components—the monoterpene alcohols, which represent more than 65% of the total 20 identified substances for the Bulgarian oil and only 26% for the Japanese oil. The results are presented as relative percentage as follows: geraniol (22.48/7.05), citronellol (39.18/17.91), and nerol (4.46/1.5), followed by the stearoptene fraction: nonadecane (14.89/26.31), nonadecene (0.83/7.38), heneicosane (4.12/8.36) and heptadecane (2.14/5.29) for Bulgarian and Japanese rose oil, respectively. A remarkable feature is the inverse deviation of the Japanese oil's composition: its aromatic compounds are sub-standard, while its stearoptene fractions are substantially higher than the upper limit defined by the standard. Statistical evaluation using a paired binomial proportion test confirmed that Bulgarian rose oil is by 58.3% superior in eleoptene composition. These findings confirm the first successful cultivation of *R. damascena* Mill. in Japan, highlighting significant yield and compositional disparities against traditional Bulgarian rose oil production.

**Keywords:** rose oil, GC–FID, paired binomial proportion test

## INTRODUCTION

Bulgarian rose oil, produced from *R. damascena* Mill., is globally recognized as the highest quality and ultimate standard in the market [1]. Regarded as "liquid gold", its exceptional value stems from low distillation yield, lack of substitutes [2], and cultivation restricted to specific climate and soil conditions. The chemical complexity of Bulgarian rose oil, with its more than 300 identified constituents, represents a remarkable example of nature's biochemical diversity. This complex mixture of terpene alcohols, hydrocarbons, phenolic compounds, and trace components creates a unique phytochemical profile that has defied complete synthetic replication and continues to reveal new therapeutic applications through scientific investigation. The oil's complex composition underpins both its exquisite fragrance and its diverse biological activities, which collectively explain the enduring value of Bulgarian rose oil in perfumery, cosmetics, and complementary medicine [3–6]. The cultivation of *R. damascena* Mill. in Bulgaria is closely associated with the unique soil and climatic conditions of the Rose Valley. Among the climatic factors, air temperature and annual precipitation play the most significant roles in influencing the growth and development of this oil-bearing rose [7]. Bulgaria and Turkey dominate global rose oil production, collectively accounting for approximately 70% of the world's supply [8]. Limited production also occurs in several other countries, including Iran, India, Egypt, Morocco, France, Afghanistan, Saudi Arabia, and China. The primary species cultivated in Bulgaria, Turkey, and Iran is *R. damascena*, whereas *Rosa centifolia* L. is prevalent in Morocco, Egypt, and France. Dobreva *et al.* [9] revealed that the chemical composition of rose oil from Saudi Arabia ranges widely depending on the local traditions of growing and processing oil-bearing rose. The distillation technology and rigor of process control are critical determinants of oil quality, alongside the influence of the specific growing micro-region.

* To whom all correspondence should be sent:
Email: *rayna.nenova@gmail.com*
*dr.kkalinov@gmail.com*

No published data exist on the essential oil of *R. damascena* Mill. cultivated in Japan. Therefore, we aimed to study and compare the rose oil obtained from Bulgarian-origin *R. damascena* Mill. cultivated in Japan with the one produced in Bulgaria. For this reason, we were particularly interested in growing *R. damascena* Mill. on two private fields - of Mr. Shimazaki in Kazanlak, Bulgaria, and of Mr. Yosuke in Yamagata, Japan.

## EXPERIMENTAL

### *Plant material*

Rooted stem cuttings of *R. damascena* Mill. (supplied by the Institute of Roses and Aromatic Plants, Agricultural Academy, Kazanlak, Bulgaria) were planted in two private rose fields: one in Kazanlak, Bulgaria (42°31′35.8″N, 25°19′39.5″E) and another in Yamagata, Japan (38°32′03.3″N, 140°23′37.5″E; Japanese Rose Valley). After five years of growth, rose blossoms were harvested during the flowering period (May–June 2024).

### *Rose oil production*

The rose oils were obtained through the classical Bulgarian water steam distillation method in a 0.5 $m^3$ industrial still of the fresh flowers, as described by Dobreva and co–workers [1].

The rose oil from Japan was obtained in a small distilling equipment – laboratory module with the volume of the still 0.1 $m^3$. The water cooler has a volume of 0.62 $m^3$ and the florentine vessel has a volume of 0.007 $m^3$. Briefly, 8 kg of fresh rose flowers were added to 50 L of water and boiled under high pressure steam 0.5 – 0.7 MPa. The first 10 L of the distillate were kept as a final product and the next 5 L were put back to the tank for second distillation. The duration of one cycle was about 90 – 120 min. The yield of both essential oils was calculated on a dry weight basis - $Y_{dw}$ (%), using the following formula: $Y_{dw}$ (%) = ($V_{oil} \times \rho_{oil}$/ $W_{dry}$) × 100, where: $V_{oil}$ - volume of the obtained essential oil (ml); ρ - density of the essential oil (g/ml); $W_{dry}$ - dry mass of the plant material, calculated as $W_{fresh} \times (1 - MC)$, $W_{fresh}$ –mass of the fresh flowers; MC - moisture content (%) = [($W_{fresh}$ - $W_{dry}$) / $W_{fresh}$] × 100, expressed as a decimal (0.85 for 85%).

The essential oil yield, calculated on a dry weight basis, was determined to be 0.191% (w/w) for the Bulgarian rose oil and 0.07% (w/w) for the Japanese rose oil. Rose oils were stored in a refrigerator at 4°C in the dark, in non-transparent containers.

To measure the density of rose oils a pycnometer acc. to Gay-Lussac, volume 1 ml, was used. The study of refractive index was conducted on cutting oil refractometer PAL-102S.

### *Gas chromatographic (GC–FID) analysis*

The GC analysis of both essential oils was performed on an Agilent 7820A GC–FID system.

Standard calibration mixture of n–alkanes $C_8$–$C_{27}$ in hexane ≥ 98% (Honeywell, Riedel–de Haën TM) was used for quantification of major and minor components. The GC system was equipped with the non–polar capillary column EconoCapTM ECTM–5 (30 m × 0.32 mm × 0.25 µm film of 5% phenyl, 95% methylpolysiloxane). The split ratio was 1:10, the inlet temperature – 250°C, and the FID temperature was set from 60°C to 300°C through a controlled program. Synthetic air (mixture of nitrogen ($N_2$) – 80% and oxygen ($O_2$) – 20%) was used as a carrier gas and hydrogen (99.999%) for the FID. Data were processed using Agilent chromatography data systems (CDS) software – Open Lab CDS – Agilent RapidControl.NET.

The identification of the compounds was performed using retention times and authentic references. The quantification of the main compounds was carried out by peak area without correction factor.

### *Statistical analysis*

We firstly made a test for normality – Shapiro–Wilkson – for every single parameter of the climate features for the two locations, Kazanlak, Bulgaria, and Yamagata, Japan, followed by a Fisher test (F–test) for the variance of all pairs of parameters of the climate for the two locations. Then we proceeded with the t–test to prove the significant difference between the parameters of climate of the two locations at the 99.999 level of confidence.

Hypothesis test was used to compare paired binomial proportion, based on differences in the relative percentage concentrations (calculated by peak area without correction factor) of aroma compounds of the studied rose oils obtained from *R. damascena* Mill. produced in Kazanlak – Bulgaria, and in Yamagata Japan, by two similar methods of distillation: classical Bulgarian technology and traditional Bulgarian technology.

All analyses were performed using R–4.4.1 (R Core Development team 2024, Copyright © 2021–2025 R Core Team) and RStudio version 2024.09.0–375.

## RESULTS AND DISSCUSION

### *Influence of climate and environmental conditions*

The most dynamic climate components that have a direct impact on the development of the oil–bearing rose are the air temperature and annual precipitation amounts. For example, the Kazanlak oil–bearing rose withstands low temperatures in winter down to minus 28.0°C. After the start of sap flow, depending on the degree of development, it freezes at temperatures from minus 5 to minus 10°C. Frosts occur in autumn–winter and winter–spring [7].

*R. damascena* Mill. flowers from early May to early June in Rose Valley of Bulgaria. Exact flowering time depends upon prevailing temperature in the locality The total period of of the flowering is about 25 – 35 days, the major part of the yield (about 75%) being obtained within 15 days of peak flowering period.

Yamagata City, known as Japanese Rose Valley, is located in the Tohoku region of northern Honshu, Japan. It has a humid continental climate, closely bordering on humid subtropical climate with large seasonal temperature differences, with warm to hot (and often humid) summers and cold (sometimes severely cold) winters. Precipitation is significant throughout the year, and is heaviest from July to September.

The climate characteristics of the regions where oil—bearing *R. damascena* Mill. was grown: Kazanlak (Bulgaria) and Yamagata (Japan) are summarized in Table 1.

**Table 1.** Climatic characteristics (weather by month/weather averages) in Kazanlak, Bulgaria, and Yamagata, Japan [10].

| | Jan. | Feb. | March | April | May | June | July | Aug. | Sept. | Oct. | Nov. | Dec. |
|---|---|---|---|---|---|---|---|---|---|---|---|---|
| **Avg. T ( °C )** | | | | | | | | | | | | |
| Kazanlak | 0.1 °C | 2.1 °C | 6.2 °C | 11.2 °C | 16 °C | 19.9 °C | 22.2 °C | 22.4 °C | 17.8 °C | 12.1 °C | 7.1 °C | 1.9 °C |
| Yamagata | -2.1 °C | -1.6 °C | 1.9 °C | 8.1 °C | 14.3 °C | 18.5 °C | 22.1 °C | 23.2 °C | 19.1 °C | 12.9 °C | 6.6 °C | 0.9 °C |
| **Min. T (°C)** | | | | | | | | | | | | |
| Kazanlak | -3.4 °C | -1.8 °C | 1.6 °C | 6.1 °C | 10.9 °C | 14.9 °C | 17.1 °C | 17.4 °C | 13.3 °C | 8.2 °C | 3.7 °C | -1.1 °C |
| Yamagata | -5.4 °C | -4.9 °C | -1.7 °C | 3.3 °C | 9.4 °C | 14.5 °C | 18.8 °C | 20 °C | 15.9 °C | 9.3 °C | 3.2 °C | -2.1 °C |
| **Max. T (°C)** | | | | | | | | | | | | |
| Kazanlak | 4.1 °C | 6.3 °C | 11 °C | 16.1 °C | 20.7 °C | 24.3 °C | 26.8 °C | 27.2 °C | 22.3 °C | 16.4 °C | 11.1 °C | 5.5 °C |
| Yamagata | 1.3 °C | 2.3 °C | 6.3 °C | 13.6 °C | 19.6 °C | 23.1 °C | 26 °C | 27.3 °C | 23.1 °C | 17.2 °C | 11 °C | 4.4 °C |
| **Rainfall mm** | | | | | | | | | | | | |
| Kazanlak | 53 | 50 | 65 | 72 | 101 | 85 | 75 | 53 | 56 | 60 | 58 | 65 |
| Yamagata | 139 | 101 | 115 | 99 | 94 | 128 | 179 | 151 | 133 | 125 | 103 | 129 |
| **Humidity(%)** | | | | | | | | | | | | |
| Kazanlak | 78 | 75 | 71 | 69 | 71 | 71 | 66 | 63 | 67 | 75 | 79 | 79 |
| Yamagata | 83 | 81 | 76 | 74 | 76 | 81 | 87 | 85 | 85 | 83 | 84 | 83 |
| **Rainy days (d)** | | | | | | | | | | | | |
| Kazanlak | 6 | 6 | 8 | 9 | 11 | 10 | 8 | 6 | 6 | 5 | 6 | 7 |
| Yamagata | 18 | 14 | 13 | 10 | 9 | 11 | 13 | 11 | 10 | 9 | 12 | 16 |
| **avg. Sun hours (h)** | 5.0 | 5.5 | 7.1 | 9.3 | 10.5 | 11.6 | 11.9 | 11.4 | 9.0 | 6.4 | 5.0 | 4.9 |
| Kazanlak | 3.7 | 4.2 | 5.6 | 7.1 | 8.0 | 7.0 | 6.2 | 6.4 | 5.7 | 5.1 | 4.4 | 3.8 |
| Yamagata | | | | | | | | | | | | |

**Table 2.** Physicochemical properties of *R. damascena* Mill. rose oil from Bulgaria (BG) and Japan (JPN).

| **Characteristics** | **Requirements / ISO 9842:2024 test method** | **BG rose oil** | **JPN rose oil** |
|---|---|---|---|
| Appearance | Liquid or more or less crystallized / – | Liquid or more or less crystallized | Liquid or more or less crystallized |
| Color | Light yellow / – | Colorless to pale yellow liquid | Colorless to pale yellow liquid |
| Odor | Floral, rosy / – | Fresh, floral rose odor | Light scent of roses |
| Relative density at 25 °C | 0.8480 to 0.8800 /ISO 279 | 0.864 | 0.889 |
| Refractive index at 25°C | 1.450 to 1.468 /ISO 280 | 1.463 | 1.451 |
| Freezing point | Range from + 16°C to 23.5°C /ISO 1041 | 16 | 19 |

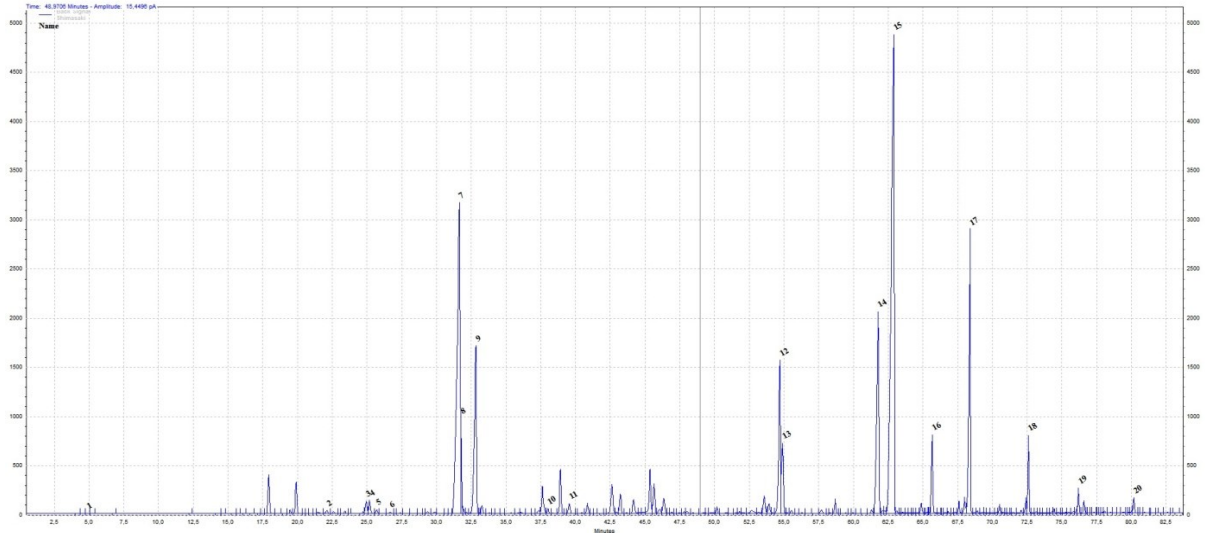

(A) Chromatographic profile of *R. damascena* Mill. essential oil from Bulgaria

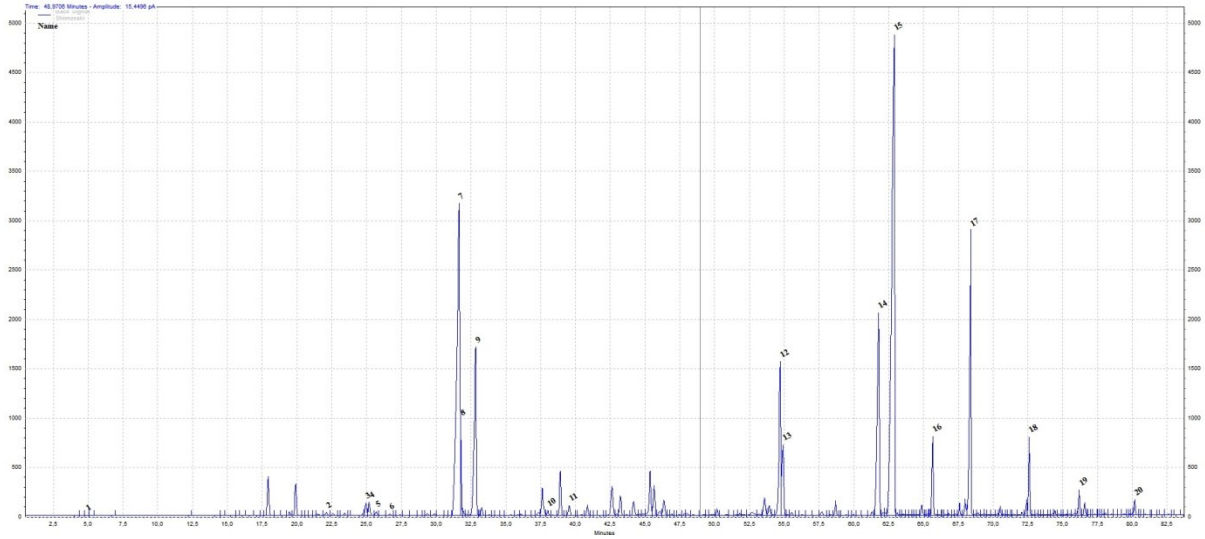

(B) Chromatographic profile of *R. damascena* Mill. essential oil from Japan

**Fig. 1.** Chromatographic profile of *R. damascena* Mill. essential oil from (A) Bulgaria (BG) and (B) Japan (JPN): x–axis – retention time (RT) – minutes; y–axis – picoamperes (pA). Sequence number by retention time of identified compounds: 1 – ethanol; 2 – limonene; 3 – linalool; 4 – phenylethanol; 5 – *cis*–rose oxide; 6 – *trans*–rose oxide; 7 – citronellol; 8 – nerol; 9 – geraniol; 10 – eugenol; 11 – methyl eugenol; 12 – heptadecane; 13 – farnesol; 14 – nonadecene; 15 – nonadecane; 16 – eicosane; 17 – heneicosane; 18 – tricosane; 19 – pentacosane; 20 – heptacosane.

Sharpio–Wilxon test showed that every single parameter of the climate for the two locations is with normal distribution (p–value > 0.05). The results from the F–test showed that all pairs are with equal variance for the two locations, (p–value > 0.05). The results of the independent t–test for all pairs of parameters of the climate showed a significant difference at a confidence level of 99.999 for humidity, rainy days and mm rainfall. There is no significant difference between the temperatures in Kazanlak and Yamagata at a confidence level of 99.999.

These findings underscore the distinct climatic regimes of the two regions, with Yamagata's consistently higher humidity and precipitation levels contrasting sharply with Kazanlak's more variable and temperate conditions. Such differences may have implications for agricultural practices, particularly in crops sensitive to moisture, such as *Rosa damascena* Mill.

### *Soil characteristics*

*R. damascena* Mill. in Bulgaria grows well on silty clay loam to sandy loam soils. It withstands a wide range of soil pH conditions from 6 to 8. Irrigation is necessary in the rose plantation at a frequency of 12–15 days during peak periods.

Yamagata is located in a valley that is surrounded to the east by the Ohu Mountains and to

the west by the Echigo Mountains. Yamagata's soil is brown forest soil with a lower humus horizon.

*Rose oil characteristics*

The traditional method of rose oil production in Bulgaria involves water steam distillation of rose flowers, followed by cohobation of the resulting distillate.

The marked difference in dry weight yield – 0.191% (w/w) for Bulgarian oil *versus* 0.07% (w/w) for Japanese oil – reflects the influence of processing technology, environmental conditions, and seasonal factors. Table 2 displays the physicochemical properties of *R. damascena* Mill. rose oil from Bulgaria (BG) and Japan (JPN).

*GC–FID analyses of rose oil. Comparison of the chemical compositions of rose oils from Bulgaria and Japan*

The rose oils from the private field of Mr. Takeshi Shimazaki in Bulgaria and those obtained from the field of Mr. Sato Yosuke in Japan were chemically characterized and the chromatographic profiles were compared. The results of both chromatograms are displayed on Table 3.

The compositions of Bulgarian and Japanese rose oils differed significantly. The main aroma components of rose oil – monoterpene alcohols, constituted over 65% of total 20 identified substances in the Bulgarian oil, but only 26% in the Japanese oil.

This aligns with previous studies. Dobreva and co-workers [12] demonstrated that oxygenated monoterpenes are the primary aroma substances in *R. damascena* Mill. essential oil, comprising 70% of all identified components. According to Topalov [13], these are L-citronellol, geraniol, and nerol, which together form the eleopten portion of the rose oil.

A direct comparison of the relative percentages for these key compounds and the major stearoptenes for Bulgarian and Japanese rose oils is as follows: geraniol (22.48 *vs*. 7.05), citronellol (39.18 *vs*. 17.91), and nerol (4.46 *vs*. 1.5), followed by the stearopten fraction: nonadecane (14.89 *vs.* 26.31), nonadecene (0.83 *vs.* 7.38), heneicosane (4.12 *vs*. 8.36) and heptadecane (2.14 *vs*. 5.29).

These compositional deviations indicate that the Japanese rose oil does not comply with the international ISO 9842 standard [11], whereas the Bulgarian oil aligns with it. It should be noted that this work represents the first successful cultivation and chemical characterization of *Rosa damascena* Mill. in Japan. A striking feature of the Japanese oil is its inverse deviation: its aroma compounds are sub-standard, while its stearoptene fractions are supra-standard.

We compared our results with those obtained earlier by Dobreva and Nedeltcheva-Antonova [14], who studied the chemical profiles of *R. damascena* Mill. cultivated in China, as well as their data for seven *R. damascena* Mill. essential oil samples collected from three main rose production micro-regions: Al-Taif, Al-Shafa, and Al-Hada in Saudi Arabia [9].

The data for Chinese oil revealed a total amount of the main terpene alcohols citronellol, nerol, geraniol on average of 52.35 %. The quality of rose oil is predominantly determined by the content and ratio of its main constituents [15]. Furthermore, Ohhloff [16] emphasized that minor components are also critical for defining its unique flavor and fragrance.

A comparative summary of the compositional data for the Bulgarian (BG), Japanese (JPN), Chinese (CHN), and Saudi Arabian (SA) rose oils (in relative %) is presented below: citronellol (39.18 / 17.91 / 36.69 / 19.64 – 28.13), nerol (4.46 / 1.5 / 5.94 / 7.02 – 14.27), geraniol (22.48 / 7.05/ 7.64 /18.29 – 27.23), followed by the stearopten fraction: heptadecane (2.14 / 5.29 / 1.67 / 1.46 – 3.25), nonadecene (0.83 / 7.38 /4.28 / 2.47 – 4.94), nonadecane (14.89 / 26.31 / 11.08 / 6.72 – 16.52), heneicosane (4.12 / 8.36 / 6.71 / 1.33 – 4.16).

This comparison reveals a remarkable singularity. Both the eleopten and stearopten profiles of the Chinese *R. damascena* Mill. oil are close to the Bulgarian benchmark, excluding geraniol, which is sub-standard. The SA oil is also close to the Bulgarian one, although, both CHN and SA oils do not meet the standard. In contrast, the Japanese oil exhibits inverse deviation: its aroma compounds are sub-standard, while its stearoptene fractions are supra-standard.

These findings place a new standpoint within the existing global spectrum of rose oil compositions. The observed variability is likely attributable to specific geographical conditions and processing methods. Comparative studies are needed to define the specific scenarios and applications where one oil may be more advantageous than the other.

Employing advanced chromatographic techniques, e.g., high-resolution mass spectrometry (HRMS), or enantio-multidimensional gas chromatography (MDGC) would be highly valuable to elucidate the complete profile of trace compounds, which could provide further insight into the oil's origin and subtle bioactivities [17].

**Table 3.** Retention time, relative percentage and retention index for 20 rose oil compounds from Bulgaria and Japan analyzed on a non–polar column EconoCapTM ECTM–5 with GC–FID. RVs–reference values of the main rose oil compounds described in the International Standard ISO 9842:2024 [11]. Relative % – area percentage – the amount of each compound in a mixture, calculated by the ratio of the area of the component to the total area; $RI_{Cal}$ depicts the calculated RI values, while $RI_{Lit}$ are the ones obtained from literature (NIST database).

| Sequence number by retention time (№) | Compound (RVs–ISO 9842:2024) | Primary Functional Group | Chemical Family / Sub–Class | Retention Time (RT) BG | Relative % BG | $RI_{Cal}/RI_{Lit}$ BG | Retention Time (RT) JPN | Relative % JPN | $RI_{Cal}/RI_{Lit}$ JPN |
|---|---|---|---|---|---|---|---|---|---|
| 1 | Ethanol (≤ 3.0 %) | Alcohol | Primary Alcohol | 4.94 | 0.46 | NA | 4.84 | 0.00 | NA |
| 2 | Limonene | Hydrocarbon (Alkene) | Monoterpene Hydrocarbon | 21.81 | 0.02 | 1027/1020 | 22.11 | 0.12 | 1023/1020 |
| 3 | Linalool | Alcohol | Monoterpene Alcohol | 25.14 | 0.38 | 1105/1100 | 24.94 | 0.39 | 1098/1100 |
| 4 | Phenylethanol (≤ 2.5 %) | Alcohol | Aromatic Alcohol | 25.39 | 0.73 | 1096/1073 | 25.18 | 0.46 | 1092/1073 |
| 5 | *Cis*–rose oxide | Ether | Cyclic Ether (Pyran) | 25.9 | 0.10 | 1106/1097 | 25.69 | 0.12 | 1104/1097 |
| 6 | *Trans*–rose oxide | Ether | Cyclic Ether (Pyran) | 26.8 | 0.05 | 1110/1079 | 26.64 | 0.06 | 1102/1079 |
| 7 | Citronellol (20.0–34.0 %) | Alcohol | Monoterpene Alcohol | 31.9 | 39.18 | 1158/1150 | 31.65 | 17.91 | 1155/1150 |
| 8 | Nerol (5.0–12.0 %) | Alcohol | Monoterpene Alcohol | 32.02 | 4.46 | 1231/1220 | 31.75 | 1.50 | 1234/1220 |
| 9 | Geraniol (14.0–22.0 %) | Alcohol | Monoterpene Alcohol | 33.15 | 22.48 | 1234/1245 | 32.84 | 7.05 | 1233/1245 |
| 10 | Eugenol | Alcohol (Phenolic) | Allylphenol, Phenylpropanoid | 37.9 | 1.08 | 1361/1350 | 37.62 | 1.02 | 1359/1350 |
| 11 | Methyl eugenol (0.8–3.0 %) | Ether (Methoxy) | Phenylpropanoid | 39.7 | 0.57 | 1369/1368 | 39.55 | 0.32 | 1367/1368 |
| 12 | Heptadecane (1.0–2.5 %) | Hydrocarbon (Alkane) | n–Alkane (Saturated) | 54.7 | 2.14 | 1705/1700 | 54.71 | 5.29 | 1702/1700 |
| 13 | Farnesol | Alcohol | Sesquiterpene Alcohol | 54.39 | 0.55 | 1672/1667 | 54.89 | 2.26 | 1668/1667 |
| 14 | Nonadecene (1.5–4.0 %) | Hydrocarbon (Alkene) | n–Alkene (Unsaturated) | 61.74 | 0.83 | 1877/1875 | 61.78 | 7.38 | 1879/1875 |
| 15 | Nonadecane (8.0–15.0 %) | Hydrocarbon (Alkane) | n–Alkane (Saturated) | 62.81 | 14.89 | 1903/1900 | 62.9 | 26.31 | 1902/1900 |
| 16 | Eicosane | Hydrocarbon (Alkane) | n–Alkane (Saturated) | 65.74 | 1.79 | 1998/2000 | 65.67 | 1.83 | 2002/2000 |
| 17 | Heneicosane (3.0–5.5 %) | Hydrocarbon (Alkane) | n–Alkane (Saturated) | 68.38 | 4.12 | 2105/2100 | 68.39 | 8.36 | 2101/2100 |
| 18 | Tricosane | Hydrocarbon (Alkane) | n–Alkane (Saturated) | 72.64 | 0.29 | 2308/2300 | 72.59 | 1.52 | 2305/2300 |
| 19 | Pentacosane | Hydrocarbon (Alkane) | n–Alkane (Saturated) | 76.24 | 0.08 | 2513/2500 | 76.19 | 0.49 | 2509/2500 |
| 20 | Heptacosane | Hydrocarbon (Alkane) | n–Alkane (Saturated) | 80.26 | 0.07 | 2711/2700 | 80.18 | 0.38 | 2708/2700 |

### *Statistical analysis*

Main advantage of using a hypothesis test for paired binomial proportion compared to the other statistical tests is the control for within–sample variability, which is the difference in mixture concentrations due to sample handling. Other is the disadvantage of independent tests (e.g., chi–square) assuming unrelated groups, increasing false positives if pairs are correlated.

We used a hypothesis test for paired binomial proportion test to compare the relative percentage concentrations of compounds of rose oil produced by classical technology (industrial with cohobation and semi-industrial distillation) from *R. damascena* Mill. grown in Bulgaria, and those obtained from

the same roses grown in Japan. We included the following components (Table 2, column 1 – sequence number by retention time: RT 1 – ethanol; RT 4 – phenylethyl alcohol, RT 7–citronellol, RT 8–nerol, RT 9– geraniol, RT 10–eugenol, RT 11 – methyl eugenol. On the other hand, only five of these components in Japanese rose oil, RT 2 – limonene, RT 3 – linalol, RT 4 – *cis*–rose oxide, RT 5 – *trans*–rose oxide, RT 13 – farnesol, have higher percentage concentrations than those in Bulgarian rose oil, as can be seen from the graph in Fig. 2 illustrating these differences. Using this approach, we calculated that there are seven "superior" for the 12 trails, corresponding to the main identified eleopten components for Bulgarian rose oil. It was estimated for this sample that the Bulgarian rose oil can be assessed as 58.3%, with a p–value = 0.7744 which is greater than 0.05, so we reject the null hypothesis with 95% significance level, there is significant difference between the two oils. The Bulgarian rose oil is superior to Japanese oil when calculating probability of superiority based on the difference between relative concentrations.

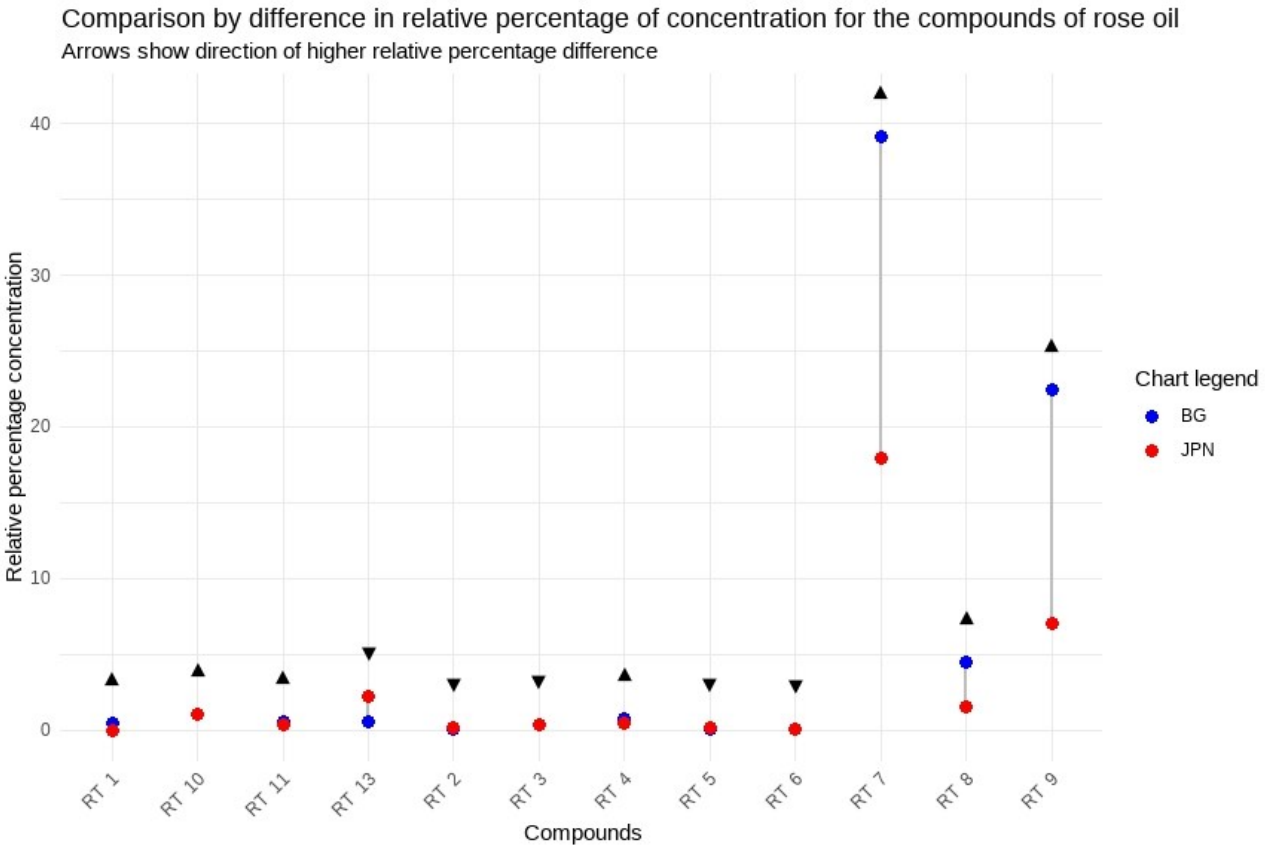


**Fig. 2.** Graph depicting the binomial test comparing the percentage differences in relative percentage concentrations of components from the eleopten group for rose oils from Bulgaria and Japan.

As easily noticeable from Fig. 2, there are large differences in percentage concentrations of compounds, in which Bulgarian oil significantly exceeds Japanese oil (seven "superior" against five): RT 7 (citronellol) – 21.27%; RT 9 (geraniol) – 15.43%; RT 8 (nerol) –2.96%; RT 11 (methyl eugenol) – 0.25%; RT 10 (eugenol) – 0.06%.

## CONCLUSION

*R. damascena* Mill. of Bulgarian origin cultivated in Japan produced rose oil displaying markedly different chemical composition compared to oil distilled in Bulgaria. GC–FID analysis combined with a paired binomial proportion test (95% confidence) showed Bulgarian rose oil to be

superior by 58.3% in eleoptene content. These differences can be primarily attributed to environmental conditions, as Yamagata is characterized by persistently high humidity and rainfall, in contrast to the more moderate climate of Kazanlak. Such climatic disparities, together with soil variability and production technology, strongly influence the growth of *R. damascena* Mill. and the quality of the essential oil. Consequently, Japanese rose oil does not fully meet international standard requirements, underlining the critical role of local ecological factors in rose oil production.

***Acknowledgement:*** *This study of the Institute of Roses and Aromatic Plants was supported by the project: "Selection, variety maintenance, research and enrichment of the gene pool of medicinal and aromatic plants. Modern approaches in the technologies of cultivation, processing and application of their products", granted by the Agricultural Academy, Sofia, Bulgaria.*

REFERENCES

1. A. Dobreva, D. Nedeva, M. Mileva, *Resour.,* **12**, 83 (2023), DOI: https://doi.org/10.3390/resources12070083
2. J. Raeber, C. Steuer, *Anal. Chim. Acta*, **1277**, 341657 (2023), DOI: https://doi.org/10.1016/j.aca.2023.341657
3. T. Gerasimova, S. Gateva, G. Jovtchev, T. Angelova, M. Topashka-Ancheva, A. Dobreva, M. Mileva, *Molecules,* **30**, 78 (2025). DOI: https://doi.org/10.3390/molecules30010078
4. D. Nedeltcheva-Antonova, P. Stoicheva, L. Antonov, *Ind. Crops Prod.,* **108** 36 (2017). DOI: https://doi.org/10.1016/j.indcrop.2017.06.007
5. N. Vilhelmova-Ilieva, R. Nenova, K. Kalinov, A. Dobreva, D. Peshev, I. Iliev, *Int. J. Mol. Sci*., **26**, 9 https://doi.org/10.3390/ijms26157521
6. R. Nenova, K. Kalinov, D. Nedeva, A. Dobreva, N. Vilhelmova-Ilieva, A. Georgieva, I. Iliev, *Curr. Issues Mol. Biol*., **47**, 649 (2025). DOI: https://doi.org/10.3390/cimb47080649
7. V. Staykov, in: Growing of the oil–bearing rose, Zemizdat, Sofia, 1950.
8. N. Kovatcheva, V. D. Zheljazkov, T. Astatkie, *Hort. Science,* **46,** 710 (2011).
9. A. Dobreva, K. Getchovska, D. Nedeltcheva-Antonova, *Flavour Fragr. J.,* **00,** 1 (2020). DOI: https://doi.org/10.1002/ffj.3601
10. Climate data for Kazanlak and Yamagata, accessed on 11 April 2025, https://en.climate–data.org/europe/bulgaria/kazanlak/kazanlak–28264/, https://en.climate–data.org/asia/japan/yamagata–2448/r/january–1/#climate–table–year
11. ISO 9842:2024 Essential oil of rose (*Rosa* x *damascena* Miller). https://www.iso.org/standard/86897.html, accessed on 4. December 2024.
12. A. Dobreva, A. Velcheva, V. Bardarov, K. Bardarov, *Bulg. J. Agric. Sci*., **19(6)**, 1213 (2013).
13. V. Topalov, in: The Kazanlak rose and the rose production in Bulgaria, Christo G. Danov Press, Plovdiv, Bulgaria, 1978, p. 211.
14. A. Dobreva, D. Nedeltcheva-Antonova, *Molecules*, **28**, 1281 (2023). DOI https://doi.org/10.3390/molecules28031281
15. N. Nikolov, A. Tsoutsoulova, N. Nenov, *Med. Biol. Info.*, **2**, 46 (1977).
16. G. Ohhloff, The importance of minor components in flavour and fragrance, VII$^{th}$ Int. Congress Ess. Oils, Kyoto, Japan, 69 (1977).
17. J. Raeber, S. Favrod, C. Steuer, *Plants,* **12**, 506 (2023). DOI: https://doi.org/10.3390/plants12030506.

*Bulgarian Chemical Communications, Volume 58, Issue 1 (pp. 74-84) 2026* *DOI: 10.34049/bcc.58.1.5670*

# Comparative account of biosynthesized zinc oxide nanomaterials from *Cassia tora* for biomedicament

S. A. Gaikwad[1,2*], E. Khatiwora[3], V. Adsul[3], R. Torane[1,2] V. R. Uttam Pandit[4], M. Parthibavarman[5]

[1] *Dr. T. R. Ingle Research Laboratory, Department of Chemistry, S. P. College (Autonomous), Pune-30, India*
[2] *Department of Chemistry, S.P. College Pune, 411030 India*
[3] *Bharati Vidyapeeth (Deemed University) Department of Chemistry, Yashwantrao Mohite College of Arts, Science and Commerce, Kothrude, Pune-38, India*
[4] *Department of Chemistry, The Poona Gujarati Kelvani Mandal's Haribhai V. Desai College, Pune 411002, India*
[5] *PG and Research Department of Physics, Chikkaiah Naicker College, Erode, Tamilnadu, 638004 India*

Received: September 11, 2025; Revised: October 31, 2025

Bio cordial and attuned methodologies were replenished by natural extracts of *Cassia tora (CT)* as efficient stabilizers that prevent an increase in size of zinc oxide nanoparticles. The bioactive metabolites present in the aqueous extracts of stem and flower of plant *cassia tora* improve the biocompatibility and non-toxicity during conversion of metal ions to nanoparticles with zinc acetate at room temperature to form a white suspension of ZnO NPs by maintaining constant pH. Biosynthesized nanoparticles were confirmed by XRD, SEM, EDX, and FTIR techniques. X-ray diffraction results revealed a hexagonal wurtzite structure and SEM analysis showed different morphology, size, and shape. Elemental composition was confirmed by EDX analysis and chemical bond formation of ZnO NPs - by FTIR study. The *in-vitro* free radical scavenging activity of *Ct*-ZnO NPs by DPPH assay showed inhibitory concentration ($IC_{50}$) of 24.31 ± 0.03 µg/ and 42.22 ± 0.03 µg/mL for *Cts*-ZnO NPs and *Ctf*-ZnO NPs, respectively. Antibacterial and antifungal activity showed effective inhibition against three bacteria: *Staphylococcus albus* (NCIM2178), *Proteus mirabilis* (NCIM2388), *Lactobacillu*s and three fungi: *Candida albicans* (NCIM3100), *Penicillium chrysogenum* (ATCC709), *Aspergillus niger* (ATCC504). It was observed that a cluster of rods with flower extract of ZnO NPs and flat thin-layered oval shaped structure was formed with deposition of particles of stem extract of ZnO NPs. The *in-vitro* free radical scavenging activity of Ct-ZnO NPs, *Cts*-ZnO NPS and *Ctf*-ZnO NPs imparts use in biomedical field. Effective inhibition of antibacterial and antifungal activity definitely provokes to carry out further cell line study. Biomedical application against tooth decay was evaluated by the antibacterial activity against *S. mutans* (ATCC25175). *S. mutans* activity of *Cts*-ZnO NPs exhibited noteworthy activity compared to *Ctf*-ZnO NPs which may be due to increased surface area. This study provides a wide window in the prevention of dental caries.

**Keywords:** *Cassia tora*, biosynthesis, free radical scavenging, dental activity

## INTRODUCTION

Nanomaterials are particles at the nanoscale, which have a great impact on applications as small size and large surface area availability enhance catalytic, optical, chemical, and thermal activity [1]. Various reports on antimicrobial activity of human pathogens open up a window for NPs started being considered as nano antibiotics [2]. Two clear approaches have been suggested for nanoparticle synthesis: The top–down approach is costly and slow as it involves synthesis of large-scale particles reduced to nano size [3]. Till now, various methods were reported for the preparation of ZnO NPs as sol-gel, precipitation, spray pyrolysis, microwave-assisted reaction, chemical vapor deposition, ultrasonic condition [4–10].

These methods involve toxic chemicals which may lead to risk. Biosynthesis of nanoparticles is an approach of synthesizing nanoparticles using microorganisms and plants having biomedical applications. This one-step easy approach is environment-friendly, cost-effective, biocompatible, safe, and green [11]. Reported green synthesis involves the use of plants, bacteria, fungi, algae, etc. They allow large-scale production of NPs free of impurities [12]. Plant parts like roots, leaves, stems, seeds, fruits have also been utilized for NPs synthesis as their extracts are rich in phytochemicals which act as both reducing and stabilizing agents [13–19].

Synthesis of NPs from inorganic metal oxides such as $TiO_2$, CuO, and ZnO pull maximum interest in recent studies. Among them, ZnO NPs are of special interest because they are inexpensive to produce, safe and easy to prepare [20–27]. US FDA has enlisted ZnO as a GRAS (generally recognized as safe) metal oxide [28]. ZnO NPs exhibit tremendous applicability to mankind [29–36].

* To whom all correspondence should be sent:
Email: *suchetag2000@gmail.com*

### *Green synthesis of ZnO NPs with Cassia fistula, Trifolium pratense, Ocimum basilicum and Laurus nobiis [37–48]*

*Cassia tora* (*Leguminosae*) is a wild weed growing in most parts of India. In Ayurveda, this plant is used as laxative, antiperiodic, anthelmintic, ophthalmic, liver tonic, cardiotonic medicament, also useful in leprosy, ringworm, dyspepsia, constipation, cough, bronchitis, cardiac disorders [49, 50].

The objective of this work was to explore the structural and biomedical properties of biosynthesized ZnO NPs from an aqueous extract of *Cassia tora* flowers and stems along with zinc acetate as precursor.

## MATERIALS AND METHOD

### *Materials*

Medicinal plant species *Cassia tora* was collected from Western Pune Maharashtra, India. It was authenticated by the Botanical Survey of India, Pune (Maharashtra) with authentication number of *Cassia tora* BSI/WC/Cert/2015/SG01. The precursors zinc acetate and sodium hydroxide were provided from Merck India.

### *Preparation of flower and stem extract and synthesis of zinc oxide nanoparticles*

Biogenic way to synthesize *Ct*-ZnO nanoparticles involves 2 g of air shade-dried powdered plant material of 100 mesh size stored at room temperature in an air-tight container utilizing separately stem and flower in 50 ml of distilled water boiled for 20 min. This extract was allowed to cool and then filtered. 0.1 g of semisolid extract in 20 ml of distilled water was utilized for synthesis of zinc oxide nanoparticles as prescribed previously [37].

Twenty ml of 0.2 M zinc acetate was added to 20 ml of extract (0.1g/20ml) at room temperature, to this solution 0.4 M NaOH (approx. 9-10 ml) was added till pH 12 controlled using a calibrated pH meter. This blend was stirred with a magnetic stirrer at room temperature 25 ± 2 °C for 2 h, which resulted in the formation of a white suspension. The product was then centrifuged at room temperature 25 ± 2 °C at 5000 rpm for 20 min, washed with distilled water, filtered and kept overnight at 60°C in an oven. The product was stored in an air-tight container for further work.

### *Characterization of green-synthesized Ct-ZnO nanoparticles*

Crystallinity of green-synthesized *Ct*-ZnO was observed on an X-ray advanced diffractometer (SC-XRD) with Cu$K_\alpha$ microfocus, Mo fine focus radiation was recorded at 2 theta angles from 200 to 800. Perkin Elmer Spectrum 100 FTIR spectrometer was used in absorbance mode from 4000 to 400 $cm^{-1}$ with resolution of 0.5 $cm^{-1}$ onwards. An overlay of FTIR spectra of synthetically prepared ZnO nanoparticles along with green-synthesized nanoparticles imparts role of reducing agents as biomolecules from extract. Morphological and qualitative, as well as quantitative elemental mapping analysis was accomplished with a field emission scanning electron microscope (FESEM-Nova Nano SEM 450) connected with an energy dispersive X-ray spectroscope (EDS-Bruker XFlash 6130) with excellent energy resolution having 123 eV at Mn$K_\alpha$ and 45eV at C$K_\alpha$. The spectrofluorometric study was carried out on a Shimadzu RF-5301 spectrofluorometer at room temperature at excitation wavelength of 325 nm.

### *Free radical scavenging activity study*

Free radical scavenging activity [51] of green-synthesized ZnO nanoparticles from an aqueous extract of *Cassia tora* was studied to examine the ability to neutralize the 2, 2-diphenyl-1-picrylhydrazyl (DPPH) radical. Various concentrations of *Ct*-ZnO nanoparticles (50, 100, 150, 200, 250, 300 µg/mL) were further diluted with methanol to a final volume of 3 ml. To this mixture 0.15 ml of freshly prepared DPPH solution (100 µM) was added, stirred and kept at room temperature (27°C) for half an hour in dark. The control utilized was DPPH and negative control was methanol. When antioxidants from the sample react, there is a change in color from purple to yellow. Decrease in absorbance was the measure for capacity reduction of DPPH radical. Absorbance was noted by using UV-VIS spectrophotometer at 517 nm.

The free radical scavenging potential was calculated as follows:

Scavenging activity (%) = {(Control abs.—Sample abs.)/Control abs} × 100

The experiments were performed in triplicate and records reported as mean % antiradical activity ± SD. $IC_{50}$ values were calculated from the plotted graph of scavenging activity against the concentrations of the samples. $IC_{50}$ is defined as the total antioxidant essential to reduction of initial DPPH radical by 50%. Linear straight-line equation was utilized to calculate $IC_{50}$ for all ZnO NPs samples based on the percentage of DPPH radicals scavenged. Reference standard as positive control utilized was ascorbic acid with concentrations of 50 to 500 µg/ml per assay.

*Antimicrobial activity*

Plant extracts along with *Ct*-ZnO nanoparticles were subjected to antimicrobial assay by the agar well diffusion method according to the National Committee for Clinical Laboratory Standards (NCCLS) [52]. The extracts were dissolved in dimethyl sulfoxide (DMSO) with different concentrations and inspected for antimicrobial activity using three bacteria: *Staphylococcus albus* (NCIM2178), *Lactobacillus* (isolate from Bhide Foundation), *Proteus mirabilis* (NCIM2388) and three fungi *Penicillium chrysogenum* (ATCC709), *Aspergillus niger* (ATCC504), *Candida albicans* (NCIM3100). Further, the highly potent oral microflora bacterium *S. mutans* (ATCC25175) was scanned for biosythesized ZnO NPs. Potato dextrose agar and Muller Hinton agar plates were prepared by pouring 20 ml of each in sterile Petri plates for fungal and bacterial assay, respectively, and allowed to solidify. Standard cultures of each organism were poured by sterile glass rods to grow in nutrient broth freshly during the assay. DMSO was used as a negative control. The concentration of sample utilized was 3.35 mg/ml and 5 µl of it was used for the study. The positive control utilized was streptomycin 100 µg/mL as a standard. At the end of the incubation period of 24-48 h at 37°C for bacteria and 48-72 h at 20°C for fungi, the inhibition zones were observed in mm. The experiments were carried out in triplicate.

*Antimicrobial assay against S. mutans*

- *Selection of patients*

*Inclusion criteria:* Patients with mixed dentition period of 6 – 12 years DMFT/dmft 4/>4 & having good general health. (Revised WHO criteria 2003).

*Exclusion criteria:* Patients having H/o antibiotic therapy use of chemical anti-plaque agents prior to 6 months of study initiation.

- *Method of saliva collection and storage:* The subjects' informed consent was taken prior to collection of saliva. The subjects were told to sit upright and rinse with water, saliva was allowed to accumulate in the floor of the mouth for approximately 2 min. Then the saliva was spit in a sterile funnel and was collected in a sterile vial. The method was followed to collect samples with 3 ml in an early morning time. Then the samples were diluted in sterile vials containing 1 ml of normal saline and utilized to inoculate on agar plates. The antimicrobial assay was performed as described above.

## RESULTS AND DISCUSSION

*Characterization of ZnO-NPs by X-ray diffraction*

Biosynthesized ZnO NPs clearly indicate crystalline structure by XRD (Figs. 1 & 2).

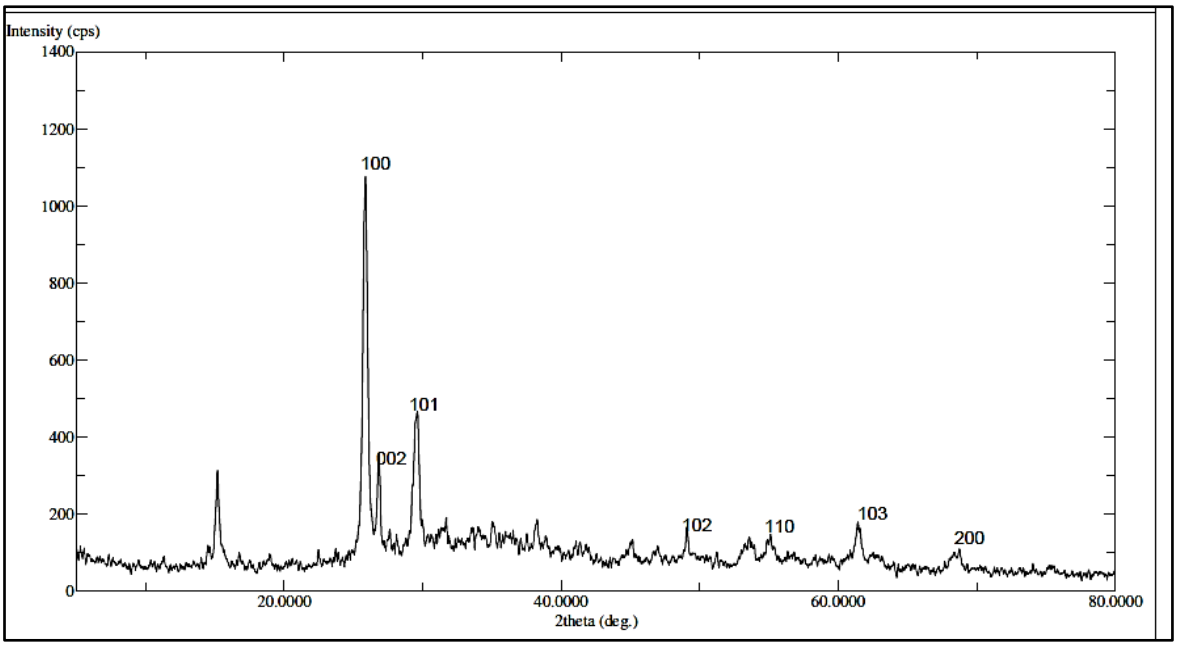


**Fig. 1.** XRD of ZnO NPs prepared from stem extract of *Cassia tora* (*Cts*-ZnO NPs)

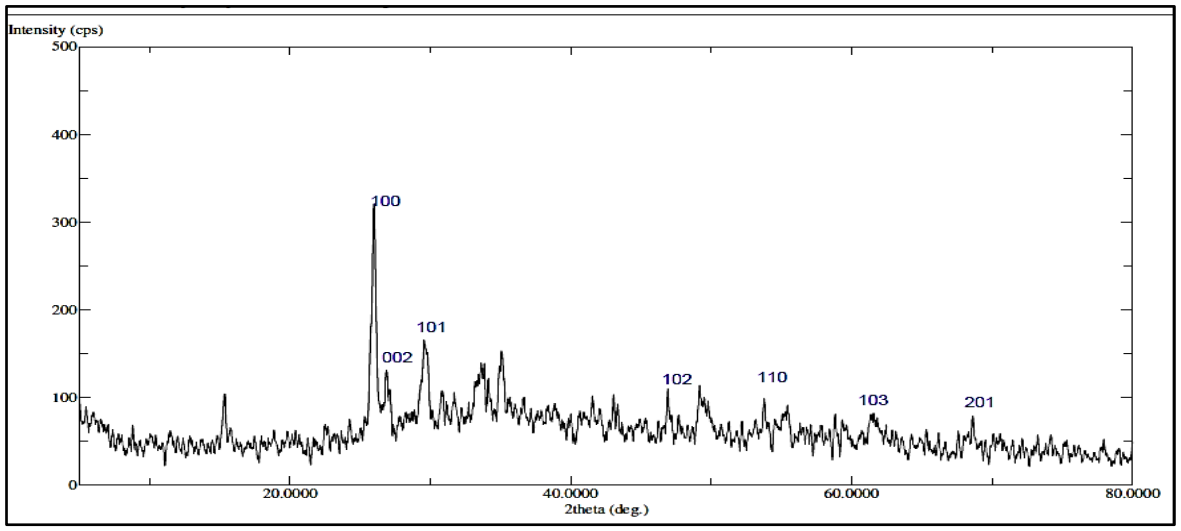


**Fig. 2.** XRD of ZnO-NPs prepared from flower extract of *Cassia tora* (*Ctf*-ZnO NPs)

Sharp diffraction peaks are observed at 2$\theta$ values at 25.86°, 31.70°, 35.04°, 38.28°, 49.08°, 61.42°, 65.78°, 68.00°. The observed peaks are indexed with Miller indices as (100), (002), (101), (102), (110), (103), (112) and (201) endorsed as hexagonal wurtzite phase of ZnO. These peaks are in accordance with diffraction data (JPCDS card number: 36-1451) [53, 54]. The presence of some unsigned small peaks may be due to bioorganic compounds. The average particle size of biosynthesized *Cts*-ZnO NPs and *Ctf*-ZnO NPs was calculated by Debye-Scherrer [55] formula (1):

$$d=0.89\lambda/\beta\cos\theta, \quad (1)$$

where 0.89 is Scherrer's constant, $\lambda$ is the wavelength of X-rays, $\theta$ is the Bragg diffraction angle, and $\beta$ is the full width at half-maximum (FWHM) of the highest diffraction peak corresponding to plane (101). The details of XRD analysis are displayed in Table 1.

**Table 1.** XRD analysis details of biosynthesized ZnO NPs

| Sample[a] | *d*-Spacing (Å) | FWHM[b] | Calculated particle size (nm) |
|---|---|---|---|
| *Cts*-ZnO NP | 3.4424 | 0.329 | 24.16 |
| *Ctf*-ZnO NP | 3.4268 | 0.094 | 84.57 |

[a] Biosynthesized ZnO NPs from *Cassia tora* aqueous extract of stem and flower; [b]Full width at half maximum

*FESEM and EDAX analysis*

Morphological characteristics of green-synthesized ZnO-NPs from *Cassia tora* stem and flower extracts were studied by field emission scanning electron microscopy (FESEM). SEM images under high magnification clearly suggest that particles separation is good enough and particle size is in µm-range forms of *Ctf*-ZnO NPs as clusters of rod-shaped nanoparticles (Figs. 3, 3a). This accumulation is due to polarity and electrostatic attraction. Flat thin-layered oval-shaped structure was observed with particle deposition with weak physical force (Figs. 4, 4a) in *Cts*-ZnO NPs.

EDAX confirmed the presence of elements in both ZnO. Figs. 3a & 4a show the elements responsible for chemical reduction of $Zn^{2+}$ in ZnO-NPs. Corresponding spectrum shows a strong intense peak signal of ZnO nanoparticles at 15 keV to the SPR absorption band for *Ctf*-ZnO-NPs biofabricated from flower extract. Green-synthesized *Cts*-ZnO-NPs from stem extract show intense peak signal. Occurrence of carbon and oxygen elemental peaks influences the biomolecules present in the extract while presence of nitrogen can be assigned to amine functionalization as a capping agent over the surface of nanoparticles. Elemental analysis of ZnO-NPs (Tables 2 & 3) confirms the good agreement between Zn and O.

**Table 2.** Elemental analysis of *Cts*-ZnO NPs

| Element | Series | Weight % | Atomic % |
|---|---|---|---|
| O | K | 45.20 | 16.79 |
| Zn | K | 54.80 | 83.21 |
| Total | | 100.00 | 100.00 |

**Table 3.** Elemental analysis of *Ctf*-ZnO NPs

| Element | Series | Weight % | Atomic % |
|---|---|---|---|
| O | K | 47.43 | 78.66 |
| Zn | L | 52.57 | 21.34 |
| Total | | 100.00 | 100.00 |

**3**

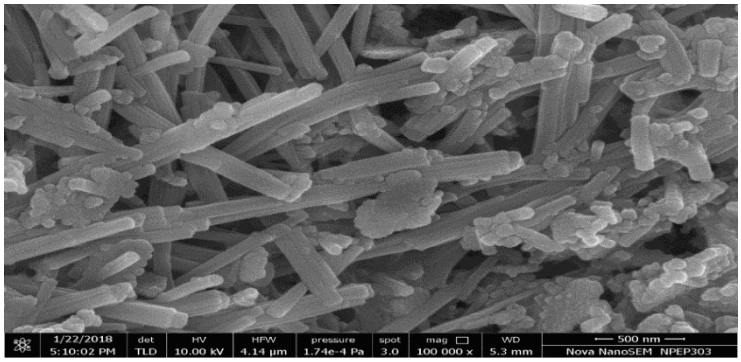


**3a**

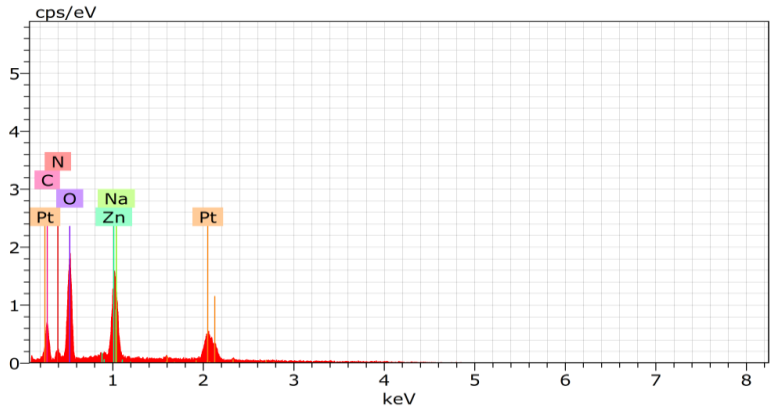


**Fig. 3.** FE-SEM and **Fig. 3a** EDX of synthesized *Cts*-ZnO NPs

**4**

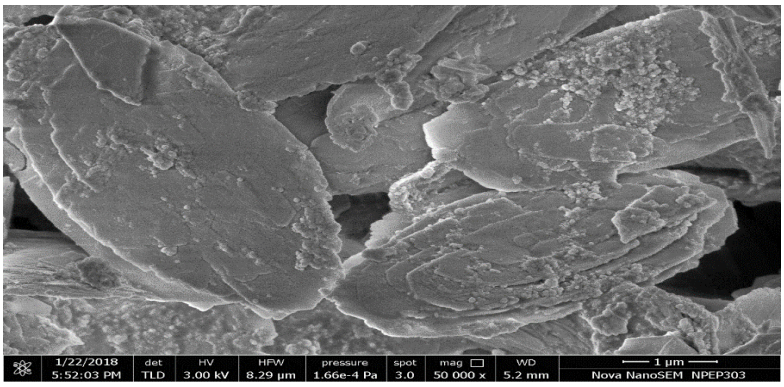


**4a**

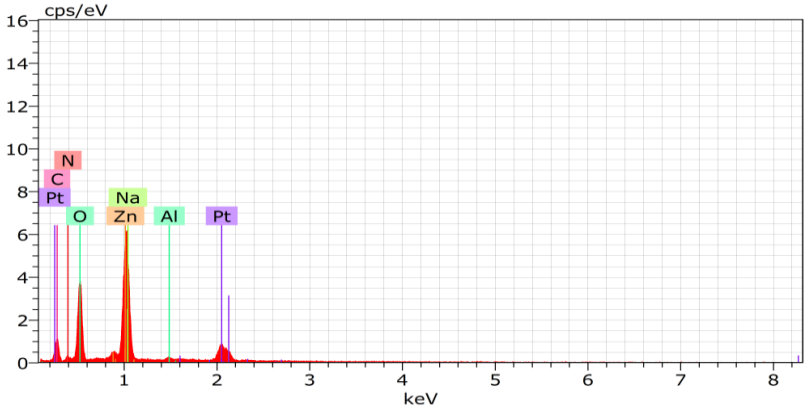


**Fig. 4.** FE-SEM and **Fig. 4a.** EDX of the synthesized *Ctf*-ZnO NPs

### *Fluorescence study*

The XRF spectrum at excitation wavelength 325 nm, shown in Fig. 5, presents the elemental composition profile of the synthesized ZnO nanoparticles. The spectrum exhibits all characteristic emission peaks at 425, 450, 475, 525, 615 nm. The blue emission peak at 425 nm may be due to Zn interstitial defects, the strong blue emission at 450 nm and the weak blue green emission at 475 nm may be due to oxygen vacancy defects formation. Green fluorescence at 525 nm may be due to antisite defect [56].

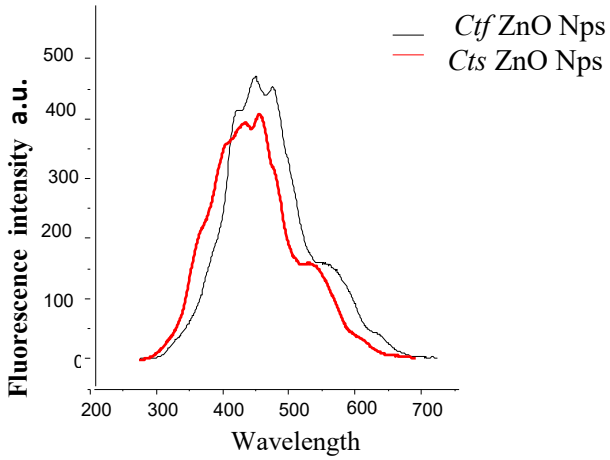


**Fig. 5.** Comparative fluorescence spectra of the prepared *Ctf*-ZnO NPs & *Cts*-ZnO NPs

Enhanced visible emission in fluorescence spectra from green synthesized *Cts*-ZnO NPS and *Ctf*-ZnO NPs shows higher surface defect density correlating to their superior antimicrobial performance, The intense signal at 450 nm strongly suggests that ZnO nanoparticles are the major components of which the flower extract from *Cassia tora* plant was synthesized.

### *Infrared spectroscopy*

The fundamental FTIR reveals the role of phytoconstituents in generation of $Zn^{2+}$ ion nanoparticles. An overlay of FTIR spectra of *Cts*-ZnO-NPs and *Ctf*- ZnO NPs (Fig. 6) was comparatively studied from 500 to 4000 $cm^{-1}$. The peaks observed near 440 $cm^{-1}$, 516 $cm^{-1}$and 650 $cm^{-1}$ impart stretching and vibration of ZnO NPs. The broad absorption peaks at 3122 $cm^{-1}$, 3082 $cm^{-1}$ 3591 $cm^{-1}$, and 3483 $cm^{-1}$ can be assigned to the hydroxyl group stretching. The absorbance peaks at 2887 $cm^{-1}$, 2835 $cm^{-1}$ indicate CH stretching vibration of $CH_3$ and $CH_2$ from lipids. The peaks at 1377 $cm^{-1}$ and 1346 $cm^{-1}$ are referred to CH stretching of aromatic amines and those at 650 $cm^{-1}$, 673 $cm^{-1}$ are accountable to CH bending in alkynes. C–N bonds vibrate at 1022 $cm^{-1}$. The spectral overlay imparts presence of protein and other ligands responsible for the formation and stabilization of ZnO NPs.

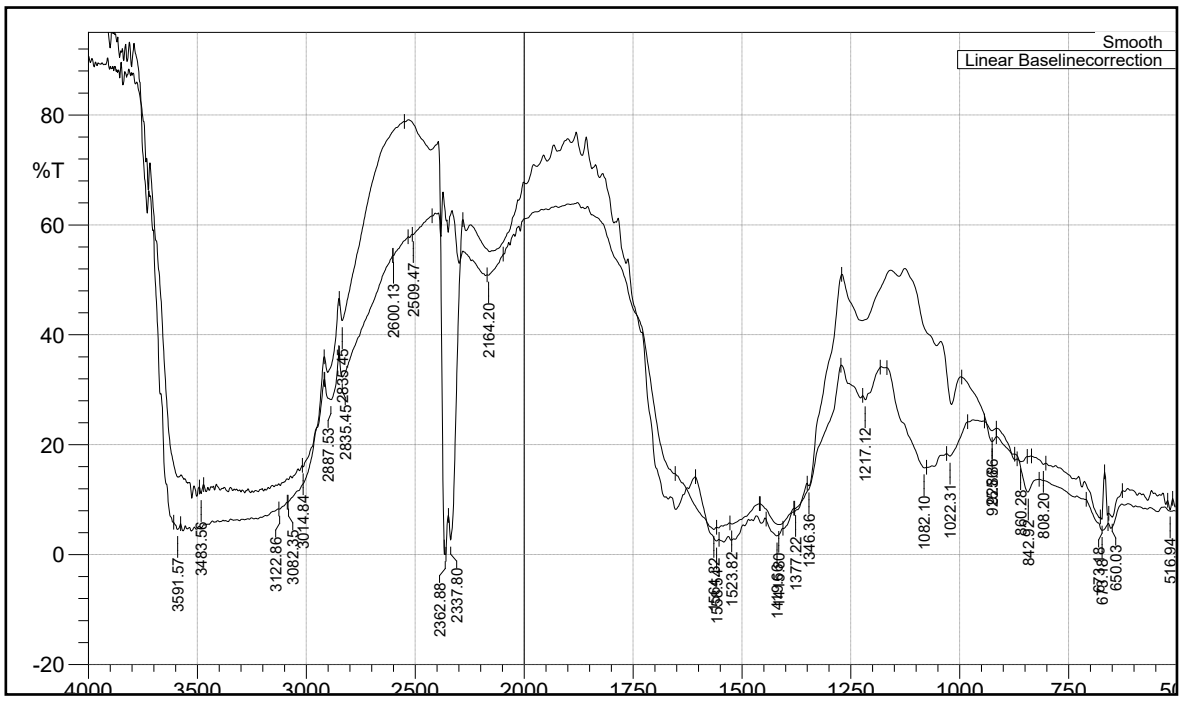


**Fig. 6.** Overlap of IR spectra of *Cts* ZnO Nps and *Ctf* ZnO NPs

*Antioxidant activity of ZnO nanoparticles*

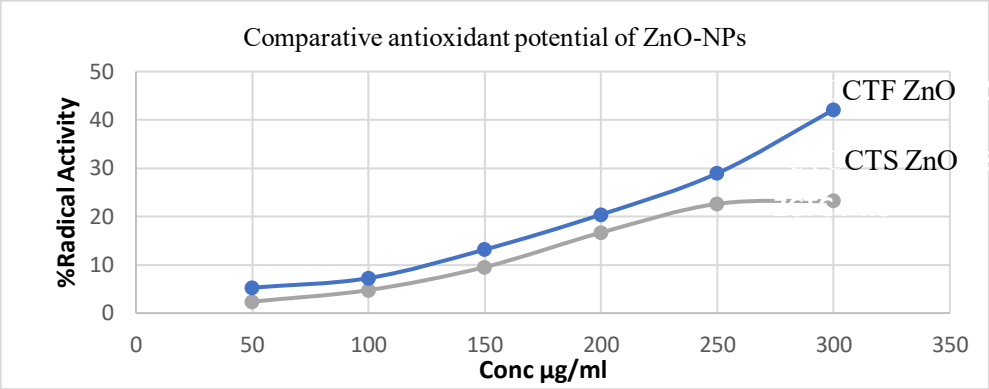


**Fig. 7.** Comparative antioxidant potential of ZnO NPs.

DPPH assay easily imparts free radical scavenging activity [57]. The IC50 values of *Ct*-ZnO NPs are tabulated (Table 4).

**Table 4.** DPPH $IC_{50}$ values of synthesized ZnO-NPs

| Method | $IC_{50}$ values | |
|---|---|---|
| | *Cts*-ZnO NPs | *Ctf*-ZnO NPs |
| DPPH assay | 24.31±0.03 | 42.22 ±0.03 |

IC50 value of ascorbic acid was found to be 29.11 ± 2.35 µg/mL. As the concentration increased from 50 to 300 µg/mL (Fig. 7), the percentage of radical scavenging progressively revealed a concentration-dependent increase in antioxidant activity for both ZnO nanoparticle samples. Among the two samples, *CTF*-ZnO nanoparticles exhibited higher antioxidant activity compared to *CTS*-ZnO across all concentrations. This suggests that the *CTF* extract-mediated synthesis produced nanoparticles with greater surface reactivity, likely due to the presence of phytochemicals acting as capping and reducing agents. The observed difference may also be attributed to variations in particle size, surface area, and defect density, which influence electron transfer processes as aligned with results from structural study. Thus, the enhanced DPPH scavenging efficiency of *CTF*-ZnO indicates its superior capacity to act as antioxidant, making it a promising candidate for biomedical and catalytic applications where oxidative stress mitigation is desired.

*Antimicrobial activity*

Plant extracts medicated with ZnO NPs exhibited good antimicrobial and antifungal activity [58]. Antimicrobial activity was determined on two g of positive strains *Staphylococcus albus* and *Lactobacillus* and one g of negative *Proteus mirabilis* of the prepared ZnO NPs, as well as plant extracts of stem and flower utilizing streptomycin as a standard. Maximum zone of inhibition accounted for minimum inhibitory concentration. The concentration of sample utilized was 3.35 mg/ml and 5 µl of it were used for the study shown in Table 5.

**Table 5.** Average zones of inhibition of *C. tora* extracts and ZnO-NPs against microbial strains

| S.No | Sample name* | A | A.I. | B* | A.I. | C* | A.I. |
|---|---|---|---|---|---|---|---|
| 1 | *Cts* Me | - | - | 11.2 | | - | - |
| 2 | Cts Ac | 8.5 | 0.435 | 7.2 | 0.36 | - | - |
| 3 | Ctf Ac | 9.8 | 0.502 | - | - | - | - |
| 4 | Ctf Me | 7.2 | 0.369 | - | - | - | - |
| 5 | Ctf ZnO-NPs | 9.75 | 0.5 | 11.75 | 0.587 | - | - |
| 6 | Cts ZnO-NPs | 11.2 | 0.574 | 11.5 | 0.575 | 10.8 | 0.54 |
| 7 | Std. (100µg/ml) | 19.5 | N.A. | 20 | N.A. | 20 | N.A. |
| 8 | Solvent DMSO | Nil | N.A. | Nil | N.A. | Nil | N.A. |

A: *Proteus mirabilis* (NCIM2388); B: *Lactobacillus* (isolate from Bhide Foundation)*;* C: *Staphyllococcus albus (NCIM2178);* *Concentration of the sample-3.35mg/ml; **A.I.=Activity Index (*A.I.=Zone of inhibition of sample/ zone of inhibition of the std.)

**Table 6.** Average zone of inhibition of *C. tora* extracts and ZnO-NPS against fungal strains

| S.No | Sample name* | D* | A.I. | E* | A.I. | F* | A.I. |
|---|---|---|---|---|---|---|---|
| 1 | CtsMe | 10.8 | 0.36 | 9 | 0.36 | 7 | 0.233 |
| 2 | CtsAc | 13.5 | 0.45 | 11.5 | 0.383 | 7.2 | 0.24 |
| 3 | CtfAc | 13.75 | 0.458 | - | -- | - | -- |
| 4 | CtfMe | 13 | 0.43 | 8.6 | 0.344 | 9.25 | 0.308 |
| 5 | CtfZnO-NPs | 10.5 | 0.35 | 13 | 0.52 | 10 | 0.333 |
| 6 | CtsZnO-NPs | 10.3 | 0.342 | 8.33 | 0.333 | 10.2 | 0.34 |
| 7 | Std. *Streptomycin* (100µg/ml) | 30 | N.A. | 25 | N.A. | 30 | N.A. |
| 8 | Sol. DMSO | Nil | N.A. | Nil | N.A. | Nil | N.A. |

D: *Candida albicans* (NCIM3100); E: *Penicilium chrysogenum (ATCC709)*; F: *Aspergillus niger (ATCC504);* *Activity Index (A.I.=Zone of inhibition of sample/ zone of inhibition of the std.*)*

*Cts*-ZnO NPs are active and show maximum zone of inhibition against all the three bacteria compared to Ctf-ZnO NPs against *Lactobacillus* and *P. mirabilis*. Green-synthesized ZnO-NPs were effective against microorganisms and this activity depended upon the magnitude of ZnO-NPs. In addition to smaller size, geometric shapes may facilitate greater surface reactions with the target bacteria [59], as flat layered pentagonal structure of *Cts*-ZnO NPs inhibits good activity compared to biosynthesized *Ctf*-ZnO NPs. Further minimum inhibitory concentration studies for *Cts*-ZnO NPs showed 187.5 µg/ml for *P. mirabilis* while 750 µg/ml for *Lactobacillus* and *S. albus.*

### *Antifungal activity*

Antifungal activity study of the prepared ZnO NPs along with plant extracts was tested at 3.35 mg/ml against 3 g of positive bacteria *Penicillium chrysogenum*, *Aspergillus niger* and *Candida albicans* and *Fluconazole* (100 µg/ml) was used as a standard as reported in Table 6. All prepared ZnO NPs inhibited the fungal growth. *Ctf*-ZnO NPs showed maximum zone of inhibition with activity indices of 0.520 against *P. chrysogenum* and 0.350 against *C. albicans*. *Cts*-ZnO NPs exhibited potent activity under similar conditions with maximum zone of inhibition 0.340 against *A. niger*. There is possibility of creating pores at the cell wall to cause membrane damage caused by direct or electrostatic interaction between ZnO and cell surfaces, cellular internalization of ZnO nanoparticles, and production of active oxygen species such as $H_2O_2$ in cells due to metal oxides, as reported in earlier studies [60].

### *Antimicrobial assay against human salivary micro flora*

Dental decay is a chemico-parasitic process in which oral microorganisms play a very pivotal role. Plant extracts, as well as phytoconstituents exhibit prevention of dental plaque and dental caries [23-29]. *S. mutans* is a Gram-positive bacterium having significant contribution towards tooth decay, hence antimicrobial study against the highly potent oral micro flora bacterium *S. mutans* was scanned from 100 to 600 µg/ml. Reported study for the mechanism of action: $Zn^{2+}$ diffusion into a biofilm and a decrease in the rate of plaque growth [61] definitely supports the present study. As reported earlier, the size, morphology and composition of ZnO NPs have a great impact on microbial inhibition [62-65]. Both ZnO NPs prepared by green synthesis show high potency against *S. mutans* (Fig. 8).

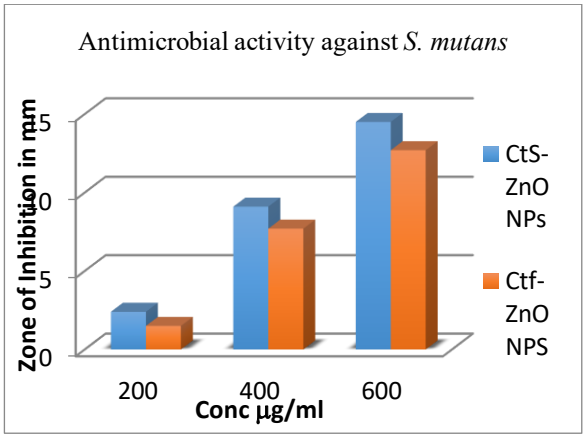


**Fig. 8.** Antimicrobial activity against *S. mutans.*

Maximum zone of inhibition is observed at 600 µg with *Cts*-ZnO NPs compared to *Ctf*-ZnO

NPs. The biosynthesized ZnO NPs can explore the application in the era of oral health for dental plaque, caries sensors of human as a medicament. Further findings for specific age groups are in process.

## CONCLUSIONS

Green synthesis of ZnO nanoparticles was easily carried out using aqueous extracts of the medicinal plant *Cassia tora* utilizing flower and stem parts. The prepared ZnO nanoparticles were characterized by various spectroscopic and imaging techniques. XRD analysis revealed basic crystalline hexagonal wurtzite structure showing intense and sharp peaks. The size and shape of the nanoparticles supported the information obtained by FESEM images. The average crystalline size observed for *Cts*-ZnO NPs 24.166 nm and for *Ctf*-ZnO NPs 84.57 nm agrees well with FESEM observations. Slight peak broadening observed, increases lattice strain which may enhance defect-medicated fluorescence. FESEM images revealed mild agglomeration due to biomolecules which are capping agents from *Cassia tora* extracts. The nanoscale roughness observed may enhance bacterial cell adhesion and reactive oxygen generation contributing to improved antimicrobial activity in *Cts*-ZnO NPs and *Ctf*-ZnO NPs. EDAx spectrum confirms the atomic ratio of Zn:O as 1:1, consistent with stoichiometry. The weak carbon signal detected in FTIR can be contributed to residual organic components from plant-derived phytochemicals acting as capping and stabilizing agent during synthesis. DPPH radical scavenging activity reveals both electron donating oxygen vacancies aligned with the observations from FTIR and fluorescence findings.

Antimicrobial and antifungal activity with long term effect (after 24 h and longer) of prepared *Ct*-ZnO nanomaterials give significant zones of inhibition for Gram-positive and Gram-negative bacteria. Further study against *S. mutans,* a Gram-positive bacterium, having significant contribution toward tooth decay, imparts comparable activity against *Ct*-ZnO NPs. Enhanced visible emission in fluorescence spectra from green-synthesized NPs shows higher surface defect density correlating to its superior antimicrobial performance with regard to *S. mutans*. The implemented method is well suited to nanotechnology with utilization of stem for generation and stabilization of zinc oxide nanoparticles. Novelty of our study lies in oxide nanoparticles using a one-step, biocompatible antimicrobial screening as the findings of the study for oral dental problem support inhibition of major oral microflora. Further cytotoxic study needs to be performed to determine non-cytotoxic dose cell line study for development of human model.

***Acknowledgement:*** *The research was financially supported by the University Grant Commission under Minor Research Project scheme (F.47-1119/14 /General/ 45/ WRO - XII Plan). The authors are thankful to the Head of the Institution S.P. College, Pune-411030, India for providing the necessary facility and Dr. Rahul Deshpande's Oral Health Clinic, India for facilitating activity study research work.*

***Compliance with ethical standards:*** *The study protocol was reviewed and approved by the Institutional Ethics Committee (IEC). Informed of D.Y. Patil Dental College and Dr. Rahul Deshpande's Oral Health Clinic, India for facilitating activity study research work. Patient consent was obtained as the procedure posed no risk to the participants.*

***Conflict of interest:*** *The authors declare no potential conflicts of interest.*

## REFERENCES

1. S. Tabrez, J. Musarrat, A.A. Al-khedhairy, *Colloids Surf. B Biointerfaces*, **146**, 70 (2016) doi:10.1016/j.colsurfb.2016.05.046.
2. M. Sastry, A. Ahmad, M. Islam Khan, R. Kumar, *Curr. Sci*, **85**, 162 (2003) doi:10.1016/S0927-7765(02)00174-1
3. T. Arasu, *J. Biosci. Res.*, **1**, 259 (2010) https://www.researchgate.net/publication/288232479
4. K. Omri, I. Najeh, R. Dhahri, J. El Ghoul, L. Elmir, *Microelectron. Eng*., **128**, 53 (2014) doi:10.1016/j.mee.2014.05.029.
5. A.K. Zak, M.E. Abrishami, W.H. Majidi, R. Abd Yosefi, S.M. Hosseini, *Ceram. Inter*., **37**, 393 (2011) doi: 10.1016/j.ceramint.2010.08.017
6. C.H. Lu, C.H. Yeh, *Ceram. Inter.*, **26**, 351 (2000) doi: 10.1016/S0272-8842(99)00063-2.
7. K. Okuyama, W.W. Lenggoro, *Chem. Eng. Sci*., **58**, 537 (2003) doi: 10.1016/S0009-2509(02)00578.
8. Y.L. Wu, S.C. Liu, *Adv. Mater*., **14**, 215 (2002). doi:10.1002/1521-4095(20020205)
9. Y.L. Wei, P.C. Chang, *J. Phys. Chem. Solids*., **69**, 688 (2008) doi: 10.1016/j.jpcs.2007.07.094
10. Y. Wang, C. Zhang, S. Bi, G. Luo, *Powder Technol*., **202**, 130 (2010) doi: 10.1016/j.powtec.2010.04.027.
11. H. Abdul, R. Sivaraj, R. Venckatesh, *Mater. Lett.*, **131**, 16 (2014) doi: 10.1016/j.matlet.2014.05.033.
12. R. Yuvakkumar, J. Suresh, A.J. Nathanael, M. Sundrarajan, S.I. Hong, *Mater. Sci. Eng*. C., **41**, 17, (2014) doi:10.1016/j.msec.2014.04.025.
13. Y. Zong, Z. Li, X. Wang, J. Ma, *Ceram. Int.*, **40**, 10375 (2014) doi:10.1016/j.msec.2014.04.025.
14. V. Nachiyar, S. Sunkar, *Der Pharma Chem.,* **7**, 31 (2015) http://www.derpharmachemica.com/

15. M. Ramesh, M. Anbuvannan, G. Viruthagiri, *Spectrochim. Acta, A Mol. Biomol. Spectrosc.*, **136**, 864 (2015) doi: 10.1016/j.saa. 2014.09.105.
16. L. Xiao, C. Liu, X. Chen, Z. Yang, *Food Chem. Toxicol.*, **90**, 76 (2016) doi:10. 1016/j.fct.2016.02.002.
17. S. Rajeshkuma, *J. Genet. Eng. Biotechnol.*, **14**, 195 (2016) doi:10. 1016/j.jgeb.2016.05.007.
18. P.C. Nagajyothi, T.N. Minh An, T.V.M. Sreekanth, J. Il Lee, D.L. Joo, K.D. *Mater. Lett.*, **108**, 160 (2013) doi:10.1016/j.matlet.2013.06. 095.
19. M.J. Chan, L.M. Peria, *Nat. Prod. Rep.,* **18,** 674 (2001) doi: 10.1039/b100455g.
20. M. Anbuvannan, M. Ramesh, G. Viruthagiri, N. Shanmugam, N. Kannadasan, *Spectrochim. Acta A Mol. Biomol. Spectrosc.*, **143**, 304 (2015) doi:10.1016/j.saa.2015.01.124.
21. M. Sundrarajan, S. Ambika, K. Bharathi, *Adv. Powder Technol.*, **26**, 1294 (2015) doi:10.1016/ j.apt.2015.07.001.
22. P. Vanathi, P. Rajiv, S. Narendhran, S. Rajeshwari, P.K.S.M. Rahman, *Mater. Lett.*, **134**, 13 (2014) doi: 10.1016/j.matlet.2014. 07.029.
23. P. Jamdagni, P. Khatri, J.S. Rana, *J. King Saud Univ. – Sci.* (2016). doi:10.1016/j.jksus.2016.10.002
24. K. Prasad, A.K. Jha, *Nat. Sci.*, **1**, 129 (2009) doi:10.4236/ns.2009.12016
25. B.N. Patil, T.C. Taranath, *Int. J. Mycobacteriology*, **5**, 197 (2016) doi:10.1016/j.ijmyco.2016.03.004.
26. S. Gunalan, R. Sivaraj, V. Rajendran, *Nat. Sci. Mater. Int.*, **22**, 693 (2012) doi:10.1016/j.pnsc.2012.11.015
27. C. Jayaseelan, A.A. Rahuman, A.V. Kirthi, S. Marimuthu, T. Santhoshkumar, A. Bagavan *et al., Spectrochim. Acta A Mol. Biomol. Spectrosc.*, **90**, 78 (2012) doi:10.1016/j.saa. 2012.01.006.
28. J. Pulit-Prociak, J. Chwastowski, A. Kucharski, M. Banach, *Appl. Surf. Sci.*, **385**, 543 (2016) doi:10.1016/j.apsusc.2016.05.167.
29. H. Mirzaei, M. Darroudi, *Ceram. Int.*, **43**, 907 (2017) doi:10.1016/j.ceramint. 2016.10.051
30. V. Patel, D. Berthold, P. Puranik, M. Gantar, *Biotechnol. Reports*, **5**, 112 (2015) doi:10.1016/j.btre.2014.12.001
31. M. Stan, A. Popa, D. Toloman, A. Dehelean, I. Lung, G. Katona, *Mater. Sci. Semicond. Process.*, **39**, 23 (2015) doi:10. 1016/j.mssp.2015.04.038.
32. E.D. Sherly, J.J. Vijaya, N.C.S. Selvam, L.J. Kennedy, *Ceram.*, doi:10.1016/j.ceramint.2013.11.006
33. G. Sangeetha, S. Rajeshwari, R. Venckatesh, *Mater. Res. Bull.*, **46**, 2560 (2011) doi:10.1016/j.materresbull. 2011.07.046.
34. K. Elumalai, S. Velmurugan, *Appl. Surf. Sci.*, **345**, 329 (2015) doi:10.1016/j.apsusc.2015.03.176.
35. D. Suresh, P.C. Nethravathi, H. Udayabhanu, H. Rajanaika, H. Nagabhushana, S.C. Sharma, *Mat. Sci. Semicond. Proc.*, **31**, 446 (2015) doi: 10.1016/j.saa.2015.01.048 ·
36. R. Dobrucks, J. Dugazewska, *Saudi J. Biol. Sci.*, **23**(4),517 (2016) doi:10.1016/j.sjbs.2015.05.016.
37. H. Abdul Salam, R. Sivaraj, R. Venckatesh, *Mater. Lett.*, **131**, 16 (2014) doi:10.1016/j.matlet.2014. 05.033.
38. D. Suresh, R.M. Shobharani, P.C. Nethravathi, M.A. PavanKumar, H. Nagabhushan, S.C. Sharma, *Spectrochim. Acta*. A, **141**, 128 (2015) https://doi.org/10.1016/j.saa.2015.01.048.
39. K. Vimala, S. Sundarraj, M. Paulpandi, S. Vengatesan, S. Kannan, *Process Biochem.*, **49**, 160 (2014) doi:10.1016/j.procbio.2013.10.007.
40. T. Bhuyan, K. Mishra, M. Khanuja, R. Prasad, A. Varma, *Mat. Sci. Semicond. Proc.*, **32**, 55 (2015) doi:10.1016/ j.mssp.2014.12.053.
41. K. Elumalai, S. Velmurugan, S. Ravi, V. Kathiravan, S. Ashokkumar, *Mat. Sci. Semicond. Proc.*, **4**, 365 (2015) doi:10.1016/j.saa.2015.02.011.
42. R. Yuvakkumar, J. Suresh, S.H. Hong, *Adv. Mat. Res.*, **952**, 137 (2014) doi:10.1016/j.saa.2014.08.022.
43. R. Yuvakkumar, J. Suresh, J. Nathanael, A. Sundrarajan, M.S.I. Hong, *Mater. Sci. Eng. C.*, **41**,17 (2014) doi:10.1016/j.msec.2014.04.025.
44. S. Iravani, *Green Chem.*, **13**, 2638 (2011) doi:10.1039/C1GC15386B.
45. M. Ramesh, M. Anbuvanna, G. Viruthagiri, *Spectrochim. Acta A*, **136**, 864 (2015) doi:10.1016/j.saa. 2014.09.105.
46. Z. Sheikhloo, M. Salouti, F. Katiraee, *J. Clust. Sci.*, **22**, 661 (2011) doi:10.1007/s10876-011-0412-4.
47. P.E. Ochieng, I. Iwuoha, M. Michira, J. Ondiek, P. Githira, G.N. Kamau, *Int. J. BioChem. Phys.*, **23**, 53 (2015)doi:10.1080/17518253.2018.1547925
48. D. Wodka, E. Bielaníska, R.P. Socha, M. Elzbieciak-Wodka, J. Gurgul, P. Nowak *et al., ACS Appl. Mater. Interfaces*, **2**, 1945 (2010) doi:10.1021/am1002684.
49. K. Gnanajobitha, M.Paulkumar, S. Vanaja, C. Rajeshkumar, G. Malarkodi, Annadurai *et al., J. Nanostruct Chem.*, **61**, 67 (2013) http://www.jnanochem.com/content/3/1/17
50. I. Ahmad, Z. Mehmood, F. Mohammad, *J. Ethnopharmacol.*, **62**(2), 183 (1998) doi: 10.1016/s0378-8741(98)00055-5 62: 183 (1998).
51. M.S. Blois, *Nature* **181**, 1199 (1958) doi:10.1038/1811199a0
52. NCCLS, Performance Standards for Antimicrobial Disc Suspectibility Tests. Approved Standard NCCLS Publication M2-A5, Villanova, PA, USA, 1993.
53. JCPDS, Powder Diffraction File, Alphabetical Index, Inorganic Compounds, International Centre for Diffraction Data, Newtown Square, Pa, USA, 1977. http://worldcat.org/identities/lccn-n78034812.
54. B. D. Cullity, Elements of X-Ray Diffraction, Addison-Wesley, Reading, Mass, USA, 3rd edn., 1967, 1, 1 (2006).https://www.worldcat.org/title/elements-of-x-ray-diffraction /oclc /256038237.

55. G. Sangeetha, S. Rajeshwari, V. Rajendran, *Mat. Res. Bull*., **46**, 2560 (2011). doi: 10.1016/j.materresbull.2011.07.046
56. L. Irimpan, V. Nampoori, P. Radhakrishnan, A. Deepthy, B. Krishnan, *J. Appl. Phys*., **102**, 063524 (2007) doi:10.1063/1.2778637.
57. G.K. Prashanth, P.A. Prashanth, U. Bora, M. Gadewar, B.M. Nagabhushana, S. Ananda, G.M. Krishnaiah, H.M. Sathyananda, *Int. J. Mod. Sci*., **1**(2), 67 (2015) doi:10.1016/j.kijoms.2015.10.007
58. Y. P. Xie, Y. P. He, P. L. Irwin, T. Jin, X. M. Shi, *Appl. Environ. Microbiol*. **77**, 2325 (2011).doi: 10.1128/AEM.02149-10.
59. O. Yamamoto, *International Journal of Inorganic Materials*, **3**, 643 (2001). doi:10.1016/S1466-6049(01)00197-0
60. G. Fu, P. S. Vary, Ch.-T. Lin, *Journal of Physical Chemistry* B, **109** (18), 8889 (2005) doi: 10.1021/jp0502196, 24
61. H. J. Gu, D. N. Fan, J. L. Gao, W. Zou, Z. X. Peng, Z. M. Zhao, J. Q. Ling, R. Z. LeGeros, *Arch. Oral Biol*. **57**, 369 (2012) doi: 10.1016/j.archoralbio.2011.10.001
62. F. Mirhosseini, M. Amiri et.al., *Front Dent*. **16**, 105 (2019) doi: 10.18502/fid.v16i2.1361
63. S. Gaikwad, *et al*., *Nanotechnologies in Russia*, **15 (**11), 760 (2021) doi:10.1134/S199507802006021X
64. S.U. Mukthamath, R. Raychaudhuri, M. Ballal, K. Chakravarthy, K.S. Shirur, S. Mutalik, *J. Appl. Pharm. Sci.,* **14**(12), 50 (2024). doi:10.7324/JAPS.2024.195780
65. R. Kumar Singh, D. Nallaswamy, S. Rajeshkumar, S.S. Varghese, C. Sengupta, *Anandan J. Nanomaterials and their application in Prosthetic Dentistry*. **14** (18S), 860 (2025) https://www.jneonatalsurg.com/index.php/jns/article/view/5351

*Bulgarian Chemical Communications, Volume 58, Issue 1 (pp. 85-92) 2026* *DOI: 10.34049/bcc.58.1.5699*

# Stefan blowing and chemical reaction influences on non-Darcian flow of Casson nanofluid over a stretched surface

M. Gnaneswara Reddy [1], S. Kiranmaiye [1], M. Eswara Rao [2]*

[1] *Department of Mathematics, Narayana Engineering College (Autonomous), Gudur, Tirupati-524 101, Andhra Pradesh, India*

[2] *Department of Mathematics, Saveetha School of Engineering, SIMATS, Chennai, Tamil Nadu, India*

Received: May 05 2025; Revised: November 20, 2025

Studying the magnetohydrodynamic flow, heat and mass transfer properties of a Casson nanofluid flow over an unstable stretched sheet with varying heat and mass fluxes while taking Stefan blowing parameter and non-Darcian porous medium into account is the goal of this paper. The motivation stanches from the prerequisite to comprehend progressive heat and mass transfer characteristics and their insinuations for science, engineering and industrial system. New aspects related to Brownian motion and thermophoresis with heat transfer are examined. The effects of chemical reaction, Eckert number, and thermal radiation are examined in this work. The critical partial differential equations that govern momentum, boundary conditions, concentration, and temperature transform a non-linear ordinary differential equations system by applying suitable similarity transformations. The outcomes of critical physical parameters are acquired by engaging the built-in bvp4c solver in the MATLAB computational software. Comparison shows that the present results are in excellent agreement with previous existing results. The profiles of temperature, velocity, and concentration as well as the related physiological traits used in the study are identified. When the chemical reaction rate manifests, the nanoparticle concentration profile decreases, but the Stefan blowing parameter exhibits the opposite behavior. The intricate relationship between the skin friction coefficient, Sherwood number, and Nusselt number, and their impact on mass and heat transfer characteristics, was a subject of extensive research in various fields, including fluid dynamics, heat transfer, and chemical engineering.

**Keywords:** Chemical reaction, Stefan blowing, Casson nanofluid, MHD, Thermal radiation.

## INTRODUCTION

The Casson fluid model, first introduced by Casson in 1959, has become a popular choice for analyzing the rheological behavior of various non-Newtonian fluids. This model is particularly suitable for describing the flow characteristics of fluids that exhibit yield stress, such as food processing, pharmaceuticals, cosmetics, and materials science. Its particular strength lies in its capacity to clarify the flow properties of materials that undergo a noticeable transition from a solid-like to a fluid-like state when exposed to applied stress [1-6]. The MHD flow of Casson fluid across an inclined permeable stretched surface was examined by Kumar and Srinivas [7] in relation to the combined effects of thermal radiation and Joule heating. Raja *et al*. [8] employed intelligent computing techniques to explore the magnetohydrodynamic (MHD) radiative drift of a Von Kármán Casson nanofluid through a Darcy-Forchheimer medium, incorporating activation energy considerations. In the presence of Stefan blowing or suction, Konai *et al*. [9] embarked the Casson nanofluid flow past a stretched surface. The analysis conducted by Sankari *et al.* [10] on the double stratification of Casson nanofluid over an exponential extending sheet demonstrates a comprehensive exploration, specifically delving into the characteristics of non-Newtonian fluids and the behavior of nanofluids. Elgendi *et al*. [11] explored the properties of a steady flow of an incompressible Casson fluid through a permeable stretched surface. In the presence of anisotropy thermal conductivity, Kumar *et al.* [12] embarked the Casson fluid flow in a permeable channel. Researchers have focused a lot of emphasis on studying MHD flows of non-Newtonian fluids in porous media because of its many potential uses. These include processing of petroleum, and textile, biological systems, heat-storage beds, irrigation problems, and polymer composite industries. Many researchers have investigated various aspects of magnetohydrodynamic flows of non-Newtonian fluids passing through a porous medium, providing valuable insights into the field [13-16]. A numerical study of magnetohydrodynamic boundary layer flow through a stretching surface was conducted by Pantokratoras [17]. The MHD dissipative flow

* To whom all correspondence should be sent:
E-mail: *mannerieswar99@gmail.com*

across a shrinking/ stretching surface was examined by Mishra *et al*. [18] in relation to the combined effects of Joule heating and heat absorption. Haider *et al.* [19] examined the unsteady MHD nanofluid flow past a stretched surface when Stefan blowing or suction was present. Using heat absorption and thermal radiation considerations, Alqahtani *et al.* [20] investigated the magnetohydrodynamic flow of a Casson hybrid nanofluid through a Darcy-Forchheimer medium using intelligent computing approaches. Thenmozhi and Rao [21] investigated the magnetohydrodynamic micropolar fluid through a Darcy-Forchheimer medium using the predictor-corrector FDM technique. In the presence of velocity slip, Ouyang *et al.* [22] embarked the magnetohydrodynamics ternary nanofluid flow over a stretching or shrinking surface. The effects of viscous dissipation and Joule heating on magnetohydrodynamics-hybrid nanofluid flow across non-isothermal stretching or shrinking surfaces were investigated by Idris *et al.* [23].

In many industrial and technical processes, the understanding of mass and heat transfer in chemical reactions is crucial. These processes are widely used in many industrial applications, including food processing, ceramic or glassware manufacturing, and polymer production [24-29]. The squeezing flow of Casson nanofluid across a stretched surface was examined by Noor *et al.* [30] in relation to the combined effects of chemical reaction and Joule heating. Manjunatha *et al.* [31] discussed the importance of convective heat transfer and Stefan blowing in nanofluid flow across a curved stretched sheet with chemical reaction. Abbasi *et al*. [32] engaged in a comprehensive discussion regarding the potential applications of Casson nanomaterials in a radiative binary reactive flow near an oblique stagnation point. This exploration involved considering how these unique materials could be utilized in scenarios where radiative heat transference and chemical reactions play significant parts, particularly regarding activation energy applications. Using nonlinear chemical reaction and Joule heating considerations, Khan *et al*. [33] investigated the magnetohydrodynamic flow of a Casson fluid *via* a permeable moving wedge using clever computing techniques. The MHD flow of a Casson nanofluid across an inclined permeable stretched surface was examined by Srinivas *et al.* [34] in relation to the combined effects of chemical reaction and Joule heating. Saleem *et al.* [35] investigation focused on numerical simulations, bolstered by an advanced computing framework, to analyze the intricate chemical reactions occurring within Casson nanofluids. These fluids are recognized for their non-Newtonian behavior and incorporation of suspended nanoparticles. The impact of ultrasonic waves on a turbulent flow with chemical reactions was numerically investigated by Shateri *et al.* [36]. The study by Razzaq *et al*. [37] emphasized the crucial role of Ohmic dissipation and chemical reactions in the Casson nano liquid flow across a extending surface. A complex and multifaceted area of research with significant implications for various engineering and industrial applications is presented by Hasan *et al*. [38] investigation on the numerical study of MHD nanofluid flow and heat transfer, especially when taking exothermic chemical reactions and radiative heat flux into account. Using chemical reaction and thermo–solutal Marangoni convection, Challa *et al*. [39] investigated the effects of gyrotactic microorganisms on Powell–Eyring nanofluid over an inclined stretched surface.

The use of chemical reactions in the magnetized flow of Casson nanofluid through an overextended sheet has not received much attention. Studying flow, heat, and mass transfer in a stretched surface with a porous layer saturated with a Casson fluid is the aim of this work. The study explores the thermal conduction of nanofluids, taking into account the effects of thermal radiation, as well as the properties of thermophoresis parameter and Brownian motion.

*Motivation*

Some motivation points are described as:

- The rising demand for enhanced thermal efficiency in industrial and engineering applications, such as cooling systems, biomedical devices, and energy technologies, underscores the importance of studying the heat transfer properties of nanofluids.
- Despite the wide applicability of non-Newtonian fluid models, the Casson fluid model remains underexplored in scenarios involving unsteady stretched surfaces and Stefan blowing/suction, necessitating further investigation.
- Phenomena such as Brownian motion and thermophoresis significantly impact the thermal and concentration profiles of nanofluids but require a deeper understanding in the context of complex fluid models like Casson.
- Magnetic fields and unsteady flow conditions are crucial in regulating fluid dynamics in advanced applications, but their combined influence on Casson nanofluid systems remains an open question.

*Research questions*

The following research questions are described below:

- How do the unique thermal and flow properties of Casson nanofluid enhance heat transfer efficiency in engineering systems subjected to unsteady stretched surfaces?
- What is the impact of Casson fluid parameters on velocity, temperature, and concentration profiles under the influence of Stefan blowing/suction?
- How do Brownian motion and thermophoresis affect the thermal conductivity and nanoparticle concentration in Casson nanofluid flows?
- What is the combined effect of magnetic fields and unsteadiness parameters on the flow behavior and heat transfer characteristics of Casson nanofluid?

## FORMULATION OF THE PROBLEM

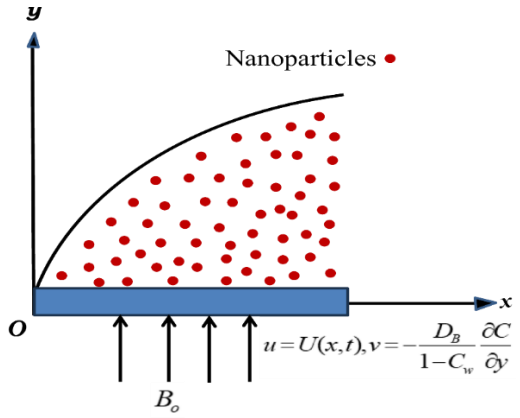


**Fig. 1.** Geometry of the problem.

Consider the unsteady hydromagnetic flow of electrically conducting Casson nanofluid across a stretching sheet. Magnetic field $B_0$ is applied perpendicularly to the surface. The schematic diagram presented in Fig. 1 depicts a complex network of interconnected elements, each playing a vital role in the overall functionality of the system. We may represent the dynamics of this system using a variety of techniques if we assume that a sheet starts stretching along the *x*-axis at time $t=0$ with velocity $U(x,t)=\frac{ax}{1-\alpha t}$ where the *y*-axis is orthogonal to the sheet. We consider the impacts of Lewis number and Stefan blowing/ suction. Chemical reactions, thermophoresis, and thermal radiations are closely intertwined phenomena that play an important part in many scientific and industrial applications. The Casson nanofluid [10, 26] rheological model is given by:

$$\tau_{ij}=\begin{cases}\left(\mu_b+\frac{P_y}{\sqrt{2\pi}}\right)2\varsigma_{ij}, & \pi>\pi_c\\ \left(\mu_b+\frac{P_y}{\sqrt{2\pi_c}}\right)2\varsigma_{ij}, & \pi<\pi_c\end{cases} \quad (1)$$

where $\varsigma_{ij}$, $\tau_{ij}$, $P_y$, and $\mu_b$ are deformation tensor, stress tensor, yield stress and plastic dynamic viscosity of the Casson fluid, respectively. The governing boundary layer equations under these presumptions can be written as [7, 9]:

$$\frac{\partial u}{\partial x}+\frac{\partial v}{\partial y}=0 \quad (2)$$

$$\frac{\partial u}{\partial t}+u\frac{\partial u}{\partial x}+v\frac{\partial u}{\partial y}=\upsilon\left(1+\frac{1}{\beta^*}\right)\frac{\partial^2 u}{\partial y^2}-\frac{\sigma B_o^{\,2}}{\rho}u-\frac{C_b}{\sqrt{k_0(t)}}u^2 \quad (3)$$

$$\frac{\partial T}{\partial t}+u\frac{\partial T}{\partial x}+v\frac{\partial T}{\partial y}=\frac{\kappa}{(\rho c_p)_f}\frac{\partial^2 T}{\partial y^2}+\frac{(\rho c_p)_p}{(\rho c_p)_f}\left[D_B\frac{\partial C}{\partial y}\frac{\partial T}{\partial y}+\frac{D_T}{T_\infty}\left(\frac{\partial T}{\partial y}\right)^2\right] \quad (4)$$
$$+\frac{\mu}{(\rho c_p)_f}\left(1+\frac{1}{\beta^*}\right)\left(\frac{\partial u}{\partial y}\right)^2-\frac{1}{(\rho c_p)_f}\frac{\partial q_r}{\partial y}$$

$$\frac{\partial C}{\partial t}+u\frac{\partial C}{\partial x}+v\frac{\partial C}{\partial y}=D_B\frac{\partial^2 C}{\partial y^2}+\frac{D_T}{T_\infty}\frac{\partial^2 T}{\partial y^2}-k_r(t)(C-C_\infty) \quad (5)$$

Boundary condition:

$$\left.\begin{aligned}&u=U(x,t), v=-\frac{D_B}{1-C_w}\frac{\partial C}{\partial y}, T=T_w, C=C_w \text{ at } y=0\\ &u\to 0, T\to T_\infty, C\to C_\infty \text{ at } y\to\infty\end{aligned}\right\} \quad (6)$$

Here the velocity components in the *x*- and *y*-axis directions are denoted by *u* and *v*, respectively, $D_B$ is the coefficient of Brownian diffusion, $k_0(t)=k(1-\alpha t)$ is a time-dependent permeability parameter, $k_r(t)=k(1-\alpha t)^{-1}$ is a chemical reaction parameter, *k* is a constant, *t* denotes time, α is positive constant, $a>0$ be any constant, μ is dynamic viscosity, ν is kinematic viscosity, $\beta^*=\frac{\mu_b\sqrt{2\pi_c}}{P_y}$ is Casson fluid parameter, σ is electrical conductivity, $D_F$ is coefficient of thermophoresis diffusion, $\kappa$ is thermal conductivity, $(\rho c_p)_p$ is heat capacity of the nanoparticle material, $C_b$ is a form of drag coefficient, $\pi_c$ is the critical value of $\pi$, $\pi=\varsigma_{ij}^{\,2}$ is the result of multiplying $\varsigma_{ij}$ by itself, $(\rho c_p)_f$ is heat capacity of the fluid, *C* is concentration, ρ̇ is density of the fluid, $q_r=-\left(\frac{4\sigma^*}{3\chi}\right)\frac{\partial T^4}{\partial y}$ is radiative heat flux, $\sigma^*$ is Stefan-Boltzmann constant.

$T^4 \cong 4T_\infty^3 T - 3T_\infty^4$ (Higher-order terms are neglected), $T$ is temperature, $T_w$ is surface temperature, $C_w$ is surface nanoparticle concentration, $\chi$ is Rosseland mean absorption coefficient, $T_\infty$ and $C_\infty$ are the temperature and nanoparticle concentration distant from the exterior.

On simplifying Eq. (4), we get:

$$\frac{\partial T}{\partial t}+u\frac{\partial T}{\partial x}+v\frac{\partial T}{\partial y}=\frac{\kappa}{(\rho c_p)_f}\frac{\partial^2 T}{\partial y^2}+\frac{(\rho c_p)_p}{(\rho c_p)_f}\left[D_B\frac{\partial C}{\partial y}\frac{\partial T}{\partial y}+\frac{D_T}{T_\infty}\left(\frac{\partial T}{\partial y}\right)^2\right] + \frac{\mu}{(\rho c_p)_f}\left(1+\frac{1}{\beta^*}\right)\left(\frac{\partial u}{\partial y}\right)^2+\frac{1}{(\rho c_p)_f}\frac{16\sigma^* T_\infty^3}{3\chi}\frac{\partial^2 T}{\partial y^2} \quad (7)$$

The skin friction coefficient ($C_f$), and the rates of mass and heat transfer $(Sh_x, Nu_x)$ can be described as:

$$C_f=\frac{\tau_w}{\rho U^2},\ Nu_x=\frac{xq_w}{\kappa(T_w-T_\infty)},\ Sh_x=\frac{xq_m}{D_B(C_w-C_\infty)} \quad (8)$$

The surface mass and heat fluxes, shear stress near the wall are:

$$\left.\begin{aligned} q_m&=-D_B\left(\frac{\partial C}{\partial y}\right)\Big|_{y=0},\ q_w=-\kappa\left(\frac{\partial T}{\partial y}\right)\Big|_{y=0},\\ \tau_w&=\mu\left(1+\frac{1}{\beta^*}\right)\left(\frac{\partial u}{\partial y}\right)\Big|_{y=0}\end{aligned}\right\} \quad (9)$$

Now, we present the similarity variable $\eta$ and the dimensionless functions $g$, $\theta$, and $\phi$ as:

$$\psi=x\sqrt{\frac{a\upsilon}{(1-\alpha t)}}\mathrm{g}(\eta),\ \theta(\eta)=\frac{T-T_\infty}{T_\omega-T_\infty},\ \phi(\eta)=\frac{C-C_\infty}{C_\omega-C_\infty},\ \eta=y\sqrt{\frac{a}{\upsilon(1-\alpha t)}} \quad (10)$$

where $\psi$ stands for stream function and is represented by the relationship that follows:

$$u=\frac{\partial\psi}{\partial y}\quad v=-\frac{\partial\psi}{\partial x} \quad (11)$$

Substituting Eqs. (10) and (11) into Eqs. (3), (7), and (5), we obtain the nonlinear ordinary differential equations:

$$\left(1+\frac{1}{\beta^*}\right)\mathrm{g}'''+\mathrm{g}''\mathrm{g}-A\left(\mathrm{g}'+\frac{\mathrm{g}''\eta}{2}\right)-M\,\mathrm{g}'-(1+Fs)(\mathrm{g}')^2=0 \quad (12)$$

$$\frac{1}{Pr}\left(1+\frac{4}{3}R_d\right)\theta''+\left(1+\frac{1}{\beta^*}\right)Ec(\mathrm{g}'')^2-\frac{A}{2}\eta\theta'+\mathrm{g}\theta'+Nb\,\theta'\phi'+Nt\,\theta'^2=0 \quad (13)$$

$$\phi''-LePr\left[\left(\frac{A}{2}\eta-\mathrm{g}\right)\phi'+\Gamma\phi\right]+\frac{Nt}{Nb}\theta''=0 \quad (14)$$

The renovated boundary constraints are:

$$\left.\begin{aligned} &\mathrm{g}'(\eta)=1,\ \mathrm{g}(\eta)=\frac{S_0}{Le}\phi'(\eta),\ \theta(\eta)=1,\ \phi(\eta)=1\ \ at\ \ \eta=0\\ &\mathrm{g}'(\eta)=0,\ \theta(\eta)=0,\phi(\eta)=0\ as\ \ \eta\to\infty\end{aligned}\right\} \quad (15)$$

where $Le=\frac{\alpha_0}{D_B}$ (Lewis number), $\alpha_0=\frac{\kappa}{(\rho c_p)_f}$ (thermal diffusivity), $Nb=\frac{(\rho c_p)_p D_B(C_w-C_\infty)}{(\rho c_p)_f\upsilon}$ (Brownian motion), $Nt=\frac{(\rho c_p)_p D_T(T_w-T_\infty)}{(\rho c_p)_f T_\infty\upsilon}$ (thermophoresis parameter), $\mathrm{Pr}=\frac{\mu c_p}{\kappa}$ (Prandtl number), $A=\frac{\alpha}{a}$ (unsteadiness parameter), $M=\frac{\sigma B_0^2(1-\alpha t)}{\rho a}$ (magnetic field parameter), $R_d=\frac{4\sigma^* T_\infty^3}{\chi\kappa}$ (radiation parameter), $Ec=(ax/1-\alpha t)^2/\left[c_p(T_w-T_\infty)\right]$ (Eckert number), $\Gamma=\frac{k}{a}$ (chemical reaction parameter), $Fs=\frac{C_b}{\sqrt{k_0(t)}}x$ (local inertia parameter), $S_0=\frac{C_w-C_\infty}{1-C_w}$ (Stefan blowing parameter) where $S_0 < 0$ and $S_0 > 0$ correspond to suction and blowing, respectively.

On simplifying Eq. (8), we get:

$$C_f\,\mathrm{Re}_x^{0.5}=\left(1+\frac{1}{\beta^*}\right)\mathrm{g}''(0),\ Nu_x\,\mathrm{Re}_x^{-0.5}=-\theta'(0),\ Sh_x\,\mathrm{Re}_x^{-0.5}=-\phi'(0) \quad (16)$$

where Reynolds number is denoted as $\mathrm{Re}_x=\frac{Ux}{\nu}$.

## NUMERICAL SOLUTION

In our MATLAB computational approach, we utilized the bvp4c algorithm to solve dimensionless non-linear differential equations (12-14) alongside their corresponding boundary constraint (15). This involves employing the bvp4c solver within the MATLAB environment to derive numerical solutions for the ordinary differential equations. We first transformed the dimensionless non-linear ODEs into a first-order initial boundary value problem to streamline this process. The ensuing procedure delineates the necessary steps for obtaining the numerical solution:

$$\mathrm{g}=h_1,\ \mathrm{g}'=h_2,\ \mathrm{g}''=h_3,\ \theta=h_4,\ \theta'=h_5,\ \phi=h_6,\ \phi'=h_7 \quad (17)$$

$$h_3'=\frac{1}{\left(1+\frac{1}{\beta^*}\right)}\left[-h_3h_1+A\left(h_2+\frac{h_3\eta}{2}\right)+(1+Fs)(h_2)^2+M\,h_2\right] \quad (18)$$

$$h_5'=\frac{Pr}{\left(1+\frac{4}{3}R_d\right)}\left[-\left(1+\frac{1}{\beta^*}\right)Ec(h_3)^2+\frac{A}{2}\eta\,h_5-h_1h_5-Nb\,h_5h_7-Nt\,h_5^2\right] \quad (19)$$

$$h_7'=LePr\left[\left(\frac{A}{2}\eta-h_1\right)h_7+\Gamma h_6\right]-\frac{Nt}{Nb}h_5' \quad (20)$$

Boundary conditions are:

$$\left.\begin{aligned} &h_2 = 1,\ h_1 = \left(S_0 / Le\right) h_7,\ h_4 = 1,\ h_6 = 1 \quad at\ \ \eta = 0 \\ &h_2 = 0,\ h_4 = 0,\ h_6 = 0 \qquad\qquad\qquad at\ \ \eta = \infty \end{aligned}\right\} \quad (21)$$

## RESULTS AND DISCUSSION

Chemical reaction and non-Darcian porous medium were taken into consideration while analyzing the Stefan blowing effect in a Casson nanofluid *via* stretched sheet. Numerical techniques and similarity transformations were used to define and solve the governing equations. The findings were displayed in tables and graphs that show how important factors affect the profiles of temperature, velocity, and concentration. The influence of Casson fluid parameter $\beta^*$ on the velocity field is shown in Figure 2. The observed augmentation in the velocity profile, concomitant with an increase in the Casson nanofluid parameter, unveils a complex interplay of rheological characteristics and momentum transport within the fluid system. Figure 3 delineates that a rise in Forchheimer number creates a resistance in fluid flow which results in abatement on velocity. The velocity significantly decreases when the magnetic field parameter M increases, as Figure 4 illustrates. This is because of the Lorentz force which opposes the fluid motion by acting as a resistive drag. The fluid's velocity decreases more dramatically as the magnetic field intensity rises because the opposing force also gets greater. Figure 5 depicts that the speed of the liquid rises for dissimilar rising data for the Stefan suction/blowing parameter $S_0$ for both steady and unsteady flows. The injection of miniature rudiments throughout the edge regenerates the dispersion of species. On the other hand, the transfer of miniature rudiments slows down dispersion, so increasing values of injection cause an enlargement of the speed of the liquid.

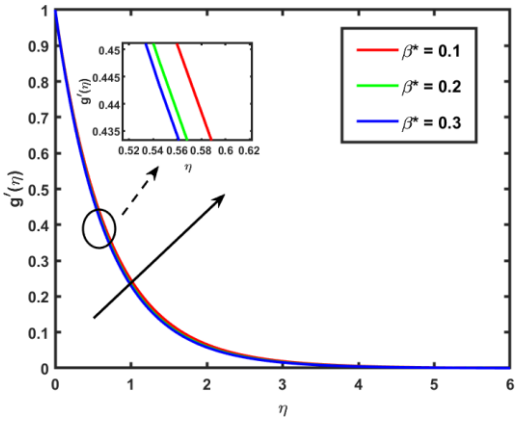


**Fig. 2.** Velocity fields with rising $\beta^*$.

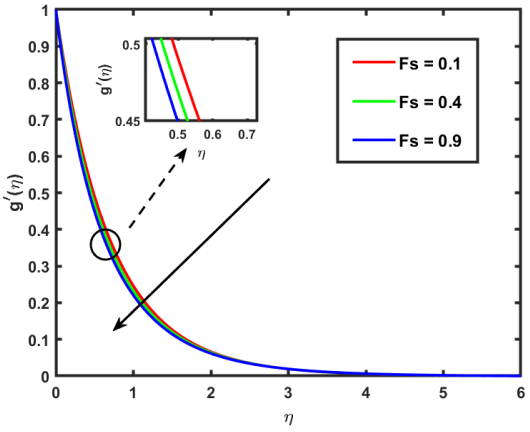


**Fig. 3.** Velocity fields with rising $Fs$ .

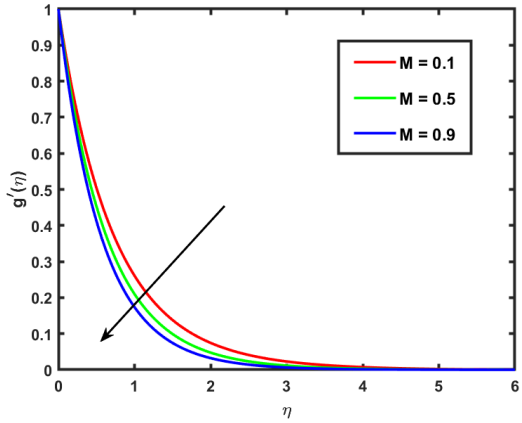


**Fig. 4.** Velocity fields with rising $M$ .

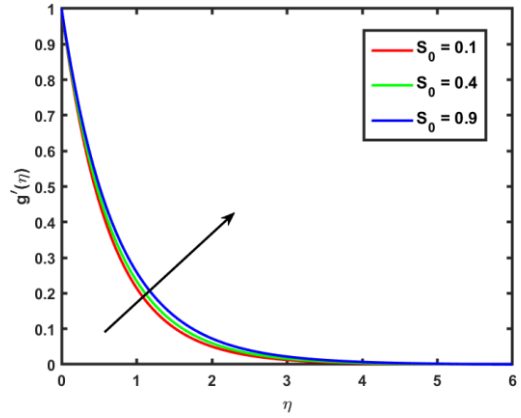


**Fig. 5.** Velocity fields with rising $S_0$ .

Figure 6 illustrates that the temperature distribution rises when the Casson fluid parameter $\beta^*$ increases. Thickening of the thermal border coating takes place owing to amplification in the elasticity stress parameter. As seen in Figure 7, the temperature progressively rises as the Brownian motion parameter $Nb$ increases. The random movement of nanoparticles is enhanced by Brownian motion which accelerates thermal energy transfer and raises the temperature. A rise in the

radiation parameter $R_d$, as Figure 8 illustrates, causes the temperature field to increase. This is because stronger radiation makes the fluid more capable of absorbing and releasing thermal energy, which boosts the temperature distribution and total heat transfer.

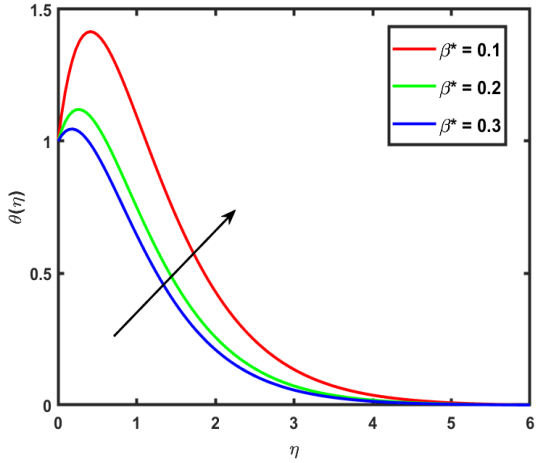


**Fig. 6.** Temperature fields with rising $\beta$*.

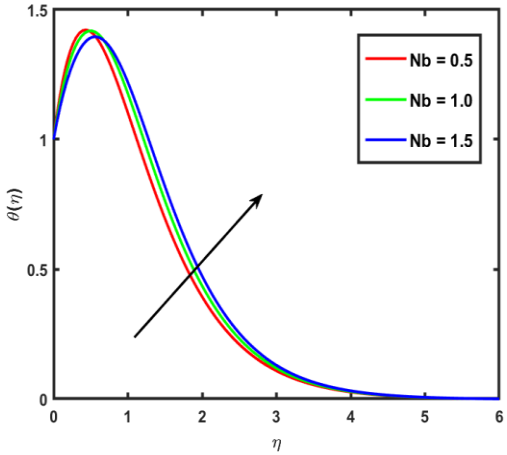


**Fig. 7.** Temperature fields with rising $Nb$.

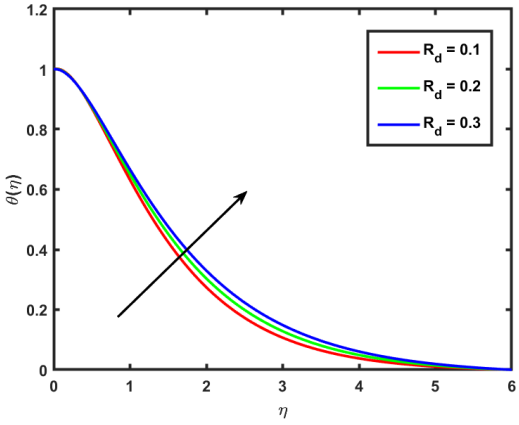


**Fig. 8.** Temperature fields with rising $R_d$.

The influence of unsteady parameter $A$ on the concentration field is shown in Figure 9. The unsteadiness increases mass diffusion, which raises nanoparticle dispersion and causes concentration to rise dramatically. These impacts demonstrate how uneven flow alters the dynamics of mass movement. Figure 10 shows that a large drop in the concentration field occurs when the chemical reaction parameter $\Gamma$ increases. This is because chemical species are consumed more quickly at a higher reaction rate, which lowers the concentration of those species overall in the border layer. Figure 11 demonstrates that a large drop in the concentration field occurs when the Lewis number $Le$ is increased. One can observe that $\phi$ is a decreasing function of $Le$. This may be due to the fact that increasing of Lewis number increases mass transfer rate and hence nanoparticle concentration decreases. Figure 12 illustrates how a minor increase in the Stefan blowing parameter $S_0$ raises the concentration. A slow increase in concentration results from the improved mass transport close to the surface.

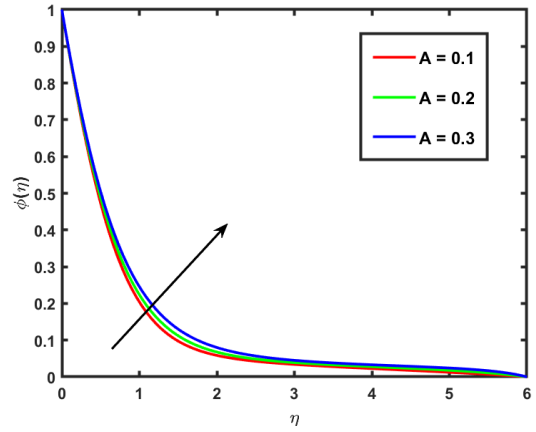


**Fig. 9.** Concentration fields with rising $A$.

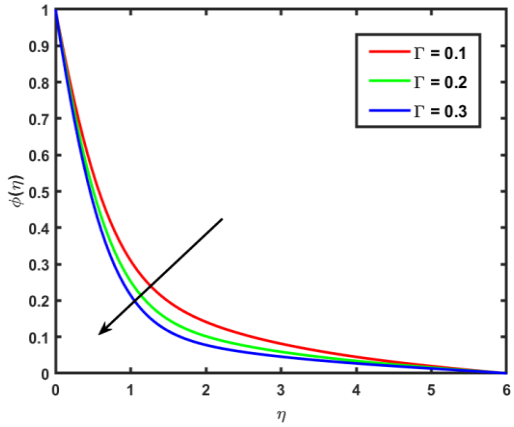


**Fig. 10.** Concentration fields with rising $\Gamma$.

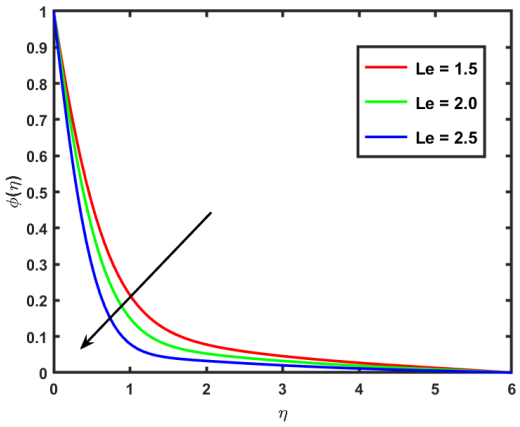


**Fig. 11.** Concentration fields with rising $Le$.

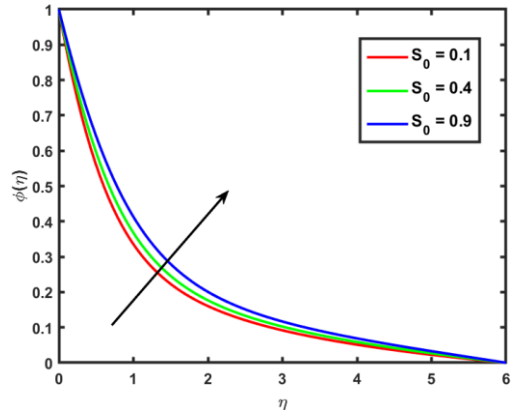


**Fig. 12.** Concentration fields with rising $S_0$.

**Table 1.** Values of -g"(0) for different values of Casson fluid parameter $\beta^*$.

| $\beta^*$ | Prasad *et al.* [26] | Konai *et al.* [9] for $S_0 = A = 0$ | Present result for $S_0 = A = 0$ |
|---|---|---|---|
| 1.0 | 0.707107 | 0.707220 | 0.707109 |
| 2.0 | 0.816497 | 0.816540 | 0.816544 |
| 5.0 | 0.912871 | 0.912889 | 0.912883 |
| $\beta^*=\infty$ (Newtonian fluid) | 1.000000 | 1.000010 | 1000030 |

**Table 2.** Values of $C_f \mathrm{Re}_x^{0.5}$, $Nu_x \mathrm{Re}_x^{-0.5}$ and $Sh_x \mathrm{Re}_x^{-0.5}$ with $M = 0.2$, $\mathrm{Pr} = 21$, $Nb = 0.1$, $Le = 1.5$, $Nt = 0.1$, $R_d = 0.1$, $\Gamma = 0.5$, $Fs = 0.4$, and $Ec = 0.1$.

| Parameter | Value | $C_f \mathrm{Re}_x^{0.5}$ | $Nu_x \mathrm{Re}_x^{-0.5}$ | $Sh_x \mathrm{Re}_x^{-0.5}$ |
|---|---|---|---|---|
| $S_0$ | 0.1 | -1.064138 | -0.351360 | -1.129400 |
| | 0.3 | -1.024300 | -0.289400 | -0.982365 |
| | 0.5 | -0.988634 | -0.186962 | -0.923577 |
| $A$ | 0.1 | -0. 548820 | -0. 406490 | -0. 600590 |
| | 0.2 | -0. 555342 | -0. 380746 | -0. 537396 |
| | 0.3 | -0. 573670 | -0. 342618 | -0. 470684 |
| $\beta^*$ | 1.0 | -0. 805948 | -0.450407 | -0. 592327 |
| | 2.0 | -0. 855042 | -0.396210 | -0.575154 |
| | 3.0 | -0. 901867 | -0. 376084 | -0. 559645 |

The comparison shown in Table 1 validates the computational technique by demonstrating great agreement between the current numerical results and earlier research. Moreover, the findings in Table 2 demonstrate how important factors affect the gradients in temperature, concentration, and velocity. The rising temperature and concentration gradients show that increasing the Stefan blowing parameter $S_0$ promotes heat and mass transmission while modestly increasing velocity. The rising mass and heat transfer rates show that increasing the unsteadiness parameter $A$ promotes heat and mass transmission while modestly decreasing velocity. Likewise, the Casson fluid parameter $\beta^*$ indicates a general improvement in thermal and solutal transport by strengthening the velocity gradient and slightly raising temperature and concentration levels.

## CONCLUSIONS

This work explores the behavior of a Casson nanofluid flowing over an expanding surface, looking at mass transference and heat transference rate *via* physical experimentation and numerical simulations. The heat transfer rate also displays notable variability in response to alterations in the Stefan blowing parameter. Numerical results are derived using the bvp4c by MATLAB software to solve the ordinary differential system. Stefan blowing parameter indicates a qualitative similarity between velocity and concentration profiles. For greater *Fs*, g'(η) indicates a diminishing tendency, but for Casson fluid parameter $\beta^*$, the reverse trend is observed. The concentration field of the boundary layer could change significantly as a result of a chemical reaction. The thickness of the solutal boundary layer significantly decreases as the chemical reaction increases. The intricate interplay between chemical reactions and boundary layer dynamics constitutes a pivotal area of research with profound implications across diverse scientific and engineering domains. Higher Lewis numbers *Le* indicate a dominance of thermal diffusivity over mass diffusivity, resulting in faster heat transfer but slower concentration adjustments. This finding underscores the importance of controlling the Lewis number *Le* to balance thermal and mass transfer in practical applications. Skin friction decreases for fluid parameter $\beta^*$ and boosts up for the Stefan blowing parameter $S_0$.

### *Future directions*

The work can be modified by adding the impact of motile microorganisms, different nanoparticles, activation energy, thermal radiation and shaped change.

REFERENCES


1. N. Casson, in: Rheology of Disperse Systems, C.C. Mills (ed.), Pergamon, New York, 1959, p. 84.
2. R. K. Dash, K. N. Mehta, G. Jayaraman, *Int. J. Eng. Sci.*, **34**(10), 1145 (1996).
3. S. Srinivas, C. K. Kumar, A. S. Reddy, *Nonlinear Anal. Mod. Control*, **23**(2), 213 (2018).
4. M. Usman, F. A. Soomro, R. U. Haq, W. Wang, O. Defterli, *Int. J. Heat Mass Transfer*, **122**, 1255 (2018).
5. T. Hayat, S. A. Khan, S. Momani, *Int. J. Hydro. Ener.*, **47**(12), 8048 (2022).
6. A. Shateri, A. M. Ganji, P. Jalili, B. Jalili, D. D. Ganji, *Res. Eng.*, **25**, 103760 (2025).
7. C. K. Kumar, S. Srinivas, *Special Top. Rev. Porous Media*, **10** (4), 385 (2019).
8. M. A. Z. Raja, K. S. Nisar, M. Shoaib, M. Abukhaled, A. Riaz, *Heliyon*, **9**(10), e20911 (2023).
9. S. Konai, H. Maiti, S. Mukhopadhyay, *Force Mech.*, **12**, 100227 (2023).
10. M. S. Sankari, M. E. Rao, W. Khan, M. H. Alshehri, S. M. Eldin, S. Iqbal, *Case Stud. Therm. Eng.*, **50**, 103492 (2023).
11. S. G. Elgendi, W. Abbas, A. A. M. Said, A. M. Megahed, E. Fares, *J. Nonlinear Math. Phys.*, **31**, 19 (2024).
12. A. Kumar, D. Bhargavi, K. Vajravelu, *Phys. Fluids*, **37**(2), 023132 (2025).
13. S. S. Ghadikolaei, M. Yassari, H. Sadeghi, Kh. Hosseinzadeh, D. D. Ganji, *Powder Tech.*, **322**, 428 (2017).
14. C. K. Kumar, S. Srinivas, *Heat Transf.*, **50**(6), 5225 (2021).
15. S. Srinivas, K. K. Challa, S. Badeti, P. B. Kumar, *Eng. Trans.*, **71**(4), 519 (2023).
16. M. S. Sankari, M. E. Rao, F. A. Awwad, E. A. A. Ismail, O. D. Makinde, W. Khan, *Front. Chem.*, **12**, 1451053 (2025).
17. A. Pantokratoras, *Int. J. Heat. Mass Transf.*, **51**(1-2), 104 (2008).
18. M. R. Mishra, S. M. Hussain, O. D. Makinde, G. S. Seth, *Bul. Chem. Comm.*, **52**(2), 259 (2020).
19. S. M. A. Haider, B. Ali, Q. Wang, C. Zhao, *Coatings*, **11**, 1048 (2021).
20. A. M. Alqahtani, M. Bilal, M. Usman, T. R. Alsenani, A. Ali, S. R. Mahmoud, *Z. Angew. Math. Mech.*, **103**, e202200213 (2023).
21. D. Thenmozhi, M. Eswara Rao, *Prop. Power Res.*, **13**(2), 257 (2024).
22. Y. Ouyang, Md F. Md Basir, K. Naganthran, I. Pop, *Alex. Eng. J.*, **116**, 427 (2025).
23. S. Idris, A. Jamaludin, R. Nazar, I. Pop, *Chin. J. Phys.*, **93**, 611 (2025).
24. S. M. Hussain, J. Jain, G. S. Seth, *Bul. Chem. Comm.*, **48**(4), 659 (2016).
25. M. Eswara Rao, S. Sreenadh, *Global J. Pure Appl. Math.*, **13**, 7529 (2017).
26. K. V. Prasad, K. Vajravelu, H. Vaidya, N. Z. Basha, V. Umesh, *Ain Shams Eng. J.*, **9**(4), 1763 (2017).
27. A. S. Reddy, K. K. Challa, S. Srinivas, T. R. Ramamohan, K. Vajravelu, *Ind. J. Chem. Tech.*, **31**, 186 (2024).
28. D. Thenmozhi, M. Eswara Rao, RLV. R. Devi, Ch. Nagalakshmi, PD. Selvi, *Int. J. Thermofluids*, **24**, 100896 (2024).
29. S. Kosar, M. Sagheer, S. Hussain, *Int. J. Modern Phy. B*, **39**(01), 2550002 (2025).
30. N. A. M. Noor, S. Shafie, M. A. Admon, *J. Adv. Res. Fluid Mech. Therm. Sci.*, **68**(2), 94 (2020).
31. P. T. Manjunatha, A. J. Chamkha, R. J. P. Gowda, R. N. Kumar, B. C. Prasannakumara, S. M. Naik, *J. Nanofluids*, **10**, 285 (2021).
32. A. Abbasi, S. U. Khan, K. Al-Khaled, M. I. Khan, W. Farooq, A. M. Galal, K. Javid, M. Y. Malik, *Chem. Phys. Lett.*, **786**, 139172 (2022).
33. Z. Khan, H. U. Rasheed, I. Khan, H. Abu-Zinadah, M. A. Aldahlan, *Materials*, **15**(3), 747 (2022).
34. S. Srinivas, C. K. Kumar, S. Badeti, A. S. Reddy, *Springer Nature, Singapore*, **155** (2023).
35. S. Saleem, T. Abbas, H. Abutuqayqah, E. U. Haq, S. U. Khan, *Alex. Eng. J.*, **79**, 629 (2023).
36. A. shateri, B. Jalili, S. Saffar, P. Jalili, D. D. Ganji, *Energy*, **289**, 129707 (2024).
37. R. Razzaq, Z. Khan, M. N. Abrar, B. Almohsen, U. Farooq, *Chaos, Soli. Frac.*, **190**, 115756 (2025).
38. Md. M. Hasan, M. J. Uddin, S. A. Faroughi, *Int. J. Thermofluids*, **26**, 101114 (2025).
39. E. R. M, K. K. Challa, T. D, M. Jawad, *Z Angew. Math. Mech.*, **105**, e70226 (2025).

*Bulgarian Chemical Communications, Volume 58, Issue 1 (pp. 93-100) 2026* *DOI: 10.34049/bcc.58.1.5730*

# Enhanced wear resistance of AISI steel *via* sequential nitriding, laser texturing, and TiN coating

R. Kumutha[1], S. Ilaiyavel[2], B. Sudhakar[3], K. Udhayakumar[4], M. Balakumar[2*], C. Anbumeenakshi[5], A. Idrish Khan[4], K. Suresh[4]

[1]*Department of Mechanical Engineering, Loyola Institute of Technology, Palanchur, Chennai - 600123, India*
[2]*Department of Mechanical Engineering, Sri Venkateswara College of Engineering, Sriperumbudur - 602117, India*
[3] *Department of Mechanical Engineering, Akshaya College of Engineering and Technology, Coimbatore, India*
[4]*Department of Mechanical Engineering, Er Perumal Manimekalai College of Engineering, Hosur, India*
[5]*Department of Mechanical Engineering, K.L.N. College of Engineering, Sivagangai, India*

Received; November 07, 2025; Revised: January 13, 2026

Enhancing the durability of bearing steels is critical for applications subjected to severe wear conditions. This study evaluates the tribological performance of AISI 52100 bearing steel treated using a combination of surface engineering techniques aimed at improving wear resistance. Although AISI 52100 exhibits high hardness and fatigue strength, it remains vulnerable to wear under demanding operating conditions. To address this limitation, nitriding, laser surface texturing, and titanium nitride (TiN) coating deposited by physical vapor deposition were applied in different sequences: nitrided + TiN, nitrided + TiN + laser textured, and nitrided + laser textured + TiN. Tribological behavior was assessed using pin-on-disc wear tests under varying normal loads and sliding durations. The nitrided + TiN + laser-textured configuration demonstrated the best performance, exhibiting minimal wear loss and a stable, low coefficient of friction. In contrast, the nitrided + laser-textured + TiN sequence showed poor coating adhesion, leading to severe wear and unstable friction behavior. The nitrided + TiN condition provided moderate improvement. The results clearly demonstrated that the processing sequence plays a decisive role in tribological performance. Laser texturing applied after TiN deposition effectively reduced wear and friction by decreasing the real contact area and facilitating debris entrapment. Overall, the synergistic application of optimized surface treatments significantly enhances the wear resistance and service life of AISI 52100 bearing steel.

**Keywords:** AISI 52100; nitriding; TiN coating; laser surface texturing; wear; tribology.

## INTRODUCTION

High-performance bearings are vital in enhancing the reliability and efficiency of industrial machineries. Among them, AISI 52100 bearing steel is a commonly employed material for bearings, particularly in demanding applications like wind mills, heavy machineries, rail transport, and automobiles [1], [2]. Bearing steels are highly susceptible to friction, wear, and rolling contact fatigue (RCF), which leads to failure of the machinery [3], [4]. Surface treatment and enhancement techniques can improve the performance of AISI 52100 bearing steel. Common surface treatment techniques include nitriding, laser surface remelting, surface coating, and laser texturing. Among these, surface modification methods such as texturing play a significant role in enhancing lubrication, reducing friction, and improving wear resistance in sliding pairs [5]. Nitriding is a surface treatment used for steel in industries. In nitriding process nitrogen is diffused into the surface of bearing steel to form hard nitrides, significantly enhancing surface hardness and wear resistance [6]. TiN coatings are found to be a reliable solution of bearing steel wearing. TiN is deposited by physical vapor deposition (PVD) that provides excellent wear resistance, high hardness, and chemical stability. When applied to bearing steels, TiN reduces friction, improves surface durability, and extends component service life under demanding conditions [7]. Surface texturing using laser beams is one of the advancements in modern material science. Laser surface texturing (LST) uses pulsed lasers to create micro-dimples with a solidified melt rim. The high energy causes melting, vaporization, and heat-affected zones, altering microstructure and properties [8], [9]. While individual surface treatments offer benefits, synergistic combinations of techniques are increasingly recognized as a more effective strategy for overcoming the limitations of single processes [10]. For instance, nitriding enhances surface hardness and load-bearing capacity by introducing nitrogen into the steel matrix, while titanium nitride (TiN) coatings, typically done by physical vapor

* To whom all correspondence should be sent:
Email: *svcebalakumar@gmail.com*

deposition, provide high hardness, chemical stability, and improved wear resistance. When combined with laser surface texturing, these treatments can potentially complement each other by simultaneously improving hardness, wear resistance, frictional behavior, and lubrication efficiency [11], [12], [13].

Wang *et al*. [14] treated 20CrMoH steel samples using ultrasonic surface rolling (USR), carburizing, and combination of carburizing and USR process, followed by analysis of rolling contact fatigue (RCF) mechanisms under a Hertz contact stress of 2.02 GPa. The combined treatment significantly enhanced surface properties, increasing hardness (370 HV0.2 → 900 HV0.2), residual compressive stress (−920 MPa), and reducing roughness (0.48 μm), which doubled the RCF life compared to carburized samples, with delamination identified as the main failure mode. Unal *et al*. [15] worked on ultrasonic nanocrystal surface modification (UNSM) of samples under different static loads (mild, moderate, and severe), and its effects on microstructure, hardness, surface roughness, and friction-wear performance were evaluated. Results indicated that increasing static load enhanced nanocrystalline layer thickness; deformation depth reduced grain size (<500 nm for mild, ~100 nm for moderate and severe), and improved surface roughness (<1 μm for mild and moderate, ~2 μm for severe). UNSM yielded the highest hardness increase (~375–430 HV, +65%), with overall improvements in surface integrity, microhardness, residual compressive stress, and wear resistance.

Guo *et al*. [16] treated GCr15 bearing steel by surface texturing (ST) and laminar plasma jet (LPJ) surface hardening, followed by ball-on-disk reciprocating wear analysis. LPJ surface hardening significantly reduced wear by improving surface hardness and lowering actual contact, while the effectiveness of ST depended on the frictional interface evolution, with stress concentration competing against the trap and hydrodynamic pressure effects under different lubrication conditions.

Humam *et al*. [17] co-deposited TaC particles onto a Ni-W matrix, and studied their influence on the microstructure using XRD, HRTEM, SEM, EDS, and surface roughness tests. Additionally, ultrasonic nanocrystal surface modification (UNSM) was done on Ni-W-TaC composite coatings to evaluate their surface, mechanical, and tribological properties. The incorporation of TaC formed a matrix, while the combined effect of TaC reinforcement and UNSM significantly enhanced surface characteristics, achieving high microhardness (~880 HV), reduced indentation, and a low coefficient of friction (~0.1) under a 15 N load in dry sliding conditions.

Neog *et al.* [18] worked on titanium carbide (TiC) reinforced steel matrix using AISI 8620 bearing steel by tungsten inert gas (TIG) arcing. Microstructural and compositional analysis was carried out using FESEM-EDS, EPMA, TEM, and XRD to examine TiC formation, distribution, and transformation characteristics. The modified sample was free of cracks and porosity, consisting of *in-situ* TiC precipitates embedded in a martensitic matrix, as confirmed by XRD. Optimization of TIG arcing parameters was controlled by dilution and TiC concentration, leading to significant improvements eventually average hardness increased 2.15 times and wear resistance 4.6 times compared to the base metal, highlighting the benefits of flux-assisted surface modification under TIG treatment without flux.

Li *et al*. [19] employed a diode laser with a rectangular spot for surface treatment of 1.0C–1.5Cr steel, supported by numerical simulations to develop an empirical equation predicting peak temperature. The latter showed a near-linear relation with the reciprocal square root of scanning rate. Laser treatment enhanced surface hardness but introduced heat-affected zone softening; under light loads, bearing capacity remained unaffected, while heavy loads caused slight reduction due to plastic deformation. Impact fractures initiated in the laser-hardened layer, propagating from intergranular to transgranular modes, with cementite particles observed along cracks. Reduced impact toughness was linked to brittleness of the hardened layer and residual stress, but preheating effectively improved toughness.

Zhang *et al*. [20] used plasma torch nitriding technique to M50 bearing steel by adjusting plasma currents between 120–160 A. The nitrided layer was analyzed for nitrogen content, phase formation, microstructure, hardness, and wear behavior using Vickers hardness testing, TEM, and wear measurements. Nitriding increased the nitrogen content from 0.00732 wt% to 0.416 wt% and produced a 2.51 mm thick nitrided layer with FeN0.076, $Fe_2N$, and $Fe_3N$ phases. Surface hardness increased from 241 HV0.2 to 778 HV0.2, while the wear coefficient and volumetric wear rate dropped to 32% and 70%, respectively. TEM revealed a martensitic structure with sub-surface precipitates refined from large irregular carbides to small, spherical carbon-nitrogen composites, reducing precipitate size by 41–68% and area by 2.3–3.7%, indicating best performance under bearing loads.

Mescheder *et al*. [8] carried out experiments on laser surface texturing of tapered roller bearings by changing the diameter, height, and density of circular textures. Tribological performance parameters including friction, wear, and fatigue life were evaluated under lubrication. Laser texturing significantly improved tribological behavior, achieving up to 18% torque reduction and notable enhancement in fatigue life, demonstrating the potential of surface texturing for demanding rolling contact applications.

Li *et al.* [21] applied textures of square shape with varying positions and density on GCr15 steel, and frictional and wearing tests were conducted in which graphene/5CB suspension was used as lubricate. The effects of dimple geometry on lubrication performance under starved conditions were analyzed, and surface chemistry was examined using XPS. Optimal lubrication performance was achieved with 10 μm dimple depth, 8% area density, and 100 μm diameter, reducing the friction coefficient to 0.031—a 32.6% reduction in comparison to not textured areas.

On reviewing the literature, a negligible number of studies is only available in systematic research on multi-step or combined surface treatments, their sequence effects, mechanistic understanding of tribological improvement. Research gaps include testing combined nitriding, laser texturing, and TiN coating under simultaneous wear-corrosion conditions relevant to bearing environments to comprehensively evaluate long-term durability. This work aims to evaluate and compare the tribological characteristics of AISI 52100 steel when subjected to different sequences of surface modifications. Specifically, the investigation focuses on three combinations: nitriding followed by TiN coating, nitriding followed by TiN coating and then laser texturing, nitriding followed by laser texturing and then TiN coating. The primary aim is to understand how the sequence of laser texturing and TiN coating, when applied after nitriding, influences key tribological parameters. These include the coefficient of friction (COF), frictional force, and overall wear behaviour under dry sliding. By comparing these combinations, the study seeks to identify the most effective surface treatment sequence for enhancing the wear resistance and reducing friction in AISI 52100 steel. This understanding could contribute to the development of more durable components for high-performance engineering applications.

## MATERIALS AND METHODOLOGY

### *Sample preparation*

The experiments were carried out on AISI 52100 bearing steel rods (composition: 0.95–1.10% C, 1.30–1.60% Cr, 0.15–0.35% Mn, 0.025–0.040% P, 0.25–0.45% Si, balance Fe) with a diameter of 8 mm and length of 30 mm, purchased from commercial suppliers. Rods were machined to ensure flat, polished end faces (surface roughness Ra < 0.1 μm) using SiC abrasive papers (up to 2000 grit) followed by diamond polishing. Prior to surface treatments, samples were ultrasonically cleaned in acetone for 10 min, moisture and contaminants were removed using nitrogen gas. Three sets of samples were prepared, each subjected to one of the following sequential surface engineering processes as shown in Table 1.

**Table 1.** Sequence and corresponding processes

| Sequence | Process | Description |
|---|---|---|
| 1 | *Nitriding + TiN Coating* | *Nitriding*: Plasma nitriding was performed as shown in Figure 1 (b), in a low-pressure chamber at 500°C for 10 h in a gas mixture of 75% $N_2$ and 25% $H_2$, with a bias voltage of -500 V. This resulted in a nitrogen diffusion layer depth of approximately 10–15 μm and a compound layer of 2–5 μm (ε-phase, $Fe_{2-3}N$)[22].<br>*TiN Coating:* Physical vapor deposition (PVD) *via* magnetron sputtering was applied immediately after nitriding. The chamber was evacuated to $10^{-6}$ mbar, and Ti targets were sputtered in an $Ar/N_2$ plasma (Ar flow: 50 sccm, $N_2$ flow: 20 sccm) at 400°C for 2 h, yielding a TiN coating with thickness of 2–3 μm [23]. The TiN coated sample is shown in Figure 1 (c and d) |
| 2 | *Nitriding + TiN Coating + Laser Surface Texturing* | *Nitriding and TiN coating:* as in Sequence 1.<br>*Laser Surface Texturing:* A femtosecond fiber laser (wavelength: 1064 nm, pulse duration: 200 fs, repetition rate: 80 MHz) was used for post-coating to create micro-dimples on the surface [24]. Dimples had a diameter of 50 μm, depth of 10 μm, and spacing of 100 μm (dimple density: 20%), covering 20% of the surface area. Laser power was 5 W, with scanning speed of 100 mm/s, performed in air [25]. |
| 3 | *Nitriding + Laser Surface Texturing + TiN Coating* | *Nitriding*: as in Sequence 1.<br>*Laser Surface Texturing*: as in Sequence 2, applied immediately after nitriding.<br>*TiN Coating*: as in Sequence 1, applied post-texturing. |

### *Wear testing*

Tribological performance was evaluated using a pin-on-disc tribometer as shown in Figure 1 (e) in dry sliding conditions at ambient temperature (25°C) and 50% relative humidity. Treated steel rods acted

as stationary pins sliding against rotating EN31 steel discs (hardness: 60 HRC, roughness Ra: 0.05 µm) under unlubricated conditions. Tests followed ASTM G99 standards [26].

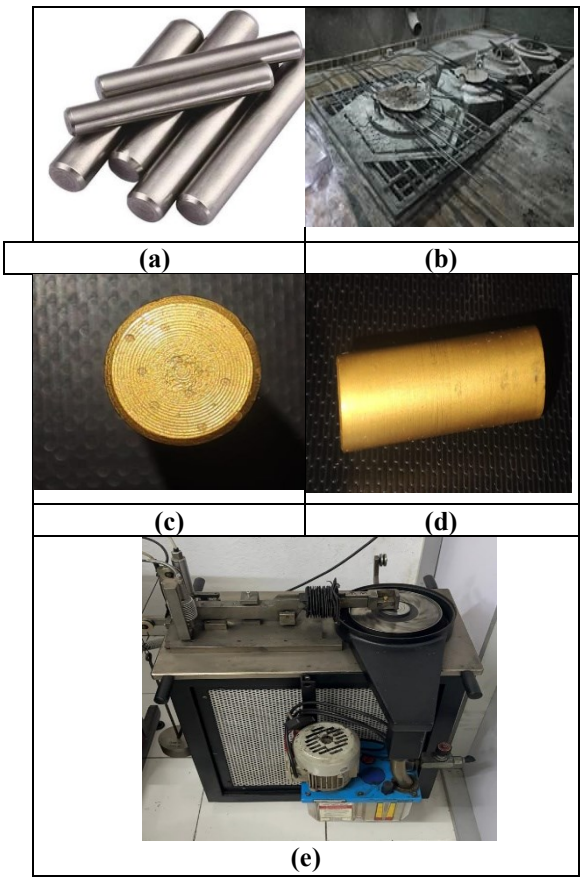


**Figure 1.** (a) AISI 52100 steel rod; (b) Salt bath nitriding process; (c) C.S view of TiN coated pin; (d) Longitudinal view of TiN coated pin; (e) Pin on disc experimental setup.

## RESULTS AND DISCUSSION

The bearing characteristics of AISI 52100 bearing steel were evaluated through pin-on-disc wear tests under dry sliding conditions, focusing on the influence of sequential surface engineering techniques of nitriding combined with TiN coating and laser surface texturing on coefficient of friction (COF) and wear loss. Three distinct process sequences were investigated: nitriding + TiN (Sequence 1), nitriding + TiN + laser texturing (Sequence 2), and nitriding + laser texturing + TiN (Sequence 3).

### *Coefficient of friction analysis*

Figure 2 reveals how the coefficient of friction varies for different sequences of nitride-coated surfaces and Figure 3 reveals the wear rate versus sliding distance for loads of 25 kN, 35 kN and 45 kNunder different normal loads (25N, 35N, and 45N), respectively. At 25N, the laser-textured nitride surface exhibits the highest coefficient of friction (1.0-1.2), while the nitride + TiN + laser textured coating shows lower, more stable friction (0.6-1.0), and the combination of nitride + laser + TiN provides intermediate performance. At 35N, the nitride + TiN coating exhibits a higher friction coefficient (around 1.0-1.2) after an initial low-friction period, suggesting a breakdown of the coating or surface modification which is shear-induced decohesion at textured protrusions.

Figure 4 depicts the cumulative wear loss (in µm) as a function of sliding distance for the surface-engineered AISI 52100 steel pins across the three sequences under progressive normal loads of 25 N (a), 35 N (b), and 45 N (c) in dry sliding against EN31 discs. Measurements were derived from LVDT height loss data, illustrating the cumulative progression of material removal and the pivotal role of treatment sequence indicating wear regimes from mild oxidative abrasion to severe delamination and ploughing. SEM images revealing flake ejections and subsurface cracks, while the laser-textured surfaces maintain relatively low and stable friction as shown in Figure 5.

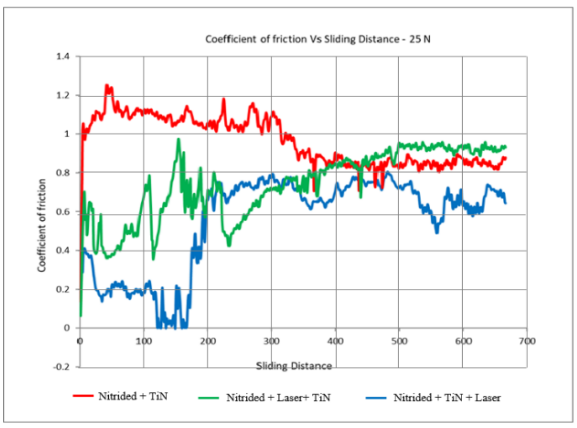


(a)

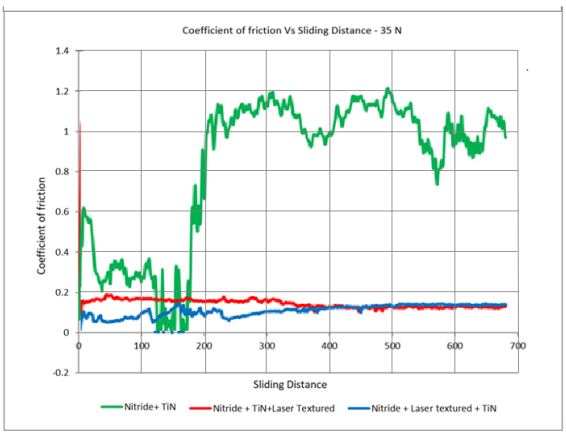


(b)

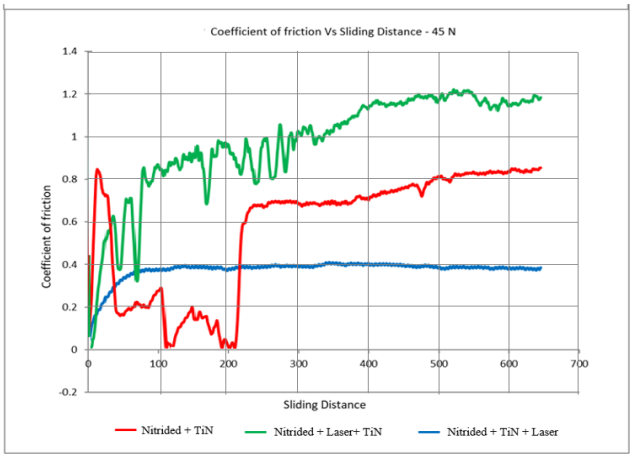


(c)

**Figure 2 (a-c).** Coefficient of friction *vs.* sliding distance for loads of 25 kN, 35 kN and 45 kN

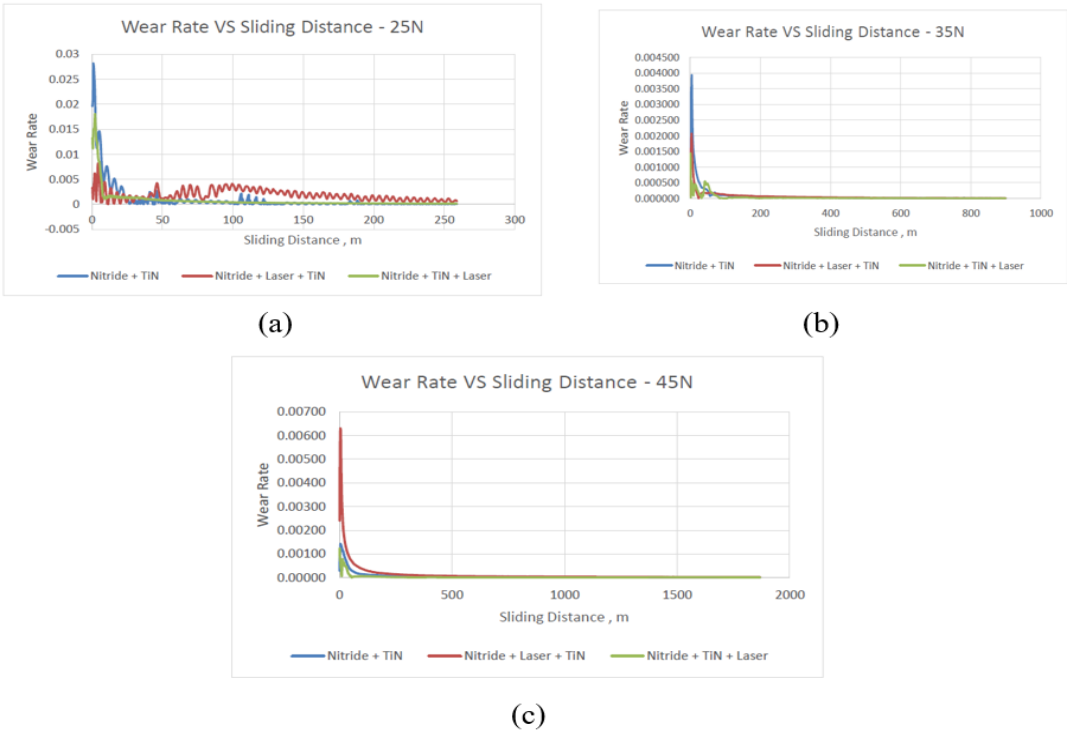


(a) (b)

(c)

**Figure 3 (a-c).** Wear rate *vs.* sliding distance for loads of 25 kN, 35 kN and 45 kN

The wear rate *versus* sliding distance plots at 25 N, 35 N, and 45 N loads show that all treated samples exhibit an initial running-in stage with a relatively high wear rate, which rapidly decreases and stabilizes over longer sliding distances. At 25 N, nitriding + TiN + laser treatments provide lower and more stable wear rates compared to nitriding + laser + TiN, indicating that the sequence of TiN deposition plays a crucial role in reducing wear. At 35 N, all samples demonstrate minimal wear rates after the initial stage, with negligible differences among treatments, reflecting the effectiveness of surface hardening and coating in withstanding moderate loads. The SEM examination. Figure 5 (a and b) reveals micro-fractures at dimple edges post-run-in, with EDX indicating transient Fe-Ti mixing from adhesive pull-out in nitriding + laser + TiN sequence (Figure 6 (a and b). At 45 N, the wear rates are very low and nearly identical across all treatments after an early transient stage, suggesting that the combined impact of nitriding and TiN coating provide resistance to wear, regardless of laser processing order. Overall, nitriding combined with TiN coating ensures superior wear resistance, and while laser processing contributes to surface modification, its effect is less significant at higher loads where the coating's hardness and load-bearing capacity impact the performance. The dimple-induced contact fragmentation is visible in SEM cross-sections confirming intact overlayers and

EDX homogeneity in Ti/N (Figure 5 (b). Sequence 1 (Figure 5 (a)) shows initial peaks (~0.004 µm/m) decaying to baseline, indicative of controlled oxidative wear on the smooth TiN, though EDX detects Ti oxidation. Sequence 3 initiates with the highest rate (~0.008 µm/m), plummeting after delamination exposes the nitride, there is also residual instability. EDX image shows fragmented TiN ejecta and EDS spectra. Figure 6(b) shows elevated subsurface O/Fe ratios.

The friction force *versus* sliding distance plots under different loads (25 N, 35 N, and 45 N) is shown in Figure 4. The graphs reveal that the sequence of surface treatments plays a decisive role in tribological performance. At 25 N, the nitrided + TiN + laser combination shows a more stable and relatively lower friction force compared to the other sequences although treatments involving laser modification exhibit higher initial fluctuations. Nitride + TiN sequence has high frictional force that leads to abrasive wear in exposed nitride surface irregularities, as SEM (Figure 5 (a)) pronounces ploughing tracks and EDX (Figure 6 (a)) reveals Fe-O enrichment from oxidative debris. At 35 N, nitriding + TiN and nitriding + TiN + laser maintain steady friction behavior in the range of 15–20 N, whereas nitriding + TiN + laser results in lower and less stable friction, indicating effective lubrication retention. Under the highest load of 45 N, all samples exhibit a running-in stage followed by stabilization, but nitriding + TiN + laser provides consistently lower friction compared to other sequences. Overall, the results indicate that nitriding enhances hardness and load support, while TiN coating significantly reduces adhesive wear and stabilizes friction [27].

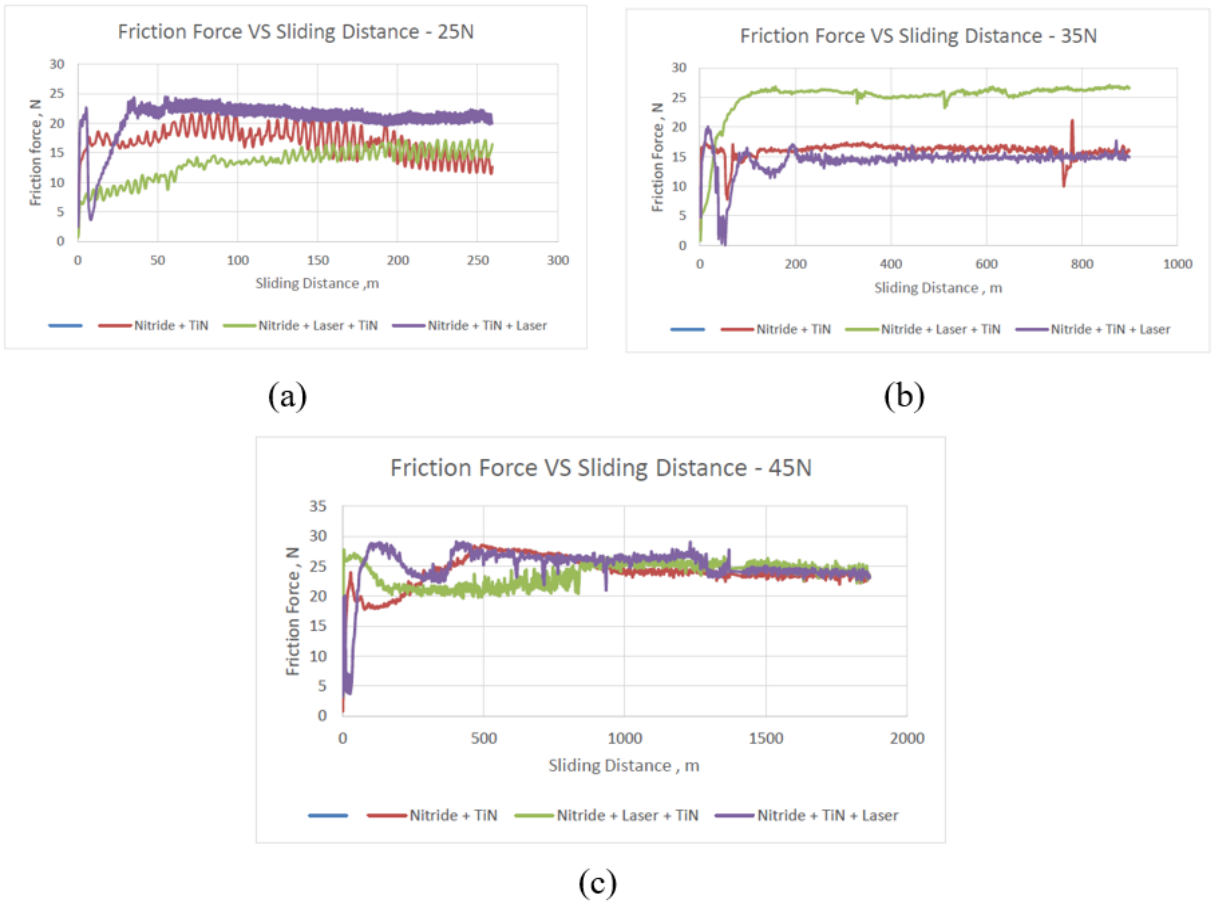


**Figure 4 (a-c).** Friction force *vs.* sliding distance for loads of 25 kN, 35 kN and 45 kN

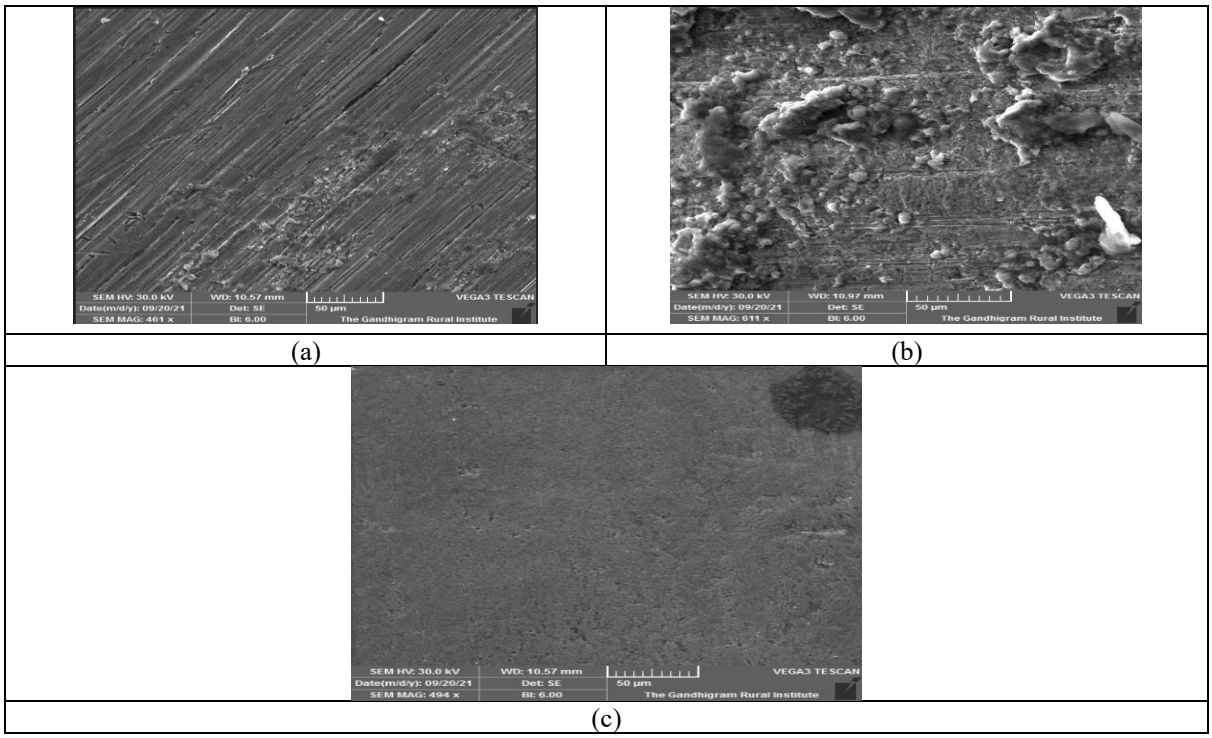


**Figure 5.** SEM images of (a) nitride + TiN, (b) nitride + laser + TiN and (c) nitride + TiN + laser

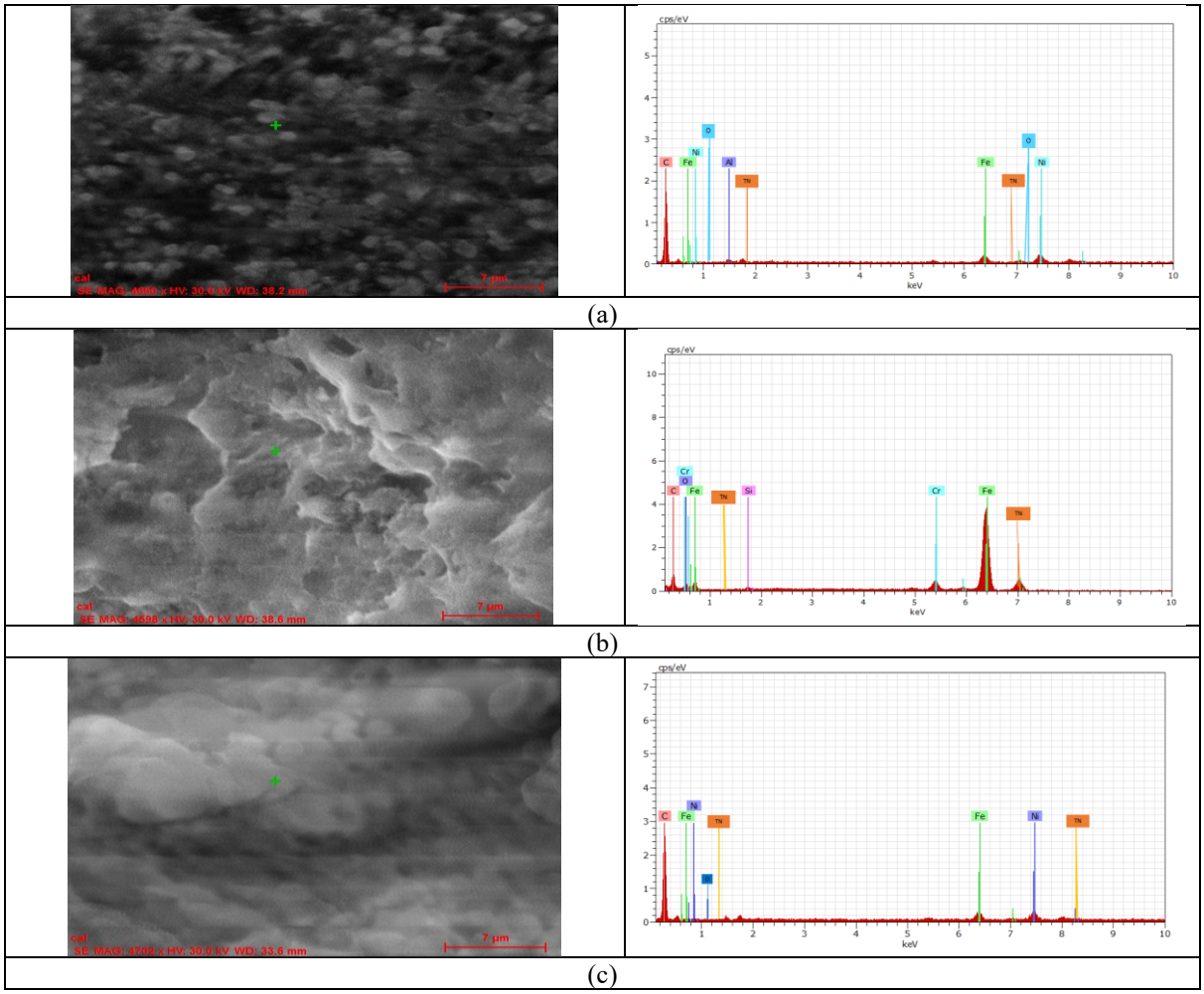


**Figure 6.** EDX images and spectra of (a) nitride + TiN, (b) nitride + laser + TiN and (c) nitride + TiN + laser

## CONCLUSION

This study demonstrates that the sequence of surface engineering treatments critically governs the tribological performance of AISI 52100 bearing steel under severe dry sliding conditions. Among the investigated configurations, the nitride + TiN + laser sequence exhibited the best performance, achieving wear losses below 5 μm and a stable low coefficient of friction (~0.13) even at 45 N over 2000 m of sliding. SEM/EDX analyses confirmed intact TiN layers, effective debris trapping within laser-textured micro-dimples, and minimal oxidation. In contrast, the nitride + laser + TiN sequence suffered catastrophic wear (>30 μm) and unstable friction due to poor TiN adhesion and coating delamination. The nitride + TiN baseline provided only moderate improvements (15–25 μm wear), highlighting the necessity of textural synergy. Overall, post-coating laser texturing was identified as a key strategy for maximizing wear resistance and frictional stability, with significant potential to extend bearing service life in high-load engineering applications.

***Declarations:***

***Funding statement:*** *No funding was received to assist with the preparation of this manuscript.*

***Competing interest:*** *The authors have no competing interests to declare that are relevant to the content of this article.*

***Author contribution statement:*** *conceptualization, investigation - R. Kumutha; supervision, project administration - S. Ilayavel; writing - review & editing - A. Idrish Khan; writing - review & editing - K. Suresh, writing – review & editing - Udhayakumar K, writing - review & editing - C. Anbumeenakshi; writing – original draft preparation - M. Balakumar.*

***Data availability statement:*** *The authors confirm that the data supporting the findings of this study are available within the article.*

***Research ethics:*** *Not applicable.*

***Use of large language models, AI and machine learning tools:*** *ChatGPT was used for language improvement.*

## REFERENCES

1. Y. Li, J. Zhang, X. Chen, H. Wang, L. Zhao, *Journal of Materials Research and Technology*, **30**, 8359 (2024).
2. R. C. Morón, J. A. Cabral-Miramontes, J. P. Flores-De los Rios, R. Martínez-Sánchez, *Materials Letters*, **320**, 132404 (2022).
3. F. Xu, Y. Liu, J. Zhang, Z. Wang, *Engineering Failure Analysis*, **152**, 107518 (2023).
4. C. Duan, S. Qu, X. Hu, S. Jia, X. Li, *Wear*, **494–495**, 204252 (2022).
5. N. Turali, A. K. Gupta, S. Kumar, P. Singh, *Engineering Research Express*, **6**(4), 045517 (2024).
6. C. A. K. Reddy, B. Venkatesh, D. Mayurnath, T. V. S. Narendra, K. Ajay, G. Jhala, *Materials Today: Proceedings*, in press (2024).
7. M. Łępicka, M. Grądzka-Dahlke, D. Pieniak, K. Pasierbiewicz, K. Kryńska, A. Niewczas, *Wear*, **422–423**, 68 (2019).
8. S. Gimeno, A. Fernández, J. A. del Val, M. Anglada, *Wear*, **522**, 204717 (2023).
9. T. Ibatan, M. S. Uddin, M. A. K. Chowdhury, *Surface and Coatings Technology*, **272**, 102 (2015).
10. V. Y. Bhalerao, S. S. Lakade, *Materials Today: Proceedings*, **55**, 441 (2022).
11. G. E. Morales-Espejel, V. Brizmer, *Tribology Transactions*, **54**(4), 625 (2011).
12. V. Tereshin, A. Pogrebnjak, V. Kshnyakin, V. Bondar, *Vacuum*, **73**(3–4), 555 (2004).
13. V. Y. Bhalerao, S. S. Lakade, *Materials Today Proceeding*, **55**, 441 (2022).
14. J. Wang, S. Qu, F. Lai, X. Hu, Y. Deng, X. Li, *International Journal of Fatigue*, **153**, 106487 (2021).
15. O. Unal, E. Maleki, I. Karademir, F. Husem, Y. Efe, T. Das, *Materials Science and Engineering B*, **285**, 115970 (2022).
16. D. Guo, P. Zhang, Y. Jiang, C. Song, D. Q.Tan, D. Yu, *Tribology International*, **169**, 107465 (2022).
17. S. Bin Humam, G. Gyawali, A. Amanov, T. H. Kim, S. W. Lee, *Surface and Coatings Technology*, **419**, 127293 (2021).
18. N. K. Paraye, S. P. Neog, P. K. Ghosh, S. Das, *Surface and Coatings Technology*, **405**, 126533 (2021).
19. Z. Xing Li, Y. Wang, Q. Liu, H. Zhang, *Materials Today Communications*, **35**, 106216 (2023).
20. H. Zhang, Y. Liu, Z. Wang, J. Chen, *Journal of Manufacturing Processes*, **124**, 1214 (2024).
21. S. Li, Y. Zhao, X. Wang, J. Liu, *Journal of Materials Research and Technology*, **18**, 3598 (2022).
22. G. Aktaş Çelik, K. Fountas, Ş. H. Atapek, Ş. Polat, E. Kamoutsi, A. D. Zervaki, *Lubricants*, **12**(5), 170 (2024).
23. Y Y. Ma, J. Hu, X. Dong, *Proceedings of the Institution of Mechanical Engineers, Part J: Journal of Engineering Tribology*, **236**(4), 786 (2022).
24. D. G. Coblas, A. Fatu, A. Maoui, M. Hajjam, *Proceedings of the Institution of Mechanical Engineers, Part J: Journal of Engineering Tribology*, **229**(1), 3 (2015).
25. A. Kovalchenko, O. Ajayi, A. Erdemir, G. Fenske, I. Etsion, *Tribology Transactions*, **47**(2), 299 (2004).
26. H. So, *Tribology International*, **29**(5), 415 (1996).
27. R. Kumutha, I. Sivakumaran, M. Mariappan, B. Rajendran, *Chemical Industry and Chemical Engineering Quarterly*, **30**(4), 295 (2024).

*Selected papers presented at the Conference "Alternative Energy Sources, Materials and Technologies" (AESMT'25), 13 - 14 May, 2025, Sofia, Bulgaria*

*Bulgarian Chemical Communications, Volume 58, Issue 1 (pp. 103-108) 2026 DOI: 10.34049/bcc.58.1.AESMT25-18*

# Photoadsorption processes on the surface of silicon dioxide

T. Tusseyev, K.D. Baizhumanov*, M.A. Zhumanov, B. Amir, A.B. Sharipkhanov

*Al-Farabi Kazakh National University, Department of Thermophysics and Technical Physics, 71 Al-Farabi Avenue, Almaty, Kazakhstan*

Received: December 09, 2025; Revised: January 27, 2026

The photoadsorption of $O_2$ on $SiO_2$ was investigated as a function of pre-treatment temperature varying from 200 to 1000 °C. The maximum photoadsorption activity was observed at a pre-treatment temperature of 800 °C. Photosorption activity is dependent on both intensity and wavelength of the incident light. The relationship between photoadsorption rate and wavelength follows a logarithmic trend. Dehydroxylation and dehydration of the silicon dioxide samples were studied using IR spectroscopy. It was found that UV irradiation leads to a decrease in the intensity of OH-group signals, while oxygen photoadsorption results in a partial restoration of surface hydroxyl groups.

**Keywords:** Photosorption, dehydroxylation, silicon dioxide, light intensity, IR spectra, pre-treatment temperature

## INTRODUCTION

Photosorption is defined as: adsorption, typically chemisorption (a stoichiometric reaction of adsorbate molecules with a solid surface), initiated by light absorbed by either the adsorbate or the adsorbent [1]. This can be represented by the following equation [2]:

$$A + Cat + hv \rightarrow ACat$$

where A denotes adsorbate molecules, ACat represents photosorbed species.

Photoadsorption processes have been studied extensively over a long period (the earliest investigations into photosorption and photodesorption date back to the 1930s). However, a comprehensive understanding of all aspects in this field is still missing. Photosorption phenomena can serve as model systems for photocatalytic reactions, aiding in the study of more complex photocatalysis scenarios. Of particular interest, crucial for catalysis and related fields, are the mechanisms of catalytically active light energy absorption and energy transfer between the catalyst and adsorbed molecules.

Equally important is the physics of photo-adsorption processes themselves, as the results obtained can be useful for understanding the mechanisms of phenomena occurring on the surface of semiconductors and dielectrics. For example, such phenomena include the photoconductivity of thin films (widely used in the electronics industry), spectral sensitization of the internal photoeffect in semiconductors, and so on [3-6].

Photoexcitation of wide band gap solids ($E_g$>3eV) is inherently complex. In heterogeneous gas/solid systems, these processes often cannot be simplified to elementary interactions.

It is conventional to distinguish between photoelectrically active and photoelectrically inactive light absorption, depending on the generation of free charge carriers in the solid upon illumination (see, for example, [6]). Light quantum absorption can be associated with regular crystalline regions (fundamental or intrinsic absorption), as well as with crystal lattice imperfections, i.e., intrinsic and extrinsic lattice defects (see, for example, [5]).

Intrinsic defects include vacancies, interstitial atoms, and their aggregates (point or zero-dimensional defects).

Amorphous silicon dioxide (silica) is a crucial technological material widely employed in numerous applications [7-10]. Silica is predominantly associated with optoelectronic applications, such as optical fibers (OFs), and as a gate insulator in metal-oxide-semiconductor field-effect transistors (MOSFETs) [8]. In optical fibers, silica provides high transparency across a broad wavelength range, enabling light transmission over long distances with exceptional speed, stability, and, importantly, reliability. Silicon-based semiconductor technology has long relied on silica due to its large band gap [11, 12].

A review of the literature reveals widespread interest in photosorption phenomena, and research in this area remains highly relevant [16-20].

* To whom all correspondence should be sent:
Email: *kadirbek_79@mail.ru*

## RESULTS AND DISCUSSION

The sample was pre-treated as follows: initial annealing in air for 72 h with intermittent evacuation, followed by heating in oxygen at 400°C. Subsequently, prior to each experiment, the sample underwent heating in oxygen for one h at 400 °C and evacuation under vacuum for 30 min at a defined temperature. This pre-treatment protocol effectively removes traces of organic contaminants from the surface.

The pre-treatment temperature of $SiO_2$ varied from 200 to 1000°C. Before each experiment, the purity of the sample was checked using the method described above.

Our selection of pre-treatment temperatures was based on the following considerations: at 200°C, physically adsorbed water (hydrogen-bonded water) is removed from the $SiO_2$ surface, while at 400°C, coordination water is also eliminated. At 600-1000°C, the surface exhibits varying hydroxyl group densities. At 600 °C, hydrogen-bonded OH-groups are still present, whereas at higher temperatures only isolated OH-groups remain. Furthermore, at temperatures exceeding 600 °C, the effect of $SiO_2$ sintering becomes relevant, potentially reducing the specific surface area of the sample.

The experimental results of $O_2$ photoadsorption on $SiO_2$ are presented in Figures 1-6.

Oxygen photoadsorption on silicon dioxide occurs at all pre-treatment temperatures considered [13]. The initial photoadsorption rates, depending on the calcination temperature, can differ by 2-3 orders of magnitude (Fig. 1). Increasing the calcination temperature to 1000°C causes a sharp decrease (5-6 times) in the photo-adsorption rate compared to the previous temperature. Presumably, at this temperature and above, surface sintering becomes significant, possibly leading to a decrease in the specific surface area of $SiO_2$.

The observation of $O_2$ photoadsorption beyond the long-wavelength edge of the intrinsic absorption band suggests the presence of photosorption sites on silicon dioxide, activated by impurity absorption. The 'pre-irradiation memory effect' (Solonitsyn effect), characterized by gas adsorption upon admission to a pre-irradiated sample, was not observed on $SiO_2$. However, post-adsorption, a type of 'memory effect', is evident on $SiO_2$. Even after the illumination is turned off, adsorption continues briefly, indicating that the adsorbent 'remembers' the irradiation. In our experiments, this post-adsorption effect was observed only at $T_{pre} \geq 700$°C. At this treatment temperature, the after-effect duration (τ) is approximately 5 sec. Our findings indicate that τ increases proportionally to the pre-treatment temperature, is independent of the irradiation duration, and weakly dependent on the amount of pre-adsorbed oxygen. At $T_{pre} = 900$ °C, τ ranges from 1 to 1.5 min.

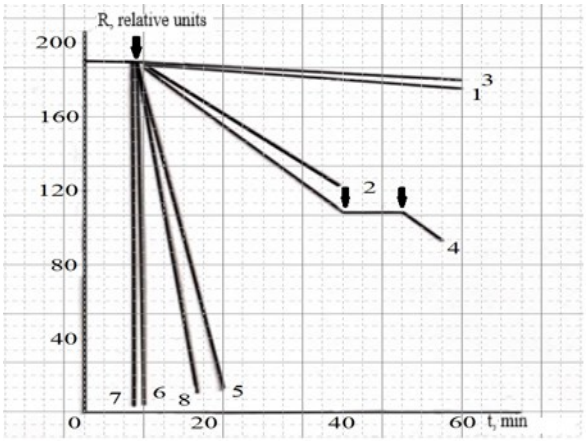


**Figure 1.** Kinetics of $O_2$ photosorption on $SiO_2$ at 1 – 400 °C, 2 - «dirty» sample, 3 – 500 °C, 4 – 600 °C, 5 – 700 °C, 6 – 800 °C, 7 – 900 °C, 8 - 1000 °C. The arrows indicate the moments of radiation exposure.

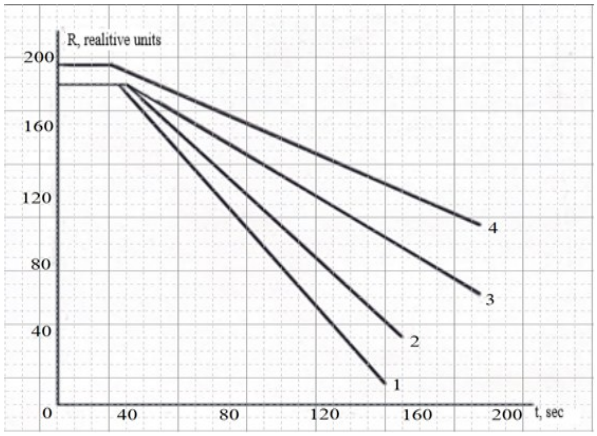


**Figure 2.** Kinetics of oxygen photosorption on $SiO_2$ at different UV radiation intensities. 1 - I=Io, 2 - I=0.89Io, 3 - I=0.69Io, 4 - I=0.39Io.

Figure 2 shows the kinetic curves (photo-barograms) of $O_2$ photo-adsorption on $SiO_2$ ($T_{pre}$= 900 °C) at different intensities of light incident on the sample. Light intensity was varied by adjusting the distance between the light source and the sample. In the figure, the intensities are in the ratios of 1:0.78:0.63:0.35, while the photoadsorption rates are in the ratios of 1:0.83:0.56:0.36. As can be easily noticed, the photoadsorption rate has a linear dependence on the intensity of the incident light, indicating a single-photon nature of the photosorption process, at least in the initial section of the kinetics.

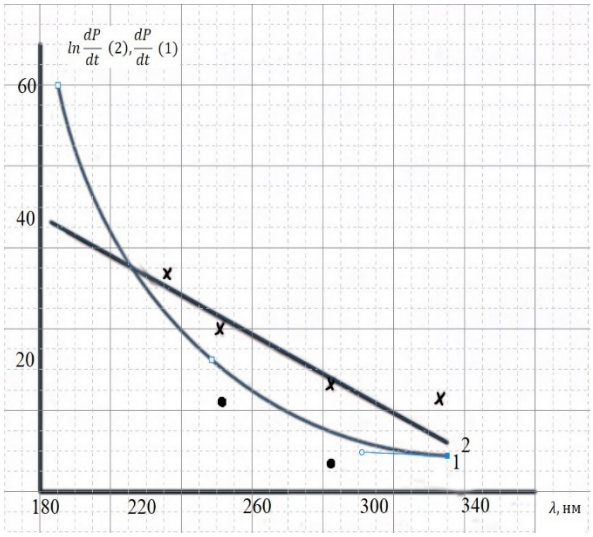


**Figure 3.** Spectral characteristics of $O_2$ photosorption on $SiO_2$ ($T_{pre}$ = 1000 °C)

As seen in Figure 3, as λ decreases from 340 to 200 nm and below, the rate of photosorption increases by 2–3 orders of magnitude. The dependence of the initial rate on λ follows a pattern of the $ln\frac{dP}{dt} \sim \frac{1}{\lambda}$ type (Figure 3, curve 2), meaning that as it approaches the intrinsic absorption region (bandgap width of $SiO_2$, $E_g$ = 10 eV), the rate increases.

In the subsequent experiments, where adsorption processes in the $SiO_2$ – $O_2$ system under irradiation were investigated, manometric and spectrometric (IR and mass spectrometry) methods were employed. Photosorption processes in these systems were examined in relation to the pre-treatment of the adsorbents [14].

Figure 4 presents the IR spectrum of silica gel synthesized in the laboratory after thermal vacuum treatment for 6 h at different temperatures (25-800 °C). A distinctive spectral feature is a narrow, intense absorption band at 3750 $cm^{-1}$, superimposed by broader bands at 3665, 3580, and 3400 - 3300 $cm^{-1}$ on the lower frequency side. The intensity of these broader bands is strongly dependent on the degree of hydroxylation of the samples (103, 105, 107). The 3750 $cm^{-1}$ band is attributed to isolated, non-interacting OH - groups. Its intensity decreases more gradually with increasing sample pre-treatment temperature in vacuum (T = 300 °C). In the region of Si-OH deformation vibrations, a broad band appears at 790-870 $cm^{-1}$, narrowing with increasing treatment temperature. The intensity of the 3665 $cm^{-1}$ band significantly weakens with increasing temperature from 300-400 °C and completely disappears at 520-620 °C. This band is generally assigned to hydrogen-bonded OH-groups [8]. An absorption band at 3580 $cm^{-1}$ is also observed in the IR spectra, with its intensity starting to diminish noticeably after sample evacuation at 300-350 °C. Complete disappearance occurs at 400-450 °C. Several interpretations exist for this band's assignment. However, its appearance is observed subsequent to the emergence of the 3665 $cm^{-1}$ absorption band associated with hydrogen-bonded OH-groups. Therefore, it can be inferred that the 3580 $cm^{-1}$ absorption band is due to water molecules adsorbed on surface hydrogen-bonded OH-groups.

In the frequency range of 3400–3300 $cm^{-1}$, a broad band is observed, attributed to the physical adsorption of water [7, 8].

Its intensity decreases upon evacuation even at room temperature, and it completely vanishes after heating with simultaneous evacuation at 150-200 °C.

The intensity of the band at 1627 $cm^{-1}$ decreases considerably upon evacuation up to 200 °C (Figure 4).

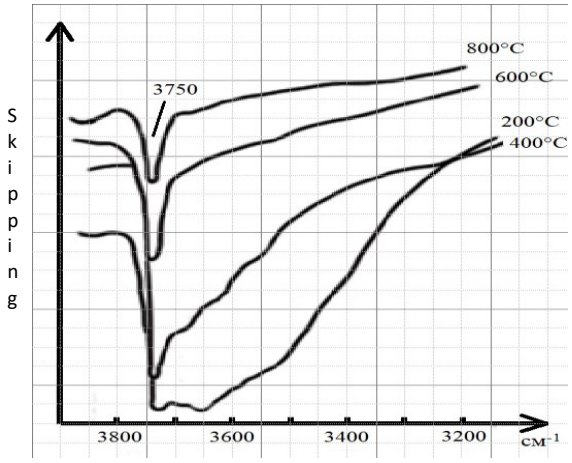


**Figure 4.** IR spectra of $SiO_2$. 1- $T_{pre}$ = 200 °C, 2 - 400 °C, 3 - 600 °C, 4 - 800 °C

The effect of UV irradiation on $SiO_2$ is characterized by the appearance of new absorption bands, and a complex evolution of the hydroxyl coverage of silica gel.

The silica gel samples under investigation were subjected to thermal vacuum treatment at 200, 400, 600, and 800 °C for 6 h. Absorption spectra were recorded in the frequency range of 800-3800 $cm^{-1}$ after 1, 4, and 5 h of irradiation. Concurrently, the kinetics of oxygen photoadsorption on silicon dioxide was also monitored.

Selecting multiple pre-treatment temperatures anticipates that the photosorption process will occur on surfaces with varying degrees of dehydration across this broad temperature range. Samples treated at 600 and 800 °C contain only isolated hydroxyl groups on their surface (absorption band at 3750 $cm^{-1}$

[1]) (Figures 5 and 6). Treatment at 400°C does not completely remove hydrogen-bonded OH-groups, hence absorption is still present in the 3300-3600 $cm^{-1}$ region. The sample evacuated at 200 °C contains water in addition to these, and the concentration of isolated OH-groups is low due to screening by physically adsorbed water.

Introducing oxygen to a partial pressure of $7\times10^{-2}$ mm Hg into the chamber containing the sample pre-treated at 200°C does not alter the spectral profile. After one h of UV irradiation, absorption bands at 1470 and 1520 $cm^{-1}$ appear, along with a slight decrease in the intensity of the isolated OH-group absorption band. In the water deformation vibration region, a band at 1627 $cm^{-1}$ emerges. With further irradiation for 4 h, the 3750 $cm^{-1}$ absorption band continues to decrease, while a band at 3665 $cm^{-1}$ appears on the lower frequency side, indicative of hydrogen-bonded OH-group formation. Bands at 1470, 1520, and 1700 $cm^{-1}$ remain unchanged.

The absorption spectra of the $SiO_2$ sample pre-treated at 400 °C reveal a complex nature of the photosorption process. In addition to absorption bands at 1470, 1520, and 1700 $cm^{-1}$, bands appear in the 3600-3700 $cm^{-1}$ range, and a weak peak emerges at 1720 $cm^{-1}$ in the water deformation vibration region. Initially, irradiation leads to an increase in the 3750 $cm^{-1}$ band, followed by a decrease upon prolonged irradiation.

A similar pattern is observed when investigating photosorption on samples treated at 600 °C. This variation in OH-group concentration suggests the possibility of not only a radical adsorption mechanism for oxygen, involving photosorption of hydroxyl groups and formation of free radicals as adsorption sites for oxygen, but also an alternative process. This alternative could be the oxidation of residual organic contaminants, accompanied by water formation and subsequent dissociation. Likely, the simultaneous occurrence of these two processes with different kinetics leads to the observed trend in the OH-group concentration curve.

On the sample treated at 800 °C, the OH-group intensity also exhibits a change following a curve with a maximum. Even upon oxygen introduction, weak peaks at 1470, 1520, 1627, and 1700 $cm^{-1}$ are observed. After one hour of irradiation, the intensity of the 1470 and 1520 $cm^{-1}$ peaks increases, a weak peak at 1720 $cm^{-1}$ appears, and the intensity of the OH-group absorption band diminishes. A band at 3680 $cm^{-1}$ emerges on the shorter wavelength side (hydrogen-bonded OH-groups). The intensity of absorption bands at 1700, 1720, 1450, and 1520 $cm^{-1}$ increases. Following another hour of irradiation, the OH-group intensity further increases, water becomes more pronounced (1627 $cm^{-1}$), and an absorption band at 3580 $cm^{-1}$ appears in the stretching vibration region. Subsequent two-hour irradiation results in a decrease in OH-group intensity.

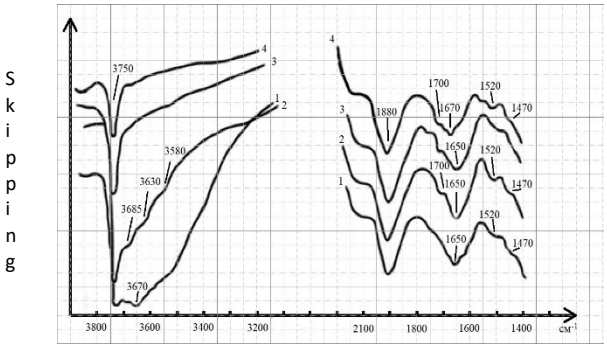


**Figure 5.** IR spectra of $SiO_2$ containing photosorbed oxygen. 1- $T_{pre}$ = 200 °C, 2 - 400 °C, 3 - 600 °C, 4 - 800 °C

To further elucidate the role of residual organic impurities in oxygen photosorption, the silica gel sample was subjected to a specific cleaning procedure. This involved sequential annealing at 600 °C in oxygen followed by evacuation at the same temperature for 30-40 min. This cycle was repeated 5-6 times, followed by a three-hour evacuation, and then the sample spectrum was recorded. Unfortunately, this rigorous treatment did not resolve the issue, as absorption bands at 1470, 1520, and 1700 $cm^{-1}$ were already present in the initial spectrum of the treated sample. These bands are typically observed in simply vacuum-treated samples only after oxygen admission and subsequent irradiation. The oxygen adsorption rate on the sample treated at 600 °C in oxygen was lower compared to the sample subjected to simple vacuum pre-treatment. This suggests that the sample is likely saturated with oxygen during the treatment process itself. Hydroxyl groups also exhibit different behavior. First, the 3750 $cm^{-1}$ absorption band displays a shoulder on the lower wavelength side. Second, the intensity of this band remains nearly constant for up to nine h of irradiation. After 9 h of UV exposure, the intensity of the 3750 $cm^{-1}$ band decreases by approximately 30%.

With UV irradiation of $SiO_2$ in the presence of oxygen, our experiments demonstrated intense oxygen adsorption, which is irreversible at room temperature. The photosorption rate, the maximum amount of photosorbed oxygen, and the reverse desorption effect are dependent on the sample pre-treatment temperature, light intensity, experimental temperature, surface cleaning conditions, and other factors that are not always controlled.

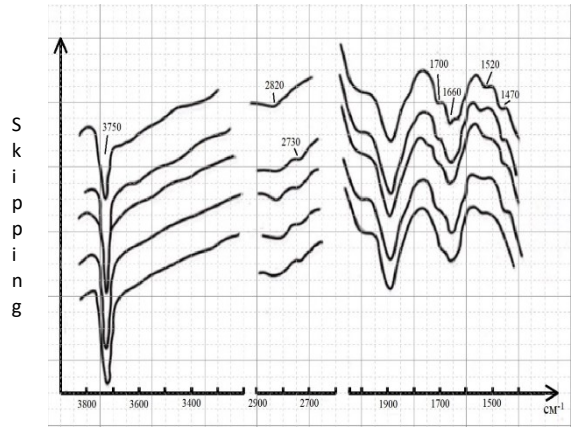


**Figure 6.** IR spectra of silicon dioxide irradiated with UV rays. 1- initial spectrum ($T_{pre}$ = 600 °C), 2 - oxygen introduction, 3 - after 1 h of irradiation, 4 – 2 h, 5 - 4 h

The pre-treatment temperature ($T_{pre}$ = 473-1273 K), the selection of which was justified previously, has a significant impact on the properties of $SiO_2$ described above. Increasing the pre-treatment temperature up to 1173 K results in a corresponding increase in the oxygen photosorption rate on $SiO_2$. However, starting from $T_{pre}$ = 1173 K, the photosorption rate decreases, potentially due to surface sintering of $SiO_2$, which can reduce the sample surface area.

The increase in photosorption rate with rising pre-treatment temperature can be attributed to an increase in the number of strained siloxane bridges of type  [8], which are readily broken under UV irradiation and in the presence of gas molecules, leading to adsorbate adsorption. Above 673K, hydroxyl groups decompose, forming strained siloxane bridges [8]. The formation of strained siloxane bridges due to hydroxyl group decomposition during $SiO_2$ heating can be indirectly observed using mass spectrometry. This process releases water and hydrogen. At relatively low pre-treatment temperatures, water is predominantly released, while at temperatures above 673 K, hydroxyl group decomposition *via* hydrogen abstraction becomes dominant. In both cases, the broken bonds are reformed according to the following schemes:

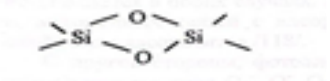
(1)

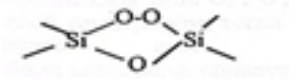
(2)

resulting in the formation of strained siloxane bridges. This is likely not the sole mechanism of oxygen adsorption. Based on general concepts of donor-acceptor interactions between adsorbed molecules and oxide adsorbent surfaces [21, 22], oxygen adsorption on $SiO_2$ may also occur through formation of coordination bond.

In our experiments, where IR spectra of $SiO_2$ with photosorbed $O_2$ were analyzed, absorption bands at 3540 (BeO), 3580 ($SiO_2$) $cm^{-1}$ in the stretching vibration region, and bands at 1640, 1627 $cm^{-1}$ in the deformation vibration region were observed. These are typically attributed to coordination-bonded water molecules [21]. This may be a consequence of organic contaminant oxidation, which is difficult to eliminate completely. Alternatively, water could form from the reaction of hydrogen with oxygen, released from OH-groups upon UV irradiation, according to:

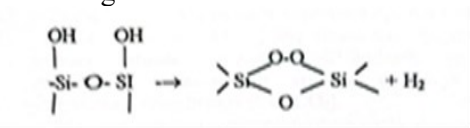
(3)

A possible representation of this reaction is:

$$O_2 \rightarrow O + O \quad (4)$$

$$H_2 + O \rightarrow H_2O \quad (5)$$

$$H_2 + 1/2\ O_2 \rightarrow H_2O \quad (6)$$

Water can also be adsorbed *via* hydrogen bonding, as indicated by the presence of bands at 3590 (BeO), 3665 $cm^{-1}$ ($SiO_2$), which are characteristic of hydrogen-bonded water molecules [23, 24].

Coordination and hydrogen bond formation with adsorbed molecules appear to be common properties of adsorbents [21, 22].

Conversely, photosorption of oxygen on $SiO_2$ with the formation of ion-radicals like $O_2^-$, $O_2^{2-}$, $O^{3-}$ is not observed at either room or liquid nitrogen temperature [15].

For oxygen photosorption on $SiO_2$, adsorption with the cleavage of strained siloxane bridges seems to be energetically more favorable than radical oxygen species formation.

Photooxidation of organic impurities is another pathway for oxygen consumption during photosorption. Although our experiments included prolonged sample annealing in oxygen, complete removal of surface organics cannot be definitively confirmed. IR spectroscopy data indicate that during oxygen photosorption, absorption bands at 1470, 1520, and 1720 $cm^{-1}$, associated with various organic compounds, are detected and their intensity increases, suggesting their involvement.

Impurity centers represent another potential type of adsorption sites. In many oxides and alkali halide crystals exhibiting photosorption activity, the action spectrum extends significantly beyond the long-

wavelength edge of intrinsic absorption. Our data on the action spectrum of oxygen photosorption on $SiO_2$ demonstrate that photosorption is possible at certain pre-treatment temperatures (above 873 K) and beyond the intrinsic absorption region. This implies that impurity absorption or absorption by crystal lattice defects is also active.

## CONCLUSION

The photoadsorption of oxygen on silicon dioxide is dependent on the pre-treatment temperature, reaching a maximum at 800°C.

The spectral dependence of $O_2$ photoadsorption on $SiO_2$ follows a logarithmic function. The photoadsorption rate exhibits an inverse relationship with light intensity.

Strained siloxane bridges and impurity atoms can act as photosorption centers. Photooxidation processes may also occur.

The binding energy of adsorbed molecules is influenced by the adsorbent pre-treatment temperature. Higher pre-treatment temperatures result in higher thermal stability of adsorbed molecules. For samples treated at 1173 K, adsorbed oxygen molecules remain stable up to 773 K and above. In contrast, for pre-treatment temperatures of 673–873 K, the surface is typically completely desorbed at significantly lower temperatures (473–673 K).

Regarding the 'memory effect' on $SiO_2$, our experiments only revealed the post-irradiation effect, which was also dependent on the pre-treatment temperature (increasing with temperature).

## REFERENCES


1. N. Serpone, A. V. Emeline, *Int. J. Photoenergy,* **4,** 91 (2002).
2. V.K. Ryabchuk, *International Journal of Photoenergy*, **6**, 95 (2004).
3. V.L. Bonch-Bruevich, S. G. Kalashnikov, Physics of Semiconductors, Nauka, Moscow, 1990, in Russian.
4. V. S. Zakharenko, E. B. Daibova, *High Energy Chemistry*, **54** (4), 237 (2020).
5. V. Sushko, A. L. Shluger, *Surface Science*, **421,** L157 (1999).]
6. V.G. Baru, F. F. Wolkenstein, The effect of irradiation on the surface properties of semiconductors, "Nauka", 1978, p. 288.
7. O.V. Dementieva, *Colloidal Journal,* **82(**5), 523 (2020).
8. G.D. Chukin, Surface chemistry and structure of dispersed silica, Moscow, Paladin Printing House, Printa LLC, 2008.
9. N. Blaz Winkler, Oxygen-excess related defects in SiO2-based materials: coupling theory and experiments. Optics [physics.optics]. Université de Lyon; Université de Nova Gorica (Nova Gorica, Slovénie), 2019. English. ffNNT: 2019LYSES014ff. fftel-03262513f.
10. S. Girard, A. Morana, A. Ladaci, Th. Robin, L. Mescia, J.-J. Bonnefois, M. Boutillier, J. Mekki, et al., *Journal of Optics*, **20**, 093001 (2018).
11. V. Titov, A. A. Lisachenko, *Kinetics and Catalysis*, **62**(1), 29 (2021).
12. V.V. Titov, N. G. Filosofov, *Solid State Physics,* **58** (9), 1709 (2016).
13. A.A. Murashkina, A.V. Rudakova, G.V. Kataeva, V.K. Ryabchuk*, Fundamental Research,* **12** (part 2), 276 (2014).
14. V.V. Titov, A.A. Lisachenko, M.E. Labzovskaya, I.K. Akopyan, B.V. Novikov, *J. Phys. Chem. C*, **123**(45), 27399 (2019).
15. I. H. Hakobyan, M. E. Labzovskaya, B. V. Novikov, A. Y. Serov, N. G. Filosofov, N. R. Grigorieva, *Phys. Solid State*, **62**(11), 2138 (2020).
16. D. S. Shtarev, R. Kevorkyants, M. S. Molokeev, A. V. Shtareva, *Inorganic Chemistry,* 59 (12), 8173 (2020).
17. A. V. Emeline, V. N. Kuznetsov, V. K. Ryabchuk, N. Serpone, *Environmental Science and Pollution Research*, **10**, 3666 (2012).
18. D. Zhang, *Acta Chimica Slovaca,* **6**, 141 (2013).
19. S. Keerthana, R. Yuvakkumar, G. Ravi, P. Kumar, M. S. Elshikh, Hussein H. Alkhamis, A. Alrefaei, D. Velauthapillai, *Chemosphere,* **270**, 129498 (2021).
20. M.M. Sajid, N.A. Shad, Y. Javed, S.B. Khan, Zh. Zhang, N. Amin, H. Zhai, *Surf. Interfaces*, **19**, 100502 (2020).
21. Yu. M. Kiselyov, N.A. Dobrynina, Chemistry of coordination compounds, Academy Publishing house, M., 2007, p. 352.
22. M.N. Sokolov, A.L. Gushchin, D.G. Samsonenko. Coordination chemistry: in 2 hours: a textbook, Novosibirsk State University. Un-T. Novosibirsk: CPI NSU, 2021. Part I. Electronic structure, stability, reaction mechanisms, non-aqueous solvents. ISBN 978-5-4437-1161-4, ISBN 978-5-4437-1234-5.
23. V.V. Eremin, N.E. Kuzmenko, V.V. Lunin, A.A Drozdov, The hydrogen bond, Moscow, Bustard, 2012, p. 183.
24. T. Coleen Nemes, J. Laconsaya Croix, J. Morrison Galbraith, *Physical Chemistry Chemical Physics,* (2018). DOI: 10.1039/C8CP03920.

*Bulgarian Chemical Communications, Volume 58, Issue 1 (pp. 109-119) 2026 DOI: 10.34049/bcc.58.1.AESMT25-29*

# Investigation of capillary-porous coatings made of mineral media

A. A. Genbach[1], D. Yu. Bondartsev[1], A. G. Georgiev[2]

[1]*Almaty University of Power Engineering and Telecommunications named after G. Daukeyev, 050013, 126 Baitursynov Str. Almaty, Republic of Kazakhstan*

[2]*University of Telecommunications and Posts, Department of General Engineering, 1 Acad. Stefan Mladenov Str., 1700 Sofia, Bulgaria*

Received: December 16, 2025; Revised: February 01, 2026

Thermal loads for cooling systems with natural material coatings were investigated. The conditions of material spraying on a heating surface were determined. The research had implications for the thermal protection of the equipment. Two most intensive processes were simultaneously used in the cooling methd: (i) interaction of turbulent jet with a barrier and (ii) boiling of the coolant on the heating surface. Devices for spraying of coatings by detonation high-temperature flares were developed. A method of holographic interferometry and high-speed filming was used in the research. Heat fluxes, temperatures, flow rates, and pressures of liquid and gas streams were measured in the experiments. The fabrication of coatings from natural materials can divert higher critical loads and stabilize the surface control process. The characteristics of torches for the generation of supersonic high-temperature detonation flares during the spraying of coatings from powders of natural materials were selected. Due to supersonic flow velocity, spraying occurs without melting of powder particles. The oxidizer excess coefficient varied in the range of 0.3÷0.8; the jet plume temperature (3500÷850) $^0$C; the jet length (0÷0.16) m; the jet radius (3÷10)×10$^{-3}$ m. The proposed heat exchange mechanism is effective for the process of spraying particles (powders) of mineral media on a heat exchange surface.

**Keywords:** heat transfer, coatings, mineral media, combustion chamber, nozzle, heat protection.

## INTRODUCTION

Natural materials such as tuffs [1, 2], marbles [3, 4], quartzites [5, 6], granites [7, 8], teschenites [9] and bentonites [10] have great potential for high-temperature and high-intensity applications, especially in fields such as thermal power generation [11], cooling systems [12-15] and thermal protection [16]. These materials have long been studied and applied in various fields of renewable energy, construction, engineering, mechanical engineering, and materials science, but their use as coatings for thermal power equipment is a relatively new and promising area [17].

Modern powder materials are not only able to significantly improve the thermal resistance and efficiency of systems, but also provide a high degree of protection against thermal damage, which in turn contributes to increasing the reliability and extending the service life of equipment [18]. The development of new technologies and methods of processing natural materials opens new horizons for their application in a wide variety of industries.

It is highly relevant to conduct scientific studies of heat transfer in capillary-porous natural materials. As such materials rocks such as tuffs, marbles, quartzites, granites and teschenites were chosen. Powders were made from them and sprayed onto the substrate. Based on the physical model in a real capillary porous structure, the heat conduction equations of the thermoelastic problem were written. The solution was obtained for the limiting values of the heat fluxes of melting $q_{\text{mel.}}$, compression $q_{\text{com.}}$ and stretching $q_{\text{ten.}}$, causing the corresponding thermal stresses $\sigma$ [1, 6]. The model was verified by experiment using high-speed filming of the formed particles (husks) with SKS-1M.

Previously, a scientific research methodology [4] was constructed with an integral experiment [17] to test nine combustion chambers of a thermal tool [6] designed for processing natural mineral media. High-speed filming was used to elucidate the nature of fracture. Along with the study of natural capillary-porous coatings for their limiting state $q_{\text{lim.}}$, $\sigma_{\text{ten.}}$ [1, 9], studies of the boiling heat transfer crisis in capillary-porous structures of metallurgical meshes were conducted [4, 17].

A physical model of the boiling flow was constructed taking into account the joint action of capillary $\Delta P_{\text{cap.}}$ and mass $\Delta P_{\text{cap.+g}}$ forces with excess $m_{\text{l.}}/m_{\text{s.}}$. The mechanism of the heat transfer process was studied by means of holographic interferometry and high-speed motion pictures. Critical specific heat fluxes $q_{\text{cr.}}$ for different pressures $P$ were determined through integral and

*To whom all correspondence should be sent:
E-mail: *d.bondartsev@aues.kz*

thermohydraulic characterizations.

To control the energy processes, the authors of [9] propose to divide the total energy into two components: the energy of the heat wave, the explosively generated vapor nucleus, and the energy of the compressed vapor flow, which is also important for modeling and comparing to boiling processes in the pores of the structure (coating).

The cooling system of various enclosed structures [11], such as combustion chambers [19, 20] and engines [21-24], turbine nozzles [25-28], and tools in the form of rocket burners for coating, has becoming important in thermal power plants. All of the above designs utilize heat transfer.

The authors of [29-31] considered heat transfer in porous coatings in which thermal stresses act. The conditions for the action of thermal stresses $\sigma$ for the limit state of the surface were developed. The proposed model takes into account the thermomechanical properties of the coating. A complex heat transfer and stress dependence was established for different coating diameters.

However, the authors of [29-31] did not describe the effect of heat transfer and stresses in coatings nor create a calculation methodology.

Today, the task of improving the efficiency of combined energy production [32], as well as cooling the turbine combustion chamber using various coolants to increase the coefficient of performance (CoP) of machines and cycles, remains relevant.

In this paper, the authors present the main scientific and practical results of their research on natural materials, with contributions on:

- natural materials (mineral media in the form of rocks) used for thermal protection of heat-loaded structures;
- creation of a detonation torch of the thermal tool for material spraying on a heating surface.

The scientific novelty of the work includes:

- For the first time, the parameters of the high-temperature supersonic detonation jet of the burner flame were investigated depending on the type of fuel combusted, jet length, inclination angle of the torch tool, and oxidizer excess ratio.
- The phenomenon of spin detonation of the plume at an oxidizer excess ratio less than 1 was registered, and the sputtering process was intensified 2 to 6 times. The range of coating superheating was (20÷75) K. The heat transfer coefficient of the gas jet was about 5-6 times higher than that given by the laminar theory and a few percent lower than that by the law of turbulent heat transfer.

## EXPERIMENTAL STUDY OF THE PROCESS OF APPLICATION OF COATINGS BY SPRAYING

For the theoretical study of capillary-porous coatings, the authors of [6] solved a thermoelasticity problem with respect to natural mineral media (natural materials: quartzites, granites, teschenites, marbles, porphyrites, and tuffs). Formulas were derived for calculating the critical specific heat fluxes for melting, compression, and tension, as well as the corresponding thermal stresses acting within the coating [1, 9].

Burners for spraying natural materials have supersonic spin detonation jets. Further development of powder spraying processes is required to create cooling for combustion chambers and increase the efficiency of the elements.

For kerosene-oxygen thermal tools, due to the reduction of water consumption by tens of times, elimination of pumps, simplification of design, and low operating costs, the annual economic effect per one thermal tool is not less than $200-300.

The thermal spraying tool for powder coating deposition is shown in Fig. 1. It enables spraying by means of a pulsating two-phase high-temperature detonation jet. The powder consists of particles of mineral media (quartzite, granite, teschenite, marble, porphyrite, and tuff).

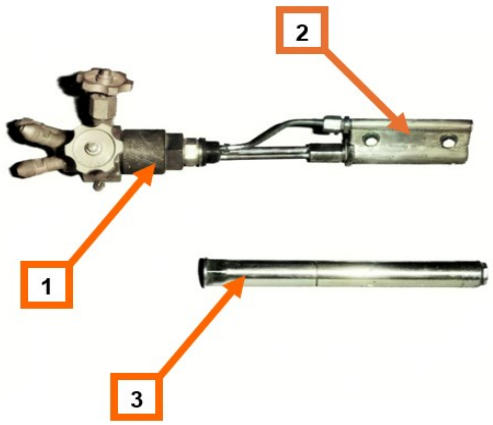


**Fig. 1.** Installation: 1 - production line, 2 - combustion chamber and nozzle, cooling system for capillary-porous coatings, 3 - casing

Fig. 2 shows an automated production flow line including four detonation torches. Powder spraying was performed on large-sized products, such as shafts with a diameter of 1 m and a length of 4.8 m, metal pipes for heating networks (external coating), balls and sliders.

**Fig. 2.** Flame pit of the production line with four machine kerosene-oxygen thermal tools, operating in automatic mode, for spraying natural materials on products.

A burner power supply circuit was assembled for conducting an experiment with a thermal tool (see Fig. 3): 1 – collector; 2 – pressure gauge; 3 – collector shut-off valve; 4 – oxygen intake shut-off valve; 5 – ramp reducer; 6 – oxygen cylinder; 7 – air cylinder; 8 – manifold pressure regulator; 9 – three-way valve; 10 – shut-off valve; 11 – water sump; 12 – water hose; 13 – air cylinder; 14 – kerosene cylinder; 15 – shut-off valve; 16 – kerosene sump; 17 – kerosene hose; 18 – plug; 19 – thermal tool; 20 – oxygen hose; 21, 25 – shut-off valves and command reducers; 22, 26 – check valves; 23, 27 – filters; 24 – reactive hose.

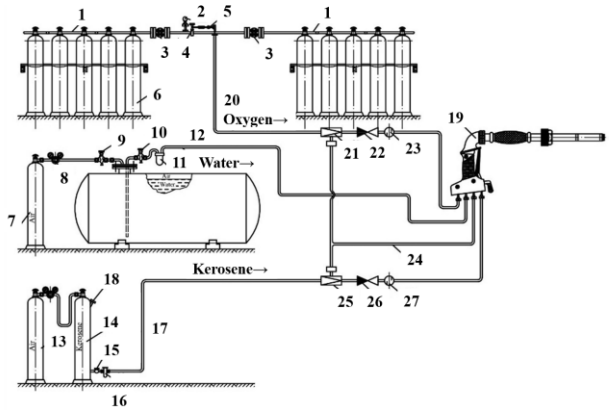


**Fig. 3.** Displacing power supply circuit of thermal tool.

The heat flows $q$ of the burner jet were measured by a sensor made of a copper cylinder, to which the heat flow of the burner jet was connected from one end, and from the other – the end of the cylinder was cooled by a heat pipe. The side surface of the cylinder was thermally insulated with ceramics based on zirconium dioxide.

Two chromel-alumel thermocouples were placed in the cylinder. The cylinder was attached to a stationary cooled barrier (coating) having an area larger than the jet braking spot area and cooled by a heat pipe. To determine the specific heat flows $q$ on the jet axis and in the braking spot (on the coating) along the radius $r$, the flow rate $G$, pressure $P$ and temperature $T$ of the cooler were measured in order to establish the heat balance. Flow rate, fuel and cooler pressure, and in-chamber pressure were also measured.

The holographic interferometry method was used to investigate the coatings. Stresses and strains were studied and recorded in real time. The photographic frequency of the interferograms was 0.5 frames per sec; 30 images were taken from each sample. Photographic prints at two-frame intervals showing the surface condition of the samples every 6 sec were obtained.

Decoding of holographic interferograms was performed according to the accepted methodology. The direction of the displacement vector $d$ was determined.

## WAYS TO CONTROL THE PROCESS OF APPLICATION OF COATING BY SPRAYING ON A METAL SUBSTRATE

- *Method of fuel combustion.* Afterburning of fuel (kerosene, gasoline) was performed on a barrier (coating). Oxidizer excess coefficient $\alpha < 1$, burner nozzle - shortened, combustion process - detonation. The afterburning process can be intensified up to two to six times. Oxidizer was added *via* jet to the coating, the fuel in the jet was in excess. Maximum specific fluxes on the barrier: from (2 to 20)×$10^6$ W/m$^2$ (Fig. 4). Application mode - without powder melting. Burners served as thermal tools.

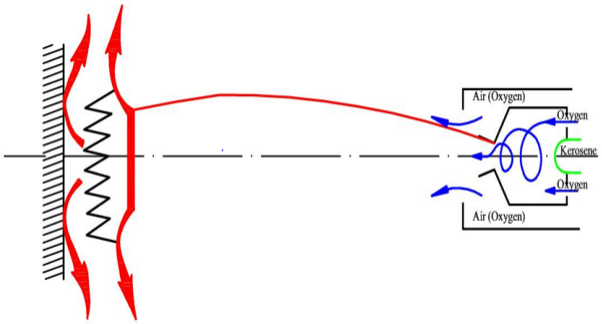


**Fig. 4.** Detonation after-burning of fuel (kerosene) on the coating surface made of natural material (granite) and a stainless steel substrate.

The afterburning scheme was constructed by observing the process using optical methods (holography, laser GL-38, and high-speed filming SKS-1M).

At gas pressure in the burner combustion chamber of 0.5 MPa (on the coating, the gas pressure is approximately the same), the frequency of pressure fluctuations in the chamber is ≈ (500÷600) Hz, and on the coating (obstacle) is reduced to 200 Hz. This enables the most intensive process of coating spraying and minimizes the possible process of its destruction. Due to supersonic flow velocity, spraying can take place without melting of powder particles.

- *Control of the length of the burner jet flowing out of the nozzle.* The dimensionless jet length is presented in Table 1. For the maximum value of the heat transfer coefficient from the jet to the coating for one of the modes we take $\alpha_1$ = 1000 W/(m$^2$×K).

**Table 1.** Dependence of $a/a_1$.

| $a/a_1$ | 0.8 | 1 | 0.7 | 0.4 | 0.3 |
|---|---|---|---|---|---|
| $z$ | 0 | 10÷30 | 40 | 50 | 60 |

For $P_{c.c}$ = 1 MPa, $z$ = (0÷0.16) m, $T$ = (3500÷850) $^0$C, $T_{st}$ = 3000 $^0$C – braking temperature (on the coating), $t_j$ = 300 $^0$C – temperature at the end of the free jet, $r_n = 3\times10^{-3}$ m, $r_j = 10\times10^{-3}$ m (jet radius).

It follows from Table 1 that, along the length of the «barrels» section of the jet, heat exchange decreases, since the boundary layer of the gas is unstable; it partially separates from the heating surface as a result of a sharp pressure fluctuation in the flow behind the wave when the jet meets the coating of this section. The velocity and temperature of the gas decrease along the length $z$.

- *Adjustment of the jet angle to the coating.* In Table 2, the following is accepted: $\alpha_{90}$ = 1000 W/(m$^2$×K); $T_{st}$ = 3500 $^0$C; $t_j$ = 300 $^0$C; $P_{c.c}$ = 1 MPa.

**Table 2.** Dependence of $a/a_{90}$.

| $a/a_{90}$ | 1 | 1.1 | 1 | 0.8 | 0.5 | 0.35 | 0.3 | 0.25 |
|---|---|---|---|---|---|---|---|---|
| $\beta$, deg | 90 | 80÷75 | 60 | 50 | 30 | 20 | 10 | 0 |

As an example, we show in Fig. 5 the texture of a teschenite surface in which a cavern of $2.5\times10^{-3}$ m in size was formed in a time of 2.2 s with $q$ equal to $1.2\times10^6$ W/m$^2$ as a consequence of heat transfer deterioration.

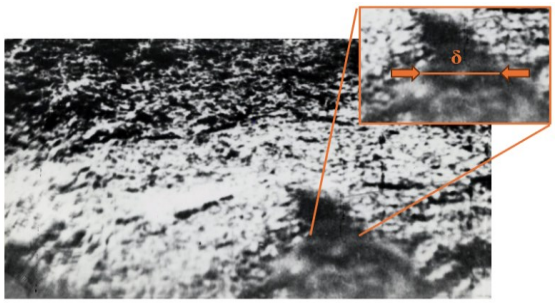


**Fig. 5.** Texture of the teschenite coating surface with a cavern as a result of thermal degradation ($\delta = 2.5\times10^{-3}$ m).

- *Regulation of the power and type of burners.* For kerosene-oxygen burners of a thermal tool, we have the following characteristics: oxygen consumption $G_{oxy}$ for pressure $P_{oxy}$ = 1.2÷1.5 MPa, m$^3$/h – 15÷18; kerosene consumption $G_{ker}$ for pressure $G_{ker}$ = 1.3÷1.5 MPa, kg/h – 10÷12; the nozzle critical diameter is $d_{nt}$, $10^{-3}$ m – 4÷5; the combustion chamber diameter is $d_{cc}$, $10^{-3}$ m – 14.

Gas-dynamic parameters of jets at the outlet of the nozzle are summarized in Table 3.

**Table 3.** Gas-dynamic parameters of jets at the outlet of the nozzle.

| $a$ | $P_{c.c}$ = 1.5 MPa | |
|---|---|---|
| | $T_g$, K | $W_g$, m/s |
| 0.7 | 2670 | 2420 |
| 0.8 | 2780 | 2410 |
| 0.9 | 2830 | 2400 |
| 1 | 2810 | 2320 |

Fig. 6 shows the technique and technology of thermal tool operation with $d_{nt} = (4\div5)\times10^{-3}$ m, $d_{cc} = 14\times10^{-3}$ m to granite impact surface. The flame structure, jet spreading radius (braking spot), the distance from the nozzle edge (outlet part) of the burner to the coating are visible.

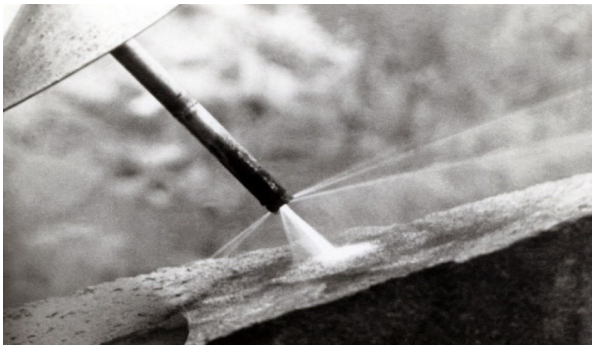

**Fig. 6.** Position of detonation supersonic flame.

Removal of cooling water from the impact surface in the form of jets was carried out for technological reasons of applying a protective coating (see Fig. 7). The protective shield is designed to protect the worker-operator of the thermal tool.

Specific heat flows $q$ on the coating surface were (5÷12) MW/m$^2$ for $r$ = 0 and $l$ = (4÷12)×10$^{-2}$ m; (2÷5) MW/m$^2$ for $r$ = 4×10$^{-2}$ m and $l$ = (4÷12)×10$^{-2}$ m.

Distribution of $q$ ($r$):

$$q\,(r) = q_{max} \times \exp\,(-1000 \times r^2),\ \mathrm{W/m^2},$$

For a more powerful burner with $d_{nt}$ = 6×10$^{-3}$ m, $d_{cc}$ = 18×10$^{-3}$ m: $G_{oxy}$ for $G_{oxy}$ = 1.8 MPa, m$^3$/h – 30÷55; $G_{ker}$ for $P_{ker}$ = (1.8-2) MPa, kg/h – 14÷18, we have $q$ ($r$ = 0) = (6÷13) MW/m$^2$.


**Fig.7.** Position of the torch to the granite processing surface: 1 - structure of the torch.

The value of heat flows $q$ can be reduced by one order when switching to another type of burner: benzo (kerosene) - air burner. Such burners are used for application of coating by spraying mineral media with a lower strength value than that of quartz or granite, for example, teschenite, porphyrite or marble.

The melting method was used to create coatings from natural and artificial mineral media (volcanic products of eruption, ashes and slags of industrial enterprises in metallurgy and power plants, tuffs). A more powerful thermal tool with a dual burner with $d_{nt}$ = 5×10$^{-3}$ m was used.

The studied thermal characteristics of coatings made of natural materials are related to high-intensity cooling systems. The comparison shows the advantages of boiling in bulk, in thin films and in heat pipes.

## RESULTS AND DISCUSSION

Studies on modern surface and coating technologies usually focus on the integrity of thermally sprayed coatings on metals and alloys under the action of tensile stresses and strains [33-35].

However, for the limiting state of natural CPCs formed of mineral media, at certain particle sizes $\delta$ and exposure times of the specific heat flux $q$, compressive stresses play a decisive role in coating failure [1, 9]. Moreover, different thermal spraying methods - atmospheric plasma spraying [36], high-velocity oxy-fuel spraying [37], and high-velocity air-fuel spraying [38] - produce different microstructures and different ratios of compressive, tensile, and shear stresses to strain.

This behavior is associated with the inter-particle bonding strength of the mineral medium, since fully or partially molten powder particles impact and solidify on the substrate, while the degree of bonding between metal particles may amount to only 20÷80% of the particle boundary surface area.

Thermally formed CPCs (see Figs. 2 and 4) are inherently anisotropic, which is advantageous during the cooling process, as capillary forces contribute more actively to the uniform distribution of the cooling fluid.

Assessment of coating stress effects reduces the probability of crack initiation during the development of new devices [4] and enables control over the propagation of critical cracks. A coating with three thermal sources acts as a screen that absorbs shock and detonation waves generated by the thermal tool jet.

Optical investigation methods [17] revealed the damage mechanisms of CPCs at the crack tip, where microstructural features lead to microscopic fracture events. A holographic experimental setup is described in [39]. As an example, interference holograms of CPCs produced from granite (Fig. 8) with a porosity of $\varepsilon$ = 5%, as well as from viscous rock with $\varepsilon$ = 30% - tuff (see Fig. 9) and marble (see Fig. 10) - are presented. Depending on the properties of the substrate material, the coatings form two media acting as thermodynamic and acoustic screens with three thermal sources, and provide control over the thermal wave penetrating the cooling surface of the combustion chamber and nozzle (see Fig. 1).

CPPs with low porosity (Fig. 8) are in a highly stressed state compared with viscous and porous media (Figs. 9 and 10). A twofold increase in q resulted in up to a threefold increase in surface strain for these coatings, whereas for samples with higher porosity the increase was only about 1.5 times. The number of interference fringes is higher for granite and marble coatings, as they exhibit higher thermal stresses.

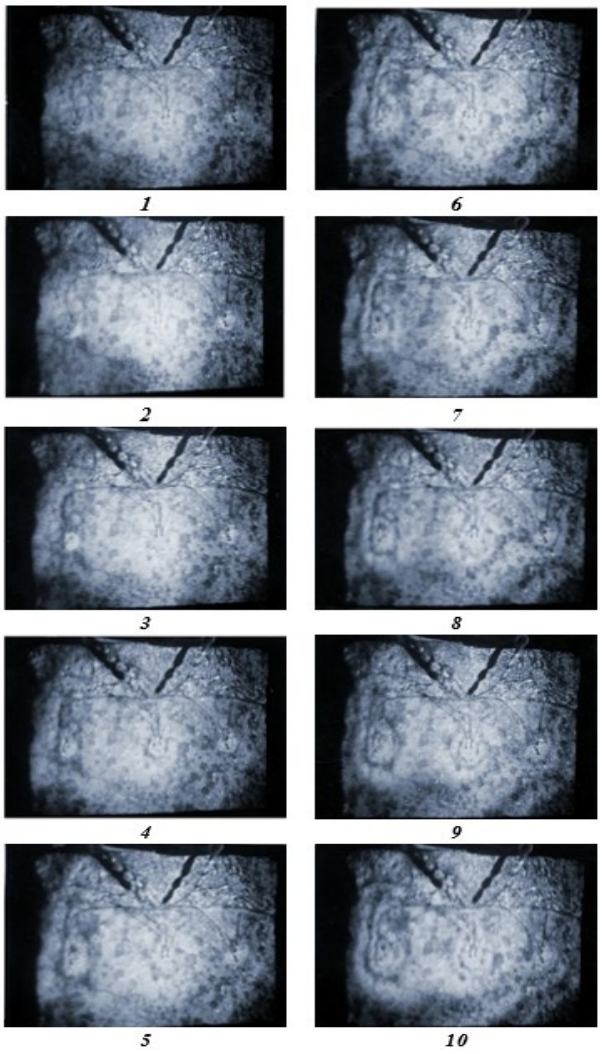


**Fig. 8.** Holographic interferograms of coatings produced of granite: 1 - $\tau$ = 6 s; 2 - $\tau$ = 12 s; 3 - $\tau$ = 18 s; 4 - $\tau$ = 24 s; 5 - $\tau$ = 30 s; 6 - $\tau$ = 36 s; 7 - $\tau$ = 42 s; 8 - $\tau$ = 48 s; 9 - $\tau$ = 54 s; 10 - $\tau$ = 60 s.

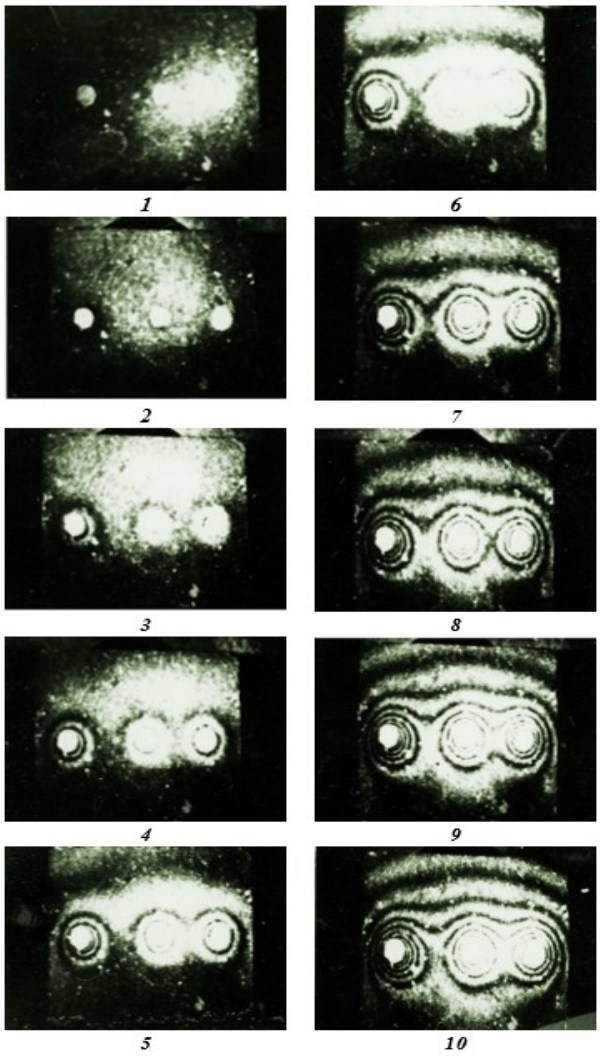


**Fig. 9.** Holographic interferograms of coatings produced of tuff: 1 - $\tau$ = 6 s; 2 - $\tau$ = 12 s; 3 - $\tau$ = 18 s; 4 - $\tau$ = 24 s; 5 - $\tau$ = 30 s; 6 - $\tau$ = 36 s; 7 - $\tau$ = 42 s; 8 - $\tau$ = 48 s; 9 - $\tau$ = 54 s; 10 - $\tau$ = 60 s.

Interferograms made it possible to detect surface defects and cracks in the coatings that were not visually observable, as well as large inclusions in whose regions the equal-strain lines exhibited discontinuities.

For interferometric investigations, the reference point is always the residual strain in the CPC, determined by a network of fine cracks that do not disappear upon removal of the thermal load.

Decoding the interferograms (Figs. 8, 9, 10) for all coatings reveals a nonlinear particle displacement curve [6], with the oxy-kerosene spraying method (see Fig. 4) offering the advantage that particle melting in the CPC is achieved using a spin detonation jet on the coating surface. This significantly reduces powder particle fracture along the boundaries of unmelted particles within the CPC.

For tuff particles, a high degree of particle melting is achieved by increasing the thermal tool power through the use of paired burners. This results in the melting of a large number of random defects formed during CPC fabrication, as well as the elimination of existing voids and caverns. The integrity of the CPC ensures the highest erosion resistance of the coating.

Strain interferograms (Figs. 8, 9, 10) demonstrate that expansion of the coating sample initially occurs around the heat source, and subsequently throughout the volume in which the temperature field is distributed. Failure of the capillary-porous material is expected when microcracks concentrate along the developing fracture zone. After this stage, the crack reaches its critical size, leading to coating failure.

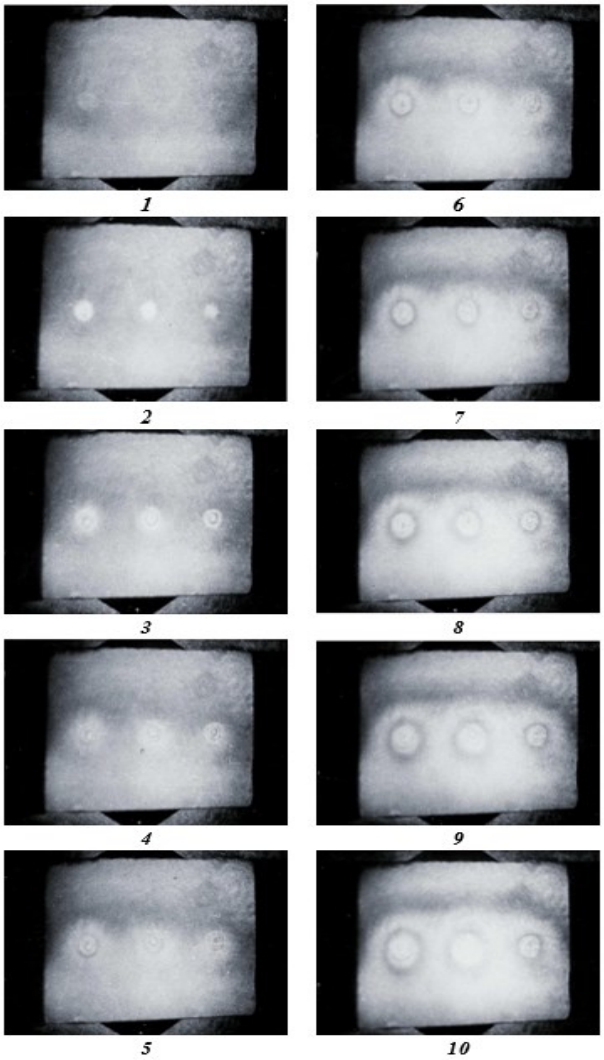


**Fig. 10.** Holographic interferograms of coatings produced of marble: 1 - $\tau$ = 6 s; 2 - $\tau$ = 12 s; 3 - $\tau$ = 18 s; 4 - $\tau$ = 24 s; 5 - $\tau$ = 30 s; 6 - $\tau$ = 36 s; 7 - $\tau$ = 42 s; 8 - $\tau$ = 48 s; 9 - $\tau$ = 54 s; 10 - $\tau$ = 60 s.

To elucidate the mechanism of coating failure, additional methods were employed, including high-speed cinematography using the SKS-1M system [39], the photoelasticity method [6], and analytical solutions of thermoelastic problems [9].

Calculation models [4] use integral values and cannot predict local failures. Optical methods, however, allow the reliability of coating performance to be forecasted. On the interferograms (see Figs. 8, 9, 10), these processes are manifested as line concentrations, including densification, pore collapse, development of tensile microcracks, layer shear, and compression, all oriented in the direction of maximum thermal stress. Optical methods enable the study of coating failure, controlling the loading rate of the specific heat flux q from seconds to hours, providing the required detailed analysis of coating rupture events.

Nonlinear fracture mechanics [1] explains the experimental results, while optical investigation methods [39, 40] reveal the physical mechanisms of material failure (damage) processes. Linear elastic fracture mechanics does not describe the limiting state of CPCs [9], nor the associated stresses, strains, displacements, or damage, since these arise from non-local inelastic energy dissipation processes near the epicenter of failure (the crack tip).

Our application of elliptical particle comminution methods [6] achieves a particle size $d$ smaller than the CPC thickness $\delta$ ($d < \delta$). In this case, a size effect becomes apparent, whereby in the notch (groove), damage tends to propagate through the full thickness, making the application of linear-elastic fracture mechanics to CPCs possible. Inelastic processes within the fracture zone will occur at the grain level d.

The inequality $\delta \gtrless d$ results in the CPC being in a transitional zone, in which neither size-independent plasticity theory nor linear-elastic fracture mechanics can provide accurate predictions, and the assumption of a homogeneous CPC does not hold. The CPC is anisotropic, which, however, is advantageous for the cooling system.

Since microcracks in mineral samples initiate from the notch (groove) and model boundaries and subsequently propagate toward the sample center, acoustic and thermodynamic screens have been constructed at the center of the CPC to compensate for crack waves [39].

The energy of the fracture process zone at the sample center where the screens are installed, is primarily expended on the formation of two new free surfaces from the viewpoint of energy dissipation under the maximum specific thermal load $q$, according to linear-elastic fracture mechanics.

Moreover, plastic processes within the sample and microcracks ahead of the crack tip also dissipate energy, demonstrating the inelastic nature of the crack tip. The combined action of these two mechanisms produces a stress-shielding effect at the crack tip [9].

Studies on the limiting state of CPCs have shown [1] that microstructural features govern the mechanisms of energy dissipation leading to macroscopic failure ($q_{max}$ and $\sigma_{max}$ in compression, tension, melting, and shear). Additionally, this model presented experimental results using high-speed cinematography.

The phenomenon of crack coalescence, which initiates in the notch (groove) and in other stress concentration regions, such as grain and particle boundaries in CPPs, propagates along the cleavage planes of the CPC, demonstrating the influence of

sample scaling. Although such studies are considered semi-blind, they allow the modelling of sample dimensions, CPC strength, and verification using optical methods [17, 39].

Experimental predictions were offered for local zones (CPP fracture cavities) and in integral form as thermal load–displacement curves, i.e., $q = f(\Delta T)$ and $q = f(\tau, \delta)$ [4, 9].

When applying the theory of the limiting state of the CPC surface (or metallic substrate) based on elastic fracture (thermoelasticity), the importance of investigating local nonlinear failure using optical methods is demonstrated; these methods must be employed during both experimentation and modelling. This is particularly important when the fracture process zone is significant relative to the size of the sample or structure.

In all studies of mineral media, the processes of modelling (or experimental prediction) and analytical calculations are semi-blind and depend on the size (geometry) of the local crack zone in the sample or coating.

For example, the effect of rock thickness (size) on the fracture process induced by the thermal jet is evident (see Fig. 6), where the thickness must exceed a critical value for «spalling» to occur. Otherwise, the processed CPC plate will fail according to scaling laws.

The analogy of the failure process across different materials follows from several considerations. The failure rate υ of the CPC is:

$$\upsilon = \frac{q}{c \cdot \rho \cdot \Delta t}, \text{ m/s}$$

where $\Delta t = t_w - t_f$.

The increase in υ with decreasing $\Delta t$ is associated with the fact that, during coating heating, the temperature at the surface $t_w$ and at the outer surface of the layer being destroyed $t_f$ become similar due to the intense heat flux $q$. This promotes volumetric failure of the coating and destruction of a layer of a given thickness.

The surface temperature of quartz and quartz-containing rocks should not exceed 1350 °C, since at temperatures of 1200÷1350 °C, $\alpha$-quartz rapidly transforms into α-cristobalite without melting, accompanied by a volumetric expansion of +17.4 %.

Another phase transformation occurs at 870 °C, where $\alpha$-quartz converts to $\alpha$-tridymite, resulting in volumetric expansion of +12.7 %.

The maximum failure rate occurs at $\Delta t$ = 100÷200 °C and $q$ > (2÷3)×10$^6$ W/m², reaching 5÷15 m/h for quartz with $\rho$ = 2500÷2700 kg/m³ and $c$ = (1÷1.2) kJ/(kg×K).

The displacement gradient which determines the magnitude of strain for a single heat source, is greatest in the region of the heater with a radius up to 10×10$^{-3}$ m and increases with prolonged thermal exposure.

Displacement distributions in the plane of the centers of three heat sources (Fig. 11) and in a plane parallel to the centers of the heat sources (Fig. 12) are presented as functions of time for the sample surface under various thermal exposures. The cooling system, implemented as coatings of natural materials, allows for an increase in the critical thermal loads for the thermal tool and the limiting state of the thermal protection coating surface.

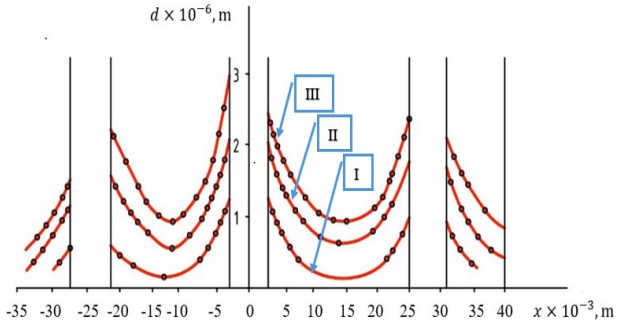


**Fig. 11.** Dependence of the displacements along the plane of the centers of three heat sources [(y = 0): I – $t$ = 15 s; II – $t$ = 25 s; III – $t$ = 30 s; angle – 38 $^0$ 55′] tuff coating surfaces for different $q$ values

The temperature gradient controls the CPC, thermotechnical properties, thermal stresses, deformations and particle movements in the coating and creates synergistic reinforcement in the graded natural material. The natural coating causes deformation of the substrate at coating temperatures when the thermal stresses are small due to adhesion or curing of the coating. The substrate will absorb dangerous tensile stresses $\sigma_{tens.}$

A different situation can also occur. The stability of mineral coatings is related to the change of tensile and compressive stresses, which we have shown by solving the thermoelastic problem [1]. If it turns out that α of the coating is larger than that of the substrate, the sign of the thermal stress will change. Therefore, it is possible to choose close values of $\alpha$ for the coating and the substrate. For example, quartz perpendicular to the axis base has $\alpha$ = 1.37×10$^{-5}$ K$^{-1}$, while marble has $\alpha$ = 1.3×10$^{-5}$ K$^{-1}$ (linear expansion coefficient).

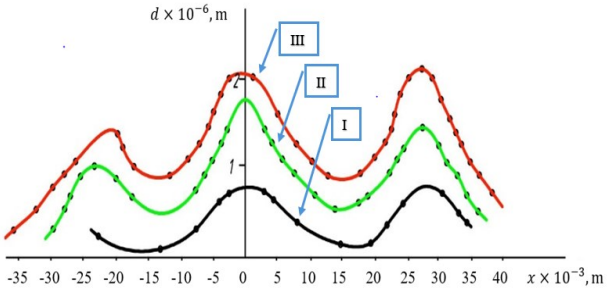


**Fig. 12.** Dependence of displacements along a plane parallel to the plane of the centers of heat sources [($y$ = $6\times10^{-3}$ m] of the tuff coating surface for different $q$ values (see Fig. 11),

In the general case we have a rather large choice not only of the value of $\alpha$, but also of the value of $\lambda$. The variation limits for rocks are given in Table 4.

**Table 4.** Limits of change in natural materials.

| | |
|---|---|
| $\lambda$, W/(m×K) | 0.2 ÷ 12 |
| $\alpha$, $K^{-1}$ | $(0.2 \div 10)\times10^{-5}$ |

An assessment of the high-intensity cooling system was conducted. The limiting thermal load ranges for CPCs composed of natural mineral media are as follows: teschenite coatings – $(2.1\div4)\times10^6$ W/m², granite coatings – $(4\div6)\times10^6$ W/m², and quartz coatings – $(6.2\div15)\times10^6$ W/m². The thermal loads were within the surface superheating range relative to the saturated steam temperature, $\Delta T = T_w - T_s = (20\div75)$ K.

Under exposure to the rocket torch jet on the CPC (see Fig. 7), the particles of the material undergoing destruction near the heating surface are in a complex stress state (see Figs. 8, 9, 10). They simultaneously experience compressive, tensile, and bending deformations [6].

Compressive stresses $\sigma_{comp}$ are greatest in the heated layer (Fig. 13). As the distance from the heated CPC increases ($l$ grows), these stresses rapidly decrease, transform into tensile stresses $\sigma_{tens}$, reach a maximum at a certain distance, and then diminish. In other words, the criterion $(\alpha\times l)/\lambda$ (the Nusselt number) increases, where $\alpha$ is the heat transfer coefficient, $l$ is the distance from the jet to the CPC, and $\lambda$ is the thermal conductivity of the coating.

For a CPC material with thermal conductivity $\lambda$ and heat transfer coefficient $\alpha$, there exists a minimum layer thickness. If the material thickness is less than $L$ (the calculated thickness of the material undergoing destruction), no $\sigma_f$ due to spalling develops within the material. The critical thickness $l_{cr}$ is several mm (determined from Figs. 11 and 12).

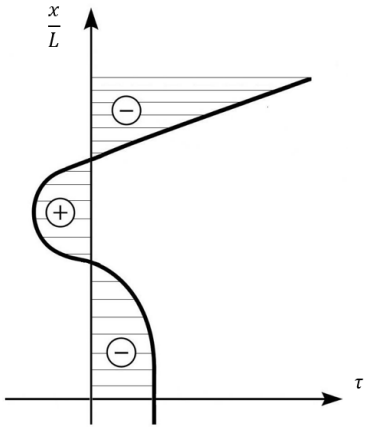


**Fig. 13.** Diagram of the distribution of compressive and tensile stresses in the heated layer of the CPC

The calculated thickness of the CPC undergoing destruction corresponds to the portion of the rock layer involved in deformation during which destructive stresses develop, which depends on the coating properties and the jet parameters.

At high $q$ [4, 17] and $\alpha$, stresses $\sigma$ appear instantly in the heated layer, rapidly reaching maximum values. Then, they quickly decrease, approaching the lower limit (see Fig. 13).

Thus, the greatest compressive stresses arise at the heated surface. These stresses decrease with distance from the surface, transform into tensile stresses, increase to a maximum, and then decrease again, becoming low compressive stresses at greater depths. At high $q$ values (see Fig. 13), CPC failure may occur due to chipping or shear stresses induced by compression. Typically, CPC failure manifests as detachment of particles from the coating surface (see Figs. 8, 9, 10).

The cross-sections where $\sigma_f^{max}$ occurs are located at 0.2÷0.3 of the calculated thickness from the heated surface, depending on $\tau$ and $\lambda$.

For $(\alpha\times L)/\lambda = 1$, $\sigma_f/\sigma_{comp} = 0.52$, while for $(\alpha\times L)/\lambda = 20 \rightarrow \sigma_f/\sigma_{comp} = 0.3$. The CPC layer must develop sufficient destructive stresses within a time $\tau$ equal to or less than that required to reach the maximum possible stress under the given conditions, i.e., $\tau_f^{comp} \le \tau_f^{comp.max}$; $\tau_f^{ten} \le \tau_f^{ten.max}$.

The values of $q$ and $\alpha$ must be such that stresses in the layer, and consequently its failure, occur before the maximum allowable stresses are reached. With increasing $q$ and $\alpha$, it is necessary to account for the delayed occurrence of $\sigma_f^{max}$ relative to the onset of surface heating; otherwise, in viscous CPCs (Fig. 10), premature melting of the material may occur.

## CONCLUSIONS

1. Efficient and controllable spraying of coatings made of various natural materials was achieved due to the dynamic characteristics of the detonation torch of thermal tools. The main parameters of coatings were identified and ways to control the spraying processes were investigated.

2. Dependencies for porous coatings under thermal loads are useful for predicting the performance of equipment (nozzles and combustion chambers), and the strain concentration in the coating was studied at thermal loads up to $4.2\times10^6$ W/m$^2$.

3. The cooling system showed high efficiency up to the critical state of the metal of combustion chambers and nozzles ($5\times10^6$ W/m$^2$).

4. The developed surfaces in the form of coatings and mesh structures provide positive effects due to the advantage of joint technologies for their fabrication with the expansion of the dissipated thermal loads and control of the coating condition.

## NOMENCLATURE

*$l$ – distance from the nozzle section to the coating, m;*
*$z$ – jet abscissa, m;*
*$\alpha$ – oxidizer excess factor, heat transfer factor, W/(m$^2$×K);*
*$\varepsilon$ – porosity;*
*$\sigma$ – thermomechanical stresses, Pa;*
*$q$ – specific heat flux, W/m$^2$;*
*$q_{cr}$ – critical (limit) heat flow, W/m$^2$;*
*$\delta$ – coating thickness, particle size, m;*
*$\tau_i$ – time, s;*
*$P$ – pressure, Pa;*
*$R_{ox}$, $R_{ker}$ – pressure of oxygen, kerosene, Pa;*
*$P_{c.c.}$ – pressure in the combustion chamber, Pa;*
*$r$ – radius of the braking spot, m;*
*$n$ – efficiency factor of a heat power plant.*

## REFERENCES


1. A. A. Genbach, D. Yu. Bondartsev, I. K. Iliev, *Bulgarian Chemical Communications*, **50**, 133 (2018).
2. Z. Ting, L. Xianglong, W. Jianguo, H. Qiwen, T. Zihao, H. Tao, *Engineering Failure Analysis*, **163**, 108584 (2024) https://doi.org/10.1016/j.engfailanal.2024.108584
3. Z. Yan, M. Chunchi, G. Yaohui, M. Kai, *Transportation Geotechnics*, **47**, 101270 (2024) https://doi.org/10.1016/j.trgeo.2024.101270
4. A. Genbach, H. Beloev, D. Bondartsev, *Energies*, **14**, 6365 (2021) https://doi.org/10.3390/en14196365
5. W. Chen, W. Liu, Y. Liang, *Fluid Dynamics and Materials Processing*, **20**(4), 859 (2024) https://doi.org/10.32604/fdmp.2023.029310
6. A. A. Genbach, D. Y. Bondartsev, *Russian Engineering Research*, **40**, 384 (2020) https://doi.org/10.3103/S1068798X20050093
7. C. Ramadji, A. Messan, E. Prud'Homme, *Materials*, **13**, 5406 (2020) https://doi.org/10.3390/ma13235406
8. W. Ju, D. Feng, L. Yi, T. Hao, Z. Pan, *Journal of Rock Mechanics and Geotechnical Engineering*, volume, page (2024) https://doi.org/10.1016/j.jrmge.2024.09.007
9. A. Genbach, D. Bondartsev, I. Iliev, A. Terziev, *E3S Web of Conferences*, **85**, 05003 (2019) https://doi.org/10.1051/e3sconf/20198505003
10. A. A. Askalany, S. J. Ernst, P. C. Hügenell, H. J. Bart, S. K. Henninger, A. S. Alsaman, *Energy*, **141**, 782e91 (2017) https://doi.org/10.1016/j.energy.2017.07.171
11. National Research Council. Coatings for high-temperature structural materials: trends and opportunities. Washington, DC: The National Academies Press (1996) https://doi.org/10.17226/5038
12. O. S. Sanjay, B. N. Prasad, *Applied Thermal Engineering*, **28** (17-18), 2315 (2008) https://doi.org/10.1016/j.applthermaleng.2008.01.022
13. M. Heyang, W. Zhongwei, N. Yaobin, *Applied Thermal Engineering*, **179**, 115751 (2020) https://doi.org/10.1016/j.applthermaleng.2020.115751
14. S.S. Baakeem, J. Orfi, H. Al-Ansary, *Applied Thermal Engineering*, **138**, 417 (2018) https://doi.org/10.1016/j.applthermaleng.2018.04.018
15. W. Wróblewski, *Applied Thermal Engineering*, **51** (1-2), 953 (2013) https://doi.org/10.1016/j.applthermaleng.2012.10.048
16. G. Jian-Jun, C. Yue, Y. Zheng-Wei, C. Bing, G. Chun-Lin, *Applied Thermal Engineering*, **159**, 113938 (2019) https://doi.org/10.1016/j.applthermaleng.2019.113938
17. A. A. Genbatch, D. Y. Bondartsev, *News of the National Academy of Sciences of the Republic of Kazakhstan-Series of Geology and Technical Sciences*, **2**, 81 (2018).
18. P. Vögelin, G. Georges, K. Boulouchos, *Energy*, **125**, 356 (2017) https://doi.org/10.1016/j.energy.2017.02.113
19. P. Zlateva, N. Penkova, K. Krumov, Analysis of combustion efficiency at boilers operating on different fuels, *Proceedings 7th International Conference on Energy Efficiency and Agricultural Engineering*, 9278784 (2020) https://doi.org/10.1109/EEAE49144.2020.9278784
20. Q. Fu, W. Song, G. Jiao, *Energy*, **266**, 126438 (2023) https://doi.org/10.1016/j.energy.2022.126438
21. Z. Wang, Y. Feng, F. Chen, J. Qin, *Energy*, **314**, 134166 (2025) https://doi.org/10.1016/j.energy.2024.134166
22. K. M. Kim, Y. H. Jeon, N. Yun, D. H. Lee, H. H. Cho, *Energy*, **36**(2), 942 (2011) https://doi.org/10.1016/j.energy.2010.12.016
23. K. Yordanov, T. Mechkarova, A. Stoyanova, P. Zlateva, in: A. Abraham, S. Kovalev, V. Tarassov,

V. Snasel, M. Vasileva, A. Sukhanov (eds.) Proceedings of the Second International Scientific Conference «Intelligent Information Technologies for Industry» (IITI'17). IITI 2017. Advances in Intelligent Systems and Computing, 680 (2018) https://doi.org/10.1007/978-3-319-68324-9-44
24. J. Xu, K. Cheng, C. Dang, Y. Wang, Z. Liu, J. Qin, X. Liu, *Energy*, **275**, 127488 (2023) https://doi.org/10.1016/j.energy.2023.127488
25. W. Wang, J. Gao, X. Shi, L. Xu, Cooling performance analysis of steam cooled gas turbine nozzle guide vane, *Int. J. of Heat & Mass Transfer*, **62**, 668 (2013), https:// doi.org/10.1016/j.ijheatmasstransfer.2013.02.080
26. S. W. Moon, H. M. Kwon, T. S. Kim, D. W. Kang, J. L. Sohn, *Energy*, **160**, 625 (2018) https://doi.org/10.1016/j.energy.2018.07.035
27. X. Yang, Z. Liu, Z. Feng, T. Simon, *Int. J. of Heat & Mass Transfer*, **140**, 25 (2019) https://doi.org/10.1016/j.ijheatmasstransfer.2019.05.109
28. W. Wang, *Int. J. of Heat & Mass Transfer*, **80**, 217 (2015) https://doi.org/10.1016/j.ijheatmasstransfer.2014.09.024
29. R. Boubaker, V. Platel, *Energy*, **111**, 402 (2016) https://doi.org/10.1016/j.energy.2016.05.102
30. G. Lei, W. Li, Q. Wen, *International Journal of Thermal Sciences*, **137**, 55 (2019) https://doi.org/10.1016/j.ijthermalsci.2018.11.017
31. N. Xu, X. Yu, Z. Liu, T. Zhang, H. Chu, *Energy*, **294**, 130818 (2024) https://doi.org/10.1016/j.energy.2024.130818
32. P. Zlateva, A. Terziev, M. Murzova, N. Mileva, M. Vassilev, *Energies*, **18**(15), 4153 (2025) https://doi.org/10.3390/en18154153
33. A. Idir, R. Younes, M. A. Bradai, A. Sadeddine, L. Baiamonte, G. Pintaude, *Coatings*, **13**, 878 (2023) https://doi.org/10.3390/coatings13050878
34. A. Wypych, T. Jankowiak, W. Sumelka, *Materials*, **16**, 7566 (2023) https://doi.org/10.3390/ma16247566
35. R. Bhaskaran Nair, R. Supekar, S. Morteza Javid, W. Wang, Y. Zou, A. McDonald, J. Mostaghimi, P. Stoyanov, *Metals*, **13**, 579 (2023) https://doi.org/10.3390/met13030579
36. M. Bellippady, S. Björklund, X. H. Li, R. Frykholm, B. Kjellman, S. Joshi, N. Markocsan, *Coatings*, **14**, 626 (2024) https://doi.org/10.3390/coatings14050626
37. M. Oksa, E. Turunen, T. Suhonen, T. Varis, S. P. Hannula, *Coatings*, **1**, 17 (2011) https://doi.org/10.3390/coatings1010017
38. A. Garfias Bulnes, V. Albaladejo Fuentes, I. Garcia Cano, S. Dosta, *Coatings*, **10**, 1157 (2020) https://doi.org/10.3390/coatings10121157
39. A. A. Genbach, D. Yu. Bondartsev, H. I. Beloev, *IOP Conf. Ser.*: *Mater. Sci. Eng.*, **1032**, 012039 (2021) doi:10.1088/1757-899X/1032/1/012039
40. A. Javan, W. R. Bennet, D. Herriot, *Physical Review Letters*, **6**, 106 (1961) https://doi.org/10.1103/PhysRevLett.6.106

Acknowledgement to Reviewers for vol. 57 (2025)

The Editors of Bulgarian Chemical Communications would like to take this opportunity to thank you for the effort and expertise that you contributed to reviewing, without which it would be impossible to maintain the high standards of our journal:

**A**

A. Addane
A.K. Tivari
A. Nikolov
A. Yoleva

**B**

B. Traikovska

**D**

D. Damyanova
D. Doykov
D. Karashanova
D. Levi
D. Pashkouleva
D. Todorovski

**E**

E. Kirilova
E. S. Agorku
E. Udochukwu
E. Zhecheva

**F**

F.A. Mohammad

**G**

G. Antova
G. Nikolova
G. N. Petkova
G. Zsivanovits

**H**

H. S. Yogananda

**I**

I. Ivanov

**K**

K. Akatan
K. Boschnakov
K. Gouthami

**M**

M. Boumediene
M. Dimov
M. Pandev
M. Ruskova
M. Shamil
M. Stancheva
M. Tsvetkov

**R**

R. Stateva
R. Vladova
Raj Kumar Arya
Rui-Zhi Cui

**S**

S. Angelova
S. Atanasova
S. Pyrvanova-Yoncheva
S. V. Patil
S. Venkatesh
St. Baycheva

**N**

N. Kantay
N. Panayotov

**P**

P. Dineva
P. Popova-Krumova
P. Randhavane

**T**

T. Dodevska
T. Petrova
Ts. Dimitrov
Ts. Rangelov

**V**

V. Beschkov
V. Kumar Sohpal
V. Raykova
V. Slavova

**Z**

Z. Denkova
Z. N. Nazif

## Instructions about Preparation of Manuscripts

***General remarks:*** Manuscripts are submitted in English by e-mail. The text must be prepared in A4 format sheets using Times New Roman font size 11, normal character spacing. The manuscript should not exceed 15 pages (about 3500 words), including photographs, tables, drawings, formulae, etc. Authors are requested to use margins of 2 cm on all sides.

Manuscripts should be subdivided into labelled sections, e.g. INTRODUCTION, EXPERIMENTAL, RESULTS AND DISCUSSION, etc. **The title page** comprises headline, author(s)' names and affiliations, abstract and key words. Attention is drawn to the following:

a) **The title** of the manuscript should reflect concisely the purpose and findings of the work. Abbreviations, symbols, chemical formulae, references and footnotes should be avoided. If indispensable, abbreviations and formulae should be given in parentheses immediately after the respective full form.

b) **The author(s)'** first and middle name initials and family name in full should be given, followed by the address (or addresses) of the contributing laboratory (laboratories). **The affiliation** of the author(s) should be listed in detail (no abbreviations!). The author to whom correspondence and/or inquiries should be sent should be indicated by an asterisk (*) with e-mail address.

**The abstract** should be self-explanatory and intelligible without any references to the text and containing up to 250 words. It should be followed by keywords (up to six).

**References** should be numbered sequentially in the order, in which they are cited in the text. The numbers in the text should be enclosed in brackets [2], [5, 6], [9−12], etc., set on the text line. References are to be listed in numerical order on a separate sheet. All references are to be given in Latin letters. The names of the authors are given without inversion. Titles of journals must be abbreviated according to Chemical Abstracts and given in italics, the volume is typed in bold, the initial page is given and the year in parentheses. Attention is drawn to the following conventions: a) The names of all authors of a certain publications should be given. The use of "et al." in the list of references is not acceptable; b) Only the initials of the first and middle names should be given. In the manuscripts, the reference to author(s) of cited works should be made without giving initials, e.g. "Bush and Smith [7] pioneered...". If the reference carries the names of three or more authors it should be quoted as "Bush et al. [7]", if Bush is the first author, or as "Bush and co-workers [7]", if Bush is the senior author.

**Footnotes** should be reduced to a minimum. Each footnote should be typed double-spaced at the bottom of the page, on which its subject is first mentioned. **Tables** are numbered with Arabic numerals on the left-hand top. Each table should be referred to in the text. Column headings should be as short as possible but they must define units unambiguously. The units are to be separated from the preceding symbols by a comma or brackets. Note: The following format should be used when figures, equations, etc. are referred to the text (followed by the respective numbers): Fig., Eqns., Table, Scheme.

**Schemes and figures.** Each manuscript should contain or be accompanied by the respective illustrative material, as well as by the respective figure captions in a separate file. As far as presentation of units is concerned, SI units are to be used. However, some non-SI units are also acceptable, such as °C, ml, l, etc. Avoid using more than 6 (12 for review articles) figures in the manuscript. Since most of the illustrative materials are to be presented as 8-cm wide pictures, attention should be paid that all axis titles, numerals, legend(s) and texts are legible.

***The authors are required to submit the text with a list of three individuals and their e-mail addresses that can be considered by the Editors as potential reviewers. Please note that the reviewers should be outside the authors' own institution or organization. The Editorial Board of the journal is not obliged to accept these proposals.***

The authors are asked to submit **the** final text (after the manuscript has been accepted for publication) in electronic form by e-mail. The main text, list of references, tables and figure captions should be saved in separate files (as *.rtf or *.doc) with clearly identifiable file names. It is essential that the name and version of the word-processing program and the format of the text files is clearly indicated. It is recommended that the pictures are presented in *.tif, *.jpg, *.cdr or *.bmp format. The equations are written using "Equation Editor" and chemical reaction schemes are written using ISIS Draw or ChemDraw programme.

**EXAMPLES FOR PRESENTATION OF REFERENCES**

REFERENCES

1. D. S. Newsome, Catal. Rev.–Sci. Eng., 21, 275 (1980).
2. C.-H. Lin, C.-Y. Hsu, J. Chem. Soc. Chem. Commun., 1479 (1992).
3. R. G. Parr, W. Yang, Density Functional Theory of Atoms and Molecules, Oxford Univ. Press, New York, 1989.
4. V. Ponec, G. C. Bond, Catalysis by Metals and Alloys (Stud. Surf. Sci. Catal., vol. 95), Elsevier, Amsterdam, 1995.
5. G. Kadinov, S. Todorova, A. Palazov, in: New Frontiers in Catalysis (Proc. 10th Int. Congr. Catal., Budapest (1992), L. Guczi, F. Solymosi, P. Tetenyi (eds.), Akademiai Kiado, Budapest, 1993, Part C, p. 2817.
6. G. L. C. Maire, F. Garin, in: Catalysis. Science and Technology, J. R. Anderson, M. Boudart (eds.), vol. 6, Springer Verlag, Berlin, 1984, p. 161.
7. D. Pocknell, GB Patent 2 207 355 (1949).
8. G. Angelov, PhD Thesis, UCTM, Sofia, 2001, pp. 121-126.
9. JCPDS International Center for Diffraction Data, Power Diffraction File, Swarthmore, PA, 1991.
10. CA 127, 184 762q (1998).
11. P. Hou, H. Wise, J. Catal., in press.
12. M. Sinev, private communication.
13. http://www.chemweb.com/alchem/articles/1051611477211.html.

***Texts with references which do not match these requirements will not be considered for publication!!!***

CONTENTS